Doctoral Thesis

Non-Precious Metal Catalysts Based on Carbon Nanomaterials for Oxygen and Hydrogen Electrocatalysis

Young Jin Sa

Department of Chemistry

Graduate School of UNIST

2018

Non-Precious Metal Catalysts Based on Carbon Nanomaterials for Oxygen and Hydrogen Electrocatalysis

Young Jin Sa

Department of Chemistry

Graduate School of UNIST

Non-Precious Metal Catalysts Based on Carbon Nanomaterials for Oxygen and Hydrogen Electrocatalysis

A thesis/dissertation
submitted to the Graduate School of UNIST
in partial fulfillment of the
requirements for the degree of
Doctor of Philosophy of Science

Young Jin Sa

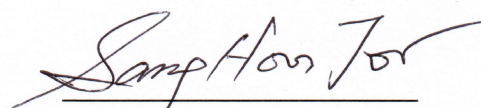11. 30. 2017 of submission
Approved by

_____

Advisor
Sang Hoon Joo

Non-Precious Metal Catalysts Based on Carbon Nanomaterials for Oxygen and Hydrogen Electrocatalysis
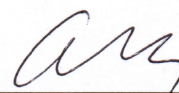
Young Jin Sa

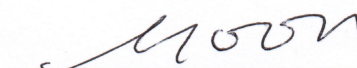This certifies that the dissertation of Young Jin Sa is approved.
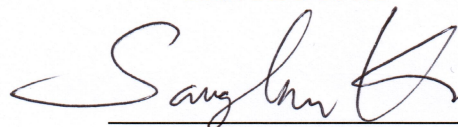
11. 30. 2017 of submission

Advisor: Sang Hoon Joo

Hyeon Suk Shin

Hoi Ri Moon

Sang Kyu Kwak

Ji-Wook Jang

Abstract

The environmental issues caused by the hydrocarbon energy sources have emerged as one of the most urgent challenges in 21st century. The development of clean and renewable energy technologies is critical to meet both the environment regulations and to circumvent dependence upon the fossil fuels. This situation has brought a new idea about the future society solely driven by hydrogen-based energy infrastructures, so-called hydrogen economy. The production and utilization of hydrogen *via* water electrolysis and fuel cells, respectively, are key ingredients to realize the hydrogen economy. However, the high cost of those devices hinders their wide adoption, which can be attributed primarily to the use of precious metal electrocatalysts such as Pt and Ir that are required for efficient operation. In this context, the development of active non-precious metal catalysts (NPMCs) is of great significance.

In this dissertation, new NPMCs based on carbon nanotube (CNT) have been designed and prepared for oxygen reduction reaction (ORR), oxygen evolution reaction (OER), and hydrogen evolution reaction (HER), where the ORR is an important half-reaction that critically affects the fuel cell performance, while the OER & HER are involved in water electrolysis. CNT was selected as the carbon support owing to its high conductivity, chemical stability, and surface tunability, advantageous for electrocatalysis.

In Chapter 2, we developed a facile and scalable synthetic method for carbon nanostructures comprising active heteroatom-doped carbon (HDC) layers coated on CNT (CNT/HDC), which was exploited as a metal-free ORR electrocatalyst. The preparation involves the adsorption of heteroatom-containing ionic liquid (IL) on the CNT walls *via* van der Waals and cationic-π interactions and subsequent carbonization, yielding CNT/HDC core–sheath nanostructures. The design enables both the efficient utilization of surface active sites of HDC layers and high electric conductivity of the CNT core. The CNT/HDC catalyst exhibited high ORR activity and reaction kinetics comparable to a commercial Pt/C catalyst in alkaline media, and an excellent anion exchange membrane fuel cell (AEMFC) performance. The IL-derived CNT/HDC catalysts could be prepared using various types of IL precursors.

Iron and nitrogen codoped carbon (Fe–N/C) catalysts have emerged as the most promising electrocatalysts for the ORR among various classes of NPMCs. A growing body of literature suggests that Fe–N_x species are major active sites in a Fe–N/C catalyst. Chapter 3 presents a general "silica-protective-layer-assisted" approach that can preferentially generate the catalytically active Fe–N_x sites in Fe–N/C catalysts while suppressing the formation of less-active large Fe-based particles. The catalyst preparation consisted of the adsorption of iron porphyrin precursor on CNT, silica layer

overcoating, high-temperature pyrolysis, and silica layer etching, which yielded CNTs coated with thin layers of porphyrinic carbon (CNT/PC) catalysts. We found that the silica-coating step plays a decisive role in preferentially generating catalytically active Fe–N$_x$ coordination sites, as revealed by temperature-controlled *in situ* X-ray absorption spectroscopy (XAS). The CNT/PC catalyst contained higher concentration of active Fe–N$_x$ sites compared to the CNT/PC prepared without silica coating. The CNT/PC showed very high ORR activity and excellent stability in alkaline media. Importantly, an alkaline AEMFC with a CNT/PC-based cathode exhibited the highest current and power densities among NPMC-based AEMFCs. In addition, a CNT/PC-based cathode exhibited a high volumetric current density of 320 A cm^{-3} in acidic proton exchange membrane fuel cell. We also demonstrated the general applicability of this synthetic strategy to other carbon supports.

Chapter 4 describes the investigation of active site structures of bifunctional oxygen electrode catalysts based on cobalt oxide (CoO$_x$) under reaction conditions. Size-controlled (3–10 nm) cobalt oxide nanoparticles (CoO$_x$ NPs) supported on CNT were prepared, and served as model catalysts. Electrochemical *in situ* XAS suggested that the initial Co$_3$O$_4$ or CoO phase was transformed to Co$_3$O$_4$–CoOOH core–shell structures under the ORR and OER conditions regardless of particle sizes. Combined with the *in situ* XAS, cyclic voltammetry study revealed that Co^{2+}/Co^{3+} and Co^{3+}/Co^{4+} redox transitions are involved in the ORR and OER, respectively. We further examined the size-dependent electrocatalytic activities. The OER activity increased with decreasing NP size, which correlated to the larger amount of Co(III) species and larger surface area in smaller NPs. For the ORR, no particle size dependence was found; the CoO$_x$ NPs mainly played an auxiliary role, promoting the reduction or disproportionation of peroxide generated from the two-electron reduction of O$_2$ by CNT.

In Chapter 5, we investigated the active site structure of NPMC comprising cobalt- and nitrogen-codoped carbon supported on CNT for the HER. For this purpose, CNT hybridized with cobalt phthalocyanic carbons (CNT/Co-PcC) were prepared *via* the silica coating strategy. A suite of Co–N/C catalysts that contain different concentrations of cobalt-based species (Co–N$_x$ and Co@C) were prepared by controlling experimental parameters. The catalytic role of two Co-based sites for the HER in both acidic and alkaline media was investigated, which revealed that the HER activity in both media was linearly increased with the portion of the Co−N$_x$ sites. This structure–activity relationship suggests that the Co–N$_x$ sites are the major active sites while Co@C species have a minimal catalytic effect for the HER. In addition, reaction kinetics study over the CNT/Co-PcC catalyst allowed us to acquire a better understanding of the Co–N$_x$ active sites for the HER.

Contents

List of Tables

List of Figures

List of Abbreviations

AB	Acetylene black
AEMFC	Anion exchange membrane fuel cell
AR-TEM	Atomic-resolution transmission electron microscopy
b	Tafel slope
BET	Brunauer–Emmett–Teller
CA	Chronoamperometry
C_{dl}	Double layer capacitance
CN	Coordination number
CNT	Carbon nanotube
$Co^{II}Pc$	Cobalt(II) phthalocyanine
CP	Chronopotentiometry
CV	Cyclic voltammetry
CVD	Chemical vapor deposition
DI	Deionized
DOE	Department of energy
E	Potential
E_a	Activation energy
ECSA	Electrochemically active surface area
EELS	Electron energy loss spectroscopy
EIS	Electrochemical impedance spectroscopy
EXAFS	Extended X-ray absorption fine structure
F	Faraday constant (96,485 C mol^{-1})
$Fe^{III}TMPPCl$	5,10,15,20-tetrakis(4-methoxyphenyl)-21H,23H-porphine iron(III) chloride
FFT	Fast Fourier transform
GC	Glassy carbon
HAADF-STEM	High-angle annular dark-field scanning transmission electron microscopy
HER	Hydrogen evolution reaction
HOR	Hydrogen oxidation reaction
HR-TEM	High-resolution transmission electron microscopy
i/j	Current / current density
i_0/j_0	Exchange current
ICP-OES	Inductively coupled plasma optical emission spectrometry
i_d	Disk current
i_k/j_k	Kinetic current / kinetic current density
IL	Ionic liquid
i_l/j_l	Diffusion-limited (or Levich) current / diffusion-limited current density
i_r	Ring current

KB	Ketjen black
LCF	Linear combination fitting
LSV	Linear sweep voltammetry
MEA	Membrane electrode assembly
M–N/C	Metal- and nitrogen-codoped carbon
n	Electron transfer number
N	Collection efficiency
NHE	Normal hydrogen electrode
NP	Nanoparticle
NPMC	Non-precious metal catalyst
OCV	Open circuit voltage
OER	Oxygen evolution reaction
ORR	Oxygen reduction reaction
PEFC	Polymer electrolyte fuel cell
PEM	Proton exchange membrane
PEMFC	Proton exchange membrane fuel cell
R	Universal gas constant (8.314 J mol^{-1} K^{-1})
RDE	Rotating disk electrode
RDF	Radial distribution function
rGO	Reduced graphene oxide
RH	Relative humidity
RHE	Reversible hydrogen electrode
RRDE	Rotating ring disk electrode
RT	Room temperature
SCE	Saturated calomel electrode
SHE	Standard hydrogen electrode
T	Temperature
TEM	Transmission electron microscopy
TEOS	Tetraethyl orthosilicate
TOF	Turnover frequency
XANES	X-ray absorption near edge structure
XAS	X-ray absorption spectroscopy
XPS	X-ray photoelectron spectroscopy
XRD	X-ray diffraction
α	Charge transfer coefficient
η	Overpotential

1

GENERAL INTRODUCTION

1.1. HYDROGEN ECONOMY

Since the industrial revolution in the 18th century, hydrocarbons have been the primary source of power sources for our planet. Most human activities are strongly dependent on fossil fuels, on which well-established technologies and industries are based. Consequently, the use of hydrocarbons (coal, oil, and natural gas) accounted for over 85% of the world energy consumption in 2016.[1] In addition, annual energy consumption has increased by 18% from 2006, and has been estimated to increase further by 28% until 2040,[1,2] suggesting continued dependence on fossil fuels. Thus far, increasing energy demand has been satisfied by hydrocarbons through the development of extractive technology. However, we need to prepare alternatives to limited natural resources that are at risk of eventual depletion. In terms of environment, CO_2 gas emitted from the combustion of fossil fuels facilitates climate change, resulting in the worldwide consensus to reduce the amount of carbon emissions. In addition, combustion of fossil fuels produces air pollutants such as NO_x, SO_x, and unburned hydrocarbons which can potentially decrease life expectancy.

Hydrogen has been considered an ideal energy carrier due to its high specific energy (120 kJ g^{-1}) and environmentally benign nature.[3] Hydrogen economy, first officially stated by John Bockris, is a proposed society where the energy distribution is based on hydrogen instead of hydrocarbons.[4] Three key components built into the hydrogen economy are hydrogen production, storage/delivery, and utilization (**Figure 1.1**), none of which should include carbon-based process to achieve zero-carbon energy cycles. Water electrolysis for H_2 production is powered by renewable energies like sunlight and wind. H_2 is then stored physically (e.g. compression and liquefaction) and materially (porous materials and metal hydrides) and distributed. Finally, the energy in H_2 is converted to electricity *via* fuel cells, completing the hydrogen cycle. Only water and oxygen are circulated around the earth in a hydrogen economy (**Figure 1.1**), enabling unlimited supply/usage and therefore realizing pollution-free energy civilization. However, the efficiency of each component is still not high enough for the system to be advantageous over the currently used hydrocarbon energy infrastructure. Therefore, technological advances are imperative.
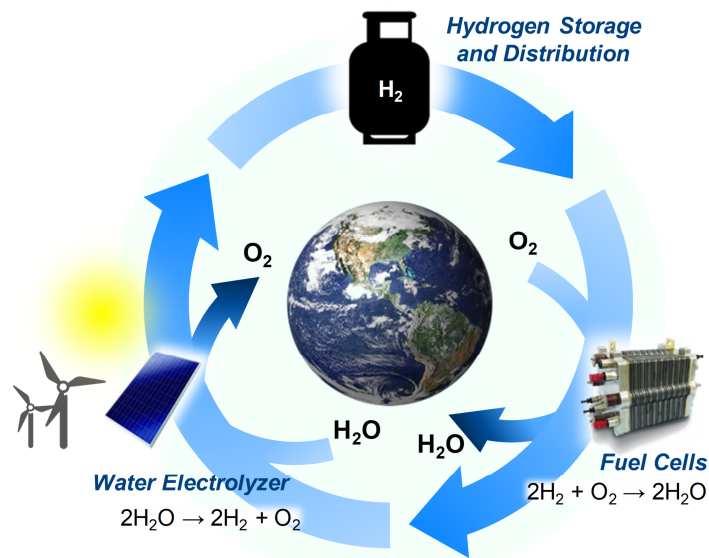
Figure 1.1. A simple schematic description for the hydrogen cycle consisting of H_2 production by renewable energies, storage/transportation, and utilization by fuel cells. Earth illustration by DonkeyHotey (https://www.flickr.com/photos/donkeyhotey/5679642883) and windmill icon designed by Vexels (https://www.vexels.com/png-svg/preview/132696/windmill-icon) were used under a Creative Common license.

1.2. FUEL CELL

1.2.1. Introduction to Fuel Cell

Fuel cells convert the chemical energy in a fuel (hydrogen and oxygen) into electricity. Unlike combustion engines, the direct conversion of energy enables the efficient operation of the fuel cell with an efficiency of 40–60%.[5] The remainder of the input energy is dissipated as heat which can also be utilized (so-called combined heat and power; CHP), leading to increase in efficiency up to 80%. Due to minimal mechanical motions, fuel cells barely produce noise and vibration. Most importantly, water is produced as the only by-product, never damaging the nature.

Fuel cells are categorized into several types depending on the electrolyte and fuels used (**Table 1.1**).[5] Among those classes, the fuel cells operating at relatively low temperatures are called proton exchange membrane fuel cell (PEMFC) and anion exchange membrane fuel cells (AEMFC) (they are collectively called polymer electrolyte membrane or polymer electrolyte fuel cells; PEFCs, to avoid confusion), which have been of particular importance in replacing traditional combustion engine in vehicles because of their compact design and fast start-up/shutdown capability. These fuel cells are expected to greatly decrease our hydrocarbon-dependence because ~50% of the total world energy consumption (therefore related to CO_2 emission) is attributed to transportation.[2] Alkaline fuel cell, the

first fuel cell that was practically applied in an aerospace program,[6] is no longer actively studied due to the drawbacks associated with the use of liquid electrolytes. The other types of fuel cells, which operate at higher temperatures, are typically employed for stationary distributed generation.

Table 1.1. The types of fuel cells

Type	Electrolyte	Operating Temperature
Proton exchange membrane fuel cell (PEMFC)	H^+ conducting polymer	<120 °C
Anion exchange membrane fuel cell (AEMFC)	OH^- conducting polymer	<100 °C
Alkaline fuel cell	Aqueous KOH	<100 °C
Phosphoric acid fuel cell (PAFC)	H_3PO_4	150–200 °C
Molten carbonate fuel cell (MCFC)	CO_3^{2-}	600–700 °C
Solid oxide fuel cell (SOFC)	O_2^- conducting oxides	500–1000 °C

1.2.2. Electrochemistry of PEMFC Electrode Reactions

Among the many classes fuel cells, this dissertation focuses on PEFCs because such low-temperature fuel cells suffer from efficiency loss due to slow electrode reactions. Two electrochemical reactions are involved in the fuel cells; hydrogen oxidation reaction (HOR) and oxygen reduction reaction (ORR). In the PEMFC, for example, protons and electrons are produced from H_2 at the anode through the HOR. The protons and electrons are conducted to the cathode by the proton exchange membrane (PEM) and electric wires, respectively. Oxygen gas provided to the cathode then reacts with the protons/electrons to generate H_2O as by-product (**Figure 1.2**). Electricity is generated whenever the fuels (hydrogen and oxygen) are supplied.

The electrochemical equations and equilibrium potentials for those reactions can be written as follows,

$$\text{HOR (acidic conditions): } H_2 \rightarrow 2H^+ + 2e^-, E^0 = 0 - 59 \times \text{pH (mV)}$$

$$\text{HOR (alkaline conditions): } H_2 + 2OH^- \rightarrow 2H_2O + 2e^-, E^0 = -828 + 59 \times \text{pH (mV)}$$

$$\text{ORR (acidic conditions): } O_2 + 4H^+ + 4e^- \rightarrow 2H_2O, E^0 = 1229 - 59 \times \text{pH (mV)}$$

$$\text{ORR (alkaline conditions): } O_2 + 2H_2O + 4e^- \rightarrow 4OH^-, E^0 = 401 + 59 \times \text{pH (mV)}$$
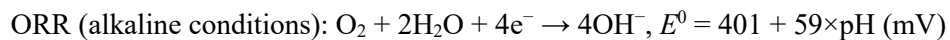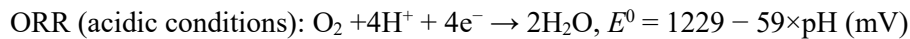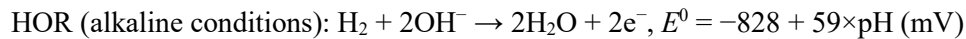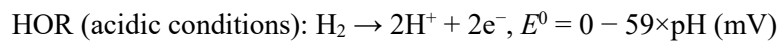
where E^0 indicates the equilibrium potential for each reaction (in normal hydrogen electrode; NHE). The value of 59 (in the unit of mV) is derived from the RT/F term in the Nernst equation, where R, T,

and F stand for the universal gas constant (8.314 J K^{-1} mol^{-1}), temperature (in Kelvin), and Faraday constant (96,485 C mol^{-1}), respectively, with temperature as 25 °C.
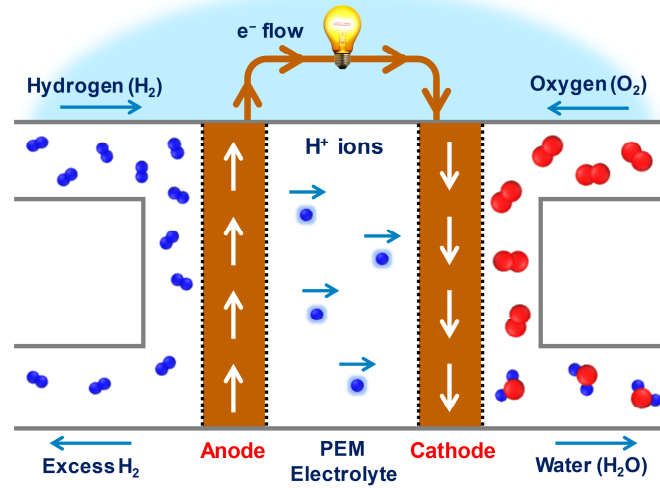
Figure 1.2. Schematic illustration of PEMFC operation

Cell potential is defined as $E_{cathode} - E_{anode}$ (cathode and anode represent the electrode where the reduction and oxidation reactions occur, respectively), and equals 1.23 V for the fuel cell at standard conditions, corresponding to the Gibbs free energy change of -237 kJ per mole of H$_2$, implying highly exothermic reactions. Theoretically, we obtain 1.23 V from the fuel cell by the thermodynamic driving force of the reactions, when the electrodes for the ORR and HOR are electrically connected in the presence of H$_2$ and O$_2$ at the anode and cathode, respectively. However, in practice, fuel cells operate at much less than 1.23 V due to several losses from activation, resistance, and diffusion-limitation (**Figure 1.3**).

The voltage loss (overvoltage) to overcome the reaction kinetics barrier and to generate current is depicted by Butler-Volmer equation (simplified version)

$$i = i_0 \times (e^{\frac{\alpha_a nF(E-E^0)}{RT}} - e^{-\frac{\alpha_c nF(E-E^0)}{RT}})$$

where i, i_0, α_a, α_c, n, and, E represent the measured current, the exchange current, the anodic charge transfer coefficient, the cathodic charge transfer coefficient, the electron transfer number, and the applied potential, respectively. Alternatively, we can write $E - E^0$ as η, the overpotential. The exchange current indicates the oxidation/reduction current at zero overpotential. Since the amount is the same as i_0, no current is measured at $\eta = 0$. The exchange current is dependent on the activation energy according to Arrhenius relation

4

$$i_0 \propto e^{-\frac{E_a}{RT}}$$

where E_a indicates the activation energy. Therefore, the kinetic loss is largely affected by the exchange current (the activation energy) of the reaction.
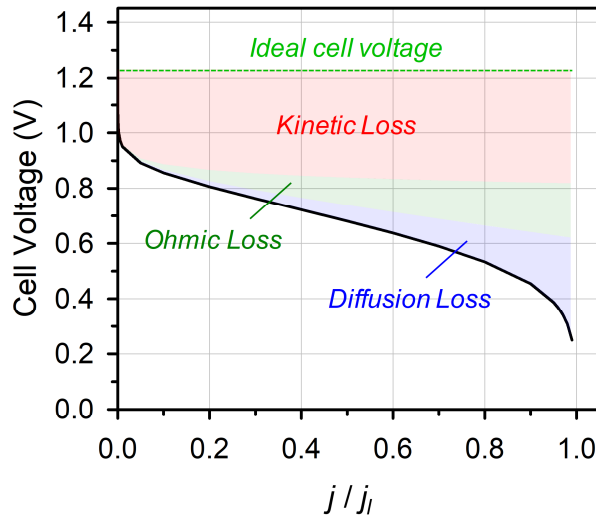
Figure 1.3. Theoretical polarization curves for the fuel cell. The cell voltage was calculated according to the equation $E = 1.23 - b \times \ln(j/j_0) - R \times j + c \times \ln(1 - j/j_l)$ where the second, third, and fourth term indicates the kinetic, Ohmic, and diffusion losses, respectively.[7] E, j, j_0, and R represent the cell voltage, the current density, the exchange current density, and resistance, respectively, while b and c are constants. The values used for this plot: $b = 0.03$, $c = 0.08$, $j_0 = 10^{-6}$, $R = 0.2$, and $j_l = 1$.

A large overpotential (> 0.3–0.4 V) is required to activate the fuel cell reactions (indicated by red shaded area in **Figure 1.3**). This is attributed to highly slow reaction kinetics (high activation energy) of the ORR on even the best Pt catalysts.[9,10] The reaction rate of the ORR is 5–6 orders of magnitude slower than that of the HOR, and thus the main reason for the performance loss of fuel cells (**Figure 1.4**). The slower reaction kinetics of the ORR has generated a great research interest aimed at seeking ways to improve the performance of the electrocatalysts for the ORR.

Ohmic loss (iR_{ohm}) mainly affects the intermediate overpotential region. The resistance (R_{ohm}) is determined by the membrane properties and the conductivity of the catalyst layer. As the last factor for the loss of the fuel cell performance, diffusion loss is caused by the limited mass transport of reactants and products. At high overpotentials, the reaction kinetics is fast enough, and thus the reaction rate is limited mainly by the diffusion speed of the provided reactants (H_2, and O_2) as well as the removal of H_2O. This can be improved by an elaborate design of the flow channels. These two influences, however, will not be discussed in further detail in this dissertation because the main purpose of the development of novel electrocatalysts is to improve the reaction kinetics. However, we

point out that diffusion and Ohmic losses are as important as the kinetics in system-level operation of fuel cells.
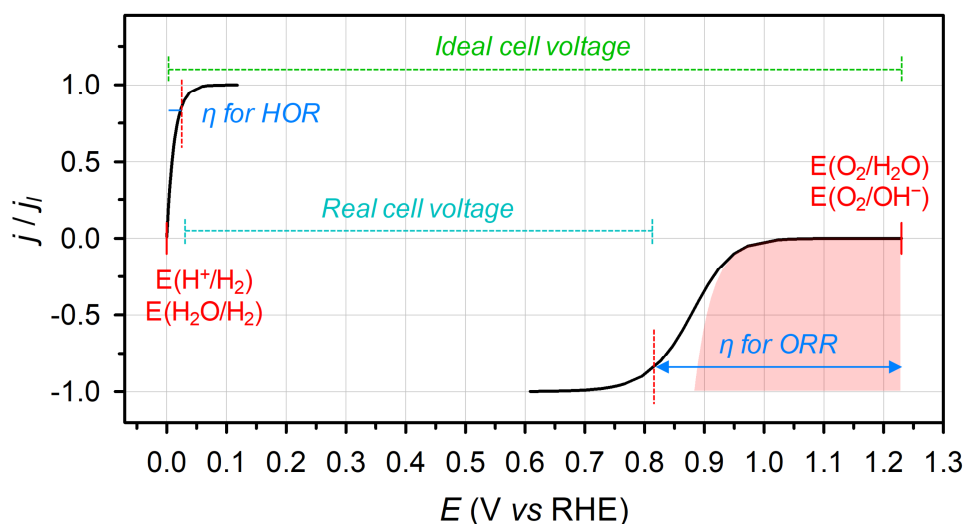
Figure 1.4. Theoretical polarization curves for the HOR and ORR. For the ORR, $b = 0.03$, $c = 0.04$, $j_0 = 10^{-5}$, $R = 0$, and $j_l = 1$ are input parameters into the equation shown in the caption of **Figure 1.3**. For the HOR, the voltage loss was assumed to primarily originate from the diffusion contribution because of fast reaction kinetics, that is $E = -(RT/2F) \times \ln(1 - j/j_l)$.[8] Parameters used for the polarization curves: $b = 0.03$, $c = 0.04$, $j_0 = 10^{-5}$, and $j_l = 1$, where b, c, j_0, and j_l represent two constants, the exchange current density, and the diffusion-limited current density. It should be noted that these plots just show the outline of the polarization curves that are typically obtained in the electrochemical experiments, and therefore those parameters are not related to real values. The red shade represents the kinetic polarization for the ORR.

1.2.3. Electrocatalysts for PEMFCs

To improve the fuel cell performance, efficient electrocatalysts are necessary to decrease the high activation barrier of fuel cell reactions. For both the ORR and HOR, Pt-based electrocatalysts have shown the highest activity.[11–13] Due to much more sluggish kinetics of the ORR, larger amounts of Pt-based catalysts are employed in the cathode, while very small amounts of the catalysts are enough for the HOR. In current fuel cell technology, Pt loading of ca. 22.5 g is required for a state-of-the-art PEMFC-powered vehicle.[14] Such high Pt loading is not desirable for the wide application of fuel cells. This is due to high Pt price ($30 g_{Pt}^{-1}, Nov 11, 2017),[15] and the scarcity of Pt on the earth crust. At a higher fuel cell production volume, the price of Pt catalysts becomes more significant compared to the remaining fuel cell components. For example, the Pt catalysts account for 23% and 43% of the cost of a PEMFC stack at a production volume of 1,000 and 500,000 systems per year.[16] The concentrated Pt reserves over 80% in South Africa and Russia is greatly responsible for the price issue.[17]

In this context, significant research has been devoted to the development of low-Pt ORR catalysts.[18–21] The strategies include: i) the preparation of Pt alloys with transition metal (PtM);[22] ii) the construction of M–Pt or PtM–Pt core–shell structures;[23,24] and iii) modification of particle sizes and shapes.[25–29] Such methods not only reduce the amount of Pt, but also enhance the intrinsic ORR activity, explained by the Sabatier principle which states that the active catalyst should have the optimum binding energy with the reaction intermediate (adsorbed O or OH for the ORR, **Figure 1.5**).[22,30] Pure Pt has a slightly higher oxygen binding energy than the optimum point. The coexistence with transition metal modifies the electronic structure to more weakly bind to the oxygenated species.[22,30] Studies within the last couple of decades has reached achievements of a mass activity improvement by a factor of >10 compared with commercial Pt/C catalyst (a factor of ~50 as the record high activity).[29] Furthermore, the progress has taken the PtM alloy catalysts to the fuel cell market with Toyota Mirai fuel cell car adopting the PtCo alloy catalysts.[31] However, the activity enhancements still have been usually demonstrated in half-cell tests, but have not been fully translated to single-cell measurements in PEMFC.[32]
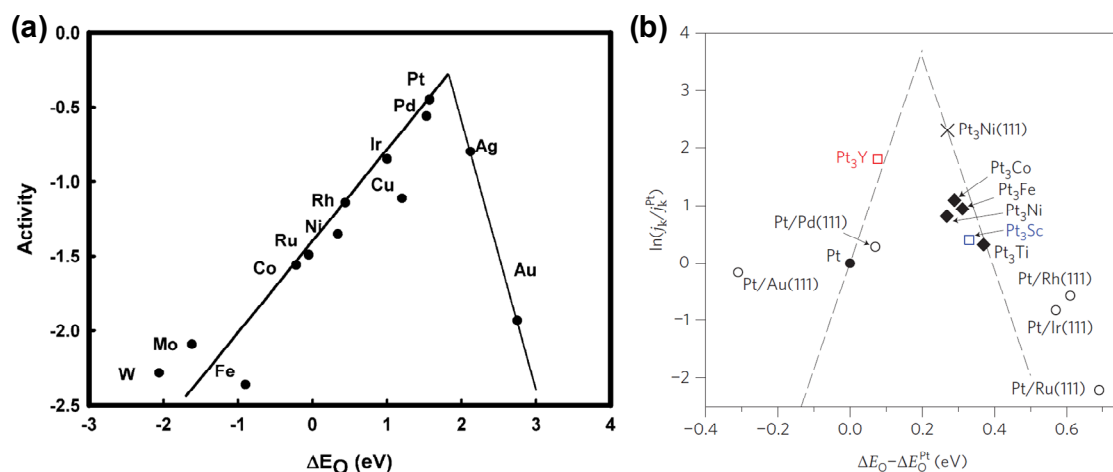
Figure 1.5. Volcano plot of the ORR activity and O binding energy of (a) some pure metals and (b) PtM alloys and Pt monolayer on other metal substrates. Reprinted with permission from refs. 30 and 22, respectively. Copyright © 2004 American Chemical Society. Copyright © 2009 Macmillan Publishers Ltd

As another class of catalysts, non-precious metal catalysts (NPMCs) have also attracted great attention as potential alternatives of Pt-based catalysts. Transition metal-based ceramic materials such as oxides,[33–37] carbides,[38,39] and chalcogenides[40,41], and even metal-free heteroatom-doped carbons[42–48] have shown promise as active ORR catalysts. However, such NPMCs are only stable and active for the ORR in alkaline electrolytes, except few examples of late transition metal oxides (e.g. TaO_x, NbO_x) stably working in acidic media.[49] For this reason, alkaline AEMFC has emerged as the more

economical type of fuel cell.

The only type of NPMC that works at low pH is transition metal- and nitrogen-codoped carbon (M–N/C) catalyst, which thus far has shown the highest activity among NPMCs. Since its first demonstration in 1964,[50] a few important milestones (introduced in **Chapter 3**) provided a synthetic guideline for improving the ORR activity of the M–N/C catalysts. Further studies on active site elucidation, development of preparation chemistry and engineering have achieved great progress in the ORR activity of M–N/C catalysts, comparable to that of Pt/C even in acidic media, and better than Pt/C in alkaline solutions in half-cell configurations.[51–58] In terms of single-cell applications, PEMFC and AEMFC employing M–N/C-based cathode have exhibited promising performance and stability, demonstrating practical applicability.[51,52] However, ORR activity only in half-cell configurations have largely been reported in the literature.

1.3. WATER ELECTROLYZER

1.3.1. Introduction to Water Electrolyzer

Pure hydrogen, unlike hydrocarbon compounds, does not exist in nature but needs to be extracted from hydrogen-containing substances using input energy. To date, ~95% of hydrogen is produced from fossil fuels through a process called steam reforming ($C_xH_y + H_2O \rightarrow H_2 + CO_2 + CO$, reaction balance not considered here).[59] This process generates massive amounts of CO_2 and CO gases, which makes the current technology for H_2 production unsuitable for future hydrogen economy. Electrolysis of water ($2H_2O \rightarrow 2H_2 + O_2$) can provide an eco-friendly way for H_2 production. Water, the hydrogen source, can be unlimitedly supplied from everywhere. In addition, water electrolysis is thermodynamically more efficient than steam reforming.[60]

The electrolyzer technology can be classified with the type of electrolyte.[61] First, as a matured technology for H_2 production, alkaline water electrolyzers (AWEs) adopt basic solutions such as 20–30% KOH in which two electrodes are soaked. The electrodes are separated by a diaphragm to prevent the mixing of H_2 and O_2 gases. Due to the use of the liquid electrolyte, AWEs suffer from several drawbacks. i) They are poisoned by atmospheric CO_2, which is dissolved in the electrolyte and forms precipitates of K_2CO_3; ii) the produced gases can diffuse to the other side, resulting in the reduction in both performance and purity. iii) efficiency is low due to high solution resistance; and iv) the device is space-inefficient. On the other hand, the stability of earth-abundant metal catalysts (e.g. Ni, Co, Fe) in alkaline electrolytes enables low-cost operation of AWEs. Second, the development of PEM (i.e. Nafion) has opened the possibility of PEM electrolyzers, which show high performance (current density) and produce high-purity product. However, the cost of Nafion membrane and the

noble metal catalyst requirement due to their corrosive, acidic conditions limits their adoption. Alkaline polymer membrane (so-called anion exchange membrane; AEM) can be employed in water electrolysis system, which has the advantages of alkaline water electrolyzer (cheap electrode materials) without the drawbacks associated with the use of liquid electrolytes. Much advancement of the AEM, however, is required for further considerations.

1.3.2. Electrochemistry of Water Electrolysis

Water electrolyzer consists of two electrochemical reactions: hydrogen evolution reaction (HER) and oxygen evolution reaction (OER). In PEM electrolyzer, for example, water is provided to the anode and split into O_2, protons, and electrons. The protons and electrons are transported through electric wire propelled by the external power and the PEM electrolyte, respectively. They subsequently undergo HER at the cathode, producing H_2 gas (**Figure 1.6**).
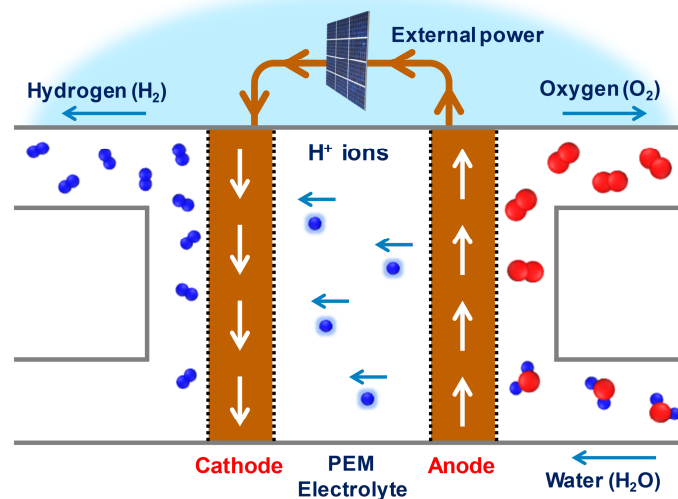
Figure 1.6. Schematic illustration of the operation of PEM electrolyzer

The electrochemical equations and equilibrium potentials for those reactions can be written as follows,

$$\text{HER (acidic conditions): } 2H^+ + 2e^- \rightarrow H_2, \; E^0 = 0 - 59 \times pH \text{ (mV)}$$

$$\text{HER (alkaline conditions): } 2H_2O + 2e^- \rightarrow H_2 + 2OH^-, \; E^0 = -828 + 59 \times pH \text{ (mV)}$$

$$\text{OER (acidic conditions): } 2H_2O \rightarrow O_2 + 4H^+ + 4e^-, \; E^0 = 1229 - 59 \times pH \text{ (mV)}$$

$$\text{OER (alkaline conditions): } 4OH^- \rightarrow O_2 + 2H_2O + 4e^-, \; E^0 = 401 + 59 \times pH \text{ (mV)}$$
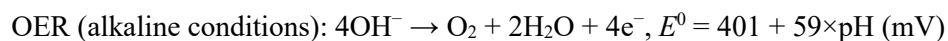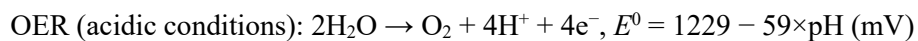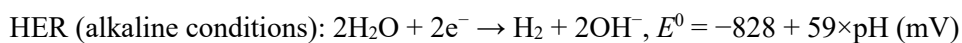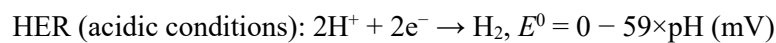
The standard cell potential for the water electrolyzer is $E_{cathode} - E_{anode} = -1.23$ V. This means that water electrolysis is a highly endothermic reaction, which requires the external voltage of at least 1.23 V (or 237 kJ per 1 mole of H_2). One can see that those reactions are completely opposite the fuel cell reactions (also for the net reaction, $2H_2O \rightarrow 2H_2 + O_2$), and thus share the equilibrium potentials with their reverse reactions.
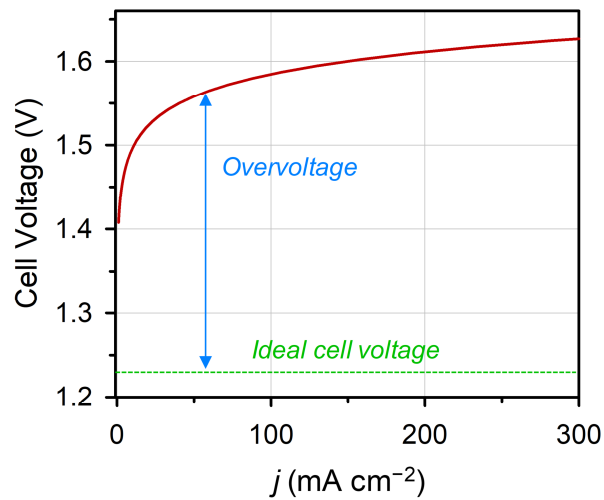
Figure 1.7. Theoretical polarization curve of water electrolyzer based on the polarization curves obtained using simplified Butler-Volmer equation, assuming $\alpha_a = \alpha_c = 0.5$, T = 298 K, and i_0 values of 10^0 and 10^{-6} mA cm^{-2} for the HER and OER, respectively.
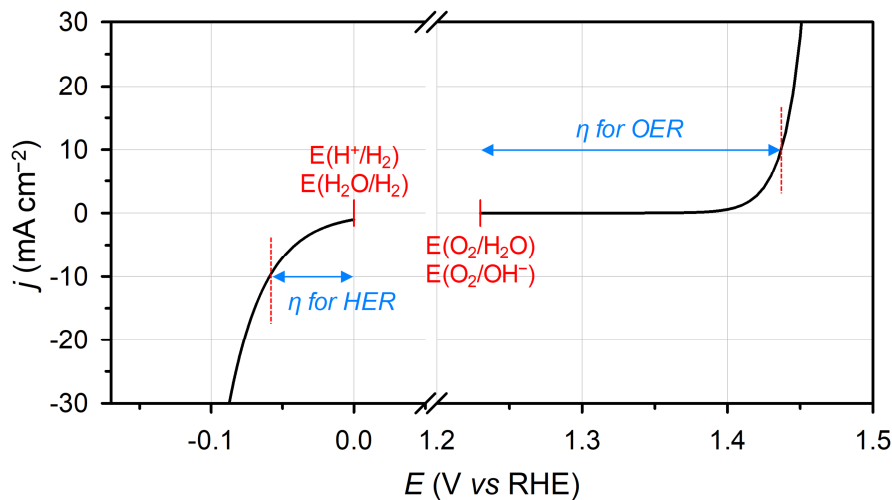
Figure 1.8. Theoretical polarization curves for the HER and OER obtained using simplified Butler-Volmer equation, assuming $\alpha_a = \alpha_c = 0.5$, T = 298 K, and i_0 values of 10^0 and 10^{-6} mA cm^{-2} for the HER and OER, respectively.

10

To operate the electrolyzer in practice, the applied voltage is set higher than the thermodynamic requirement due to the reaction kinetics. When comparing the reaction rate of the OER and HER, OER involving four proton-coupled electron transfers shows more sluggish reaction kinetics than HER, i.e. larger activation energy and lower exchange current. The lower exchange current results in higher overpotential requirement for the operation (**Figures 1.7** and **1.8**). In water electrolyzers, the overvoltage from the reaction kinetics barrier of over ~0.3 V serve as the major source of loss of performance, and therefore active electrocatalysts are required to increase the efficiency of the device.

1.3.3. Electrocatalysts for Water Electrolysis

For the HER, Pt-based electrocatalysts have shown the highest activity compared to other materials, which can be attributed to the most optimum H binding energy of Pt (**Figure 1.9a**).[62] Whereas, oxide and (oxy)hydroxide of Ir and Ru are the most active phases for the OER (metallic phase of the elements is transformed to these oxidized phases under OER conditions.[63] The high OER activity of Ir and Ru also has been ascribed to the balance between the binding energy with oxygenated reaction intermediates (**Figure 1.9b**). Although Ru is a much cheaper element and more active for the OER than Ir, Ir-based OER catalysts are more desirable in terms of stability.[64] However, such noble metals are expensive and very scarce in nature, making the operation of the device uneconomical.
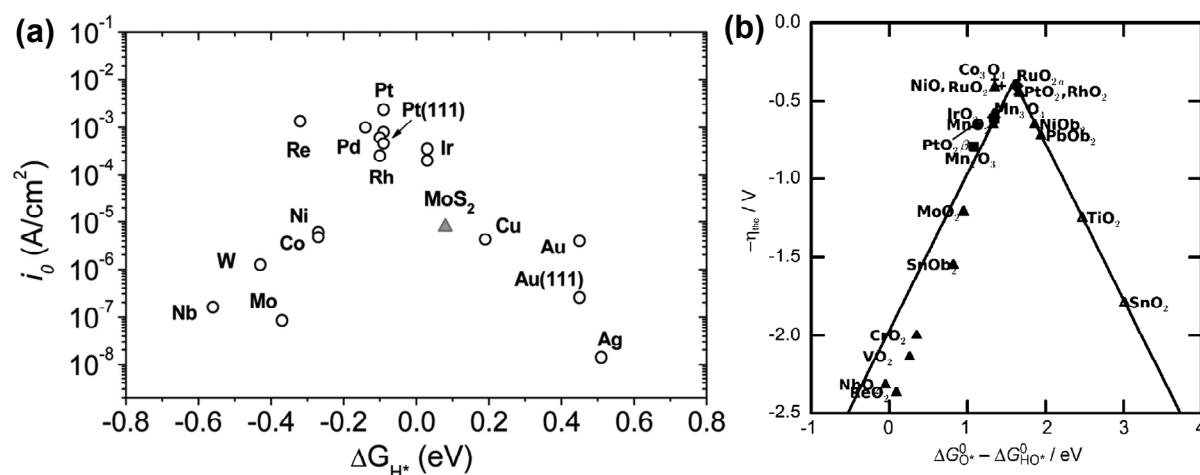
Figure 1.9. Volcano plot of (a) the exchange current density for the HER and the Gibbs free energy of hydrogen binding (obtained from theoretical calculations) for some metals, and (b) the overpotential for the OER and the binding energy difference between O and OH absorbed species of some metal oxides. Reprinted with permission from refs. 62 and 63, respectively. Copyright © 2007 American Association for the Advancement of Science. Copyright © 2011 Wiley-VCH Verlag GmbH & Co. KGaA, Weinheim.

For the OER, transition metal oxides/(oxy)hydroxide have been most actively investigated as NPMCs.[65–69] Among them, Ni–Fe mixed and Co-based oxide/(oxy)hydroxide have exhibited the highest OER activity, sometimes even better than commercial Ir-based catalysts.[67–69] Recent reports show that regardless of the initial phase, the catalyst undergoes phase transformation under the oxidation potential, mostly into the oxyhydroxide phase which is therefore considered as active phase for the OER.[70,71] This is also the case for transition metal nitrides/phosphides/sulfides, where their surfaces are converted into oxyhydroxides, generating core–shell type structure during operation.[72] However, the high OER activity of the NPMCs has been proven only in alkaline electrolyte due to their low stability in acidic solutions.[73]

Early studies on non-precious HER catalysts focused on layered transition metal dichalcogenide such as MoS_2 and WS_2.[74–77] MoS_2-based HER catalysts (generally more active than WS_2) have been subjected to detailed spectroscopic analysis including *operando* measurement for deeper understanding of active sites.[78,79] Meanwhile, extensive exploration of novel HER NPMCs has found much more active substances including transition metal borides,[80] carbides,[81] nitrides,[82] and phosphides,[83,84] where the latter has been shown to be the most effective candidate, exhibiting the HER activity close to that of Pt/C. The active species in such phosphide catalysts are still unknown while efforts are being made to use computational methods to find the origin of high HER activity.

Finally, the OER and HER catalysts operate at the same pH to implement the water electrolyzer. This presents a serious limitation since most HER NPMCs are active in acid, where the OER NPMCs cannot survive. The development of active OER and HER catalysts in acidic and alkaline electrolytes, respectively, will be necessary for cheaper H_2 production from water electrolysis.

1.4. CARBON NANOTUBES

Since its first discovery,[85] carbon nanotubes (CNTs) have been the subject of a tremendous amount of research. Their extraordinary properties such as high thermal, electrical conductivities, and mechanical strength have enabled the wide range of applications of CNTs in electronics, biosensors, and materials for electrochemical energy storage and conversion.[86–88] In particular, the excellent electrical conductivity, chemical stability, and chemical tunability enables its potential for electrocatalytic applications.

CNT can be divided into two types according to the number of tubular walls: single-walled and multi-walled CNTs. For CNT-based electrocatalysts, surface functionalization for better adherence to electroactive materials is necessary. This however causes a decline of electrical conductivity due to the partial destruction of graphitic networks. Heteroatom-doping is often exploited to improve the

electrocatalytic activity by increasing the number of active sites, but the process for the doping also decreases the graphiticity and conductivity. In multi-walled CNTs, the inner tubes are protected from surface damage from functionalization and doping processes (however too harsh conditions such as Hummer's method can cause total unzipping of CNTs) thereby making them more suitable for electrocatalytic applications.

CNT is typically produced by chemical vapor deposition of carbonaceous gases onto metals at high temperatures and pressures. The metal catalyst plays an important role to catalyze nucleation and growth of the CNT, and remains in the product. Such metal impurities have catalytic effects and cause side reactions and/or overestimation of a synthesized catalysts. This indicates the importance of CNT purification before the preparation of CNT-based electrocatalysts. The method includes the most typical acid-washing CNT (more effective in hot acid solutions), and annealing under air followed by acid-washing. In the latter case, amorphous carbons, which are also considered as impurities, can be removed as well as the trace metals, and the dual-treatment can make CNT more metal-free.

1.5. ASSESSMENT OF ELECTROCATALYSIS

1.5.1. General Methodology

Precise measurement of electrocatalytic activity is an important high priority task for the development of improved catalysts. In this section, we deal with the experimental details and requirements for the determination of electrocatalysis, especially for NPMCs in the lab experiments. The evaluation of the electrocatalytic activity is typically carried out using three-electrode system, consisting of working electrode, reference electrode, counter electrode, and electrolyte. For a special case of the OER and HER, two-electrode system is sometimes exploited to imitate the water electrolyzer system. After the three (or two)-electrode cell is built, current response with respect to the applied potential (or *vice versa*) using a potentiostat are obtained. We need to carefully choose the type of reference and counter electrodes and electrolytes that have strong influence the electrochemical results.

1.5.2. Selection of Reference Electrode

The reference electrode provides a thermodynamic potential standard, because a potential of a single redox reaction is hard to be separately measured. The equilibrium potentials in textbooks are defined with respect to standard hydrogen electrode (SHE), which is the equilibrium potential of HER/HOR in acid solution with proton activity of unity and 1 bar H_2 pressure (defined as 0 V). In the

laboratory, SHE is not well reproduced due to the difficulty in the adjustment of unit proton activity. Instead, normal hydrogen electrode (NHE) where Pt is soaked in 1 N acid solution under 1 bar H_2 is used.

Nevertheless, the construction of NHE is still rather complicated, such that many scientists prefer to use other compact reference electrodes for convenient experiments. Ag/AgCl, saturated calomel electrode (SCE; Hg/Hg_2Cl_2), and Hg/HgO are the most representative reference electrodes to provide a reference potential. Different potential scale from the use of different reference electrode can be adjusted by conversion of the scale into reversible hydrogen electrode (RHE). RHE is pH-independent (i.e., E(RHE) = E(NHE) + RT/F × pH), and provides the same reference point in any electrolytes (for example the equilibrium potential for the ORR is $1.23 − RT/F$ × pH (V *vs* NHE) and 1.23 V (*vs* RHE)). This allows the direct comparison between reported works. Two methods for the RHE conversion are explained in the *Sections 2.2.4* and *3.2.5* by measuring equilibrium potential for the HER/HOR. Finally, it is better to use Hg/HgO reference electrode for the electrochemical measurement in alkaline solution due to possibility of etching of the glass frit that separates the main body of Ag/AgCl and SCE from the electrolyte.

1.5.3. Selection of Counter Electrode

Counter electrode (or auxiliary electrode) is used in three-electrode system for the balance of electron flows with the working electrode. Since the potential of the counter electrode is not controlled, the electrochemical reaction occurring at the counter electrode is arbitrary (but follows thermodynamics). This operational characteristic can cause a serious problem especially when Pt-based counter electrodes are used for reduction reactions (ORR and HER). To balance the reduction reactions at the working electrode, oxidation reactions take place at the counter electrode, resulting in the electrochemical dissolution of Pt into the electrolyte. The dissolved Pt can be cathodically deposited onto the working electrode. In the tests of NPMCs, small amount of Pt can potentially overestimate their electrocatalytic activity; Pt is the best catalyst both for the ORR and HER. The problem becomes more serious during long-term stability tests. Such activation effect of the Pt-based counter electrode was reported in the case of HER;[89,90] hence, the use of carbon-based (graphite rod and glassy carbon) counter electrode is recommended.

1.5.4. Working Electrode: Rotating (Ring) Disk Electrode

In laboratory, rotating disk electrode (RDE) is typically used as the working electrode for electrochemical tests. For gas-generating reactions, the electrode rotation helps the removal of O_2 and H_2 bubbles from the OER and HER, respectively. In the ORR test, the electrode rotation facilitates the diffusion of O_2 by convective force. In this case, at sufficiently high overpotential, the diffusion rate is slower than reaction kinetics, resulting in zero reactant concentration at the vicinity of the electrode. This leads to a diffusion-limited current, especially when the concentration of reactant (O_2, typically ~1 mM) is low. As a result, the rate of the reaction is limited by the supply of O_2. With rotation of the electrode (hydrodynamic system), the reaction rate (i.e. current) can be expressed by Levich equation.[91]

$$i_l = 0.62 n F A D^{\frac{2}{3}} \omega^{\frac{1}{2}} v^{-\frac{1}{6}} C$$

where i_l, A, D, ω, v, and C represent the diffusion-limited current (or Levich current), the electrode area, the diffusion coefficient, the rotation speed (in rad s^{-1}), the kinematic viscosity, and the reactant concentration (in molarity). The electron transfer number can be estimated from the diffusion-limited current.

Another type of RDE with Pt (or Au) ring surrounded by the disk electrode, known as rotating ring disk electrode (RRDE), can provide information about reaction selectivity of developed catalysts. The RRDE technique has been particularly used for the ORR field to estimate four-electron selectivity (**Figure 1.10**). Inefficient ORR catalysts reduce O_2 to H_2O_2 (or HO_2^- in alkaline solutions) *via* two-electron reduction while more efficient four-electron reduction of O_2 generates H_2O. Since H_2O_2 damages polymer membranes, H_2O_2 production yield on newly developed catalysts should be evaluated using RRDE prior to being employed to fuel cells. During electrochemical measurement, the electrode rotation transports H_2O_2 to the ring and the ring potential is held at an oxidation potential (i.e. > 1.2 V *vs* RHE) to oxidize generated H_2O_2 at the ring. Then, the selectivity can be calculated using the ratio of the ring current to the disk current as follows.

$$n = \frac{4}{1 + \dfrac{i_r}{N \times i_d}}$$

$$H_2O_2(HO_2^-) \text{ yield} = \frac{200}{1 + \dfrac{N \times i_d}{i_r}} = 50 \times (4 - n)$$

where n, i_r, N, and i_d stand for the electron transfer number (four-electron selectivity), the ring current,

the collection efficiency, and the disk current. The collection efficiency is dependent on the diameters of the ring and disk. This parameter is usually provided by the manufacturer, but should be empirically determined using the $[Fe(CN)_6^{3-}]/[Fe(CN)_6^{4-}]$ redox reaction, a facile single-electron transfer reaction.[91]
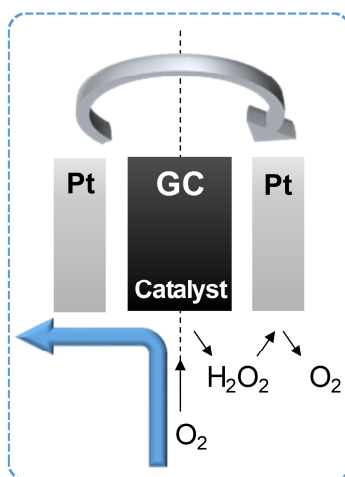
Figure 1.10. Schematic illustration of RRDE measurement for the ORR to obtain four-electron selectivity.

The four-electron selectivity evaluation by the RRDE is dependent on catalyst loading.[92] It is generally accepted that with increased catalyst loading, higher electron transfer number can be obtained because peroxide species produced by less-efficient active centers can be further reduced before escaping thicker catalyst layer or can be trapped in the catalyst layer. Hence, the measurement of electron transfer number (by RRDE) with lower catalyst loading may result in lower electron transfer number.

Recently, the RRDE technique has been exploited to measure Faradaic efficiency for the OER. Under the oxidizing OER conditions, undesirable oxidation reactions can occur such as oxidation of carbon support. To confirm that the measured current is derived from the OER, the potential of the Pt ring is fixed at ~0.4 V (*vs* RHE).[93] This potential is sufficiently low to rapidly reduce the O_2 molecules generated from the disk electrode where the OER takes place. Then, we can calculate the Faradaic efficiency (ε) using the disk and ring currents.

$$\varepsilon\,(\%) = 100 \times \left| \frac{i_r}{N \times i_d} \right|$$

1.5.5. Electrolyte

Electrolyte is one of the important experimental conditions that have critical effect on the catalytic activity. First, electrolyte concentration is important because of its relationship with the amounts of reactants and products. In addition, the use high-purity chemicals for preparation of the electrolytes to prevent possible contamination is encouraged, especially when measuring precious metal catalysts, which are critically affected by the electrolyte purity.[94]

In the OER, trace Fe and Ni have been shown to significantly enhance the catalytic activity. Boettcher et al. demonstrated that trace Fe (even at very low concentration of 36 ppb) in the electrolyte can be incorporated into NiOOH, thereby modifying the electronic properties and the local structure of the active site leading to the great enhancement of OER activity.[95] Symes et al. showed that nanomolar Ni (~17 nM) can efficiently catalyst the OER in weakly to strongly alkaline electrolytes.[96] The presence of these impurities is inevitable since the highest purity chemicals contain ppb- or nanomolar-scale trace metal contaminants. Electrolyte purification first follows NiOOH-treatment, which spontaneously adsorbs the trace Fe atoms, followed by treatment with a special cation exchange resin.

In addition, ths choice of cation and anion that also can change the electrocatalytic activity *via* modification of electric double layer structure should be carefully made. For example, the ORR activity of Pt(111) in alkaline electrolytes increases as the ionic radius of the cation decreases (i.e. Li^+ > Na^+ > K^+ > Cs^+).[97]

1.5.6. Kinetics Analysis by Tafel Plot

For better understanding of the electrocatalytic behavior of catalysts, reaction kinetics analysis sometimes gives important mechanistic insights, enabling rational design strategy of efficient catalyst. The kinetic insights can be easily attained from Tafel plot, which is described by Tafel equation.[91]

$$\eta = \frac{RT}{\alpha nF} \ln(i / i_0)$$

where α is charge transfer coefficient, which can be replaced as α_a and $-\alpha_c$ for oxidation and reduction reactions, respectively. Tafel plot shows the relation between the overpotential and logarithmic scale of current, giving a slope of $RT/\alpha nF$ or shortly b (Tafel slope). The αn term is highly dependent on the reaction kinetics. The value allows us to deduce the rate determining step and/or gain the information about the interaction between and the coverage of adsorbed species.[98]

1.5.7. Measurement of Benchmark Catalysts

The electrocatalytic activity of benchmark catalysts (i.e. Pt for ORR and HER, Ir or IrO$_x$ for OER) is an important criterion to determine how much a novel electrocatalyst is active. Underestimation of the benchmark catalyst due to inappropriate measurement method can exaggerate the activity of developed electrocatalysts. The low activity of the precious metal catalysts can originate from the high concentration of impurities in the electrolyte, poor cell construction, and problem in the catalyst deposition. For reliable measurement of novel electrocatalysts, it is necessary to first establish and optimize the experimental conditions for well-known benchmark catalysts for fair comparison.

The measurement methodology has been systematically established only for the evaluation of the ORR activity of Pt/C catalyst, supported by U.S. DOE.[99,100] The activity is affected by numerous experimental conditions such as catalyst ink composition, ink drying method, electrolyte purity, glassware cleanness, scan rate, and scan direction. According to the standard measurement protocol, commercial Pt/C catalysts should exhibit a half-wave potential of 0.89 ± 0.02 V (*vs* RHE). For NPMCs, however, there has been no established methodology for activity evaluation which provides fair comparison of newly developed catalyst with reported catalysts. Only reported example is for oxide catalysts for the ORR.[101] Pt/C catalyst also serves as an activity standard for the HER, but there has been no report on the activity measurement methodology.

Typical benchmark catalyst for the OER is Ir/C or Ru/C, which transforms into active oxidized species *in situ* during the OER. In the case of the OER, no standard measurement protocol has been established as well. However, Ir/C is more suitable as the activity benchmark because Ru is unstable and thus undergoes quick dissolution during the electrocatalysis.[64]

1.5.8. Figure of Merit of the Activity

HER/OER: For water electrolysis, scientists have typically used the overpotential to deliver 10 mA cm^{-2} as the activity metric since the first proposal.[102] The calculation is based on photovoltaic-powered water splitting. Under 1 sun illumination (AM1.5G), the solar energy of ca. 100 mW cm^{-2} is provided. As 10% solar-to-fuel (STH) efficiency has been regarded as the "Holy Grail" for this application,[103] the current extracted from the "ideal device" when operated at a cell voltage of 1.23 V is

$$(100 \text{ mW cm}^{-2}) \times (10\% \text{ STH efficiency})/(1.23 \text{ V}) = 8.1 \text{ mA cm}^{-2}$$

which approximates to 10 mA cm^{-2}, and serving as the figure of merit for water splitting research.

Care should be taken when measuring the activity if catalysts: i) are composed of a significant amount of carbon, ii) contains a large number of Ni and Co; the oxidation peak for Ni^{2+}/Ni^{3+} and Co^{2+}/Co^{3+} is usually overlapped with the OER current, especially when little amount of Fe is doped,[67] and iii) have high surface area which can lead to large capacitive current. In all the cases, the oxidation and the capacitive currents in the OER region can overestimate the activity.

ORR in half-cell configuration: The ORR activity in half-cell configuration is typically compared in terms of half-wave potential and kinetic current. The half-wave potential indicates the potential at which half of the diffusion-limited current was obtained. The kinetic current has already been discussed in *Section 1.5.6*. These parameters provide the rational activity metric as the current for the ORR increases with higher electrode rotation speed, according to Levich equation.

ORR in single-cell application: The current and power densities are usually compared at the cell voltage of 0.6 V at which the fuel cell systems are typically operated. U.S. department of energy (DOE) has established the technical target of acidic PEMFC made of non-precious metal catalysts-based membrane electrode assembly (MEA). MEA is a stack of anode-membrane-cathode that is the key component for PEMFC operation. The PEMFC performance of a developed MEA should drive the current density larger than 0.044 A cm^{-2} at *iR*-free cell voltage of 0.90 V at the operating temperature of 80 °C; this objective was derived from 10% of the activity target (0.44 A cm^{-2}) of Pt-based MEA.[104]

1.6. OUTLINE OF THIS DISSERTATION

This dissertation contains novel synthetic strategies for CNT-based electrocatalysts as well as the preparation of CNT-supported electrocatalysts for ORR, OER, and HER, which play a crucial role in fuel cells and water electrolyzer for realizing hydrogen economy. **Chapter 2** introduces the novel synthetic method for preparation of CNTs coated by heteroatom-doped carbon layers derived from ionic liquid as the heteroatom source. **Chapter 3** presents the role of silica for the synthesis of active-site-rich Fe–N/C catalysts wrapped on CNTs. The electrocatalysts in Chapters 2 and 3 successfully demonstrated the record high activity when employed in AEMFC. In **Chapter 4**, cobalt oxide nanoparticles (CoO$_x$ NPs) supported on CNTs were investigated as bifunctional catalysts for ORR/OER and active species in the CoO$_x$ NPs were studied using *in situ* X-ray absorption spectroscopy. **Chapter 5** shows the structure-activity relationship established in the HER activity of Co–N/CNT catalysts.

1.7. REFERENCES

(1)   *BP Statistical Review of World Energy*; London, **2017**.

(2)   International Energy Outlook 2017 (#IEO2017), U.S. Energy Information Administration, https://www.eia.gov/outlooks/ieo/pdf/0484(2017).pdf, **2017** (accessed Nov 3, 2017).

(3)   Ni, M.; Leung, M. K. H.; Sumathy, K.; Leung, D. Y. C. *Int. J. Hydrogen Energy* **2006**, *31*, 1401–1412.

(4)   Bockris, J. O'M. *Int. J. Hydrogen Energy* **2002**, *27*, 731–740.

(5)   *Fuel Cells Fact Sheet*; U.S. Department of Energy, Fuel Cell Technologies Office: Washington, DC, **2015**.

(6)   Perry, M. L.; Fuller, T. F. *J. Electrochem. Soc.* **2002**, *149*, S59–S67.

(7)   O'Hayre, R. P.; Cha, S.-W.; Colella, W. G.; Prinz, F. B. In *Fuel Cell Fundamentals*, 2nd Edition; John Wiley & Sons: Hoboken, NJ, **2009**; pp 195–224.

(8)   Zheng, J.; Sheng, W.; Zhuang, Z.; Xu, B.; Yan, Y. *Sci. Adv.* **2016**, *2*, e1501602.

(9)   Gu, W.; Baker, D. R.; Liu, Y.; Gasteiger, H. A. In *Handbook of Fuel Cells—Fundamentals, Technology and Applications*; Vielstich, W.; Gasteiger, H. A.; Yokokawa, H., Eds.; John Wiley & Sons: Chichester, **2009**; Vol. 6, pp 631–657.

(10)   Wang, Y.; Chen, K. S.; Mishler, J.; Cho, S. C.; Adroher, X. C. *Appl. Energy* **2011**, *88*, 981–1007.

(11)   Steele, B. C. H.; Heinzel, A. *Nature* **2001**, *414*, 345–352.

(12)   Gasteiger, H. A.; Kocha, S. S.; Sompalli, B.; Wagner, F. T. *Appl. Catal. B: Environ.* **2005**, *56*, 9–35.

(13)   Debe, M. K. *Nature* **2012**, *486*, 43–51.

(14)   Kongkanand, A.; Mathias, M. F. *J. Phys. Chem. Lett.* **2016**, *7*, 1127–1137.

(15)   Historical Platinum Prices and Price Chart. http://www.infomine.com/investment/metal-prices/platinum/1-year (accessed Nov 11, 2017).

(16)   Wilson, A.; Marcinoski, J.; Papageorgopoulos, D. DOE Hydrogen and Fuel Cells Program Record # 16020: Fuel Cell System Cost. https://www.hydrogen.energy.gov/pdfs/16020_fuel_cell_system_cost_2016.pdf (accessed Nov 8, 2017).

(17)   U.S. Geological Survey. Mineral Commodity Summaries 2016; U.S. Government Printing Office: Washington, DC, **2016**; p 126–127.

(18)   Stephens, I. E. L.; Bondarenko, A. S.; Grønbjerg, U.; Rossmeisl, J.; Chorkendorff, I. *Energy Environ. Sci.* **2012**, *5*, 6744–6762.

(19)   Wang, C.; Markovic, N. M.; Stamenkovic, V. R. *ACS Catal.* **2012**, *2*, 891–898.

(20)   Wu, J.; Yang, H. *Acc. Chem. Res.* **2013**, *46*, 1848–1857.

(21)   Mistry, H.; Varela, A. S.; Kühl, S.; Strasser, P.; Cuenya, B. R. *Nat. Rev. Mater.* **2016**, *1*, 16009.

(22)   Greeley, J.; Stephens, I. E. L.; Bondarenko, A. S.; Johansson, T. P.; Hansen, H. A.; Jaramillo, T.

F.; Rossmeisl, J.; Chorkendorff, I.; Nørskov, J. K. *Nat. Chem.* **2009**, *1*, 552–556.

(23) Zhang, J.; Lima, F. H. B.; Shao, M. H.; Sasaki, K.; Wang, J. X.; Hanson, J.; Adzic, R. R. *J. Phys. Chem. B* **2005**, *109*, 22701–22704.

(24) Strasser, P.; Koh, S.; Anniyev, T.; Greeley, J.; More, K.; Yu, C.; Liu, Z.; Kaya, S.; Nordlund, D.; Ogasawara, H.; Toney, M. F.; Nilsson, A. *Nat. Chem.* **2010**, *2*, 454–460.

(25) Kinoshita, K. *J. Electrochem. Soc.* **1990**, *137*, 845–848.

(26) Stamenkovic, V. R.; Fowler, B.; Mun, B. S.; Wang, G.; Ross, P. N.; Lucas, C. A.; Marković, N. M. *Science* **2007**, *315*, 493–497.

(27) Lim, B.; Jiang, M.; Camargo, P. H. C.; Cho, E. C.; Tao, J.; Lu, X.; Zhu, Y.; Xia, Y. *Science* **2009**, *324*, 1302–1305.

(28) Chen, C.; Kang, Y.; Huo, Z.; Zhu, Z.; Huang, W.; Xin, H. L.; Snyder, J. D.; Li, D.; Herron, J. A.; Mavrikakis, M.; Chi, M.; More, K. L.; Li, Y.; Markovic, N. M.; Somorjai, G. A.; Yang, P.; Stamenkovic, V. R. *Science* **2014**, *343*, 1339–1343.

(29) Li, M.; Zhao, Z.; Cheng, T.; Fortunelli, A.; Chen, C.-Y.; Yu, R.; Zhang, Q.; Gu, L.; Merinov, B. V.; Lin, Z.; Zhu, E.; Yu, T.; Jia, Q.; Guo, J.; Zhang, L.; Goddard, W. A.; Huang, Y.; Duan, X. *Science* **2016**, *354*, 1414–1419.

(30) Nørskov, J. K.; Rossmeisl, J.; Logadottir, A.; Lindqvist, L.; Kitchin, J. R.; Bligaard, T.; Jónsson, H. *J. Phys. Chem. B* **2004**, *108*, 17886–17892.

(31) Yoshida, T.; Kojima, K. *Electrochem. Soc. Interface* **2015**, *24*, 45–49.

(32) Stephens, I. E. L.; Rossmeisl, J.; Chorkendorff, I. *Science* **2016**, *354*, 1378–1379

(33) Liang, Y.; Li, Y.; Wang, H.; Zhou, J.; Wang, J.; Regier, T.; Dai, H. *Nat. Mater.* **2011**, *10*, 780–786.

(34) Suntivich, J.; Gasteiger, H. A.; Yabuuchi, N.; Nakanishi, H.; Goodenough, J. B.; Shao-Horn, Y. *Nat. Chem.* **2011**, *3*, 546–550.

(35) Guo, S.; Zhang, S.; Wu, L.; Sun, S. *Angew. Chem., Int. Ed.* **2012**, *51*, 11770–11773.

(36) Lee, J. H.; Sa, Y. J.; Kim, T. K.; Moon, H. R.; Joo, S. H. *J. Mater. Chem. A* **2014**, *2*, 10435–10443.

(37) Aijaz, A.; Masa, J.; Rösler, C.; Xia, W.; Weide, P.; Botz, A. J. R.; Fischer, R. A.; Schuhmann, W.; Muhler, M. *Angew. Chem., Int. Ed.* **2016**, *55*, 4087–4091.

(38) Deng, D.; Yu, L.; Chen, X.; Wang, G.; Jin, L.; Pan, X.; Deng, J.; Sun, G.; Bao, X. *Angew. Chem., Int. Ed.* **2013**, *52*, 371–375.

(39) Hu, Y.; Jensen, J. O.; Zhang, W.; Cleemann, L. N.; Xing, W.; Bjerrum, N. J.; Li, Q. *Angew. Chem., Int. Ed.* **2014**, *53*, 3675–3679.

(40) Wang, H.; Liang, Y.; Li, Y.; Dai, H. *Angew. Chem., Int. Ed.* **2011**, *50*, 10969–10972.

(41) Falkowski, J. M.; Surendranath, Y. *ACS Catal.* **2015**, *5*, 3411–3416.

(42) Zheng, Y.; Jiao, Y.; Jaroniec, M.; Jin, Y.; Qiao, S. Z. *Small* **2012**, *8*, 3550–3566.

(43)   Wang, D.-W.; Su, D. *Energy Environ. Sci.* **2014**, *7*, 576–591.

(44)   Gong, K.; Du, F.; Xia, Z.; Durstock, M.; Dai, L. *Science* **2009**, *323*, 760–764.

(45)   Liang, J.; Jiao, Y.; Jaroniec, M.; Qiao, S. Z. *Angew. Chem., Int. Ed.* **2012**, *51*, 11496–11500.

(46)   Zhao, Y.; Yang, L.; Chen, S.; Wang, X.; Ma, Y.; Wu, Q.; Jiang, Y.; Qian, W.; Hu, Z. *J. Am. Chem. Soc.* **2013**, *135*, 1201–1204.

(47)   Cheon, J. Y.; Kim, J. H.; Kim, J. H.; Goddeti, K. C.; Park, J. Y.; Joo, S. H. *J. Am. Chem. Soc.* **2014**, *136*, 8875–8878.

(48)   Guo, D.; Shibuya, R.; Akiba, C.; Saji, S.; Kondo, T.; Nakamura, J. *Science* **2016**, *351*, 361–365.

(49)   Liu, Y.; Ishihara, A.; Mitsushima, S.; Kamiya, N.; Ota, K. *J. Electrochem. Soc.* **2007**, *154*, B664–B669.

(50)   Jasinski, R. *Nature* **1964**, *201*, 1212–1213.

(51)   Lefèvre, M.; Proietti, E.; Jaouen, F.; Dodelet, J.-P. *Science* **2009**, *324*, 71–74.

(52)   Wu, G.; More, K. L.; Johnston, C. M.; Zelenay, P. *Science* **2011**, *332*, 443–447.

(53)   Chung, H. T.; Won, J. H.; Zelenay, P. *Nat. Commun.* **2013**, *4*, 1922.

(54)   Cheon, J. Y.; Kim, T.; Choi, Y.; Jeong, H. Y.; Kim, M. G.; Sa, Y. J.; Kim, J.; Yang, T.-H.; Kwon, K.; Terasaki, O.; Park, G.-G.; Adzic, R. R.; Joo, S. H. *Sci. Rep.* **2013**, *3*, 2715.

(55)   Shui, J.; Chen, C.; Grabstanowicz, L.; Zhao, D.; Liu, D.-J. *Proc. Natl. Acad. Sci. USA* **2015**, *112*, 10629–10634.

(56)   Sahraie, N. R.; Kramm, U. I.; Steinberg, J.; Zhang, Y.; Thomas, A.; Reier, T.; Paraknowitsch, J.-P.; Strasser, P. *Nat. Commun.* **2015**, *6*, 8618.

(57)   Zitolo, A.; Goellner, V.; Armel, V.; Sougrati, M.-T.; Mineva, T.; Stievano, L.; Fonda, E.; Jaouen, F. *Nat. Mater.* **2015**, *14*, 937–942.

(58)   Gasteiger, H. A.; Marković, N. M. *Science* **2009**, *324*, 48–49.

(59)   Gandía, L. M.; Oroz, R.; Ursúa, A.; Sanchis, P.; Diéguez, P. M. *Energy Fuels* **2007**, *21*, 1699–1706.

(60)   Shinnar, R. *Technol. Soc.* **2003**, *25*, 455–476.

(61)   Carmo, M.; Fritz, D. L.; Mergel, J.; Stolten, D. *Int. J. Hydrogen Energy* **2013**, *38*, 4901–4934.

(62)   Jaramillo, T. F.; Jørgensen, K. P.; Bonde, J.; Nielsen, J. H.; Horch, S.; Chorkendorff, I. *Science*, **2007**, *317*, 100–102.

(63)   Man, I. C.; Su, H.-Y.; Calle-Vallejo, F.; Hansen, H. A.; Martínez, J. I.; Inoglu, N. G.; Kitchin, J.; Jaramillo, T. F.; Nørskov, J. K.; Rossmeisl, J. *ChemCatChem*, **2011**, *3*, 1159–1165.

(64)   Danilovic, N.; Subbaraman, R.; Chang, K.-C.; Chang, S. H.; Kang, Y. J.; Snyder, J.; Paulikas, A. P.; Strmcnik, D.; Kim, Y.-T.; Myers, D.; Stamenkovic, V. R.; Markovic, N. M. *J. Phys. Chem. Lett.* **2014**, *5*, 2474–2478.

(65)   Esswein, A. J.; McMurdo, M. J.; Ross, P. N.; Bell, A. T.; Tilley, T. D. *J. Phys. Chem. C* **2009**, *113*, 15068–15072.

(66) Suntivich, J.; May, K. J.; Gasteiger, H. A.; Goodenough, J. B.; Shao-Horn, Y. *Science* **2011**, *334*, 1383–1385.

(67) Trotochaud, L.; Ranney, J. K.; Williams, K. N.; Boettcher, S. W. *J. Am. Chem. Soc.* **2012**, *134*, 17253–17261.

(68) Song, F.; Hu, X. *Nat. Commun.* **2014**, *5*, 4477.

(69) Gao, M.; Sheng, W.; Zhuang, Z.; Fang, Q.; Gu, S.; Jiang, J.; Yan, Y. *J. Am. Chem. Soc.* **2014**, *136*, 7077–7084.

(70) Yeo, B. S.; Bell, A. T. *J. Am. Chem. Soc.* **2011**, *133*, 5587–5593.

(71) Louie, M. W.; Bell, A. T. *J. Am. Chem. Soc.* **2013**, *135*, 12329–12337.

(72) Jin, S. *ACS Energy Lett.* **2017**, *2*, 1937–1938.

(73) McCrory, C. C. L.; Jung, S.; Peters, J. C.; Jaramillo, T. F. *J. Am. Chem. Soc.* **2013**, *135*, 16977–16987.

(74) Li, Y.; Wang, H.; Xie, L.; Liang, Y.; Hong, G.; Dai, H. *J. Am. Chem. Soc.* **2011**, *133*, 7296–7299.

(75) Xie, J.; Zhang, J.; Li, S.; Grote, F.; Zhang, X.; Zhang, H.; Wang, R.; Lei, Y.; Pan, B.; Xie, Y. *J. Am. Chem. Soc.* **2013**, *135*, 17881–17888.

(76) Seo, B.; Jung, G. Y.; Sa, Y. J.; Jeong, H. Y.; Cheon, J. Y.; Lee, J. H.; Kim, H. Y.; Kim, J. C.; Shin, H. S.; Kwak, S. K.; Joo, S. H. *ACS Nano* **2015**, *9*, 3728–3739.

(77) Voiry, D.; Yamaguchi, H.; Li, J.; Silva, R.; Alves, D. C. B.; Fujita, T.; Chen, M.; Asefa, T.; Sheoy, V. B.; Eda, G.; Chhowalla, M. *Nat. Mater.* **2013**, *12*, 850–855.

(78) Zegkinoglou, I.; Zendegani, A.; Sinev, I.; Kunze, S.; Mistry, H.; Jeon, H. S.; Zhao, J.; Hu, M. Y.; Alip, E. E.; Piontek, S.; Smialkowski, M.; Apfel, U.-P.; Körmann, F.; Neugebauer, J.; Hickel, T.; Cuenya, B. R. *J. Am. Chem. Soc.* **2017**, *139*, 14360–14363.

(79) Tran, P. D.; Tran, T. V.; Orio, M.; Torelli, S.; Truong, Q. D.; Nayuki, K.; Sasaki, Y.; Chiam, S. Y.; Yi, R.; Honma, I.; Barber, J.; Artero, V. *Nat. Mater.* **2016**, *15*, 640–646.

(80) Vrubel, H.; Hu, X. *Angew. Chem., Int. Ed.* **2012**, *124*, 12875–12878.

(81) Liao, L.; Wang, S.; Xiao, J.; Bian, X.; Zhang, Y.; Scanlon, M. D.; Hu, X.; Tang, Y.; Liu, B.; Girault, H. H. *Energy Environ. Sci.* **2014**, *7*, 387–392.

(82) Cao, B.; Veith, G. M.; Neuefeind, J. C.; Adzic, R. R.; Khalifah, P. G. *J. Am. Chem. Soc.* **2013**, *135*, 19186–19192.

(83) Popczun, E. J.; McKone, J. R.; Read, C. G.; Biacchi, A. J.; Wiltrout, A. M.; Lewis, N. S.; Schaak, R. E. *J. Am. Chem. Soc.* **2013**, *135*, 9267–9270.

(84) Popczun, E. J.; Read, C. G.; Roske, C. W.; Lewis, N. S.; Schaak, R. E. *Angew. Chem., Int. Ed.* **2014**, *126*, 5531–5534.

(85) Iijima, S. *Nature*, **1991**, *354*, 56–58.

(86) Avouris, P.; Appenzeller, J.; Martel, R.; Wind, S. J. *Proc. IEEE* **2003**, *91*, 1772–1784.

(87) Wang, J. *Electroanal.* **2005**, *17*, 7–14.

(88)   Zhang, J.; Xia, Z.; Dai, L. *Sci. Adv.* **2015**, *1*, e1500564.

(89)   Dong, G.; Fang, M.; Wang, H.; Yip, S.; Cheung, H.-Y.; Wang, F.; Wong, C.-Y.; Chu, S. T.; Ho, J. C. *J. Mater. Chem. A* **2015**, *3*, 13080–13086.

(90)   Chen, R.; Yang, C.; Cai, W.; Wang, H.-Y.; Miao, J.; Zhang, L.; Chen, S.; Liu, B. *ACS Energy Lett.* **2017**, *2*, 1070–1075.

(91)   Bard, A. J.; Faulkner, L. R. *Electrochemical Methods: Fundamentals and Applications*, 2nd edition; John Wiley & Sons: New York, **2001**.

(92)   Bonakdarpour, A.; Lefevre, M.; Yang, R.; Jaouen, F.; Dahn, T.; Dodelet, J.-P.; Dahn, J. R. *Electrochem. Solid State Lett.* **2008**, *11*, B105–B108.

(93)   Ma, T. Y.; Ran, J.; Dai, S.; Jaroniec, M.; Qiao, S. Z. *Angew. Chem., Int. Ed.* **2015**, *54*, 4646–4650.

(94)   Kocha, S. S. Best Practices and Benchmark Activities for ORR Measurements by the Rotating Disk Electrode Technique, https://www.hydrogen.energy.gov/pdfs/review14/fc111_kocha_2014_o.pdf, **2014** (accessed Nov 12, 2017).

(95)   Trotochaud, L.; Young, S. L.; Ranney, J. K.; Boettcher, S. W. *J. Am. Chem. Soc.* **2014**, *136*, 6744–6753.

(96)   Roger, I.; Symes, M. D. *J. Am. Chem. Soc.* **2015**, *137*, 13980–13988.

(97)   Strmcnik, D.; Kodama, K.; van der Vliet, D.; Greeley, J.; Stamenkovic, V. R.; Marković, N. M. *Nat. Chem.* **2009**, *1*, 466–472.

(98)   Conway, B. E.; Salomon, M. *Electrochim. Acta* **1964**, *9*, 1599–1615.

(99)   Garsany, Y.; Baturina, O. A.; Swider-Lyons, K. E.; Kocha, S. S. *Anal. Chem.* **2010**, *82*, 6321–6328.

(100) Kocha, S. S.; Garsany, Y.; Myers, D. Testing Oxygen Reduction Reaction Activity with the Rotating Disc Electrode Technique, https://energy.gov/sites/prod/files/2014/03/f12/webinarslides_rde_technique_031213.pdf, **2013** (accessed Nov 12, 2017).

(101) Suntivich, J.; Gasteiger, H. A.; Yabuuchi, N.; Shao-Horn, Y. *J. Electrochem. Soc.* **2010**, *157*, B1263–B1268.

(102) Gorlin, Y.; Jaramillo, T. F. *J. Am. Chem. Soc.* **2010**, *132*, 13612–13614.

(103) Bard, A. J.; Fox, M. A. *Acc. Chem. Res.* **1995**, *28*, 141–145.

(104) Zelenay, P. Non-Precious Metal Fuel Cell Cathodes: Catalyst Development and Electrode Structure Design, https://www.hydrogen.energy.gov/pdfs/review16/fc107_zelenay_2016_o.pdf, **2016** (accessed Nov 6, 2017).

2

CARBON NANOTUBES/HETEROATOM-DOPED CARBON CORE–SHEATH NANOSTRUCTURES FOR OXYGEN REDUCTION REACTION

2.1. INTRODUCTION

Oxygen reduction reaction (ORR) plays a crucial role on governing the performance of electrochemical energy devices such as fuel cells[1,2] and metal–air batteries.[3] Platinum-based electrocatalysts have been prevalently used for the ORR; however, their ORR activity deteriorates rapidly with long-term operation. In addition, the high cost and scarcity of Pt have further hampered widespread use of fuel cell systems. Consequently, tremendous research has been devoted to the development of highly active and stable, yet low-cost ORR electrocatalysts based on low-Pt or Pt-free compositions.[4–9] Among such classes of catalysts, carbon nanomaterials doped with heteroatoms have shown excellent ORR activity, particularly in alkaline media.[9] Over the last few years, various nanocarbons, including carbon nanotubes,[10–14] graphene,[15–18] nanoporous carbons,[19–21] and carbon nitrides,[22–24] doped with various heteroatoms, have been investigated as electrocatalysts for the ORR in alkaline media. Despite a rapid progress, there still exists a multitude of challenges in the doped nanocarbon-based electrocatalysts. First, the preparation of doped carbon nanostructures, particularly carbon nanotubes and graphene, is predominantly achieved by *in situ* doping *via* chemical vapor deposition (CVD) or annealing of pure carbons under reactive gas; however, these methods are unfavorable for large-scale synthesis and unavoidably involve the use of toxic gases such as ammonia or acetonitrile. Second, the ORR activity of doped carbon nanostructures is still inferior to that of Pt/C catalysts; Pt/C catalysts generally show a half-wave potential of around 0.85–0.90 V (*vs* reversible hydrogen electrode; RHE), whereas the half-wave potential of doped carbon nanostructures ranges between 0.60 and 0.80 V (*vs* RHE). Finally, the application of doped carbon nanostructures in alkaline anion exchange membrane fuel cell (AEMFC) has rarely been demonstrated, which is critical to their

practical use.[25]

Herein, we report an ionic liquid (IL)-derived, facile, scalable route to new carbon nanostructures comprising heteroatom-doped carbon sheath layers coated on CNT (CNT/HDC). The CNT/HDC nanostructures show excellent electrocatalytic activity for the ORR, evidenced by their high half-wave potential and kinetic current density in alkaline media. The ORR activity of CNT/HDC nanostructures is one of the best performances among the reported heteroatom-doped nanocarbon catalysts. The kinetic parameters of the CNT/HDC nanostructures compare favorably with those of a Pt/C catalyst. The CNT/HDC nanostructures also exhibit superior long-term durability and poison-tolerance relative to Pt/C. In addition, the CNT/HDC nanostructures show very high current and power densities when employed as cathode catalysts in alkaline AEMFC.

2.2. EXPERIMENTAL METHODS

2.2.1. Synthesis of CNT/HDC Catalysts

Multi-walled CNTs (< 10 nm in diameter, 5–15 μm in length, TCI chemical) were treated with HNO_3 (63%) at 118 °C for 6 h and HCl (37%) at 105 °C for 6 h to remove metallic impurities and to increase hydrophilicity of the CNTs. 200 mg of the treated CNTs were suspended in 2 mL of IL (1-butyl-3-methylimidazolium bis(trifluoromethylsulfonyl)imide; BMITFSI), and the mixture was ground in an agate mortar for 15 min. 1 mL of tetraethyl orthosilicate (TEOS) was added to this gel, and the mixture was ground for 15 min. 1 mL of formic acid was added to trigger the formation of the silica-based gel. Volatiles were evaporated to give a monolithic CNT-IL-silica composite. The composite was added into an alumina crucible and located in a quartz tube furnace. The temperature was elevated to the desired temperature (800, 900, and 1000 °C) at a ramping rate of ~2 °C min^{-1} and maintained at that temperature for 2 h under 1 L min^{-1} of N_2 flow. The resulting CNT/HDC-silica composite was added to 2 : 1 (v/v) = ethanol : 10% HF (diluted from 50% HF, JT Baker) solution and stirred for 30 min to etch the silica. The suspension was filtered and washed with ethanol. Acid-treatment and filtration were carried out once more in the same manner. The product was dried at 60 °C and collected. The catalysts were denoted as CNT/HDC-X (X: pyrolysis temperature). For comparison, HDC catalyst was synthesized in the same manner described above in the absence of CNTs. A physical mixture of CNTs and HDC was prepared by grinding them in an agate mortar for 10 min.

N-doped CNTs were synthesized by two methods using ammonia gas and urea as N source (denoted as N-CNT-NH_3 and N-CNT-Urea, respectively). For the preparation of N-CNT-NH_3, the acid-treated CNTs were heated at 1000 °C under an NH_3 gas flow (60 sccm of NH_3 and 40 sccm of

Ar) for 2 h (ramping rate = ~2.5 °C min^{-1}). N-CNT-Urea was prepared by grinding the acid-treated CNT and urea (99%, Junsei) in the weight ratio of 1 : 3 in an agate mortar, and annealing the mixture at the same pyrolysis conditions described above except 1 L min^{-1} of N$_2$ flow.

For other heteroatom-doped CNT/HDC catalysts, 1-butyl-3-methylimidazolium salts with four different anions were used; hexafluorophosphate (CNT/HDC-PNF), tetrafluoroborate (CNT/HDC-BNF), trifluoroacetate (CNT/HDC-NF), and acetate (CNT/HDC-N). Except the type of IL used, the synthetic procedure is the same as described above while the pyrolysis temperature was 1000 °C.

2.2.2. Characterization Methods

The structure of the catalysts was observed using an image-side spherical aberration-corrected TEM (Titan^3 G2 cube 60-300, FEI Company) under an accelerating voltage of 80 kV, which enabled the atomic resolution imaging of the samples with minimized sample damage by electron irradiation. The catalysts were dispersed in ethanol and dropped on a holey carbon grid for TEM analyses.

The atomic species and chemical compositions of the samples were analyzed using an XPS (K-alpha, ThermoFisher Scientific) with a monochromatic Al Kα X-ray source (1486.6 eV). Approximately 10 mg of sample was pelletized into a self-supporting wafer for the XPS analysis. The XPS spectra were analyzed using the XPSPeak41 software. First, Shirley-type background was removed with a zero slope. N 1s spectra were deconvoluted into four peaks using a Gaussian-Lorentzian mixed function (70% Gaussian and 30% Lorentzian). The peak location for N1 (pyridinic), N2 (pyrrolic), N3 (graphitic), and N4 (N–O) was confined at 398.0, 399.3, 400.7, and 402.1 eV (± 0.1 eV), respectively. The FWHM of each peak was fixed at 1.5, 1.5, 1.55 and 1.6 eV, respectively. The content of each species was estimated by the relative peak area. The XPS curve-fitting parameters are summarized in **Table 2.1** (in *Section 2.3.2*).

Raman spectra of the catalysts were obtained by using a confocal Raman microscope (Alpha300R, WITec) with an excitation wavelength of 532 nm and a laser power of 1 mW. The spectra were normalized by setting the maximum and minimum signal values to 1 and 0, respectively. The spectra were measured at least three times for each sample and averaged spectrum is shown.

The porous and textural properties were analyzed using a nitrogen sorption analyzer (BELSORP-max, MicrotracBEL) operated at −196 °C. The specific surface areas were calculated using the BET equation in the relative pressure range of 0.05 to 0.20. The pore volumes were determined at a relative pressure of 0.995.

2.2.3. Electrochemical Characterizations

Electrochemical measurements were performed using an IviumStat electrochemical analyzer (Ivium Technologies) at RT and the atmospheric pressure. Three-electrode system was built with a Pt coil counter electrode, an Hg/HgO (XR400, Radiometer Analytical) reference electrode, and a rotating ring disk electrode (RRDE, ALS) working electrode. Before every measurement, the RRDE was polished with a 1.0 μm alumina suspension and subsequently with 0.3 μm alumina suspension on a micro-cloth to generate a mirror finish. The catalyst ink was prepared by mixing the catalyst (30 mg), Nafion (75 μL; 5 wt%, Sigma-Aldrich), DI water (100 μL), and anhydrous ethanol (1.01 mL) and sonicating the mixture for at least for 30 min. The Pt/C catalyst ink was made from a commercial Pt/C catalyst (5 mg; 20 wt% Pt, HiSPEC-3000, Johnson-Matthey), Nafion (40 μL), and anhydrous ethanol (1.15 mL). 3 μL of the catalyst ink was pipetted with a micro-syringe (Hamilton) and deposited onto the glassy carbon (GC) disk, dried at RT, and subsequently dried at 70 °C for 5 min. Prior to the electrochemical measurements, the deposited catalyst film was electrochemically cleaned by 50 potential cycles from 0.05 to 1.20 V (*vs* RHE) at a scan rate of 100 mV s^{-1} in N_2-saturated (99.999%) 0.1 M KOH (diluted from 99.99% KOH (Sigma-Aldrich) in 18.2 MΩ cm, Millipore). Cyclic voltammetry (CV) was then performed under the same conditions used for electrochemical cleaning, except for the change in the scan rate to 20 mV s^{-1} for three cycles. After O_2 bubbling (99.995%), linear sweep voltammetry (LSV) curves for the ORR were obtained from 1.1 to 0.2 V (*vs* RHE) with continuous O_2 bubbling at a rotating speed of 1,600 rpm (RRDE-3A, ALS). The potential scan direction was opposite for the Pt/C catalyst because the oxide layer was formed during the cathodic scan. The measurements were independently repeated three times and the average data are presented. To assess the long-term durability of the catalysts, the potential cycles from 0.6 to 1.0 V were applied 10,000 times at a scan rate of 50 mV s^{-1} in N_2-saturated 0.1 M KOH solution. ORR polarization curves were obtained after 500, 5000, and 10000 cycles. Before each ORR measurement, the electrolyte was replaced with a fresh batch, and purged with oxygen gas. The LSV scans for the ORR were conducted in the same manner as described above. The methanol tolerance test was carried out in the presence of 0.5 M methanol (≥99.9%, Sigma-Aldrich) in 0.1 M KOH solution.

2.2.4. RHE Calibration

To convert the potential to RHE scale, a three-electrode system was built with two Pt coils as working and counter electrodes and Hg/HgO as the reference electrode. The CV was performed around zero-current region at a scan rate of 1 mV^{-1} in H_2-saturated (99.9999%) 0.1 M KOH. After averaging the cathodic and anodic current, the potential at the zero current, that is the equilibration point of H^+/H_2 redox reaction, is the conversion factor (**Figure 2.1**).
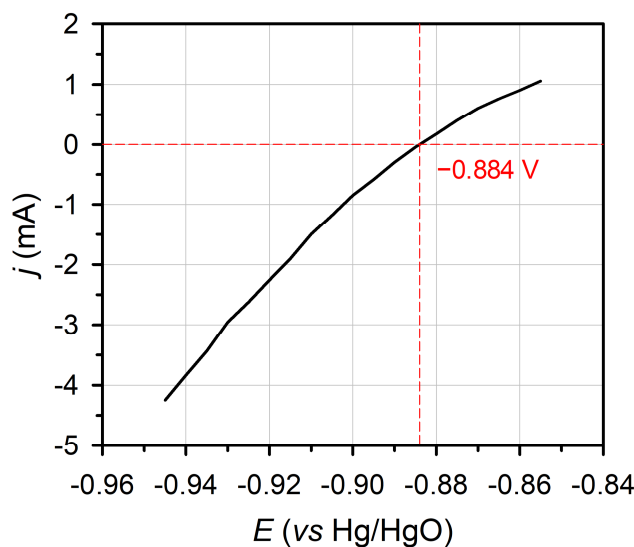
Figure 2.1. HER/HOR polarization curve measured on Pt coil in H_2-saturated 0.1 M KOH at a potential scan rate of 1 mV s^{-1} to obtain the potential difference between the RHE and the Hg/HgO reference electrode.

2.2.5. Analysis of ORR Kinetics

For the evaluation of the 4-electron selectivity during the LSV scans for the ORR, the potential of the Pt ring was fixed at 1.3 V (*vs* RHE). The number of electrons transferred was calculated from the following equation

$$n = \frac{4}{1 + \dfrac{i_r}{N \times i_d}}$$

where n, i_r, N, and i_d are the electron transfer number, the ring current, the collection efficiency (0.47 provided by manufacturer), and the disk current, respectively.

To compare the ORR kinetics, the kinetic current was extracted from the following equation

$$\frac{1}{j} = \frac{1}{j_k} + \frac{1}{j_l}$$

where j, j_k, and j_l indicate the measured current density, the kinetic current density, and the diffusion-limited current density, respectively (normalized by GC electrode area). Then, the Tafel plot was derived by plotting the kinetic current density in the logarithmic scale versus the overpotential according to the Tafel equation

$$\eta = -b\log j_k + b\log j_0$$

where η, b, and j_0 represent the overpotential, the Tafel slope, and the exchange current density, respectively. The exchange current density was obtained by extrapolation of the line from the linear region of the Tafel plot to the point of zero overpotential ($\eta = 0$), where the x-intercept of the line is j_0.

2.2.6. AEMFC Performance Tests

CNT/HDC, CNTs, or 20 wt% Pt/C catalysts (HiSPEC-3000, Johnson Matthey) were used cathode catalysts while 40 wt% Pt/C catalysts (Johnson Matthey HiSPEC-4000) were used as anode catalysts. The catalyst slurries were prepared by mixing catalyst powders with commercial ionomer I2 (Acta S.p.A.) in methanol and DI water. The ionomer contents in cathode and anode slurries were controlled to be 20 and 25 wt%, respectively. The catalyst slurries were well dispersed by stirring and ultrasonication (Ultra TURRAX, IKA Labortechnik, 10,000 rpm). The membrane electrode assemblies (MEAs, active area: 25 cm^2) were prepared by spraying the catalyst slurry directly onto the in-house pore-filling anion-conducting membrane which has an ion conductivity and a durability similar to those of a commercial membrane. A more detailed procedure of this pore-filling membrane has been published previously.[26] The loading of the anode catalyst was 0.5 mg cm^{-2}, and the loadings of the cathode CNT and CNT/HDC catalysts, and the Pt/C catalyst were 2.0 and 0.5 mg cm^{-2}, respectively. The MEAs were pressed at 10 bar cm^{-2} at RT for 5 min before cell fabrication. Single cells were assembled using stainless-steel current collectors, graphite bipolar plates with serpentine flow channels (1.0 mm channel width, 1.0 mm channel depth, 1.0 mm rib width), Teflon seals, and gas diffusion layers (10BC, SGL, hydrophobic treatment).

The performances of the MEAs were measured using a single cell test station (OsunTech) at 100% RH, atmospheric pressure, and 50 °C. H$_2$ and O$_2$ were used as anode and cathode reactant gases, respectively, which were humidified by bubbling them through DI water before they entered the test station. The 100% RH condition of the gases was controlled by the temperature of the humidifiers. Before the single cell operation, the humidifiers for both the anode and cathode were calibrated with a humidity sensor (HS-1000, Viasensor). The anode was fed with fully humidified H$_2$ gas at a constant flow rate of 400 mL min^{-1}, and the cathode was fed with fully humidified O$_2$ air gas at a constant flow rate of 1200 mL min^{-1} at atmosphere pressure on both sides. After the open circuit voltage (OCV) was stabilized, the polarization curves of the prepared MEAs were obtained at a scan rate of 2 mV s^{-1} from OCV to 0.2 V.

2.3. RESULTS AND DISCUSSION

2.3.1. Synthesis of CNT/HDC Catalysts

The synthetic scheme for the CNT/HDC core-sheath nanostructures is illustrated in **Figure 2.2**. ILs were selected as precursors for the formation of the HDC layers owing to their versatility as environmentally benign sources for carbon nanostructures, as well as their atomic composition with various heteroatoms.[27,28] Briefly, we began by producing a monolithic gel of CNT-IL-silica composite using multi-walled CNTs, an IL (1-butyl-3-methylimidazolium bis(trifluoromethylsulfonyl)imide; BMITFSI), and a silica source (TEOS). The CNTs were treated with acid to remove metallic impurities prior to formation of the composite. By grinding the powder of CNTs with IL, CNTs were exfoliated,[29] and the mixture became a black paste-like gel. The subsequent addition of TEOS and formic acid resulted in the formation of CNT-IL-silica composite monolith after several hours. Subsequent carbonization at desired temperature from 800 to 1000 °C, followed by the etching of silica afforded CNT/HDC-X (X = carbonization temperature) nanostructures. The same synthesis without the presence of CNTs yielded HDC catalyst. It should be noted that the IL contains nitrogen in the imidazolium cation and nitrogen, sulfur, and fluorine in the anion; these elements can serve as heteroatom sources in the HDC sheath layer.
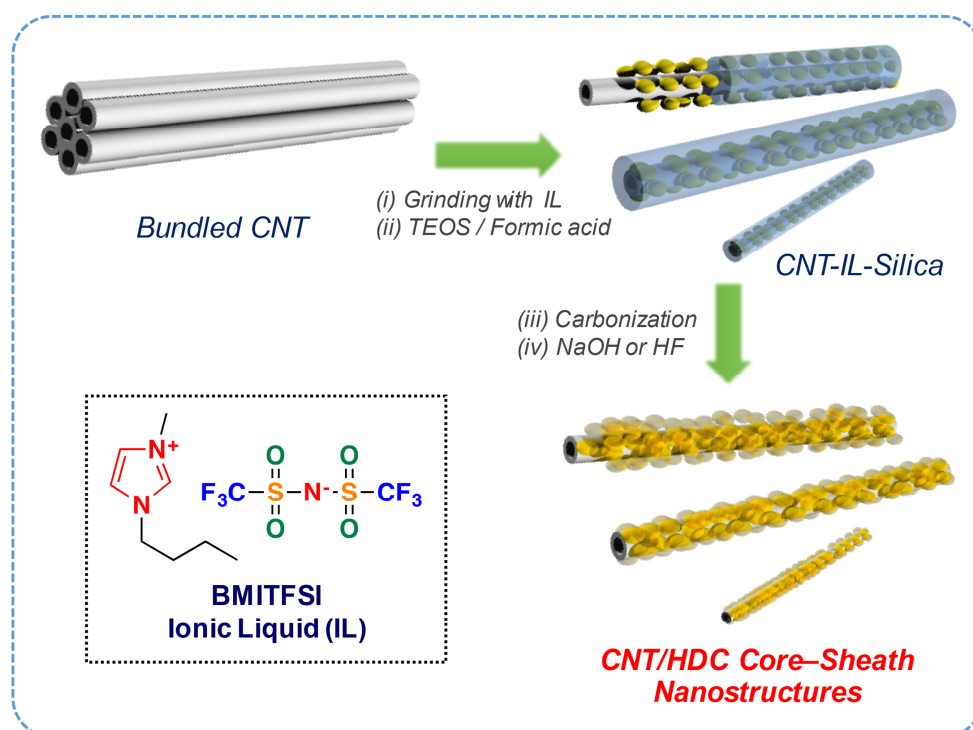
Figure 2.2. Schematic illustration of the synthesis of the CNT/HDC core–sheath nanostructure catalyst.

2.3.2. Physicochemical Characterizations

The formation of the CNT/HDC nanostructures was observed using atomic resolution transmission electron microscopy (AR-TEM) (**Figure 2.3**). The AR-TEM image of the CNTs (**Figure 2.3a**) shows the atomic structure of the CNTs, which were composed of three to eight multi-walls with an outer diameter of ca. 5–10 nm. The AR-TEM image of CNT/HDC-1000 (**Figure 2.3b**), clearly shows the successful formation of rough carbon layers on the CNT walls. The HDC sheaths were closely contacted with the walls of pristine CNTs, and their thickness was 1–5 nm. The HDC sheaths were identified to partly have graphitic structures, as clearly confirmed in hexagonal lattice image (**Figure 2.3b**, inset).
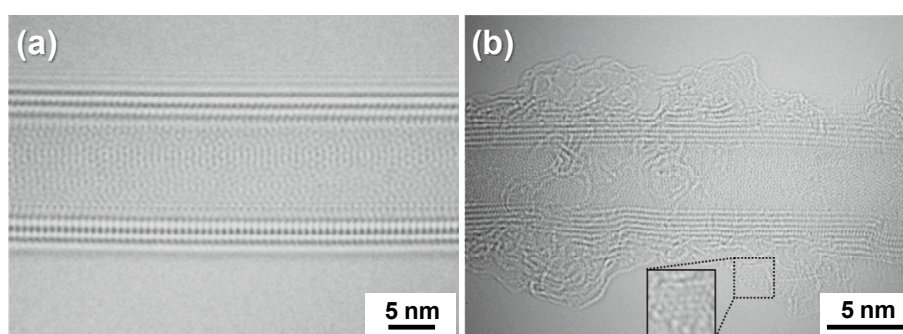
Figure 2.3. AR-TEM images of (a) CNTs and (b) CNT/HDC-1000.

The composition and structure of the CNTs and CNT/HDC nanostructures were assessed by XPS analysis. The XPS survey spectrum of the CNTs (**Figure 2.4a**) showed a pronounced C 1s peak and a trace peak for O 1s, and confirmed that the CNTs were free of metals after the acid pre-treatment. The noticeable changes after formation of the HDC sheath layer on the CNTs were the appearance of new peaks corresponding to heteroatoms at 400 eV (N 1s), 165 eV (S 2p), and 690 eV (F 1s) and an increase in the intensity of the peak at 530 eV (O 1s) (**Figure 2.4**), indicating the formation of HDC layers with triple (N, S, and F) dopants. More detailed analyses of the N 1s XPS spectra of CNT/HDC nanostructures and HDC are presented in **Figure 2.5a** and **Table 2.1**. The N 1s peaks of the samples were deconvoluted into four peaks at 398.0, 399.3, 400.7, and 402.1 eV, which could be assigned to pyridinic (N1), pyrrolic (N2), graphitic (N3), and N–O (N4) nitrogen species, respectively.[16] While the position of each peak was preserved with heating temperature, the relative ratios of each peak changed significantly. Notably, the peak area of the graphitic nitrogen increased gradually with increasing temperature, whereas that of the pyridinic nitrogen decreased. Furthermore, the peak area of the N–O species also increased with temperature, which may be suggestive of stronger interaction of the surfaces of the CNT/HDC nanostructures with oxygen. Detailed XPS quantitative analysis of the respective elements (**Table 2.2**) revealed that the total amount of

heteroatoms (N, S, and F) on the surface decreased from 8.8 to 6.6 at% with increasing temperature from 800 to 1000 °C.
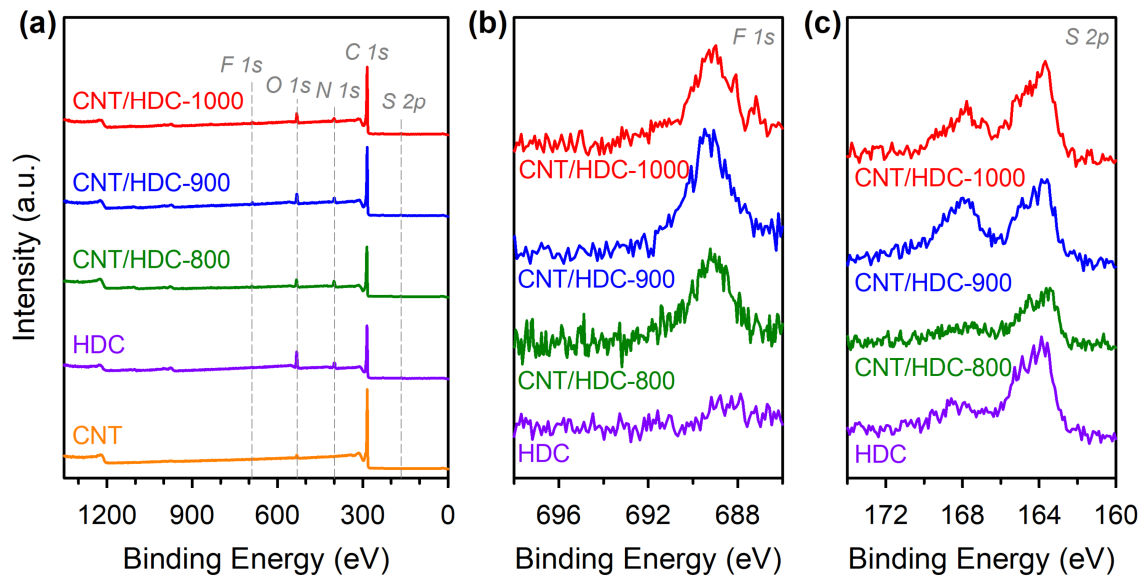
Figure 2.4. (a) XPS survey spectra of CNT, HDC, and CNT/HDC-X. (b,c) High-resolution (b) F 1s and (c) S 2p XPS spectra of HDC and CNT/HDC-X.
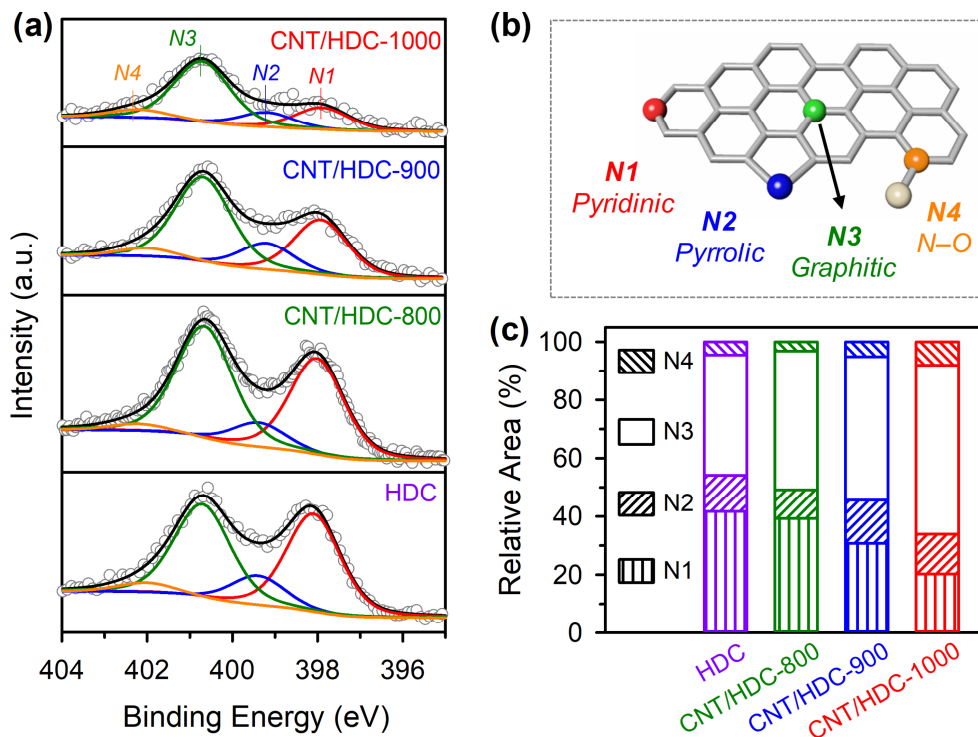
Figure 2.5. (a) High-resolution N 1s XPS spectra and deconvoluted peaks of HDC and CNT/HDC-X. (b) Schematic illustration of the atomic configuration of N1–N4 species. (c) Bar graph showing the relative contents of each N species in the catalysts.

Table 2.1. Summary of deconvolution parameters of N 1s XPS spectra for the CNT/HDC nanostructures and HDC.

Sample	Binding energy (eV)				N content (%)			
	N1	N2	N3	N4	N1	N2	N3	N4
CNT/HDC-1000	397.90	399.20	400.71	402.20	20.3	13.6	58.0	8.1
CNT/HDC-900	397.92	399.20	400.69	402.00	30.8	14.8	49.2	5.2
CNT/HDC-800	398.02	399.38	400.66	402.20	39.3	9.9	47.6	3.2
HDC	398.10	399.40	400.71	402.00	41.7	12.5	41.3	4.5

Table 2.2. Summary of surface elemental composition of the CNT/HDC nanostructures of HDC analyzed by XPS.

Sample	Surface composition (at%)				
	C	N	S	O	F
CNT/HDC-1000	88.0	4.6	1.1	5.4	0.9
CNT/HDC-900	85.1	5.5	1.1	6.9	1.2
CNT/HDC-800	85.6	7.5	0.6	5.5	0.7
HDC	79.0	8.5	1.0	11.0	0.4

The graphitic nature of the samples was probed by Raman spectroscopy (**Figure 2.6a**). The Raman spectra of the untreated pristine CNTs exhibited typical spectral characters with pronounced, sharp G-band at 1580 cm^{-1} and negligible D-band at 1345 cm^{-1}. The acid treatment of CNTs resulted in a broadening of the G-band as well as an increase of the D-band. The CNT/HDC nanostructures regained graphitic character, which was evidenced by a substantial decrease in the D-band, compared to acid-treated CNTs. The porous structure of these materials was analyzed using N$_2$ physisorption (**Figure 2.6b**). The adsorption-desorption isotherms of CNTs show a large uptake of N$_2$ in the high-pressure region, indicating the presence of macropores which originate from the space between the CNT bundles. In contrast, decreased adsorption was evident in the high-pressure region of the isotherms of CNT/HDC nanostructures, which could be associated with exfoliation of the bundled CNTs into individual CNTs. In addition, the isotherms of the CNT/HDC show hysteresis loops in the relative pressure range of 0.4–0.6, indicating the generation of mesopores in HDC layers due to removal of the silica from the CNT-IL-silica composites. The numerical textural data are summarized in **Table 2.3**.
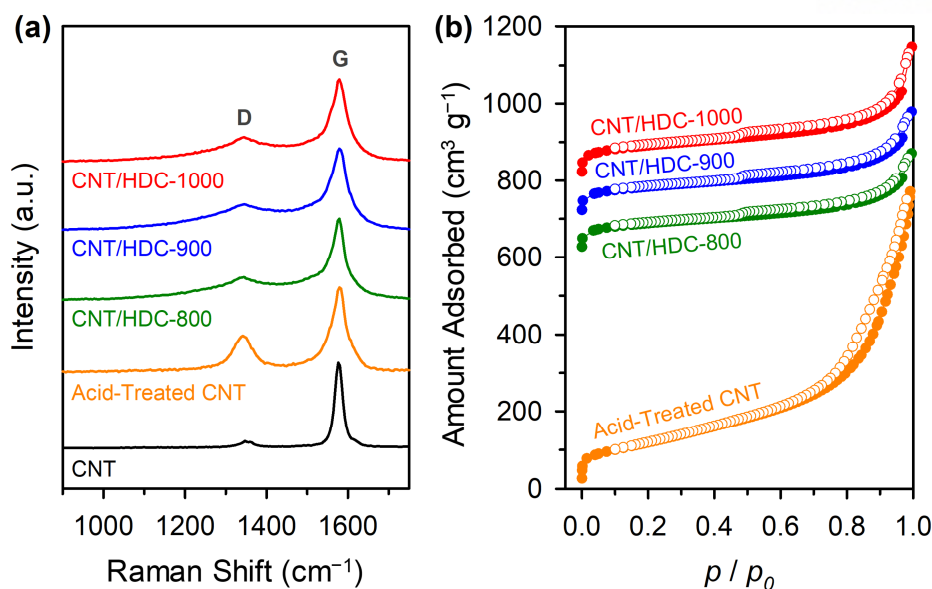
Figure 2.6. (a) Raman spectra of CNT, acid-treated CNT, and CNT/HDC catalysts carbonized at different temperatures. (b) N_2 adsorption-desorption isotherms of acid-treated CNT and CNT/HDC carbonized at different temperatures.

Table 2.3. Summary of textural properties of the CNT/HDC nanostructures, HDC, and the acid-treated CNT.

Sample	BET surface area ($m^2 g^{-1}$)	Total pore volume ($cm^3 g^{-1}$)
CNT/HDC-1000	325	0.53
CNT/HDC-900	293	0.43
CNT/HDC-800	315	0.42
HDC	489	0.39
Acid-treated CNT	428	1.19

2.3.3. ORR Activity in Half-Cell Configurations

The electrocatalytic activity of the heteroatom-doped CNT/HDC core–sheath nanostructures, and reference catalysts, was evaluated using the RRDE technique. **Figure 2.7a** shows the LSV polarization curves of the catalysts for the ORR, measured in 0.1 M KOH electrolyte at a rotating speed of 1,600 rpm and a scan rate of 5 mV s^{-1}. The LSV curve of the CNTs exhibited onset and half-wave potentials at 0.82 and 0.72 V (*vs* RHE), respectively, and showed no current plateau, indicative of being far from efficient 4-electron transfer. HDC as well as the physical mixture of CNTs and HDC (CNT + HDC) also exhibited similar onset and half-wave potentials to those of the CNTs. The direct formation of HDC sheath layers on the CNTs markedly improved ORR activity and kinetics; the onset

and half-wave potentials of the CNT/HDC nanostructures were significantly shifted to positive potentials with well-defined plateaus, indicating the synergistic effect of hybridization between CNT cores and HDC sheath layers. The highest ORR activity was achieved with the CNT/HDC-1000, followed by CNT/HDC-900 and CNT/HDC-800. The most active CNT/HDC-1000 showed onset and half-wave potentials at 0.92 and 0.82 V, respectively, and had a kinetic current density of 8.3 mA cm^{-2} at 0.8 V. Such a high activity of CNT/HDC nanostructures compared favorably with that of a benchmark Pt/C catalyst, which showed onset and half-wave potentials at 0.98 and 0.85 V, respectively. We compared the ORR activity of CNT/HDC nanostructure catalysts with N-doped CNTs. The N-doped CNTs were prepared by using ammonia or urea as an N source, and the resulting catalysts were denoted as N-CNT-NH$_3$ and N-CNT-Urea, respectively. **Figure 2.7b** shows the ORR activity of the N-CNT catalysts, along with those of undoped CNTs and the CNT/HDC-1000. The two N-CNT catalysts showed better ORR activity than undoped CNT, as consistent with the previous results[10–14]; however, their activity is inferior to that of the CNT/HDC-1000. The CNT/HDC-1000 is one of the best-performing ORR catalyst in alkaline electrolytes when compared to reported doped carbons.
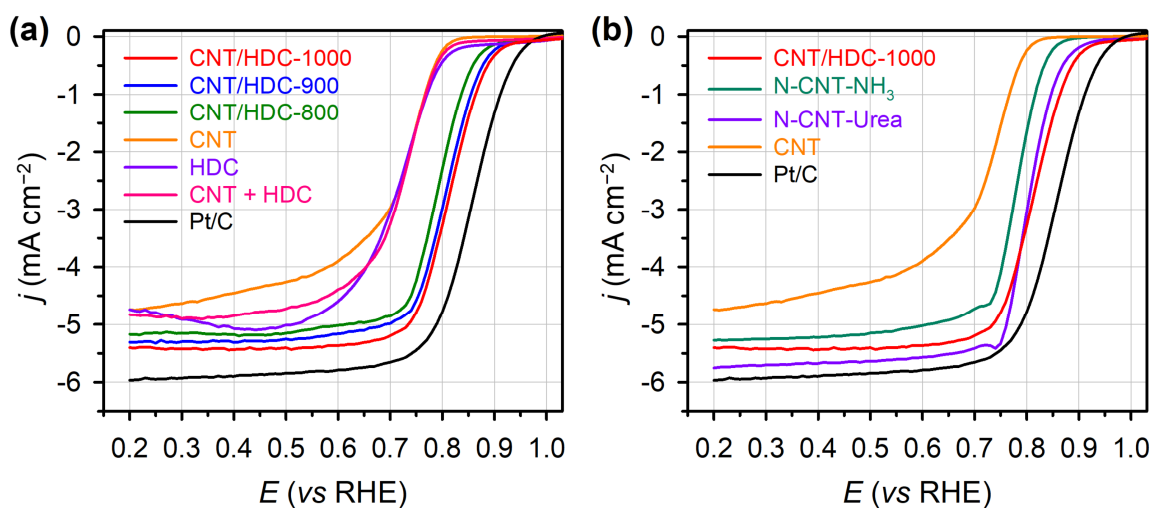
Figure 2.7. (a,b) ORR polarization curves of (a) CNT/HDC-X, CNT, HDC, the physical mixture of the CNT and HDC (CNT + HDC), and a commercial Pt/C, and (b) CNT/HDC-1000, N-CNT-NH$_3$, N-CNT-Urea, CNT, and the Pt/C measured in O$_2$-saturated 0.1 M KOH at an electrode rotation speed of 1,600 rpm.

The ORR kinetics was evaluated based on the Tafel plots and the 4-electron selectivity measurements. The Tafel slopes (**Figure 2.8a**) for the CNT/HDC catalysts ranged from 65 to 68 mV dec^{-1}, and were comparable to that of Pt/C (62 mV dec^{-1}), indicating that the ORR kinetics of the CNT/HDC catalysts is similar to that of Pt/C. **Figures 2.8b** and **2.8c** clearly reveal that the number of electrons transferred by the CNT/HDC catalysts was higher than those by the other samples and

similar to that of Pt/C catalyst, approaching 4 in the high potential region. More intrinsic kinetic insight could be gained from the exchange current densities of these catalysts for the ORR (**Figure 2.8d**). Notably, the exchange current density of the CNT/HDC-1000 is the same order of magnitude as that of Pt/C. In contrast, the CNTs, HDC, and their mixture showed one or two orders of magnitude lower exchange current densities than those of CNT/HDC catalysts and Pt/C.
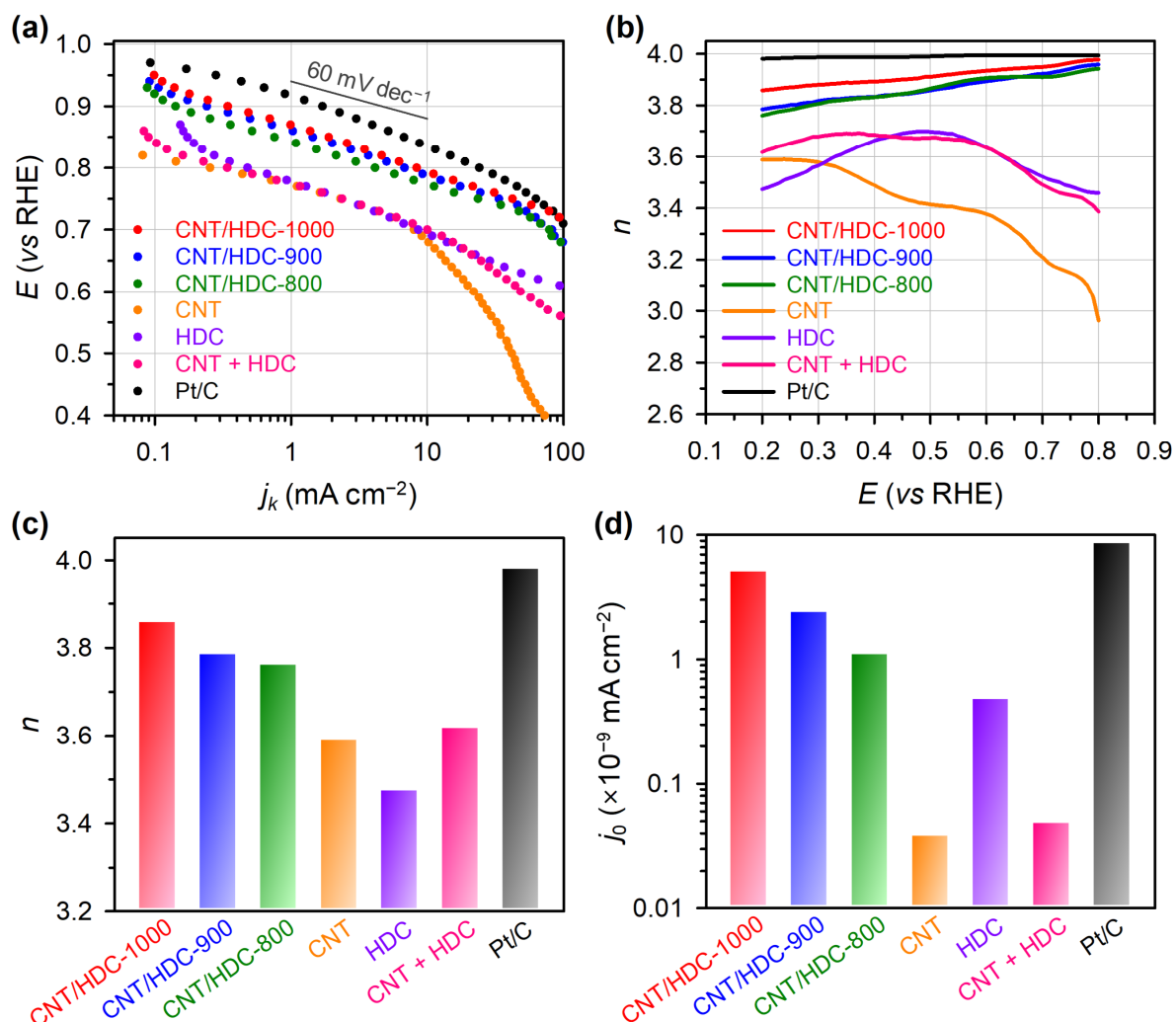
Figure 2.8. (a) ORR Tafel plots and (b) electron transfer number (n) of CNT/HDC-X, CNT, HDC, the physical mixture of the CNT and HDC (CNT + HDC), and the Pt/C. (c,d) Bar graph comparing (c) the electron transfer number at 0.20 V (vs RHE) and (d) the exchange current density (j_0) of the catalysts.

Previous routes to doped carbon-based ORR catalysts required the judicious selection of precursor and experimental conditions for CVD or the unavoidable use of toxic gases. In contrast, in our approach to CNT/HDC catalysts, the formation of HDC sheath layers relies on a simple solution process, followed by annealing in mild atmosphere, which is more amenable to large-scale preparation. Furthermore, the choice of ILs can allow for the facile control of type and quantity of

heteroatoms in the HDC layers. We extended the IL-derived synthetic methods for preparing CNT/HDC catalysts with other four different ILs, which contains B, N, P, and F heteroatoms, demonstrating the universal applicability of IL-coating synthetic strategy for heteroatom-doped carbon electrocatalysts. The resulting catalysts also exhibited excellent ORR activity in an alkaline solution (**Figure 2.9**). The information about ILs used is provided in *Section 2.2.1*.
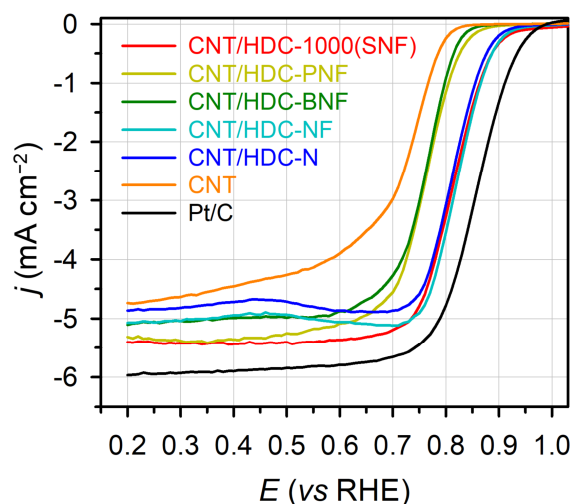
Figure 2.9. ORR polarization curves of CNT/HDC catalysts derived from different ILs, CNT, and Pt/C measured in O_2-saturated 0.1 M KOH at an electrode rotation of 1,600 rpm.

As demonstrated in the ORR activity and kinetics data, the CNT/HDC catalysts show high electrocatalytic activity for the ORR, surpassing those of doped CNTs as well as previous catalysts. In the CNT/HDC nanostructures, the CNT cores could enable efficient transport of electrons, while the thin HDC sheath layers with numerous heteroatoms provides catalytically active sites. Particularly, the presence of multiple dopants (N, S, and F) in the sheath layers could further enhance ORR activity, in accordance with recent reports demonstrating enhanced ORR activity in dual-doped carbon structures. We also note that the highest ORR activity of the CNT/HDC-1000 catalyst could originate from the increased ratios of graphitic nitrogen atoms as well as their enhanced electrical conductivity.

We next investigated the durability of the most active catalyst, CNT/HDC-1000, with Pt/C during 10,000 potential cycles between 0.6 and 1.0 V (*vs* RHE) at a scan rate of 50 mV s^{-1}. The changes in the current density percentages for the ORR at 0.85 V with cycling (**Figure 2.10a**) clearly show the superior durability of the CNT/HDC-1000 relative to the Pt/C catalyst. The initial current density of the CNT/HDC-1000 composites was minimally decreased (4.5% after cycling), whereas that of Pt/C declined dramatically by 32%. The CNT/HDC-1000 catalyst also showed superior tolerance against poison molecule such as methanol, compared to the Pt/C (**Figure 2.10b**).
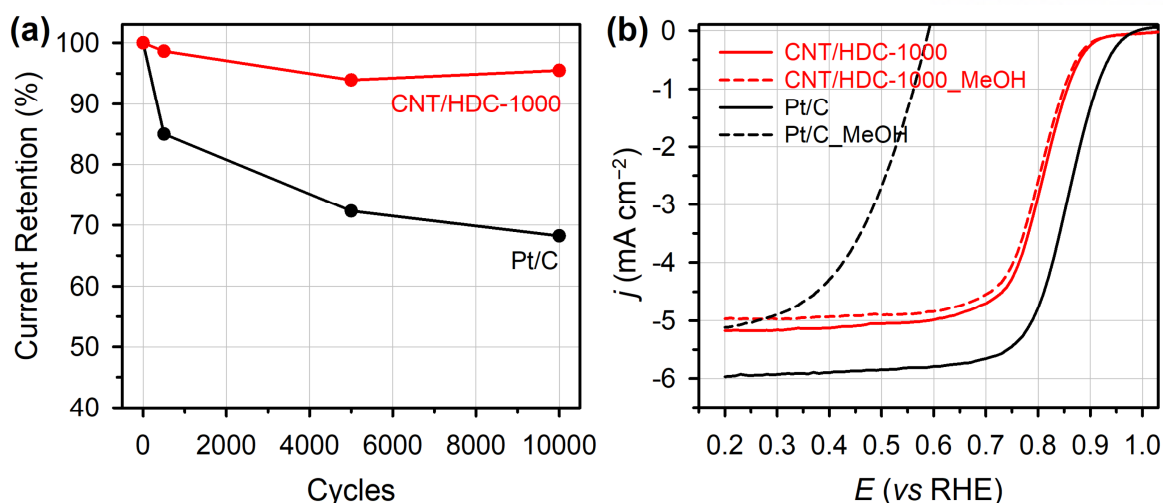
Figure 2.10. (a) The current changes at 0.85 V (*vs* RHE) versus the number of the potential cycling, and (b) ORR polarization curves measured in the presence (dotted lines) and the absence (solid lines) of 0.5 M methanol (MeOH) in 0.1 M KOH.

2.3.4. AEMFC Performance

Finally, we tested the applicability of the CNT/HDC-1000 as a cathode catalyst for alkaline AEMFC. **Figure 2.11** shows the polarization and power density curves of the MEAs that employed CNT/HDC-1000 as a cathode catalyst. For benchmark, CNTs as well as Pt/C were also tested as cathode catalysts for alkaline AEMFC. The polarization curve of CNT/HDC-1000-based MEA shows a very high onset potential at 0.85 V, consistent with ORR polarization curve obtained in half-cell configuration. The performance of CNT/HDC-1000-based MEA is significantly better than that of CNT-based MEA. At 0.6 V under H_2/O_2 operation, the CNT/HDC-1000-based cathode produced current and power densities of 368 mA cm^{-2} and 221 mW cm^{-2}, respectively, which are 23.3 times higher than those of CNT-based cathode. The performance of CNT/HDC-1000 cathode is also substantially better than a reported MEA based on nitrogen doped CNT (33.7 mA cm^{-2} and 20.2 mW cm^{-2} at 0.6 V).[25] It is also noteworthy that the current and power densities of CNT/HDC-1000-based MEA compared favorably with those of Pt/C-based MEA. Hence, these results clearly suggest that very high ORR activity of the CNT/HDC catalyst was also demonstrated in single cell tests.
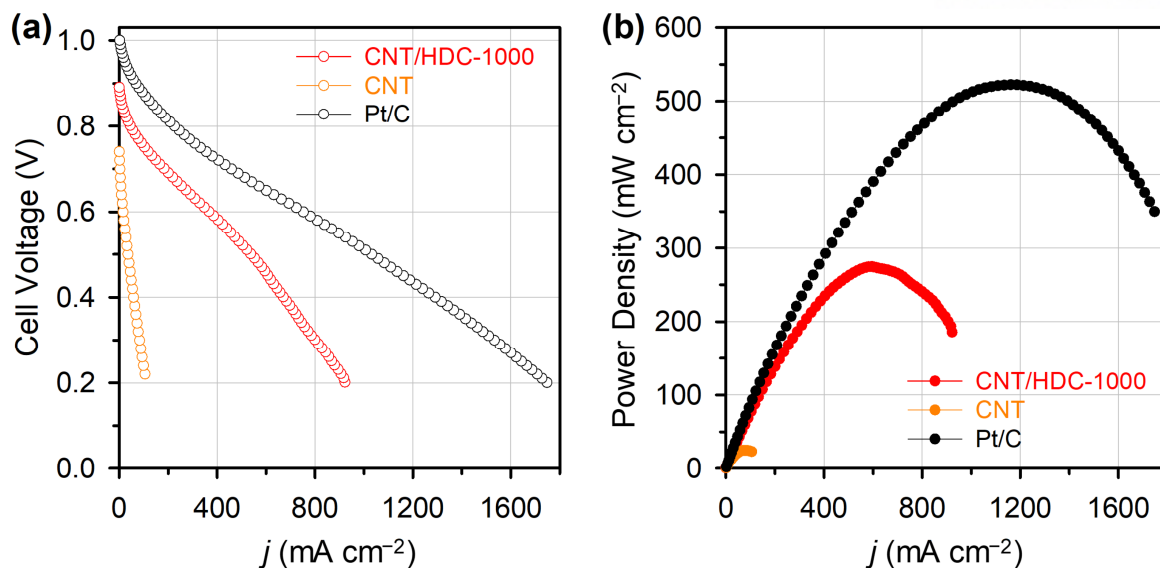
Figure 2.11. (a) Polarization curves and (b) power density curves of the MEAs based on the CNT/HDC-1000, CNT, and Pt/C catalyst in alkaline AEMFC.

2.4. CONCLUSION

In summary, we developed an IL-driven, facile, scalable route to heteroatom-doped carbon ORR electrocatalysts based on the CNT/HDC core-sheath nanostructures. The CNT/HDC nanostructures showed excellent electrocatalytic activity and kinetics for the ORR, which is one of the best performances among the metal-free, heteroatom-doped nanocarbon catalysts and compared favorably with the Pt/C catalyst. Furthermore, the CNT/HDC nanostructures exhibited superior durability and MeOH-tolerance to the Pt/C. Importantly, the high ORR activity of CNT/HDC core-sheath nanostructures was translated in alkaline fuel cells. We note that the design of core-sheath structure can be further applicable to other conductive core materials such as graphene. In addition, the use of metal-free CNT/HDC catalysts can be extended to other electrocatalytic and heterogeneous catalytic reactions.

2.5. REFERENCES

(1) Gasteiger, H. A.; Kocha, S. S.; Sompalli, B.; Wagner, F. T. *Appl. Catal. B: Enrivon.* **2005**, *56*, 9–35.

(2) Debe, M. K. *Nature* **2012**, *486*, 43–51.

(3) Bruce, P. G.; Freunberger, S. A.; Hardwick, L. J.; Tarascon, J.-M. *Nat. Mater.* **2012**, *11*, 19–29.

(4) Guo, S.; Zhang, S.; Sun, S. *Angew. Chem., Int. Ed.* **2013**, *52*, 8526–8544.

(5) Sasaki, K.; Naohara, H.; Choi, Y.; Cai, Y.; Chen, W.-F.; Liu, P.; Adzic, R. R. *Nat. Commun.* **2012**, *3*, 1115.

(6) Lefèvre, M.; Proietti, E.; Jaouen, F.; Dodelet, J.-P. *Science* **2009**, *324*, 71–74.

(7) Wu, G.; More, K. L.; Johnston, C. M.; Zelenay, P. *Science* **2011**, *332*, 443–447.

(8) Cheon, J. Y.; Kim, T.; Choi, Y.; Jeong, H. Y.; Kim, M. G.; Sa, Y. J.; Kim, J.; Yang, T.-H.; Kwon, K.; Terasaki, O.; Park, G.-G.; Adzic, R. R.; Joo, S. H. *Sci. Rep.* **2013**, *3*, 2715.

(9) Zheng, Y.; Jiao, Y.; Jaroniec, M.; Jin, Y.; Qiao, S. Z. *Small* **2012**, *8*, 3550–3566.

(10) Gong, K.; Du, F.; Xia, Z.; Durstock, M.; Dai, L. *Science* **2009**, *323*, 760–764.

(11) Wang, S.; Yu, D.; Dai, L. *J. Am. Chem. Soc.* **2011**, *133*, 5182–5185.

(12) Yang, L.; Jiang, S.; Zhao, Y.; Zhu, L.; Chen, S.; Wang, X.; Wu, Q.; Ma, J.; Ma, Y.; Hu, Z. *Angew. Chem., Int. Ed.* **2011**, *50*, 7132–7135.

(13) Wang, S.; Iyyamperumal, E.; Roy, A.; Xue, Y.; Yu, D.; Dai, L. *Angew. Chem., Int. Ed.* **2011**, *50*, 11756–11760.

(14) Zhao, Y.; Yang, L.; Chen, S.; Wang, X.; Ma, Y.; Wu, Q.; Jiang, Y.; Qian, W.; Hu, Z. *J. Am. Chem. Soc.* **2013**, *135*, 1201–1204.

(15) Qu, L.; Liu, Y.; Baek, J.-B.; Dai, L. *ACS Nano* **2010**, *4*, 1321–1326.

(16) Sheng, Z.-H.; Shao, L.; Chen, J.-J.; Bao, W.-J.; Wang, F.-B.; Xia, X.-H. *ACS Nano* **2011**, *5*, 4350–4358.

(17) Wang, S.; Zhang, L.; Xia, Z.; Roy, A.; Chang, D. W.; Baek, J.-B.; Dai, L. *Angew. Chem., Int. Ed.* **2012**, *51*, 4209–4212.

(18) Liang, J.; Jiao, Y.; Jaroniec, M.; Qiao, S. Z. *Angew. Chem., Int. Ed.* **2012**, *51*, 11496–11500.

(19) Liu, R.; Wu, D.; Feng, X.; Müllen, K. *Angew. Chem., Int. Ed.* **2010**, *49*, 2565–2569.

(20) Yang, W.; Fellinger, T.-P.; Antonietti, M. *J. Am. Chem. Soc.* **2011**, *133*, 206–209.

(21) Yang, D.-S.; Bhattacharjya, D.; Inamdar, S.; Park, J.; Yu, J.-S. *J. Am. Chem. Soc.* **2012**, *134*, 16127–16130.

(22) Yang, S.; Feng, X.; Wang, X.; Müllen, K. *Angew. Chem., Int. Ed.* **2011**, *50*, 5339–5343

(23) Zheng, Y.; Jiao, Y.; Chen, J.; Liu, J.; Liang, J.; Du, A.; Zhang, W.; Zhu, Z.; Smith, S. C.; Jaroniec, M.; Lu, G. Q.; Qiao, S. Z. *J. Am. Chem. Soc.* **2011**, *133*, 20116–20119.

(24) Kwon, K.; Sa, Y. J.; Cheon, J. Y.; Joo, S. H. *Langmuir* **2012**, *28*, 991–996.

(25) Rao, C. V.; Ishikawa, Y. *J. Phys. Chem. C* **2012**, *116*, 4340–4346.

(26) Lee, M.-S.; Kim, T.; Park, S.-H.; Kim, C.-S.; Choi, Y.-W. *J. Mater. Chem.* **2012**, *22*, 13928–13931.

(27) Wang, X.; Dai, S. *Angew. Chem., Int. Ed.* **2010**, *49*, 6664–6668.

(28) Paraknowitsch, J. P.; Zhang, J.; Su, D.; Thomas, A.; Antonietti, M. *Adv. Mater.* **2010**, *22*, 87–92.

(29) Fukushima, T.; Kosaka, A.; Ishimura, Y.; Yamamoto, T.; Takigawa, T.; Ishii, N.; Aida, T. *Science* **2003**, *300*, 2072–2074.

3

STRATEGY FOR PREFERENTIAL GENERATION OF ACTIVE Fe–N$_X$ SITES FOR EFFICIENT OXYGEN REDUCTION REACTION

3.1. INTRODUCTION

Polymer electrolyte fuel cells (PEFCs) represent one of the most promising energy conversion devices available today, because of their high energy conversion efficiency and zero emission of greenhouse gases.[1–6] However, the high cost and scarcity of platinum pose a great challenge to the widespread adoption of PEFC technologies. Particularly for acidic proton exchange membrane fuel cells (PEMFCs) where Pt-based catalysts are primarily used in both the cathode and the anode, these catalysts are solely responsible for 40–50% of the total cost of the PEMFC stack.[7,8] As an alternative type of PEFCs, anion exchange membrane fuel cells (AEMFCs) incorporating solid alkaline electrolytes have received increasing attention during the last few years.[9,10] In particular, the higher oxygen reduction reaction (ORR) activity and enhanced durability of low-cost non-precious metal catalysts (NPMCs) in alkaline media than in acidic media have prompted the current surge of interest in AEMFC as an economically viable energy conversion device. In this context, a wide range of NPMCs, including transition metal and nitrogen co-doped carbons (M–N/C),[11–41] metal-free heteroatom-doped carbons,[42–48] and metal oxide-carbon composites,[49–52] have been investigated for replacing Pt-based catalysts. Among NPMCs, the M–N/C catalysts especially have emerged as the most promising ORR catalysts due to their high ORR activity.[11–35]

The field of heterogeneous M–N/C catalysts has a history dating back more than fifty years. More specifically, in 1964, Jasinski first demonstrated that cobalt phthalocyanine can catalyze the ORR in alkaline media, opening up the possibility of M–N/C catalysts as potential alternatives to Pt-based catalysts.[53] Since then, several types of metallomacrocyclic compounds, such as

metalloporphyrins and metallotetraazaannulenes, have been widely investigated as potential new M–N/C catalysts.[54,55] However, the ORR activity and durability of these initial catalysts were significantly lower than those of established Pt-based catalysts. Thus, to address these issues, the preparative chemistry of M–N/C catalysts underwent several stages of breakthroughs. For example, Jahnke and coworkers suggested that the high-temperature heat treatment of metallomacrocyclic compounds could significantly improve the activity and durability of M–N/C catalysts.[56] Indeed, the Yeager group demonstrated that a M–N/C catalyst prepared from a mixture of metal, nitrogen, and carbon precursors exhibited a comparable ORR activity to catalysts derived from expensive metallomacrocyclic compounds, thereby representing a more economical route towards M–N/C catalyst.[57] This method could also provide a combination of various precursors for each component, allowing for the more flexible design of M–N/C catalysts. However, despite continued research into the development of high-performance M–N/C catalysts prior to 2008, the ORR activities of M–N/C catalysts remained more than two orders of magnitude lower than those of Pt-based catalysts.

In 2009, a major breakthrough in the field of M–N/C catalysts was pioneered by the Dodelet group.[13] They prepared Fe–N/C catalysts by filling microporous carbon black with iron acetate and 1,10-phenanthroline, followed by heat treatment under NH_3. The optimized Fe–N/C catalyst achieved a PEMFC volumetric current density of 99 A cm^{-3} at 0.8 V, which was ~35 times higher than that of the previously reported best-performing catalyst. Notably, this performance was close to the target of 130 A cm^{-3} set by the US Department of Energy (DOE) in 2010. Subsequently, in 2011, the Zelenay group developed a M–N/C catalyst based on Fe, Co, and polyaniline, which achieved a highly promising PEMFC durability up to 700 h at 0.4 V along with a high initial current density.[14] The results obtained by the Dodelet and Zelenay groups suggested the potential practicality of M–N/C catalysts for PEMFC applications, and triggered a tremendous surge of research interest in this field.

In parallel with efforts to enhance the ORR activity, significant advances have been made to decipher the structure of the active sites of Fe–N/C catalysts. A growing body of literature based on spectroscopic studies suggests that the active site of these catalysts involve Fe–N$_x$ coordination, thus providing the scientific basis for designing highly active Fe–N/C catalyst.[58–73] However, a rational design strategy that can preferentially generate active Fe–N$_x$ sites yet to be explored. Most synthetic approaches to Fe–N/C catalysts involve a high-temperature pyrolysis step to endow conductivity and stability to the catalysts. However, this step generates not only catalytically active Fe–N$_x$ sites as well as a significant amount of less-active large Fe-based particles. Therefore, additional synthetic steps including post acid- and heat-treatments are commonly required to boost the ORR activity.[32,35]

Herein, we report a generalized "silica-protective-layer-assisted" strategy that can preferentially produce catalytically active Fe–N$_x$ sites during high-temperature pyrolysis toward highly efficient Fe–N/C electrocatalysts. The catalyst synthesis involved an adsorption of porphyrinic precursor on carbon

nanotube (CNT), silica layer overcoating, high-temperature pyrolysis, and silica layer etching, yielding the nanohybrid structure of CNT coated with thin layer of porphyrinic carbon (CNT/PC). We point out that while "silica coating" strategy has been widely used in catalysis for mitigating the sintering of catalytic particles under high-temperature and/or harsh reaction conditions,[74–78] in our work this method is exploited to promote the formation of catalytically active sites at the molecular level. Temperature-controlled *in situ* X-ray absorption spectroscopy (XAS) suggested that interaction of the silica layers with the Fe–N$_4$ moieties protects the Fe–N$_4$ sites and prevents the formation of large Fe-based particles. The final CNT/PC catalyst comprised relatively high density of Fe–N$_x$ sites, as revealed by XAS analysis combined with atomic-resolution transmission electron microscopy (AR-TEM) and ^{57}Fe Mössbauer spectroscopy. The CNT/PC catalysts showed very high ORR activity in alkaline media with a half-wave potential of 0.88 V (*vs* reversible hydrogen electrode; RHE), and they also demonstrated remarkable stability in alkaline media. Importantly, the CNT/PC cathode-based alkaline AEMFC exhibited record high current and power densities among NPMC-based AEMFCs. In addition, the CNT/PC cathode showed high performance for acidic PEMFCs, with a volumetric current density of 320 A cm^{-3}, which is comparable to the DOE 2020 target (300 A cm^{-3}). Finally, our synthetic strategy was generalized to other carbon supports such as carbon blacks and reduced graphene oxides.

3.2. EXPERIMENTAL METHODS

3.2.1. Synthesis of CNT/PC Catalysts

5,10,15,20-tetrakis(4-methoxyphenyl)-21H,23H-porphine iron(III) chloride (Fe^{III}TMPPCl) was purchased from Porphyrin Systems. Tetraethyl orthosilicate (TEOS) and formic acid were purchased from Sigma-Aldrich. All chemicals were used as received. Multi-walled carbon nanotubes (CNTs, < 10 nm in diameter, 5–15 μm in length) were purchased from Carbon Nano-material Technology Co. In order to remove metal impurities, the as-received CNTs were treated with 6 M HNO$_3$ at 80 °C for 12 h and subsequently with 6 M HCl at 80 °C for 12 h.

For the optimized preparation of CNT/PC catalysts, acid-treated CNTs were mixed with Fe^{III}TMPPCl (mass ratio of 1 : 2) using agate mortar and pestle for 5 min. The mixture was heated from RT to 400 °C in a quartz-tube furnace at a ramping rate of 2 °C min^{-1} and maintained at that temperature for 3 h under N$_2$ gas (99.999%) at a flow rate of 1 L min^{-1} (denoted as low-temperature treatment step; LT). The heat-treated CNT/Fe^{III}TMPPCl composite was mixed with TEOS in a mortar. The subsequent addition of formic acid triggered the polymerization of TEOS to silica (the volume of TEOS and formic acid added: 0.5 mL per 100 mg acid-treated CNTs used). The CNT-Fe^{III}TMPPCl-

silica composite was dried in a 60 °C oven for 3 h. The composite in an alumina boat was then heated to 800 °C at a ramping rate of 2 °C min^{-1} and maintained at that temperature for 3 h under N$_2$ gas at a flow rate of 1 L min^{-1}. The resulting CNT/PC-silica composite was mixed with 2 : 1 (v/v) = ethanol : 10% aqueous HF solution and stirred for 30 min to etch the silica, followed by filtering and washing with ethanol several times. The HF etching process was repeated in the same manner, and the resulting sample was dried at 60 °C to afford CNT/PC catalysts. CNT/PC_w/o SiO$_2$ and CNT/PC_w/o LT were prepared in the same manner as described above, except the omission of TEOS/formic acid addition and LT step at 400 °C, respectively.

3.2.2. Characterization Methods

X-ray diffraction (XRD) patterns of the samples were obtained using an X-ray diffractometer (D/MAX2500V/PC, Rigaku) equipped with a Cu Kα source operating at 40 kV and 200 mA. High resolution transmission electron microscopy (HR-TEM) images were obtained using a JEOL JEM-2100 microscope. High-angle annular dark-field scanning TEM (HAADF-STEM) images and the corresponding elemental mapping images were obtained using a JEOL JEM-2100F microscope with a probe-forming Cs corrector at 200 kV. Atomic resolution structures of the samples were observed using an image-side spherical aberration corrected TEM (Titan^3 G2 cube 60-300, FEI Company, Netherlands) under an accelerating voltage of 80 kV. X-ray photoelectron spectroscopy (XPS) measurements were performed on an ESCLAB 250Xi (ThermoFisher Scientific), equipped with a monochromatic Al Kα X-ray source (1486.6 eV). N 1s XPS spectra were deconvoluted using the XPSPeak41 software with the mixed (Gaussian 70, Lorentzian 30)-function after a linear (Shirley)-type background subtraction. The Raman spectra were obtained using a WITec alpha300R coupled with a He-Ne laser of 532 nm at 1.0 mW. Fe contents in the catalysts were analyzed using inductively coupled plasma optical emission spectrometer (700-ES, Varian). Combustion analysis was conducted using an elemental analyzer (Flash 2000, ThermoFisher Scientific) to determine the contents of C, N, H, and O in the catalysts.

3.2.3. XAS Experiments

XAS was performed at the beamline 6D and 10C of the Pohang Accelerator Laboratory (PAL). The incident X-ray had the electron beam energy and current of 3.0 GeV and 300 mA, respectively. A Si(1 1 1) double crystal monochromator was used to filter the incident photon energy, which was detuned by 30% to remove high-order harmonics. *Ex situ* Fe K-edge XAS experiments were performed with pelletized samples in both transmission and fluorescence detection modes.

For temperature-dependent *in situ* Fe K-edge XAS, a mixture of CNTs and Fe^{III}TMPPCl, and CNT/PC-silica composites were ground in an agate mortar, pressed into pellets of 16 mm in diameter, and fixed in a heating chamber under N_2 gas flow. For the CNT and Fe^{III}TMPPCl mixture, the temperature was raised from RT to 400 °C, during which total eight XAS spectra were obtained. For the CNT/PC-silica composite, the temperature was rapidly increased to 400 °C, and gradually raised to 700 °C, during which eight XAS spectra were taken.

For electrochemical *in situ* XAS, a CNT/PC catalyst ink (described in the *Section 3.2.6*) was deposited onto a piece of carbon paper, and heat-pressed. The catalyst-coated carbon paper was attached to a home-made spectroelectrochemical cell using a Kapton tape, with the catalyst layer in contact with 0.1 M KOH. Then, Fe K-edge XAS spectra were obtained without applied potential, and subsequently under potentials of 0.3 and 0.9 V (*vs* RHE, *iR*-corrected) in fluorescence detection mode.

3.2.4. ^{57}Fe Mössbauer Spectroscopy

The Mössbauer spectra were recorded in transmission mode with a ^{57}Co source in a rhodium matrix. The Mössbauer spectrometer of the electromechanical type was fixed absorber and operated source on constant acceleration mode, which was calibrated by using an α-Fe foil. Mössbauer spectra were least-squares fitted, providing the values of hyperfine field (H_0), isomer shift (δ_{iso}), electric quadrupole splitting (ΔE_Q), and relative area of each Fe species.[79]

3.2.5. RHE Calibration

The Hg/HgO (CHI152, CH Instruments; 1 M KOH filling solution) and Ag/AgCl (RE-1B, ALS; saturated KCl filling solution) reference electrodes were calibrated with respect to the RHE before use. For this purpose, a two-electrode electrochemical cell was built in which a Pt coil and the reference electrode to be calibrated were connected. Ultra-pure hydrogen gas was then sparged into the electrolyte. In this case, H^+/H_2 equilibrium was established on the Pt coil, which thus acted as an RHE. A stable open circuit voltage could be observed within several minutes, which was the potential difference, and thus could be taken to be the conversion value. The calibration values were measured to be E(RHE) = E(Hg/HgO) + 0.89 V and E(RHE) = E(Ag/AgCl) + 0.26 V in 0.1 M KOH and 0.1 M HClO$_4$, respectively.

3.2.6. Electrochemical Characterizations

Electrochemical experiments were performed with an electrochemical workstation (CHI760E, CH Instruments) and electrode rotator (AFMSRCE, Pine Research Instrumentation) at RT (25 °C) using a three-electrode electrochemical cell. Hg/HgO and Ag/AgCl reference electrodes were used for measurements in 0.1 M KOH and 0.1 M $HClO_4$, respectively, and a graphite rod was used as the counter electrode. A rotating ring-disk electrode (RRDE, AFE7R9GCPT, Pine Research Instrumentation) was used as the working electrode. Prior to every measurement, the RRDE was polished with a 1.0 μm alumina suspension and then with a 0.3 μm suspension to afford a mirror finish. To prepare the catalyst ink, the catalyst (30 mg) was mixed with DI water (0.1 mL), ethanol (1.01 mL), and Nafion® (0.075 mL, 5 wt% in isopropanol, Sigma-Aldrich), and the resulting slurry was ultra-sonicated for 30 min. For the benchmark Pt/C catalyst (20 wt% Pt, HiSPEC-3000, Johnson-Matthey), a catalyst ink was prepared with the Pt/C catalyst (3.5 mg), DI water (0.1 mL), ethanol (1.07 mL), and Nafion® (0.03 mL). The catalyst ink (8 μL of for the CNT/PC, 6 μL for Pt/C) was pipetted with a micro-pipette onto the glassy carbon (GC) disk (5.61 mm in diameter, 0.247 cm^2) of the RRDE, resulting in a catalyst loading of 800 μg cm^{-2} (14 $μg_{Pt}$ cm^{-2} for Pt/C). 0.1 M $HClO_4$ (diluted from 70% $HClO_4$, Veritas double distilled, GFS Chemicals) and 0.1 M KOH (diluted from 99.99% KOH, Sigma-Aldrich) were used as the alkaline and acidic electrolytes, respectively. Before the electrochemical measurements, the catalyst was cleaned by cycling the potential between 0.05 and 1.20 V (*vs* RHE) for 50 cycles at a scan rate of 100 mV s^{-1} (500 mV s^{-1} for Pt/C) in an N_2-saturated electrolyte. Subsequently, cyclic voltammetry (CV) was performed in the potential range of 0.05 to 1.20 V at a scan rate of 20 mV s^{-1} (50 mV s^{-1} for Pt/C). Linear sweep voltammetry (LSV) polarization curves for the ORR were obtained by sweeping the potential from 1.20 to 0.20 V (from −0.01 V to 1.10 V for Pt/C) in an O_2-saturated electrolyte with continuous O_2 purging at a rotating speed of 1,600 rpm. In order to correct the non-Faradaic current (capacitive current) from the LSV curve, the same LSV measurement was conducted in N_2-saturated electrolyte. To measure solution resistance for *iR*-compensation, electrochemical impedance spectra were obtained at 0.68 V with AC potential amplitude of 10 mV from 10,000 to 1 Hz. For CNT/PC and the control samples, ORR measurements were independently repeated at least three times and the average data were presented. The long-term durability of the catalysts was assessed by 10,000 CV scans between 0.60 and 1.00 V at a scan rate of 50 mV s^{-1} in N_2-saturated electrolytes. Before the ORR measurement after 10,000 cycles, the electrolyte was replaced with a fresh batch.

3.2.7. Four-Electron Selectivity Evaluation

For the evaluation of the four-electron selectivity, the potential of the Pt ring was fixed at 1.30 V (*vs* RHE) during the LSV scans for the ORR. The number of electrons transferred during the ORR (*n*) was calculated from the following equation

$$n = \frac{4}{1 + \dfrac{i_r}{N \times i_{d,F}}}$$

where i_r is the ring current, and N is the collection efficiency (0.37, provided by manufacturer), and $i_{d,F}$ is the Faradaic current from the ORR collected at the GC disk, which can be obtained after capacitive-current-correction.

$$i_{d,F} = i - i_{cap}$$

where i and i_{cap} indicate the currents measured in an O_2- and an N_2-saturated electrolyte, respectively.

The kinetic current was extracted to compare the ORR activity using the following equation

$$\frac{1}{i_{d,F}} = \frac{1}{i_k} + \frac{1}{i_l}$$

where i_k and i_l are the kinetic current and the diffusion-limited current, respectively.

3.2.8. AEMFC Performance Tests

Anion exchange membranes (23 μm thick) for the alkaline AEMFC were fabricated by a pore-filling approach in a microporous substrate purchased from Asahi Kasei. These porous substrates were first treated with sodium dodecyl sulfate (Sigma-Aldrich) surfactant to increase the hydrophilicity of the substrate, and then immersed in an aqueous monomer solution to totally fill the vacant open micropores. The monomer used was (vinylbenzyl)trimethylammonium chloride with N,N´-bis(acryloyl)piperazine as a cross-linker. The monomer-impregnated substrate was sandwiched between two polyethylene terephthalate films and placed in an ultraviolet reactor to polymerize the monomer. The polymer membranes were washed several times with DI water to remove any byproducts and water-soluble components. In these procedures, care must be taken not to scratch the surface of the polymer membrane. The resulting membranes were soaked in a 2 N NaOH aqueous solution to convert the chloride to the hydroxide form in a N_2 environment.[80]

A slurry of the anode catalyst was prepared by mixing 0.16 g of Pt/C catalyst (40 wt% Pt,

HiSPEC-4000, Johnson-Matthey), 0.91 g methanol, 0.11 g DI water, and 1.67 g of a commercial alkaline ionomer I2 (4 wt% solid weight, Acta S.P.A.). The ionomer content in the anode slurry was controlled to 30 wt%. Slurry of the cathode catalyst was prepared by mixing 0.29 g CNT/PC hybrid, 0.56 g methanol, 0.06 g DI water, and 3.12 g of alkaline ionomer I2. The ionomer content in the cathode slurry was 30 wt%. Both catalyst slurries were well dispersed by agitation in an ultrasonic water bath for 3 h. During the ultra-sonication, the catalyst slurries were stirred with a hard stick every 1 h to minimize the agglomerate attached on the sidewall of the vial. After ultra-sonication, a three-roll milling procedure was conducted to sufficiently break the agglomerates in the catalyst ink, and the slurries were then ultra-sonicated for a further 20 min. The Pt loading on the anode layer was around 0.50 mg cm^{-2} and the CNT/PC loading on the cathode was approximately 2.0 mg cm^{-2}.

A membrane electrode assembly (MEA) with an active area of 25 cm^2 was fabricated by the spray method on in-house anion exchange membrane. In the process of spraying, it is important to minimize exposure to atmospheric CO_2 by significantly reducing the spraying time. All single cell experiments were conducted at 80 °C, and the temperature of the gas lines to the anode and the cathode were always set at 10 °C above the temperature of the humidifier to avoid condensation of water vapor. H_2 and O_2 gases were used as the anode and cathode reactants, respectively. The reactant gases were supplied to the single cell apparatus under 100% relative humidity (RH) at atmospheric pressure. The reactant flow rates for the anode and cathode were 400 and 1200 mL min^{-1}, respectively. After confirmation of an open circuit voltage (OCV) over 0.95 V, the polarization curves were obtained several times at a scan rate of 10 mV s^{-1} from OCV to 0.2 V to activate the MEA.

3.2.9. PEMFC Performance Tests

The anode catalyst slurry was made with 0.72 g Pt/C (HiSPEC-4000), 2.57 g of DI water, 0.51 g of isopropyl alcohol, and 6.18 g of 5 wt% Nafion ionomer (1100 EW, DuPont Fuel Cells). The ionomer content in the anode slurry was 30 wt%. The cathode catalyst slurry was prepared with 0.39 g CNT/PC hybrid, 2.35 g of 5 wt% Nafion ionomer, 2.16 g DI water, and 0.43 g isopropyl alcohol. The ionomer content in the cathode slurry was 23 wt%. Both the anode and cathode slurries were well stirred in an ultrasonic water bath for 4 h. Next, three-roll milling was conducted to sufficiently break the total agglomerates in the catalyst slurries, followed by additional stirring in an ultrasonic water bath for 30 min.

The MEA with an active area of 25 cm^2 was fabricated by the decal method. Both catalyst inks were coated onto a decal substrate by a doctor blade film applicator. The decal substrate was dried completely in atmosphere conditions and hot-pressed onto a Nafion NRE 211 (25.4 μm thick) polymer membrane at 100 kgf cm^{-2} and 120 °C. The resulting thickness of the cathode catalysts was

ca. 10 μm. The Pt content on anode catalyst was controlled at ca. 0.15 mg cm^{-2}, the CNT/PC loading of the cathode catalyst was 3.05 mg cm^{-2}. All single cell experiments were conducted at 80 °C, 100% RH, and 1 bar gauge pressure. The temperature of the gas lines to the anode and the cathode were always set 10 °C above the temperature of the humidifier to avoid condensation of water vapor. H$_2$ and O$_2$ gases were used as anode and cathode reactants, respectively. The reactant flow rates for the anode and cathode were 400 and 1200 mL min^{-1}, respectively.

3.3. RESULTS AND DISCUSSION

3.3.1. Synthesis Optimization of CNT/PC Catalysts

Figure 3.1 illustrates the overall preparation scheme for the CNT/PC catalyst. CNTs were mixed with Fe^{III}TMPPCl precursor. The CNT-Fe^{III}TMPPCl mixture was heated to 400 °C to form CNTs wrapped with porphyrin layers *via* π–π interactions. This composite was overcoated with a silica layer. Finally, the ternary composite was subjected to high temperature pyrolysis, followed by etching of the silica layer. The pyrolysis temperature and the ratio of CNT to a porphyrin precursor were controlled to optimize the synthetic condition. The best-performing catalyst was obtained by 2.0 g Fe^{III}TMPPCl per gram of CNTs at the pyrolysis temperature of 800 °C (**Figure 3.2**).
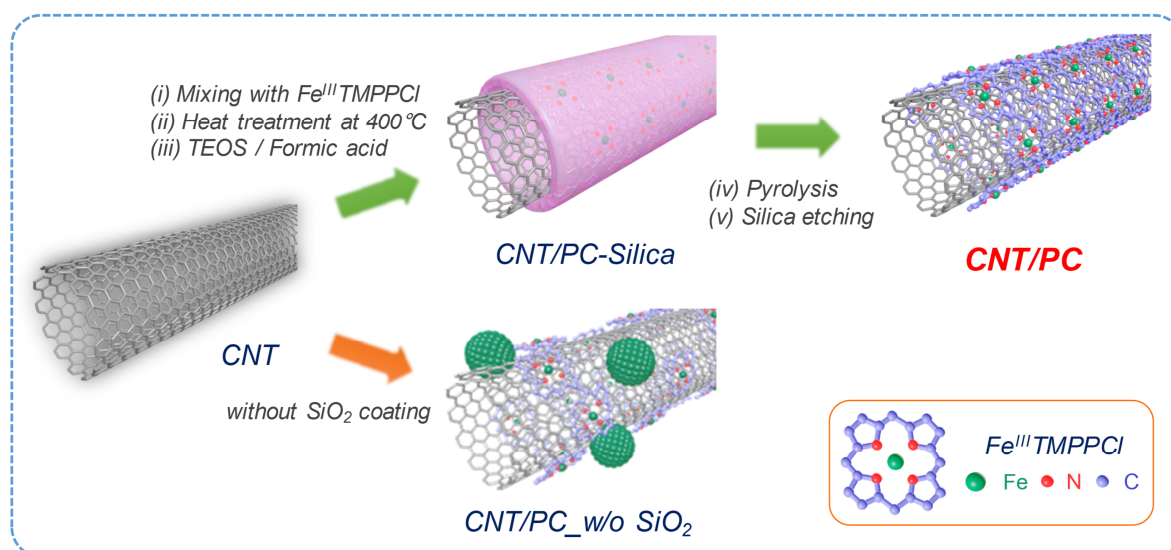
Figure 3.1. Schematic illustration of the synthetic procedure for the CNT/PC and CNT/PC_w/o SiO$_2$ catalysts.
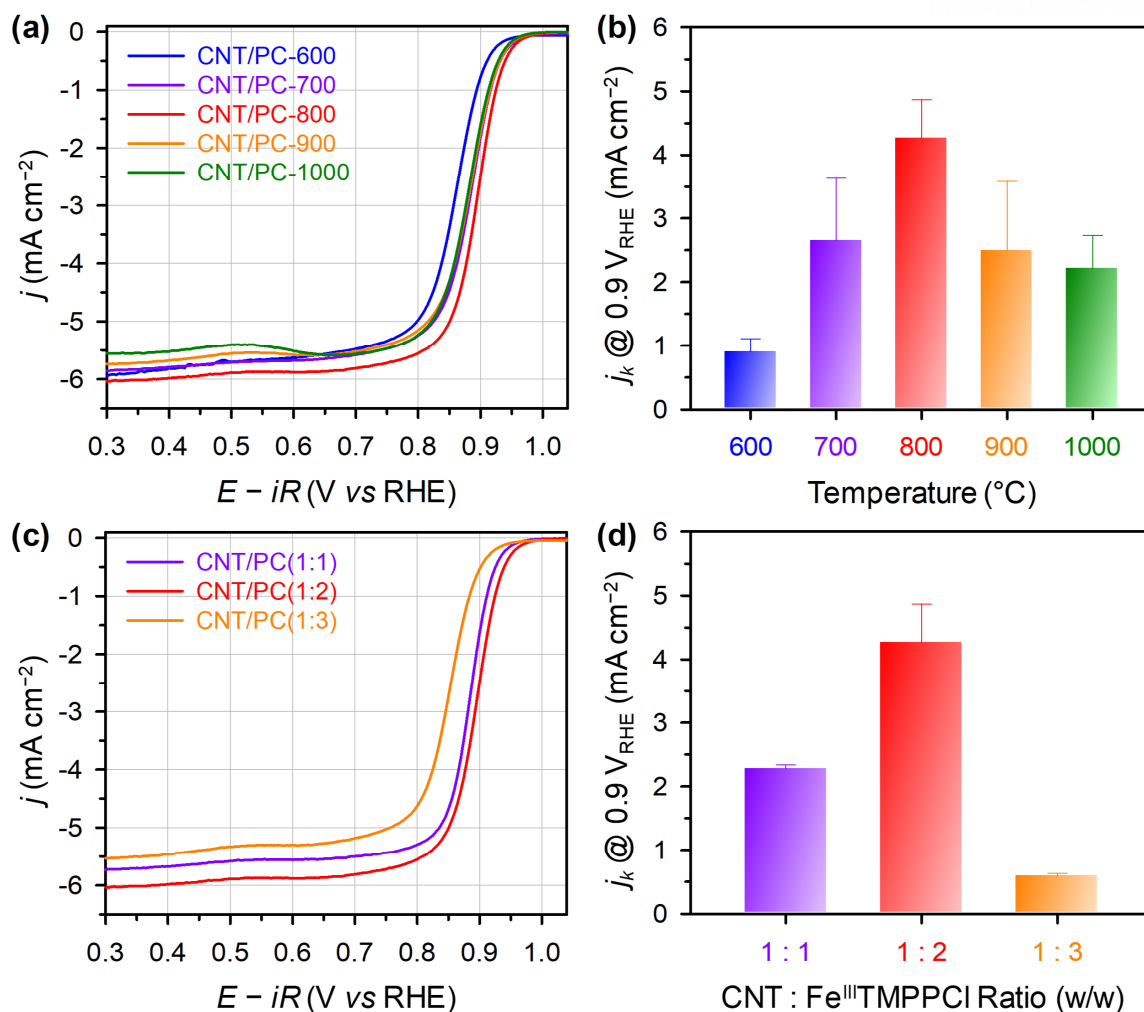
Figure 3.2. (a) ORR polarization curves of CNT/PC catalysts prepared at different pyrolysis temperatures measured in 0.1 M KOH at an electrode rotation speed of 1,600 rpm, and (b) bar graph comparing the kinetic current density of the catalysts at 0.9 V (*vs* RHE). (c) ORR polarization curves of CNT/PC catalysts prepared with different CNT : Fe^{III}TMPPCl mass ratio, and (d) bar graph comparing the kinetic current density of the catalysts at 0.9 V (*vs* RHE).

3.3.2. Physicochemical Characterizations

TEM images of the acid-treated CNTs (**Figure 3.3a**) and (AR-)TEM images of CNT/PC (**Figures 3.3b,c**) clearly show the formation of a uniform few-nanometer-thick carbonaceous layer on an individual CNT. The tracking of each synthetic step of CNT/PC by HAADF-STEM combined with elemental mapping images confirmed the formation of the silica layer after high-temperature pyrolysis at 800 °C (**Figure 3.4a**). In the final CNT/PC structure, a uniform porphyrinic carbon layer containing iron and nitrogen species can be confirmed (**Figure 3.4b**). Electron energy loss spectroscopy (EELS) data (**Figure 3.5**) taken from a very small area (the red spot in the HAADF-STEM image in **Figure 3.5a**) showed the presence of Fe and N species.
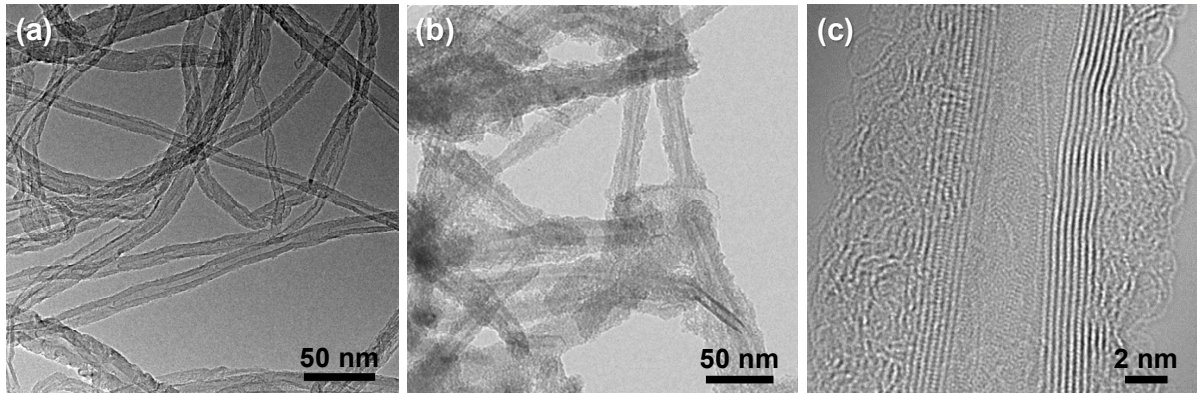
Figure 3.3. (a,b) TEM images of (a) the acid-treated CNT and (b) CNT/PC. (c) AR-TEM image of the CNT/PC catalyst.
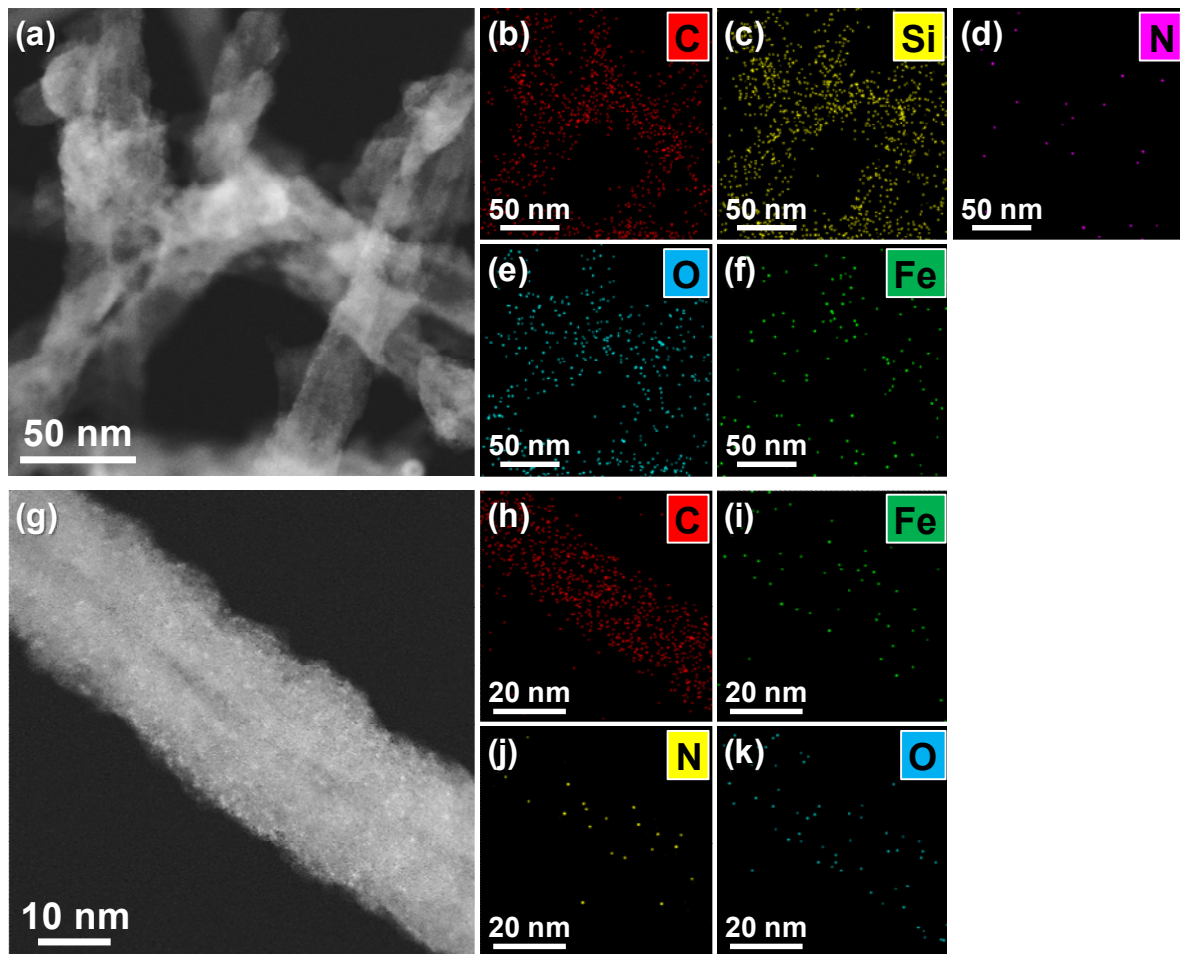
Figure 3.4. (a) HAADF-STEM image of CNT/PC-silica composite after the pyrolysis at 800 °C and corresponding elemental mapping images for (b) carbon, (c) silicon, (d) nitrogen, (e) oxygen, and (f) iron. (g) HAADF-STEM image of the CNT/PC catalyst and corresponding elemental mapping images for (h) carbon, (i) iron, (j) nitrogen, and (k) oxygen.
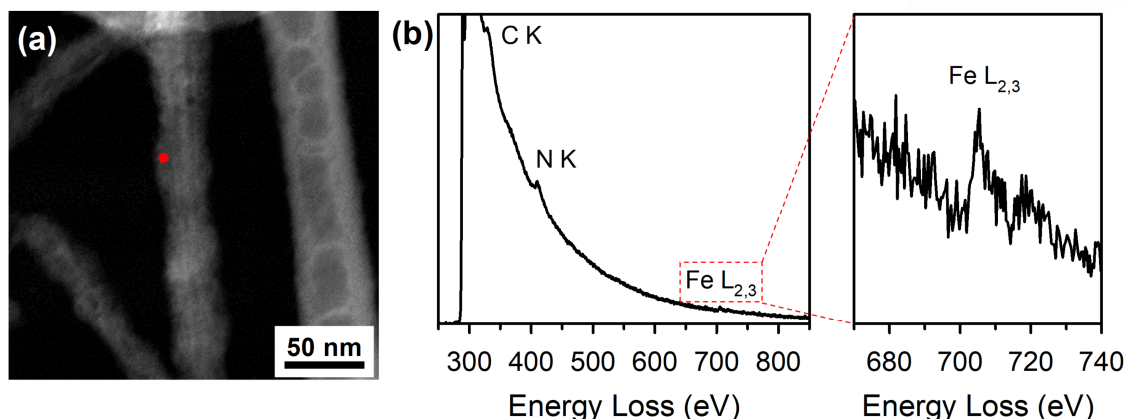
Figure 3.5. (a) HAADF-STEM image of the CNT/PC catalyst. (e) EELS spectrum taken at the position marked by the red dot. Inset shows the enlarged spectrum at the Fe L$_{2,3}$ edge.

The XRD pattern along the with EELS spectrum (**Figure 3.6a**) of the CNT/PC consistently indicates that Fe species are dispersed in the carbon layer as sub-nanometer entities without the formation of large nanoparticles. The Fe and N contents of the CNT/PC were determined to be 0.6 at% (2.9 wt%) and 1.6 at% (1.9 wt%), respectively by inductively coupled plasma optical emission spectroscopy and combustion elemental analysis. In the Raman spectra (**Figure 3.6b**), broadening of D-band was clearly observed in the CNT/PC compared to the pristine CNTs, indicating the formation of relatively amorphous carbon on the surface. This amorphous signal could originate from the porphyrinic carbon layer on the CNT. Carbon 1s XPS (**Figure 3.6c**) confirmed that the CNT/PC is composed of amorphous carbon on its surface, evidenced by negatively-shifted carbon-carbon binding energy (284–285 eV) compared to that of the pristine CNTs. In addition, the broad π–π* shake-up peak at around 291 eV, which is the characteristic signal of CNT, was not observed for the CNT/PC. From the deconvolution of N 1s XPS spectra, the presence of four or more types of nitrogen is suggested (**Figure 3.6d**). Raman and XPS data consistently indicate the formation of amorphous porphyrinic carbon layers on the CNT in the CNT/PC, which is in line with the TEM observations.

To examine the role of the silica layers, CNT/PC was prepared without the silica overcoating step (CNT/PC_w/o SiO$_2$). The TEM image of the CNT/PC_w/o SiO$_2$ (**Figure 3.7a**) shows that porphyrinic carbon layers were not formed uniformly on the CNTs. Notably, nanoparticles (NPs) of size up to a few tens of nanometers are also shown, which were found to be Fe and Fe$_3$C phases indicated by XRD pattern of CNT/PC_w/o SiO$_2$ (**Figure 3.6a**). As another control sample, CNT/PC was prepared without low-temperature heat-treatment at 400 °C (CNT/PC_w/o LT). The TEM image of CNT/PC_w/o LT (**Figure 3.7b**) indicates an aggregated morphology with non-uniform formation of porphyrinic layers. The formation of Fe-based NPs is not remarkable as in the case of CNT/PC_w/o SiO$_2$. These control experiments clearly suggest that the silica layer overcoating step is

important to suppress the formation of the large NPs while the low-temperature annealing step facilitate the formation of uniform porphyrinic carbon layers on individual CNTs.
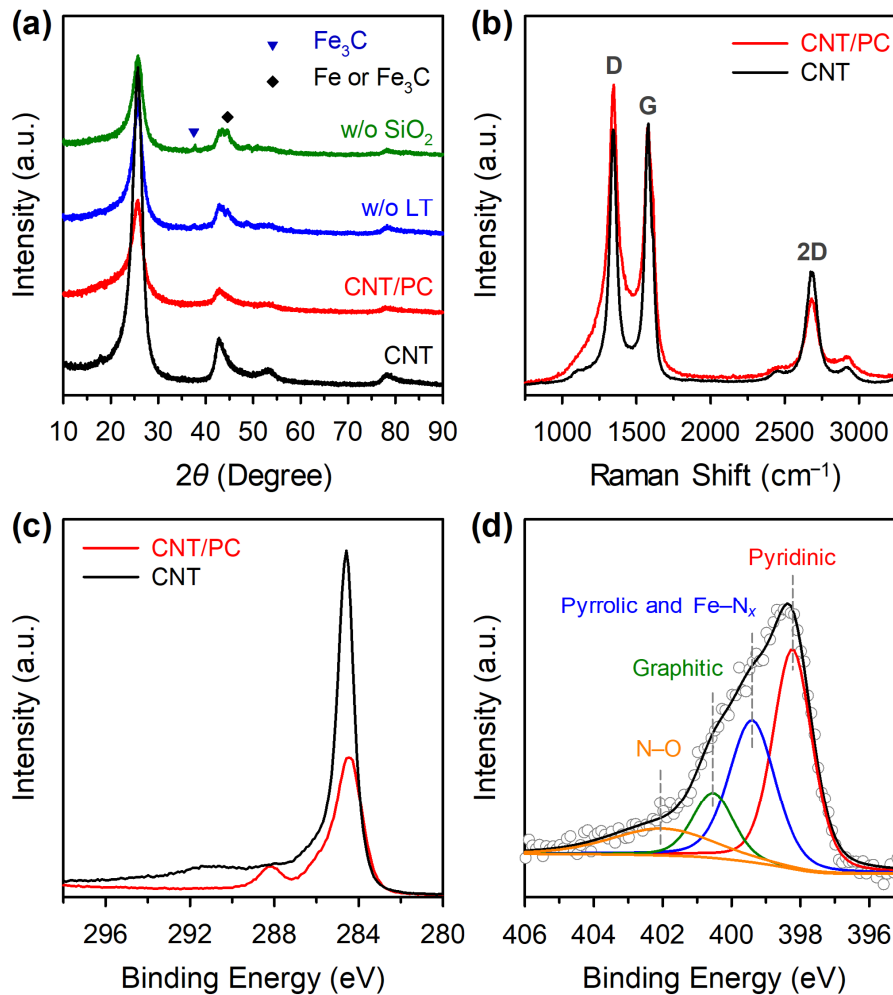
Figure 3.6. (a) XRD patterns of the CNT/PC catalyst, the comparison samples (w/o SiO$_2$ and w/o LT), and CNT. (b) Raman and (c) C 1s XPS spectra of the CNT/PC catalyst and CNT. (d) High-resolution N 1s XPS spectrum and deconvoluted peaks of the CNT/PC catalyst.
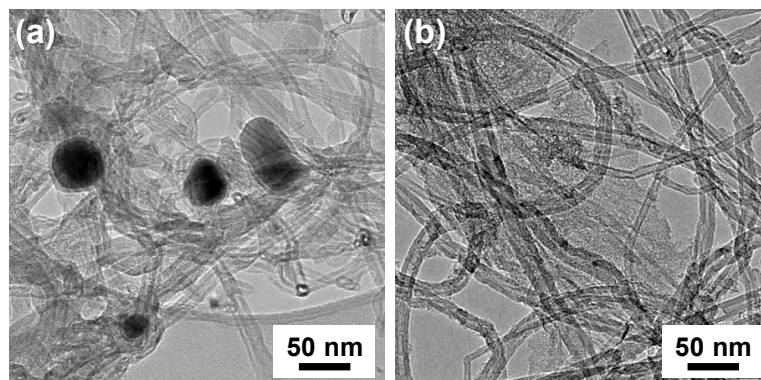
Figure 3.7. TEM images of (a) CNT/PC_w/o SiO$_2$ and (b) CNT/PC_w/o LT.

3.3.3. XAS Analysis

Unraveling the local and electronic structure of catalytically active iron-containing species is critical in establishing a structure-activity relationship of Fe–N/C catalysts. **Figure 3.8** shows temperature-dependent *in situ* Fe K-edge X-ray absorption near edge structure (XANES) spectra taken under N_2 flow, which revealed the thermally-induced structural changes around Fe sites from the precursor mixture to the final CNT/PC. In the initial heat-treatment region (RT to 400 °C), the pre-edge peak feature (peak A) shown for a mixture of CNT and Fe^{III}TMPPCl (thick solid black curve) and does not changed until the mixture was heated to 400 °C. The peak A originates from the square pyramidal symmetry of the Fe^{III}TMPPCl precursor (bottom dashed line). A new pre-edge feature (peak B) for square planar D_{4h} symmetry appeared at ~400 °C, indicative of the structural change from the removal of the axial Cl^- ion from the Fe^{III}TMPPCl (see also the XANES spectrum of iron(II) phthalocyanine (Fe^{II}Pc) shown as top dashed line). Importantly, after the silica layer coating, the peak B disappeared, and the peak A evolved again. These imply the formation of a new coordination bond between silica (Si and/or O atoms) and the axial position of the square planar Fe–N_4 site. This suggests that the interaction with the silica protective layer stabilizes the Fe–N_4 site, thereby suppressing the formation of Fe-based nanoparticles during high-temperature pyrolysis. In the course of the pyrolysis to 700 °C, the peak A negatively shifts to peak A* and peak B appeared again, which are correlated to effective reduction of Fe^{III} to Fe^{II}, and the recovery of the square planar Fe–N_4 site, respectively.

In addition, we found a noticeable change in the intensity for the peaks C (~7131 eV) and D (~7138 eV). With increased temperature, the intensity of the peak C gradually increased, while that of the peak D decreased, resulting in an increase in the relative intensity ratio of the peak C to peak D. Recently, Mukerjee and coworkers demonstrated that these phenomena are attributed to the off-center of the Fe atom in the Fe–N_4 structure (distortion), which can be related to the enhancement of ORR activity.[71] On the other hand, Dodelet et al. revealed that N_{axial}–Fe–N_{2+2} site (i.e., D3 site), identified using ^{57}Fe Mössbauer spectroscopy, is responsible for high ORR activity.[62] In the D3 site, the Fe atom is slightly out of plane of the planar Fe–N_{2+2}, approaching the axial N, thus yielding a distorted local structure. Based on these results, we suppose that the Fe–N_x site in the CNT/PC transformed gradually into a structure with higher degree of distortion that can boost ORR activity.

The relative amount of Fe–N_x sites to Fe-based particles in the CNT/PC and CNT/PC_w/o SiO_2 could be estimated by the linear combination fitting (LCF) analysis of the XANES spectra, using pure Fe^{II}Pc and Fe foil as references (**Figure 3.9**). The LCF results indicate that the ratio of Fe–N_4 sites to metallic phase Fe is higher for the CNT/PC (73%:27%) than for CNT/PC_w/o SiO_2 (48%:52%). This clearly demonstrates the critical role of the silica protective layer in promoting the formation of Fe–N_x sites.
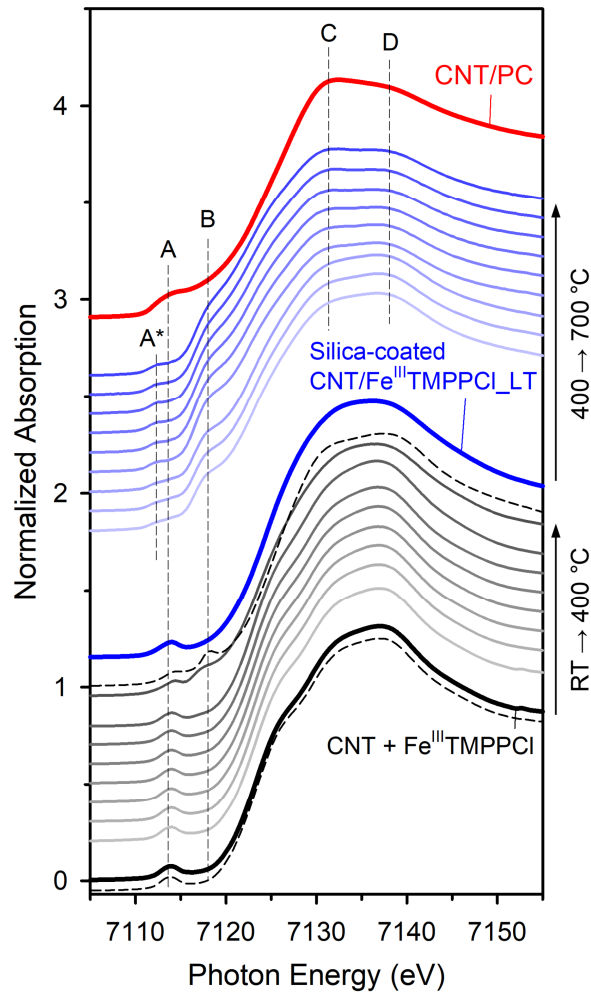
Figure 3.8. *In situ* Fe K-edge XANES spectra during the low-temperature annealing and the pyrolysis steps for the CNT/PC catalyst. The XANES spectra of Fe^{III}TMPPCl (bottom) and Fe^{II}Pc (top) are indicated as dotted lines.
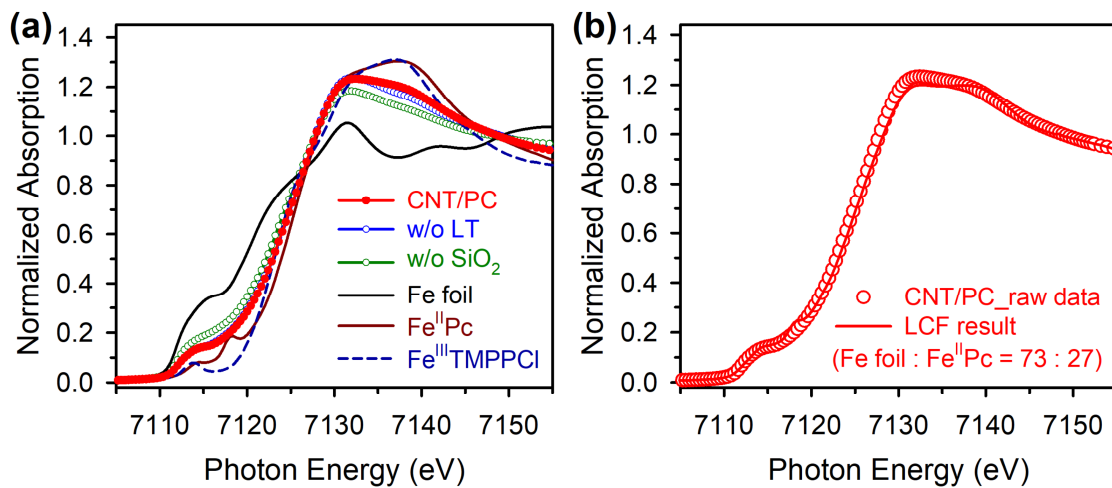
Figure 3.9. (a) *Ex situ* Fe K-edge XANES spectra of the CNT/PC catalyst, comparison samples, and reference materials. (b) The LCF result of the XANES spectrum of the CNT/PC catalyst.

The evolution of local structure was further investigated by *in situ* Fe K-edge extended X-ray absorption fine structure (EXAFS) spectroscopy. The radial distribution functions (RDFs) of the EXAFS spectra (**Figure 3.10**) during the heat-treatments suggest that Fe–N_4 sites with axially positioned Cl^- ions (peak A1) and ring carbons (peaks A2 and A3) in the precursor mixture are transformed into Fe–N_x sites (peak B1) and metallic Fe (peak B2) in the final CNT/PC catalyst, consistent with the XANES results. The EXAFS analysis further confirmed the importance of metallic cluster growth on the silica coating step.
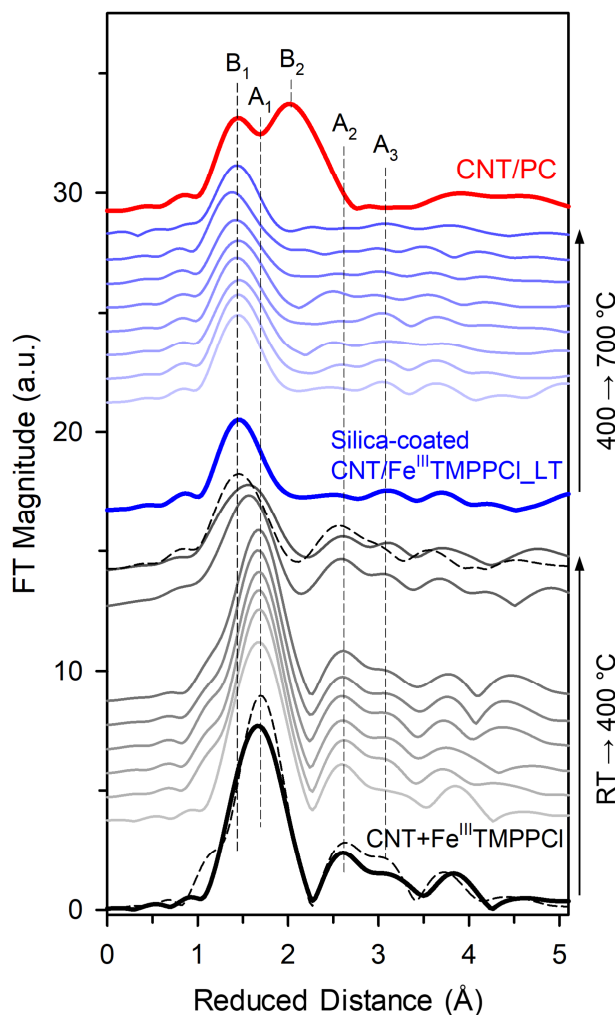
Figure 3.10. RDFs obtained from *in situ* Fe K-edge EXAFS spectra during the low-temperature annealing and the pyrolysis steps for the CNT/PC catalyst. The EXAFS spectra of $Fe^{III}TMPPCl$ (bottom) and $Fe^{II}Pc$ (top) are indicated as dotted lines.

The EXAFS spectrum of CNT/PC_w/o SiO$_2$ shows higher peak intensity for Fe–Fe bonding at around 2.0 Å (**Figure 3.11a**) compared to that for the CNT/PC, which indicates the larger and/or more abundant Fe-based particulate species, confirming the TEM observations. Based on the well-known relationship between coordination number and particle size (or the number of atoms) in the EXAFS spectra, the average number of Fe atoms comprised of a metallic Fe NP in the CNT/PC was estimated to be ~10 corresponding to few-angstroms in size, whereas the CNT/PC_w/o SiO$_2$ contained averagely ~1,000 Fe atoms in each Fe NP (**Figure 3.11b**). The tiny Fe clusters in the CNT/PC could be directly observed with the HAADF-STEM images (**Figures 3.4g** and **3.11c**), which show sub-nanometer particles corresponding to a few Fe atoms and monatomic dispersion of the Fe site (perhaps Fe–N$_x$ sites).
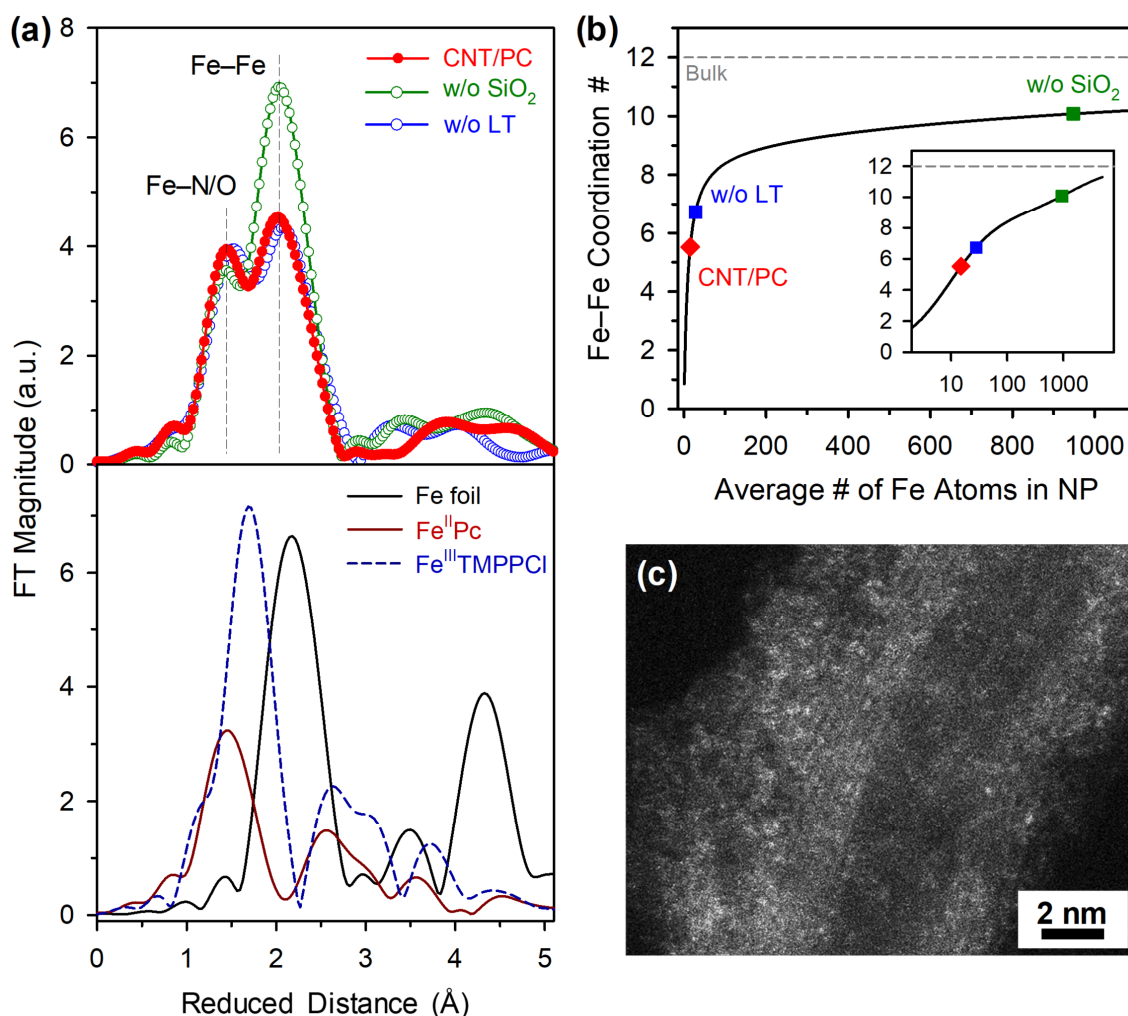
Figure 3.11. (a) RDFs obtained from *ex situ* Fe K-edge EXAFS spectra of the CNT/PC catalyst, comparison samples, and standard bulk materials. (b) The relation between Fe–Fe coordination number and average size of Fe NPs. Inset shows the logarithmic representation of the correlation. (c) HAADF-STEM image of the CNT/PC catalyst.

3.3.4. ^{57}Fe Mössbauer Spectroscopy

To gain deeper insight into the structure of Fe-related species in CNT/PC and CNT/PC_w/o SiO$_2$ catalysts pyrolyzed at 800 °C, ^{57}Fe Mössbauer spectroscopy was conducted at 295 K (**Figure 3.12**). The Mössbauer spectra were least-squares fitted with sub-spectra. The Mössbauer spectrum of CNT/PC shows greater areas for doublet peaks (D1, D2, and D3), which are assigned to structurally distinct Fe–N$_4$ species, compared to that of CNT/PC_w/o SiO$_2$. In contrast, the CNT/PC_w/o SiO$_2$ was found to show a relatively larger Mössbauer signals for singlet (Sing) and sextet (Sext1 and Sext2) peaks than the CNT/PC. Those spectral fingerprints originate from Fe and Fe$_3$C species, indicating that CNT/PC_w/o SiO$_2$ is more abundant in less active Fe and Fe$_3$C phases.

The Fe-site assignment, corresponding fitting parameters, and the relative peak area are summarized in **Table 3.1**. Mössbauer spectroscopy analysis over our catalysts further evidences that the silica coating is effective to preserve Fe–N$_4$ species and to suppress the formation of Fe-based particles. Relative absorption areas for doublets of CNT/PC are larger than that of CNT/PC_w/o SiO$_2$ (76% and 49% of Fe–N$_4$ species with and without silica coating, respectively). 24% of Fe and Fe$_3$C species in CNT/PC are attributed to the presence of sub-nanometer-sized Fe clusters, while tens-of-nanometer-sized Fe and Fe$_3$C nanoparticles (accounting for 51%) are included in CNT/PC_w/o SiO$_2$. The Mössbauer spectroscopy results are consistent with XRD, TEM, and XAS analyses.
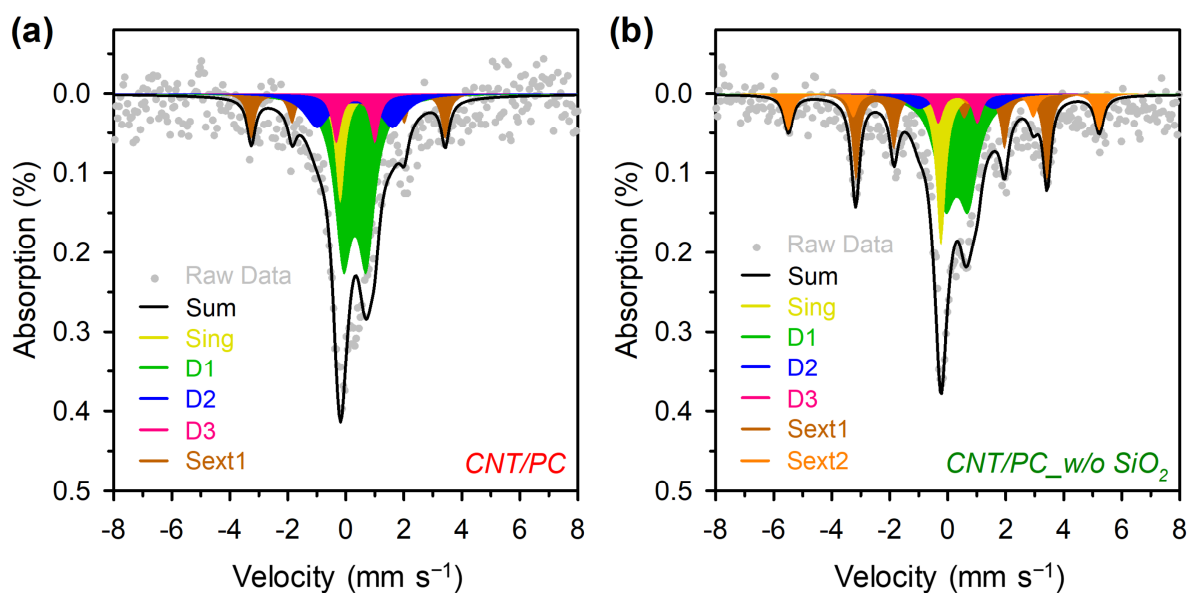
Figure 3.12. ^{57}Fe Mössbauer spectra of (a) CNT/PC and (b) CNT/PC_w/o SiO$_2$.

Table 3.1. Summary of ^{57}Fe Mössbauer fitting parameters, the Fe-site assignment, and relative absorption area for CNT/PC and CNT/PC_w/o SiO$_2$.

Type	δ_{iso} (mm s^{-1}) ^{a}	ΔE_Q (mm s^{-1}) ^{b}	H_0 (T) ^{c}	Assignment	Relative abs. area		Ref.
					CNT/PC	w/o SiO$_2$	
Sing	−0.21 (3)	-	-	Superparamagnetic Fe	10.2%	14.0%	35,61,81
D1	0.32	0.80	-	Low-spin, Fe^{II}–N$_4$	51.4%	37.0%	35,61,81
D2	0.32	2.60	-	Intermediate-spin, Pc-type Fe^{II}–N$_4$	16.3%	7.2%	35,81
D3	0.35 (1)	1.34 (1)	-	Intermediate-spin, Por-type Fe^{II}–N$_4$	8.6%	5.1%	35
Sext1	0.09 (1)	0.02 (3)	20.6 (2)	Fe$_3$C	13.6%	24.6%	81
Sext2	−0.14	0.01	33.3	α-Fe	-	12.1%	35,81

3.3.5. ORR Activity in Half-Cell Configurations

The ORR activities of the CNT/PC catalyst and a commercial Pt/C were evaluated using RRDE measurements in both alkaline and acidic media (**Figure 3.13a**). The linear sweep voltammetry (LSV) curve in 0.1 M KOH (**Figure 3.13a**) clearly demonstrates the very high ORR activity of CNT/PC in alkaline electrolyte, with the half-wave potential at 0.88 V (*vs* RHE), which compares favorably to Pt/C. The LSV curve of CNT/PC in 0.1 M HClO$_4$ demonstrates its high ORR activity with a half-wave potential at 0.79 V. We found that the ORR activity of CNT/PC is one of the highest compared to reported M–N/C catalysts. We note that, however, different experimental conditions such as catalyst loading can influence the ORR activity. Moreover, the number of transferred electrons during the ORR was close to four in the entire potential region, indicating near-four-electron selectivity (**Figures 3.13c,d**). The long-term durability of the CNT/PC catalyst, measured by cycling the potential between 0.6 and 1.0 V up to 10,000 times, was remarkably high evidenced by a nearly identical LSV curve after the tests, whereas Pt/C underwent a significant decrease in its catalytic activity with a negative shift of its half-wave potential by 25 mV (**Figure 3.13b**).

To verify the activity promotion effect by the silica coating and low-temperature treatment, we also measured the ORR activities of CNT/PC_w/o SiO$_2$ and CNT/PC_w/o LT (**Figure 3.14**). The comparison catalysts exhibited less remarkable ORR activity than CNT/PC, as indicated by the lower onset and half-wave potentials. These results confirm the critical role of the silica protective layer as well as low-temperature annealing step for enhancing ORR activity. Interestingly, the effectiveness of the silica-protective strategy appeared to be more prominent in acidic media. The difference in the activities of CNT/PC and CNT/PC_w/o SiO$_2$ was larger in acidic media, where the improvement factor was 3 and 4 in 0.1 M KOH and 0.1 M HClO$_4$, respectively. This can be attributed to a different ORR mechanism on Fe–N$_x$ sites with the pH of electrolyte, which needs further investigations.[65,66]
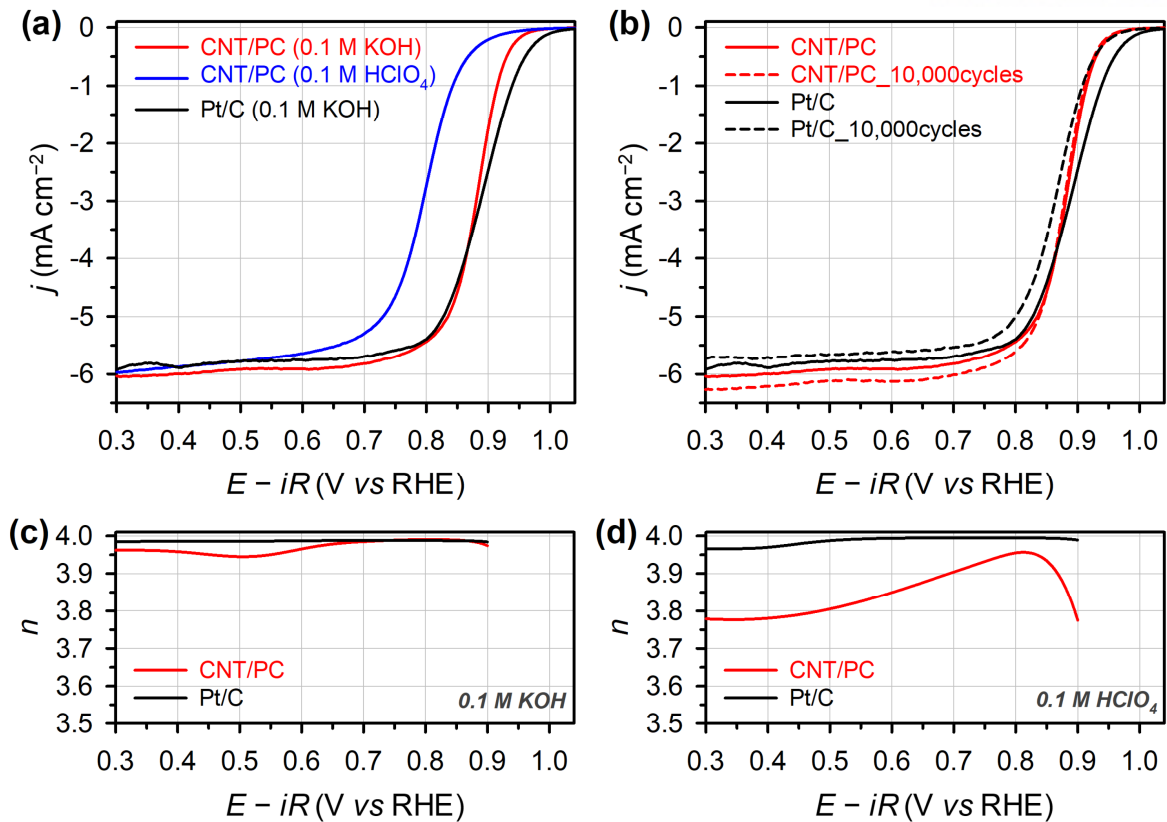
Figure 3.13. (a) ORR polarization curves of the CNT/PC catalyst measured in 0.1 M KOH and 0.1 M HClO$_4$, and of the Pt/C catalyst measured in 0.1 M KOH with an electrode rotation of 1,600 rpm. (b) ORR polarization curves of the CNT/PC and Pt/C catalysts before and after 10,000 potential cycles between 0.6 and 1.0 V in N$_2$-saturated 0.1 M KOH. (c,d) Electron transfer number (n) of the CNT/PC and Pt/C catalysts assessed by the RRDE technique measured in (c) 0.1 M KOH and (d) 0.1 M HClO$_4$.
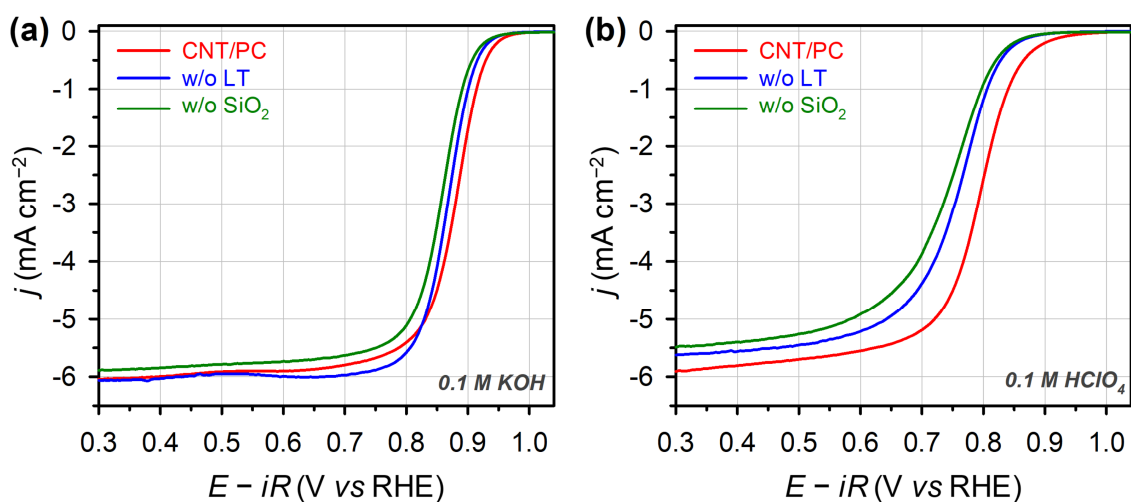
Figure 3.14. ORR polarization curves of the CNT/PC catalyst and control samples measured in (a) 0.1 M KOH and (b) 0.1 M HClO$_4$.

3.3.6. Effect of Catalyst Surface Area

The silica coating could not only promote the formation of active Fe–N$_x$ sites, but also possibly increase the catalytically active surface area. To investigate the surface area effect, the specific surface areas of CNT/PC and CNT/PC_w/o SiO$_2$ was measured using N$_2$ physisorption analysis, where the adsorption-desorption isotherms of them are shown in **Figure 3.15**. Brunauer–Emmett–Teller (BET) surface areas were calculated to be 300 and 114 m^2 g^{-1} for CNT/PC and CNT/PC_w/o SiO$_2$, respectively. The larger surface area of CNT/PC could contribute to the higher ORR activity than CNT/PC_w/o SiO$_2$, given 3 and 4 times higher ORR activity of CNT/PC than CNT/PC_w/o SiO$_2$ in 0.1 M KOH and 0.1 M HClO$_4$, respectively.
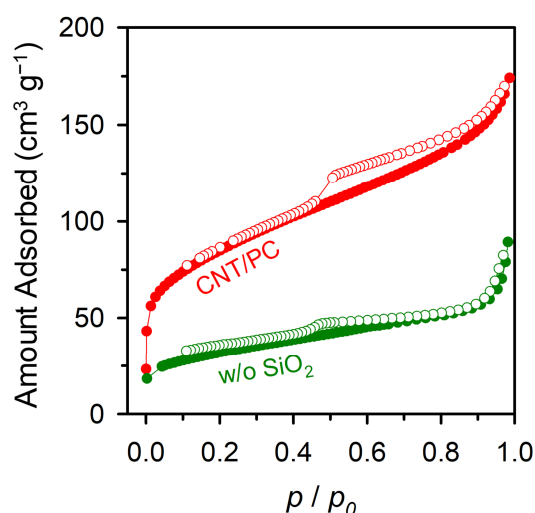
Figure 3.15. N$_2$ adsorption-desorption isotherms of CNT/PC and CNT/PC_w/o SiO$_2$.

Physical surface area is an important factor for catalytic activity, more relevant parameter in the electrocatalysis is an electrochemically active surface area (ECSA). Double layer capacitance (C_{dl}) is considered to be proportional to the ECSA, and thus has been widely used to estimate the ESCA of electrocatalysts.[82] C_{dl} is usually measured according to the following relation

$$i_{cap} = C_{dl} \times v$$

where i_{cap} and v indicate the capacitive current and the potential scan rate, respectively. To obtain capacitive (non-Faradaic) current response, CV measurement was performed in N$_2$-saturated electrolyte with various scan rate from 5 to 25 mV s^{-1} in the potential range where Faradaic current is not detected (**Figures 3.16a,b**). Plotting the capacitive current as a function of the scan rate gives a line with a slope of C_{dl} (**Figures 3.16c,d**).
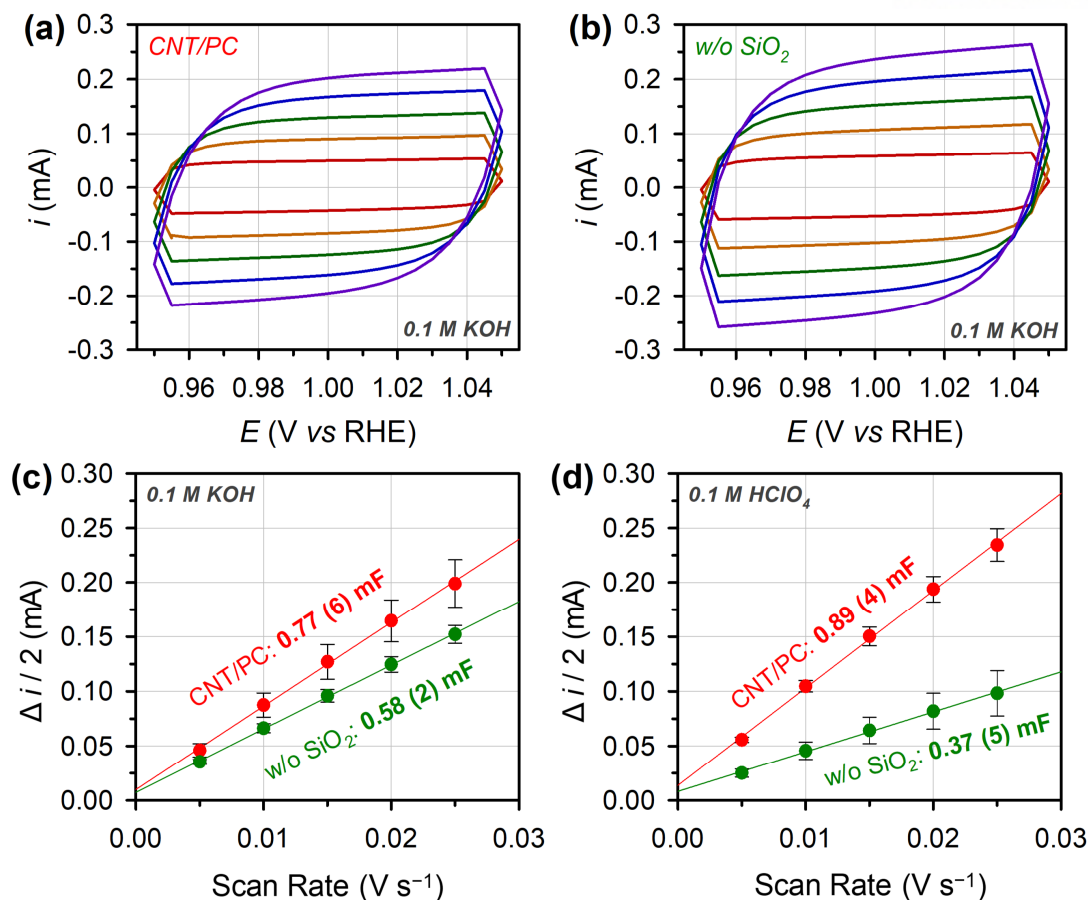
Figure 3.16. (a,b) Representative CV curves measured in N_2-saturated 0.1 M KOH at various scan rates for (a) CNT/PC and (b) CNT/PC_w/o SiO$_2$. The results in 0.1 M HClO$_4$ are not shown. (c,d) Linear correlation between the scan rate and half of the CV height in (c) 0.1 M KOH and (d) 0.1 M HClO$_4$.

CNT/PC has larger ECSAs than CNT/PC_w/o SiO$_2$, by 1.3 and 2.4 times in 0.1 M KOH and HClO$_4$, respectively, which is consistent with the N_2 physisorption results. The ECSA difference between the catalysts is not as remarkable as the difference of the BET surface area, which may imply that the physical surface is not fully reflected in the electrocatalysis. We note that 1.3 and 2.4 times higher ECSA of CNT/PC cannot explain 3 and 4 times higher ORR activity than CNT/PC_w/o SiO$_2$ in 0.1 M KOH and 0.1 M HClO$_4$, respectively. Hence, we conclude that while the higher surface area of CNT/PC partly contributes to better ORR activity, there are additional factors such as the density of catalytically active sites and intrinsic activity of individual site that could further enhance the ORR activity of CNT/PC.[83]

3.3.7. Electrochemical In Situ XAS

To identify changes in the chemical environment of Fe in the CNT/PC during the ORR, we performed electrochemical *in situ* Fe K-edge XAS. **Figure 3.17** shows the XANES and EXAFS spectra for the CNT/PC under applied potentials of 0.3 and 0.9 V (*vs* RHE) in 0.1 M KOH. The XANES spectrum taken at 0.9 V [denoted as $\mu(0.9\ V)$], shows slightly shifted absorption edge towards higher energy, compared to that at 0.3 V [$\mu(0.3\ V)$]. To clearly monitor the shift, the delta-mu ($\Delta\mu$) method was used, which was obtained by subtracting $\mu(0.3\ V)$ from $\mu(0.9\ V)$ (inset of **Figure 3.17a**). The negative peak in the $\Delta\mu$ spectra at 7126 eV indicates the adsorption of oxygenated species onto the Fe–N_x sites, accompanied by Fe oxidation from Fe^{II} to Fe^{III}.[71] This result could be further corroborated by a change in the RDFs of the EXAFS spectra (**Figure 3.17b**). The intensity of the first peak for the Fe–N/O bonding increased at 0.9 V compared to that at 0.3 V, indicating the formation of (H)O–Fe–N_x species. As a result, the local structural environment around Fe at 0.9 V can be assigned to (H)O–Fe^{III}–N_x, while adsorbate-free Fe^{II}–N_x sites are dominant at 0.3 V. The (H)O– Fe^{III}–N_x species are known as spectator in the ORR. Therefore, applying overpotential produces adsorbate-free Fe^{II}–N_x sites at which O_2 can be adsorbed for reduction reaction.[65,66,84] Our electrochemical *in situ* XAS analyses suggest that the ORR over CNT/PC catalyst proceeds predominantly *via* direct participation of the Fe–N_x sites.
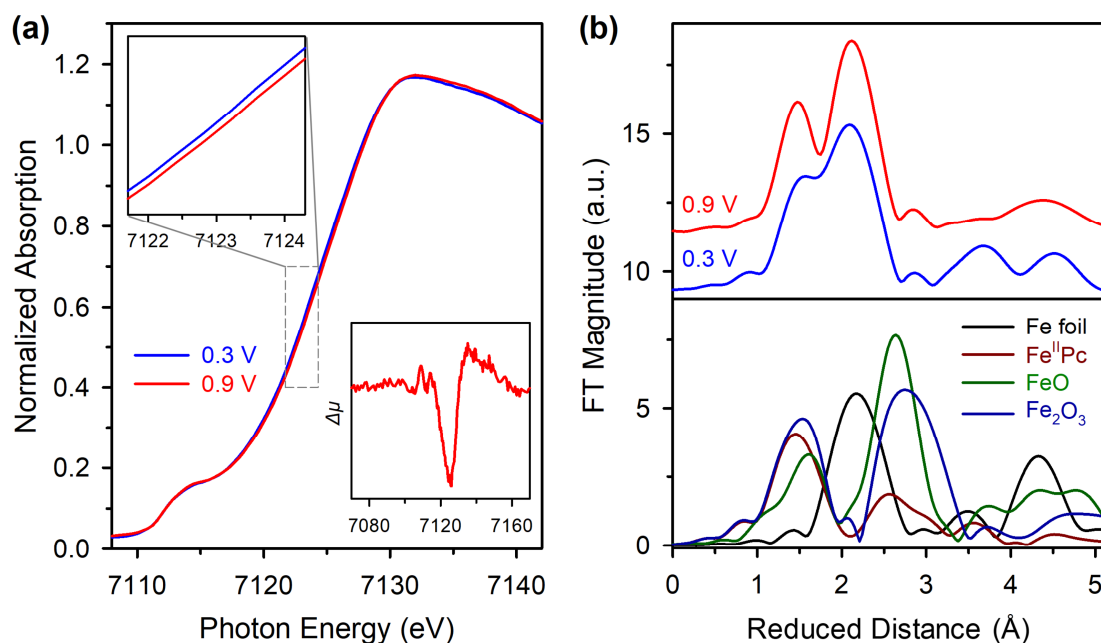
Figure 3.17. (a) Electrochemical *in situ* Fe K-edge XANES spectra of the CNT/PC catalyst measured in 0.1 M KOH under applied potentials. Upper inset represents the enlarged spectra of the area marked by the dotted gray box. Lower inset shows the $\Delta\mu$ spectrum obtained from the subtraction of $\mu(0.3\ V)$ from $\mu(0.9\ V)$. (b) RDFs of electrochemical *in situ* EXAFS spectra of the CNT/PC catalyst and the RDFs of some reference materials.

3.3.8. TOF Calculations

Turnover frequencies (TOFs), representing an activity per each active site, of our catalysts were calculated at 0.8 and 0.9 V (*vs* RHE) for the ORR in acidic and alkaline media, respectively, according to the following equation

$$\text{TOF (e site}^{-1}\text{ s}^{-1}) = \frac{j_k \times M_{Fe}}{(\text{Catalyst loading}) \times c_{Fe} \times c_{D,Fe} \times F}$$

where j_k, M_{Fe}, c_{Fe}, $c_{D,Fe}$, and F indicate the mass-transfer-corrected kinetic current density, the atomic weight of Fe (55.845 g_{Fe} mol^{-1}), the Fe content in the catalyst, the relative absorption area for doublets in Mössbauer spectra, and the Faraday constant (96,485 C mol^{-1}).

For the evaluation of TOF for Fe–N/C catalysts, understanding of the active sites is important. Mössbauer spectroscopy analysis revealed that the three doublets, D1–D3, correspond to three structurally distinct Fe–N$_4$ sites.[35,61,81] D1 is assigned to in-plain low-spin (S = 0) ferrous Fe–N$_4$ site. Koslowski et al.[61] revealed that D1 site is responsible for 4-electron ORR in 0.5 M H_2SO_4. Since then, the in-plane D1 has been considered as the active site for the ORR in acidic media. D2 is crystalline-FePc-like Fe–N$_4$ site with pseudo-octahedral coordination with axial N atoms from the adjacent FePc. This coordination environment and fully occupied d_{z^2} orbital of Fe center in D2 render the adsorption of O_2 on this site unfavorable, suggesting negligible contribution of the site to the ORR activity.[35,61,62,81] D3, porphyrin-like Fe–N$_4$ site with intermediate-spin, is proposed to exist through the stabilization from carbon frameworks.[35] However, in-depth investigation of D3 site and its relation to the ORR activity has not been discussed yet. It should be noted that this D3 is different from the "D3" mentioned in the second paragraph of the *Section 3.3.2*, because the latter appears only in special cases and has been barely reported. Based on these considerations on each doublet site, we decided to use the D1 as the active site for the acidic ORR, that is, $c_{D1,Fe}$ was used to calculate the TOF in acid. In acidic media, the TOF of CNT/PC was calculated to be 0.22 e $site^{-1}$ s^{-1}, which is in the similar range of the activity previously reported.[35,61,70] For the ORR in alkaline media, there has been no report that clearly reveals which Fe–N$_4$ species is responsible for the ORR. Hence, TOFs were calculated under two assumptions; only D1 site ($c_{D1,Fe}$) or all doublet sites ($c_{D,Fe}$) is/are active, which yield 2.6 and 1.7 e $site^{-1}$ s^{-1}, respectively. When the TOF values of CNT/PC are compared to those of CNT/PC_w/o SiO_2, the CNT/PC catalyst shows 300% and 40–50% higher TOF in acidic and alkaline electrolytes, respectively. The difference in the TOFs may suggest implications about the role of the silica coating in promoting the activity of the individual Fe–N$_x$ sites.

3.3.9. AEMFC and PEMFC Performances

We exploited the CNT/PC catalyst as a cathode for an AEMFC. **Figure 3.18a** shows polarization and power density curves of AEMFCs based on CNT/PC and Pt/C catalysts. The CNT/PC-based MEA exhibited very high AEMFC performance, which was comparable to a Pt/C-based MEA. The current density at 0.6 V and peak power density of the CNT/PC-based MEA are 0.50 A cm^{-2} and 0.38 W cm^{-2}, respectively, which are one of the highest performances among NPMC-based MEAs for AEMFCs (**Figure 3.18b**).[46,85–91] High performance of a CNT/PC-based MEA was also demonstrated in a PEMFC (**Figure 3.18c**). The CNT/PC-based MEA exhibited a current density at 0.6 V and peak power density of 0.55 A cm^{-2} and 0.58 W cm^{-2}, respectively. Significantly, the extrapolated volumetric current density at 0.8 V of the CNT/PC-based MEA in the PEMFC is 320 A cm^{-3}, which compares favorably with the US DOE 2020 target (300 A cm^{-3}) and exceeds the performances of many reported catalysts (**Figure 3.18d**). The excellent single cell performances indicate that the high ORR activity of the CNT/PC catalyst significantly enhances the MEA performances in both alkaline and acidic electrolytes.
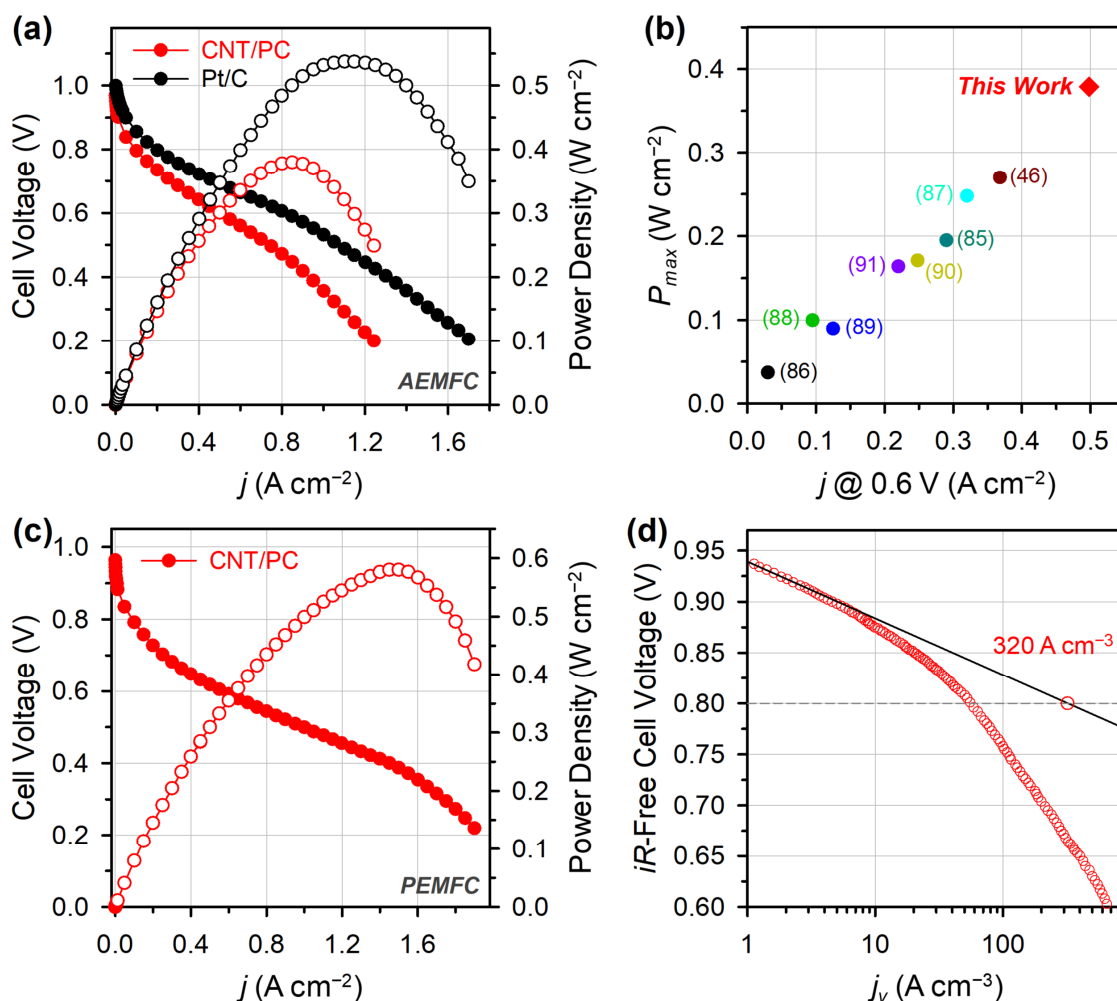
Figure 3.18. (a) Polarization curves and power density curves of the CNT/PC and Pt/C catalysts in

AEMFC. (b) Comparison of the current density at 0.6 V and peak power density of the CNT/PC-based AEMFC with those of some reported NPMC-based AEMFCs. The numbers in (b) indicate the reference numbers. (c) Polarization curve and power density curve of the CNT/PC catalyst in PEMFC. (d) Volumetric current density curves and an extrapolated curve of the CNT/PC catalyst in PEMFC. P_{max} and j_v indicate the peak power density and the volumetric current density, respectively.

3.3.10. Role of the Silica Coating

To more clearly reveal the effect of the silica coating on the composition, coordination environment, and ORR activity of CNT/PC-based catalysts, a set of CNT/PC catalysts with and without silica layer were prepared at various pyrolysis temperatures from 600 to 1000 °C (denoted as CNT/PC-X and CNT/PC-X_w/o SiO_2, X = temperature). First, combustion elemental analysis was used to determine N contents in the samples (**Table 3.2**).

Table 3.2. Summary of elemental analysis results for CNT/PC-X and CNT/PC-X_w/o SiO_2 samples.

Sample	C (wt%)	N (wt%)	O (wt%)	H (wt%)
CNT/PC-600	81.3	**4.1**	9.1	1.3
CNT/PC-600_w/o SiO_2	80.8	**3.3**	7.1	0.9
CNT/PC-700	86.6	**2.7**	5.4	0.76
CNT/PC-700_w/o SiO_2	83.7	**2.5**	5.6	0.68
CNT/PC-800	90.3	**1.9**	3.2	0.54
CNT/PC-800_w/o SiO_2	86.3	**1.9**	4.2	0.54
CNT/PC-900	92.1	**1.4**	2.3	0.46
CNT/PC-900_w/o SiO_2	88.1	**1.5**	3.4	0.36
CNT/PC-1000	94.4	**1.0**	1.7	0.36
CNT/PC-1000_w/o SiO_2	91.6	**1.1**	2.2	0.27

CNT/PC has a larger amount of N than CNT/PC_w/o SiO_2 when they were pyrolyzed at 600 and 700 °C. In the case of the CNT/PC catalysts pyrolyzed at higher than 800 °C, the N contents of CNT/PC and CNT/PC_w/o SiO_2 are almost similar to each other. These results indicate that the silica coating does not always produce the catalyst with more abundant N atoms. We note that N atoms can have at least three atomic configurations after high-temperature treatment and acid-washing steps: (i) N atoms remain coordinated to Fe in Fe–N_x species. (ii) N atoms can be incorporated within graphitic

carbon shells encapsulating Fe (and/or Fe_3C) particles generated during the pyrolysis at higher temperature ($\geq$ 800 °C). (iii) N-doped carbon species without Fe-coordination can be generated when Fe atoms in unstable Fe–N_x species are leached out during the acid-washing step. Hence, the similar N contents in CNT/PC and CNT/PC_w/o SiO_2 cannot suggest that they contain a similar amount of Fe–N_x sites.

The deconvolution of N 1s XPS spectra was conducted to gain further insight into the chemical states of N species in the catalysts (**Figure 3.19**). Four deconvoluted peaks are found: 398.1–398.3 eV for pyridinic N (N1), 399.4 eV for pyrrolic N and Fe–N_x species (N2), 400.4–400.7 eV for graphitic N (N3), and > 402 eV for N–O species (N4).[26,72,92] The most remarkable difference in the XPS spectra is larger relative peak area of N2 peak (pyrrolic N and Fe–N_x) for the CNT/PC catalysts than CNT/PC_w/o SiO_2, regardless of pyrolysis temperature. This suggests that the silica coating effectively preserve Fe–N_x species for the Fe–N/C catalyst with a higher active site density.
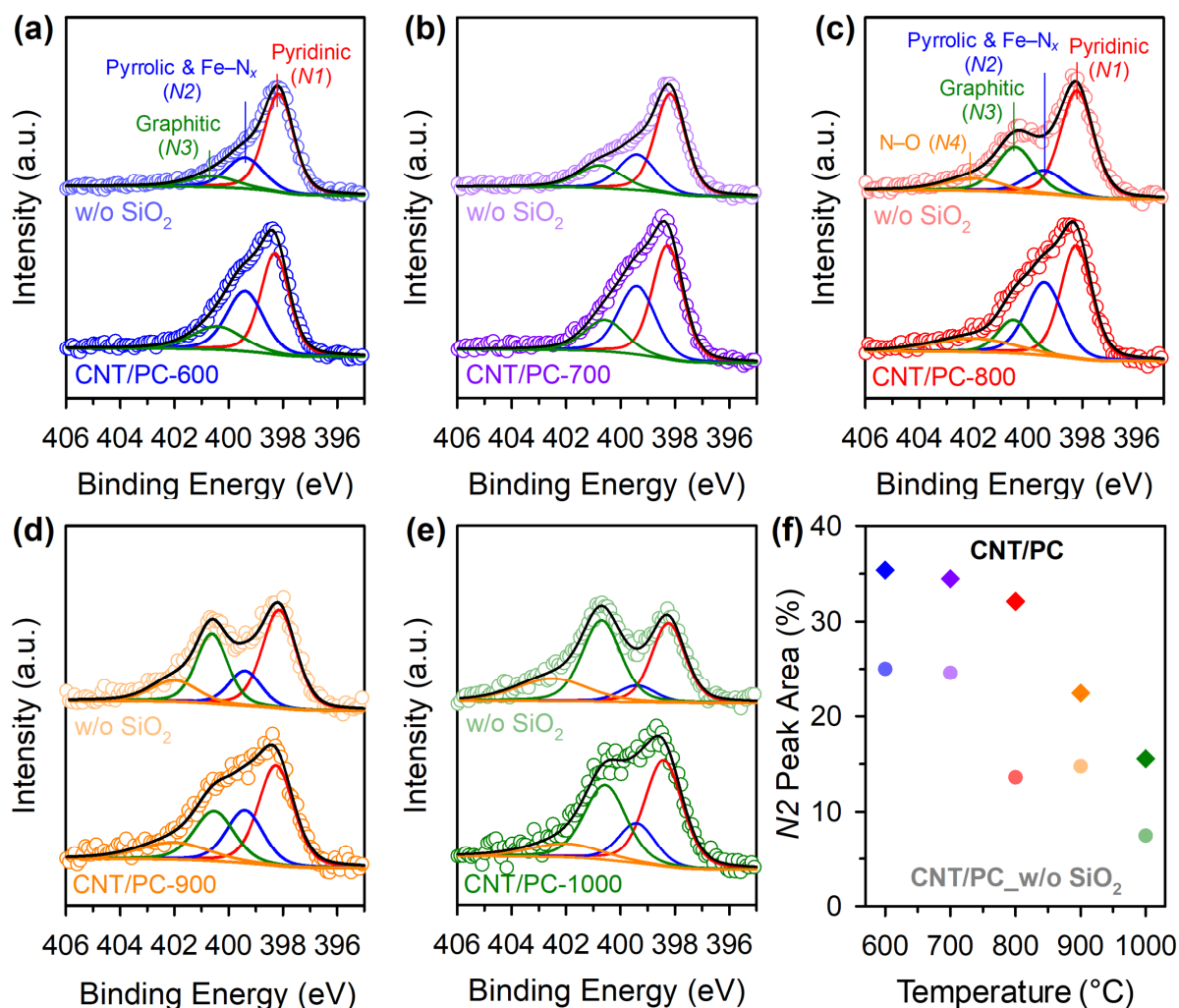
Figure 3.19. (a–e) High-resolution N 1s XPS spectra and deconvoluted peaks for the CNT/PC and CNT/PC_w/o SiO_2 catalysts pyrolyzed at (a) 600 °C, (b) 700 °C, (c) 800 °C, (d) 900 °C, and (e) 1000 °C. (f) Comparison of the N2 peak area of the catalysts.

Another notable point from XPS analysis is higher N3 peak area (graphitic N) for CNT/PC_w/o SiO$_2$ samples pyrolyzed at higher temperatures ($\geq$ 800 °C). As described above, high-temperature pyrolysis usually produces Fe (and/or Fe$_3$C) NPs, which are encapsulated by graphitic carbon shells. The larger N3 peak area in CNT/PC_w/o SiO$_2$ samples implies that higher amounts of N atoms were incorporated within graphitic shells in these catalysts than the CNT/PC catalysts.

We verified the presence/absence of crystalline phases in the catalysts by XRD. The CNT/PC catalysts prepared with the silica layer show no characteristic XRD peaks for Fe and Fe$_3$C (**Figure 3.20**). In contrast, CNT/PC_w/o SiO$_2$ catalysts pyrolyzed at 700–1000 °C were found to have Fe and Fe$_3$C NPs. The formation of the Fe and Fe$_3$C particles were particularly prominent for CNT/PC-900_w/o SiO$_2$ and CNT/PC-1000_w/o SiO$_2$. We highlight that the silica coating strategy is highly efficient in suppressing Fe-based particle formation at high temperature up to 1000 °C.
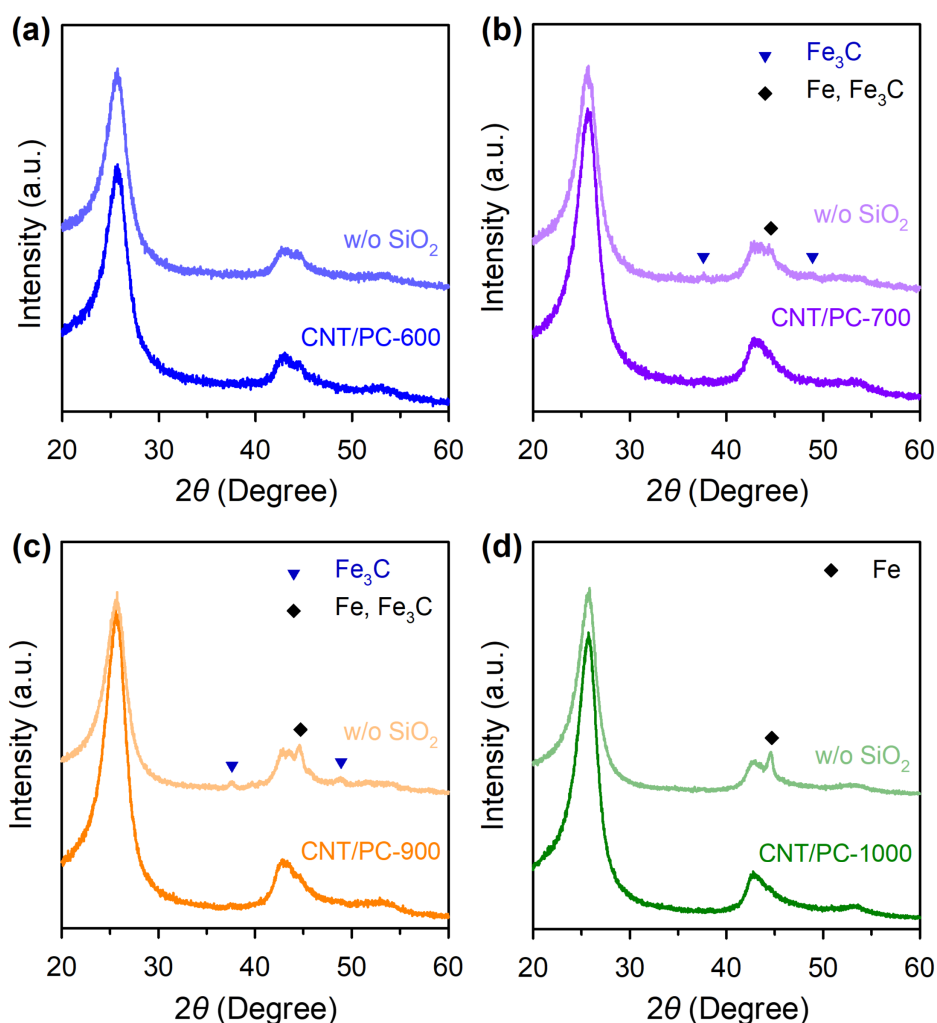
Figure 3.20. XRD patterns of the CNT/PC and CNT/PC_w/o SiO$_2$ catalysts pyrolyzed at (a) 600 °C, (b) 700 °C, (c) 900 °C, and (d) 1000 °C.

Finally, we investigated the electrocatalytic activity of the prepared catalysts for the ORR in both alkaline and acidic media. The silica coating is generally effective to enhance the ORR activity of the Fe–N/C catalysts in both electrolytes (**Figure 3.21**). In all pyrolysis temperature range investigated, CNT/PC exhibited 20–60 mV and 50–70 mV positive half-wave potentials than CNT/PC_w/o SiO$_2$ in 0.1 M KOH and 0.1 M HClO$_4$, respectively. Interestingly, the CNT/PC-600 exhibited about 2–3 times higher ORR activity than CNT/PC-600_w/o SiO$_2$ in spite of the absence of Fe-based NPs in both catalysts. XPS results (**Figure 3.19**) suggest that the CNT/PC-600 contains a 30% larger quantity of Fe–N$_x$ species than CNT/PC-600_w/o SiO$_2$, which however cannot explain fully the improvement factor. In the work reported by Kramm et al., Mössbauer spectra demonstrated that Fe-sites in Fe^{III}TMPPCl-based catalysts pyrolyzed at 600 °C are mostly composed of Fe–N$_4$ sites without crystalline Fe NPs. However, it showed an inferior ORR activity to the catalyst pyrolyzed at 800 °C, which contained smaller amounts of active Fe–N$_4$ species. This literature emphasizes the importance of the electron density as well as the site density of the Fe–N$_4$ center.[83] In our work, we suppose that the silica coating plays a role not only in preserving active Fe–N$_x$ sites, but also in modifying the electronic structure (and/or local structure) of the Fe–N$_x$ site *via* interaction between the silica and Fe–N$_4$ in the precursor. The modulation may be related to the distortion of Fe–N$_x$ site.[71]
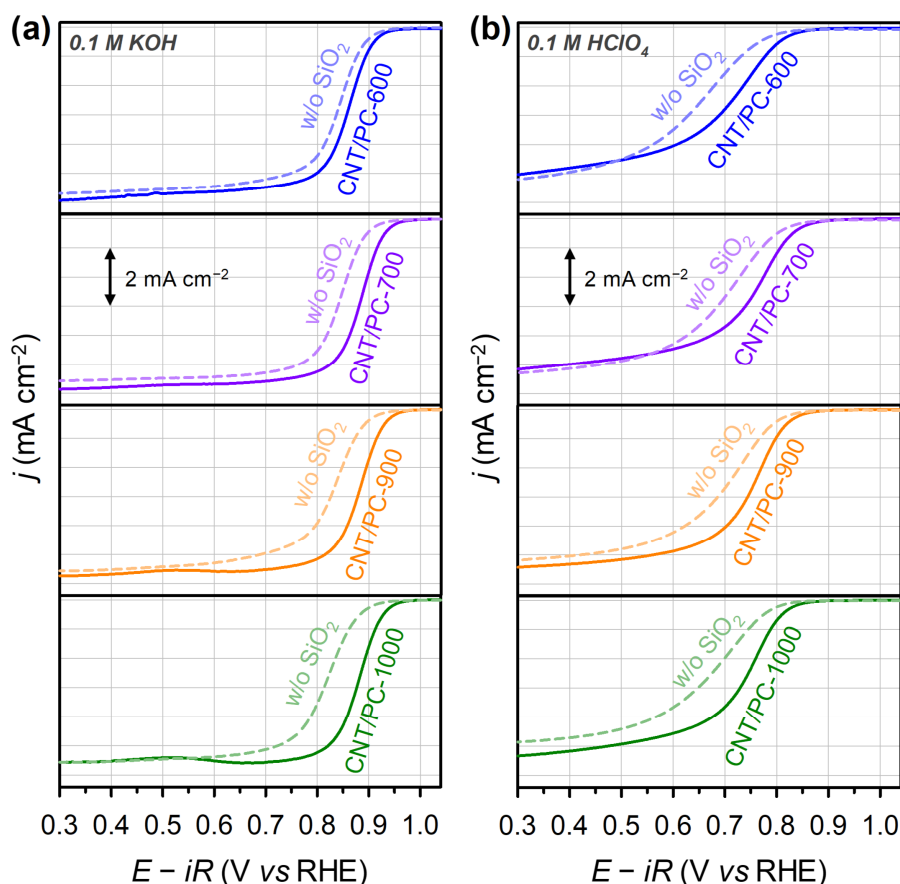
Figure 3.21. ORR polarization curves of the CNT/PC and CNT/PC_w/o SiO$_2$ catalysts pyrolyzed at different temperatures measured in (a) 0.1 M KOH and (b) 0.1 M HClO$_4$.

3.3.11. Generalization of the Silica Coating to Other Carbon Supports

To validate the generality, we extended the silica-protected-layer-assisted strategy to other carbon supports, i.e. reduced graphene oxides (rGO), Ketjen black (KB), acetylene black (AB), Vulcan; the resulting catalysts were denoted as carbon/PC (carbon: rGO, KB, AB, and Vulcan). The carbon/PC catalysts show only XRD peaks from pristine carbon supports, whereas carbon/PC_w/o SiO$_2$ catalysts show additional diffraction peaks, corresponding to Fe and Fe$_3$C phases, bolstering the role of silica overcoating layer in suppressing the formation of Fe-based particles during pyrolysis (**Figure 3.22a**). RDFs of Fe K-edge EXAFS spectra further support the role of the silica, indicated by higher peak intensity for Fe–Fe scattering (**Figure 3.22b**). Relatively higher density of active Fe–N$_x$ sites in the carbon/PC catalysts resulted in greater ORR activity (**Figure 3.23**). Therefore, the silica-protective-layer-assisted synthetic method is extensively applicable to other carbon supports for developing pyrolyzed M–N/C catalyst with higher density of active M–N$_x$ sites.
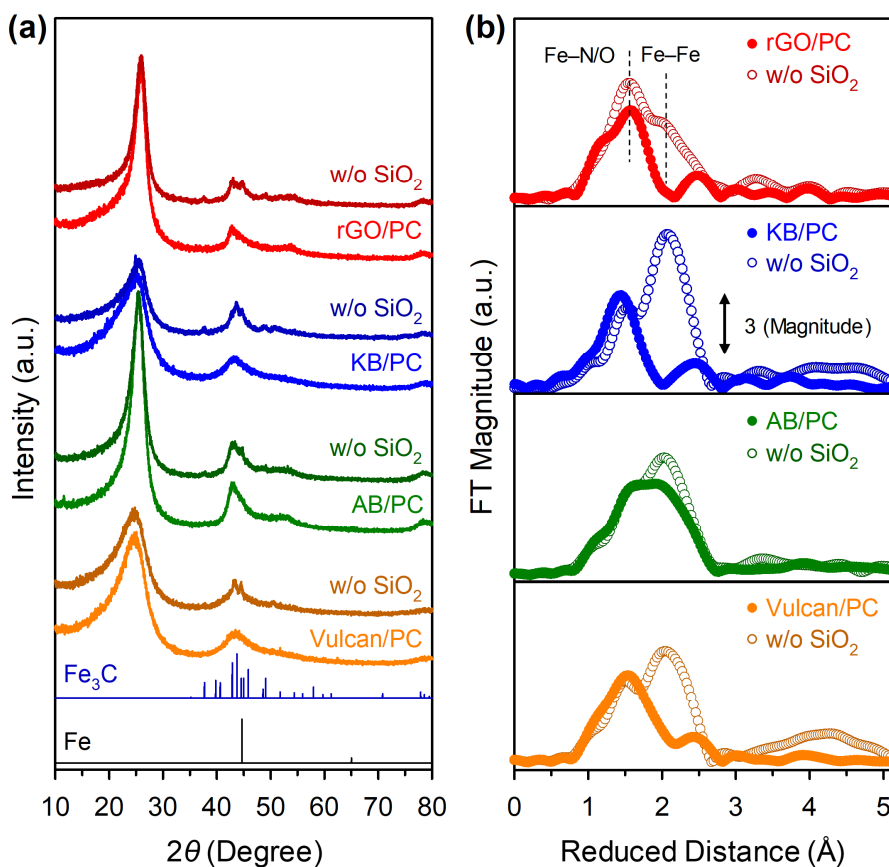
Figure 3.22. (a) XRD patterns and (b) RDFs of the EXAFS spectra of carbon/PC and carbon/PC_w/o SiO$_2$.
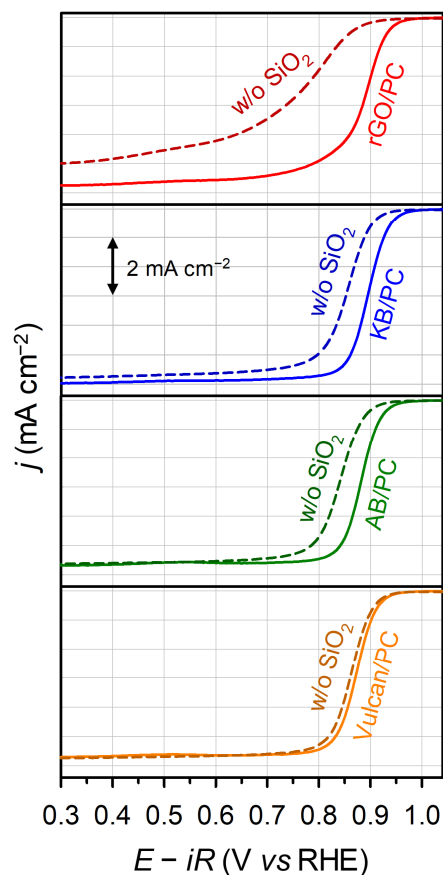
Figure 3.23. ORR polarization curves of carbon/PC and carbon/PC_w/o SiO$_2$ catalysts measured in 0.1 M KOH.

3.3.12. Catalytic Role of Fe–N$_x$ Sites and Fe/Fe$_3$C NPs

Finally, we discuss the catalytic role of the Fe–N$_x$ site and Fe-based particles in carbon/PC catalysts for the ORR. Fe and Fe$_3$C encapsulated by carbon shells recently have been suggested to be possible active species, along with Fe–N$_x$ sites,[18,19,27,31,73] though their roles are still controversial. Bao et al. reported that Fe NPs encapsulated in CNTs modulate the electronic structure of the carbons, and thus indirectly participate in the ORR electrocatalysis.[19] In addition, Fe$_3$C NPs were suggested to boost the ORR activity of Fe–N$_x$ sites.[73] In our study, the higher ORR activity of the carbon/PC catalysts mainly stems from the larger quantity Fe–N$_x$ sites, which thus are regarded as the active site for the ORR. However, we found that the four-electron selectivity of the carbon/PC_w/o SiO$_2$ catalysts was slightly, yet consistently, higher than the carbon/PC catalysts in the diffusion-limited potential region, in spite of lower ORR activity of the former than the latter (**Figure 3.24**). These results suggest that the Fe-based particles present in the carbon/PC_w/o SiO$_2$ catalysts reduce HO$_2^-$, which is the product of 2-electron ORR, completing the 4-electron reduction of oxygen.[93,94]
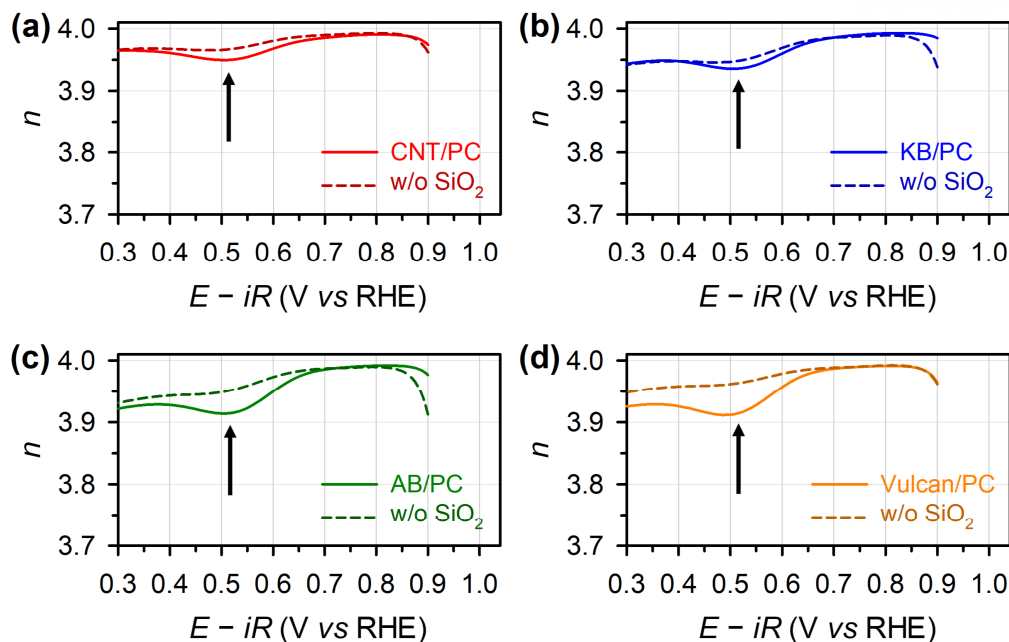
Figure 3.24. Electron transfer number of the carbon/PC and carbon/PC_w/o SiO$_2$ catalysts measured in (a) 0.1 M KOH and (b) 0.1 M HClO$_4$.

3.4. CONCLUSION

We have demonstrated a general silica-protective-layer-assisted strategy to preferentially create catalytically active Fe–N$_x$ sites during the preparation of Fe–N/C catalysts. Temperature-controlled *in situ* XAS provided evidences for the possible role of the silica layer in protecting Fe–N$_x$ sites, thereby suppressing the formation of Fe-based particles, as well as for the distortion of the planar Fe–N$_4$ site to more active distorted Fe–N$_x$ sites. The resulting highly active non-precious metal ORR catalyst, CNT/PC, showed very high ORR activity in both alkaline and acidic media in half-cell configurations, and demonstrated excellent fuel cell performances in both an AEMFC and a PEMFC. Significantly, the AEMFC with a CNT/PC cathode showed record high current and power densities among NPMC-based MEAs. We further demonstrated the general applicability of the synthetic strategy to other carbon supports including rGO and carbon blacks. This work indicates that the "silica-protective-layer-assisted" strategy can be exploited to promote the formation of active molecular entity (Fe–N$_x$ sites) during the catalyst synthesis, beyond the previous role of preventing the sintering of nanoparticle catalysts under harsh catalytic reaction conditions. We believe that our catalyst design can provide an important guideline for the development of novel M–N/C catalysts and so-called "single-atom catalysts" as well, for a wide range of applications such as energy conversion and catalysis.

3.5. REFERENCES

(1)   Steele, B. C. H.; Heinzel, A. *Nature* **2001**, *414*, 345–352.

(2)   Gasteiger, H. A.; Kocha, S. S.; Sompalli, B.; Wagner, F. T. *Appl. Catal. B: Environ.* **2005**, *56*, 9–35.

(3)   Debe, M. K. *Nature* **2012**, *486*, 43–51.

(4)   Shao, M.; Chang, Q.; Dodelet, J.-P.; Chenitz, R. *Chem. Rev.* **2016**, *116*, 3594–3657.

(5)   Xia, W.; Mahmood, A.; Liang, Z.; Zou, R.; Guo, S. *Angew. Chem., Int. Ed.* **2016**, *55*, 2650–2676.

(6)   Mistry, H.; Varela, A. S.; Kühl, S.; Strasser, P.; Cuenya, B. R. *Nat. Rev. Mater.* **2016**, *1*, 16009.

(7)   Lee, K.; Zhang, J.; Wang, H.; Wilkinson, D. P. *J. Appl. Electrochem.* **2006**, *36*, 507–522.

(8)   Papageorgopoulos, D. Fuel Cells Program – Plenary Presentation, http://www.hydrogen.energy.gov/pdfs/review15/fc000_papageorgopoulos_2015_o.pdf, **2015** (accessed Oct 31, 2017).

(9)   Jiang, R.; Chu, D. Electrocatalysts for Alkaline Polymer Exchange Membrane (PEM) Fuel Cells – Overview. In *Non-Noble Metal Fuel Cell Catalysts*; Chen, Z., Dodelet, J.-P., Zhang, J., Eds.; Wiley-VCH, Weinheim, **2014**; pp. 271–317.

(10)   Gu, S.; Xu, B.; Yan, Y. *Annu. Rev. Chem. Biomol. Eng.* **2014**, *5*, 429–454.

(11)   Jaouen, F.; Proietti, E.; Lefèvre, M.; Chenitz, R.; Dodelet, J.-P.; Wu, G.; Chung, H. T.; Johnston, C. M.; Zelenay, P. *Energy Environ. Sci.* **2011**, *4*, 114–130.

(12)   Chen, Z.; Higgins, D.; Yu, A.; Zhang, L.; Zhang, J. *Energy Environ. Sci.* **2011**, *4*, 3167–3192.

(13)   Lefèvre, M.; Proietti, E.; Jaouen, F.; Dodelet, J.-P. *Science* **2009**, *324*, 71–74.

(14)   Wu, G.; More, K. L.; Johnston, C. M.; Zelenay, P. *Science* **2011**, *332*, 443–447.

(15)   Proietti, E.; Jaouen, F.; Lefèvre, M.; Larouche, N.; Tian, J.; Herranz, J.; Dodelet, J.-P. *Nat. Commun.* **2011**, *2*, 416.

(16)   Li, Y.; Zhou, W.; Wang, H.; Xie, L.; Liang, Y.; Wei, F.; Idrobo, J.-C.; Pennycook, S. J.; Dai, H. *Nat. Nanotechnol.* **2012**, *7*, 394–400.

(17)   Zhao, Y.; Watanabe, K.; Hashimoto, K. *J. Am. Chem. Soc.* **2012**, *134*, 19528–19531.

(18)   Chung, H. T.; Won, J. H.; Zelenay, P. *Nat. Commun.* **2013**, *4*, 1922.

(19)   Deng, D.; Yu, L.; Chen, X.; Wang, G.; Jin, L.; Pan, X.; Deng, J.; Sun, G.; Bao, X. *Angew. Chem., Int. Ed.* **2013**, *52*, 371–375.

(20)   Cao, R.; Thapa, R.; Kim, H.; Xu, X.; Kim, M. G.; Li, Q.; Park, N.; Liu, M.; Cho, J. *Nat. Commun.* **2013**, *4*, 2076.

(21)   Cheon, J. Y.; Kim, T.; Choi, Y.; Jeong, H. Y.; Kim, M. G.; Sa, Y. J.; Kim, J.; Lee, Z.; Yang, T.-H.; Kwon, K.; Terasaki, O.; Park, G.-G.; Adzic, R. R.; Joo, S. H. *Sci. Rep.* **2013**, *3*, 2715.

(22)   Yuan, S.; Shui, J.-L.; Grabstanowicz, L.; Chen, C.; Commet, S.; Reprogle, B.; Xu, T.; Yu, L.; Liu, D.-J. *Angew. Chem., Int. Ed.* **2013**, *52*, 8349–8353.

(23) Lin, L.; Zhu, Q.; Xu, A.-W. *J. Am. Chem. Soc.* **2014**, *136*, 11027–11033.

(24) Sahraie, N. R.; Paraknowitsch, J. P.; Göbel, C.; Thomas, A.; Strasser, P. *J. Am. Chem. Soc.* **2014**, *136*, 14486–14497.

(25) Liang, J.; Zhou, R. F.; Chen, X. M.; Tang, Y. H.; Qiao, S. Z. *Adv. Mater.* **2014**, *26*, 6074–6079.

(26) Serov, A.; Artyushkova, K.; Atanassov, P. *Adv. Energy Mater.* **2014**, *4*, 1301735.

(27) Yang, W.; Liu, X.; Yue, X.; Jia, J.; Guo, S. *J. Am. Chem. Soc.* **2015**, *137*, 1436–1439.

(28) Ding, W.; Li, L.; Xiong, K.; Wang, Y.; Li, W.; Nie, Y.; Chen, S.; Qi, X.; Wei, Z. *J. Am. Chem. Soc.* **2015**, *137*, 5414–5420.

(29) Niu, W.; Li, L.; Liu, X.; Wang, N.; Liu, J.; Zhou, W.; Tang, Z.; Chen, S. *J. Am. Chem. Soc.* **2015**, *137*, 5555–5562.

(30) Wang, Y.-C.; Lai, Y.-J.; Song, L.; Zhou, Z.-Y.; Liu, J.-G.; Wang, Q.; Yang, X.-D.; Chen, C.; Shi, W.; Zheng, Y.-P.; Rauf, M.; Sun, S.-G. *Angew. Chem., Int. Ed.* **2015**, *54*, 9907–9910.

(31) Strickland, K.; Miner, E.; Jia, Q.; Tylus, U.; Ramaswamy, N.; Liang, W.; Sougrati, M.-T.; Jaouen, F.; Mukerjee, S. *Nat. Commun.* **2015**, *6*, 7343.

(32) Sahraie, N. R.; Kramm, U. I.; Steinberg, J.; Zhang, Y.; Thomas, A.; Reier, T.; Paraknowitsch, J.-P.; Strasser, P. *Nat. Commun.* **2015**, *6*, 8618.

(33) Shui, J.; Chen, C.; Grabstanowicz, L.; Zhao, D.; Liu, D.-J. *Proc. Natl. Acad. Sci. USA* **2015**, *112*, 10629–10634.

(34) Cheon, J. Y.; Kim, K.; Sa, Y. J.; Sahgong, S. H.; Hong, Y.; Woo, J.; Yim, S.-D.; Jeong, H. Y.; Kim, Y.; Joo, S. H. *Adv. Energy Mater.* **2016**, *6*, 1501794.

(35) Kramm, U. I.; Herrmann-Geppert, I.; Behrends, J.; Lips, K.; Fiechter, S.; Bogdanoff, P. *J. Am. Chem. Soc.* **2016**, *138*, 635–640.

(36) Liang, H.-W.; Wei, W.; Wu, Z.-S.; Müllen, K. *J. Am. Chem. Soc.* **2013**, *135*, 16002–16005.

(37) Wang, J.; Wang, K.; Wang, F.-B.; Xia, X.-H. *Nat. Commun.* **2014**, *5*, 5285.

(38) Wu, Z.-S.; Chen, L.; Liu, J.; Parvez, K.; Liang, H.; Shu, J.; Sachdev, H.; Graf, R.; Feng, X.; Müllen, K. *Adv. Mater.* **2014**, *26*, 1450–1455.

(39) Han, J.; Sa, Y. J.; Shim, Y.; Choi, M.; Park, N.; Joo, S. H.; Park, S. *Angew. Chem., Int. Ed.* **2015**, *54*, 12622–12626.

(40) You, B.; Jiang, N.; Sheng, M.; Drisdell, W. S.; Yano, J.; Sun, Y. *ACS Catal.* **2015**, *5*, 7068–7076.

(41) Xia, B. Y.; Yan, Y.; Li, N.; Wu, H. B.; Lou, X. W.; Wang, X. *Nat. Energy* **2016**, *1*, 15006.

(42) Zheng, Y.; Jiao, Y.; Jaroniec, M.; Jin, Y.; Qiao, S. Z. *Small* **2012**, *8*, 3550–3566.

(43) Wang, D.-W.; Su, D. *Energy Environ. Sci.* **2014**, *7*, 576–591.

(44) Gong, K.; Du, F.; Xia, Z.; Durstock, M.; Dai, L. *Science* **2009**, *323*, 760–764.

(45) Liang, J.; Zheng, Y.; Chen, J.; Liu, J.; Hulicova-Jurcakova, D.; Jaroniec, M.; Qiao, S. Z. *Angew. Chem., Int. Ed.* **2012**, *51*, 3892–3896.

(46) Sa, Y. J.; Park, C.; Jeong, H. Y.; Park, S.-H.; Lee, Z.; Kim, K. T.; Park, G.-G.; Joo, S. H. *Angew.*

Chem., Int. Ed. **2014**, *53*, 4102–4106.

(47) Liang, H.-W.; Zhuang, X.; Brüller, S.; Feng, X.; Müllen, K. *Nat. Commun.* **2014**, *5*, 4973.

(48) Cheon, J. Y.; Kim, J. H.; Kim, J. H.; Goddeti, K. C.; Park, J. Y.; Joo, S. H. *J. Am. Chem. Soc.* **2014**, *136*, 8875–8878.

(49) Liang, Y.; Li, Y.; Wang, H.; Zhou, J.; Wang, J.; Regier, T.; Dai, H. *Nat. Mater.* **2011**, *10*, 780–786.

(50) Chen, Z.; Yu, A.; Higgins, D.; Li, H.; Wang, H.; Chen, Z. *Nano Lett.* **2012**, *12*, 1946–1952.

(51) Wu, Z.-S.; Yang, S.; Sun, Y.; Parvez, K.; Feng, X.; Müllen, K. *J. Am. Chem. Soc.* **2012**, *134*, 9082–9085.

(52) Masa, J.; Xia, W.; Sinev, I.; Zhao, A.; Sun, Z.; Grutzke, S.; Weide, P.; Muhler, M.; Schuhmann, W. *Angew. Chem., Int. Ed.* **2014**, *53*, 8508–8512.

(53) Jasinski, R. *Nature* **1964**, *201*, 1212–1213.

(54) Alt, H.; Binder, H.; Sandstede, G. *J. Catal.* **1973**, *28*, 8–19.

(55) Randin, J.-P. *Electrochim. Acta* **1974**, *19*, 83–85.

(56) Jahnke, H.; Schönborn, M.; Zimmermann, G. *Top. Curr. Chem.* **1976**, *61*, 133–181.

(57) Gupta, S.; Tryk, D.; Bae, I.; Aldred, W.; Yeager, E. *J. Appl. Electrochem.* **1989**, *19*, 19–27.

(58) Lefèvre, M.; Dodelet, J.-P.; Bertrand, P. *J. Phys. Chem. B* **2000**, *104*, 11238–11247.

(59) Jaouen, F.; Lefèvre, M.; Dodelet, J.-P.; Cai, M. *J. Phys. Chem. B* **2006**, *110*, 5553–5558.

(60) Ziegelbauer, J. M.; Olson, T. S.; Pylypenko, S.; Alamgir, F.; Jaye, C.; Atanassov, P.; Mukerjee, S. *J. Phys. Chem. C* **2008**, *112*, 8839–8849.

(61) Koslowski, U. I.; Abs-Wurmbach, I.; Fiechter, S.; Bogdanoff, P. *J. Phys. Chem. C* **2008**, *112*, 15356–15366.

(62) Kramm, U. I.; Herranz, J.; Larouche, N.; Arruda, T. M.; Lefèvre, M.; Jaouen, F.; Bogdanoff, P.; Fiechter, S.; Abs-Wurmbach, I.; Mukerjee, S.; Dodelet, J.-P. *Phys. Chem. Chem. Phys.* **2012**, *14*, 11673–11688.

(63) Ferrandon, M.; Kropf, A. J.; Myers, D. J.; Artyushkova, K.; Kramm, U.; Bogdanoff, P.; Wu, G.; Johnston, C. M.; Zelenay, P. *J. Phys. Chem. C* **2012**, *116*, 16001–16013.

(64) Grumelli, D.; Wurster, B.; Stepanow, S.; Kern, K. *Nat. Commun.* **2013**, *4*, 2904.

(65) Ramaswamy, N.; Tylus, U.; Jia, Q.; Mukerjee, S. *J. Am. Chem. Soc.* **2013**, *135*, 15443–15449.

(66) Tylus, U.; Jia, Q.; Strickland, K.; Ramaswamy, N.; Serov, A.; Atanassov, P.; Mukerjee, S. *J. Phys. Chem. C* **2014**, *118*, 8999–9008.

(67) Wang, Q.; Zhou, Z.-Y.; Lai, Y.-J.; You, Y.; Liu, J.-G.; Wu, X.-L.; Terefe, E.; Chen, C.; Song, L.; Rauf, M.; Tian, N.; Sun, S.-G. *J. Am. Chem. Soc.* **2014**, *136*, 10882–10885.

(68) Asazawa, K.; Kishi, H.; Tanaka, H.; Matsumura, D.; Tamura, K.; Nishihata, Y.; Saputro, A. G.; Nakanishi, H.; Kasai, H.; Artyushkova, K.; Atanassov, P. *J. Phys. Chem. C* **2014**, *118*, 25480–25486.

(69) Zhu, Y.; Zhang, B.; Liu, X.; Wang, D.-W.; Su, D. S. *Angew. Chem., Int. Ed.* **2014**, *53*, 10673–10677.

(70) Zitolo, A.; Goellner, V.; Armel, V.; Sougrati, M.-T.; Mineva, T.; Stievano, L.; Fonda, E.; Jaouen, F. *Nat. Mater.* **2015**, *14*, 937–942.

(71) Jia, Q.; Ramaswamy, N.; Hafiz, H.; Tylus, U.; Strickland, K.; Wu, G.; Barbiellini, B.; Bansil, A.; Holby, E. F.; Zelenay, P.; Mukerjee, S. *ACS Nano* **2015**, *9*, 12496–12505.

(72) Artyushkova, K.; Serov, A.; Rojas-Carbonell, S.; Atanassov, P. *J. Phys. Chem. C* **2015**, *119*, 25917–25928.

(73) Jiang, W.-J.; Gu, L.; Li, L.; Zhang, Y.; Zhang, X.; Zhang, L.-J.; Wang, J.-Q.; Hu, J.-S.; Wei, Z.; Wan, L.-J. *J. Am. Chem. Soc.* **2016**, *138*, 3570–3578.

(74) Joo, S. H.; Park, J. Y.; Tsung, C.-K.; Yamada, Y.; Yang, P.; Somorjai, G. A. *Nat. Mater.* **2009**, *8*, 126–131.

(75) Deng, Y.; Cai, Y.; Sun, Z.; Liu, J.; Liu, C.; Wei, J.; Li, W.; Liu, C.; Wang, Y.; Zhao, D. *J. Am. Chem. Soc.* **2010**, *132*, 8466–8473.

(76) Guerrero-Martínez, A.; Pérez-Juste, J.; Liz-Marzán, L. M. *Adv. Mater.* **2010**, *22*, 1182–1195.

(77) Park, J. C.; Bang, J. U.; Lee, J.; Ko, C. H.; Song, H. *J. Mater. Chem.* **2010**, *20*, 1239–1246.

(78) Zhang, Q.; Lee, I.; Joo, J. B.; Zaera, F.; Yin, Y. *Acc. Chem. Res.* **2013**, *46*, 1816–1824.

(79) Lim, J. T.; Kim, C. S. *J. Appl. Phys.* **2015**, *117*, 17B743.

(80) Lee, M.-S.; Kim, T.; Park, S.-H.; Kim, C.-S.; Choi, Y.-W. *J. Mater. Chem.* **2012**, *22*, 13928–13931.

(81) Kramm, U. I.; Lefèvre, M.; Larouche, N.; Schmeisser, D.; Dodelet, J.-P. *J. Am. Chem. Soc.* **2014**, *136*, 978–985.

(82) McCrory, C. C. L.; Jung, S.; Peters, J. C.; Jaramillo, T. F. *J. Am. Chem. Soc.* **2013**, *135*, 16977–16987.

(83) Kramm, U. I.; Abs-Wurmbach, I.; Herrmann-Geppert, I.; Radnik, J.; Fiechter, S.; Bogdanoff, P. *J. Electrochem. Soc.* **2011**, *158*, B69–B78.

(84) Li, J.; Alsudairi, A.; Ma, Z.-F.; Mukerjee, S.; Jia, Q. *J. Am. Chem. Soc.* **2017**, *139*, 1384–1387.

(85) Mamlouk, M.; Kumar, S. M. S.; Gouerec, P.; Scott, K. *J. Power Sources* **2011**, *196*, 7594–7600.

(86) Rao, C. V.; Ishikawa, Y. *J. Phys. Chem. C* **2012**, *116*, 4340–4346.

(87) He, Q.; Li, Q.; Khene, S.; Ren, X.; López-Suárez, F. E.; Lozano-Castelló, D.; Bueno-López, A.; Wu, G. *J. Phys. Chem. C* **2013**, *117*, 8697–8707.

(88) Ng, J. W. D.; Gorlin, Y.; Nordlund, D.; Jaramillo, T. F. *J. Electrochem. Soc.* **2014**, *167*, D3105–D3112.

(89) Lee, S.; Choun, M.; Ye, Y.; Lee, J.; Mun, Y.; Kang, E.; Hwang, J.; Lee, Y.-H.; Shin, C.-H.; Moon, S.-H.; Kim, S.-K.; Lee, E.; Lee, J. *Angew. Chem., Int. Ed.* **2015**, *54*, 9230–9234.

(90) Kim, O.-H.; Cho, Y.-H.; Chung, D. Y.; Kim, M. J.; Yoo, J. M.; Park, J. E.; Choe, H.; Sung, Y.-E.

Sci. Rep. **2015**, *5*, 8376.

(91)   Chen, C.; Yang, X.-D.; Zhou, Z.-Y.; Lai, Y.-J.; Rauf, M.; Wang, Y.; Pan, J.; Zhuang, L.; Wang, Q.; Wang, Y.-C.; Tian, N.; Zhang, X.-S.; Sun, S.-G. *Chem. Commun.* **2015**, *51*, 17092–17095.

(92)   Artyushkova, K.; Kiefer, B.; Halevi, B.; Knop-Gericke, A.; Schlogl, R.; Atanassov, P. *Chem. Commun.* **2013**, *49*, 2539–2541.

(93)   Kim, J. H.; Sa, Y. J.; Jeong, H. Y.; Joo, S. H. *ACS Appl. Mater. Interfaces* **2017**, *9*, 9567–9575.

(94)   Choi, C. H.; Choi, W. S.; Kasian, O.; Mechler, A. K.; Sougrati, M. T.; Brüller, S.; Strickland, K.; Jia, Q.; Mukerjee, S.; Mayrhofer, K. J. J.; Jaouen, F. *Angew. Chem., Int. Ed.* **2017**, *56*, 8809–8812.

4

IN SITU X-RAY ABSORPTION SPECTROSCOPY STUDY ON OXYGEN REDUCTION AND EVOLUTION REACTIONS CATALYZED BY SIZE-CONTROLLED COBALT OXIDE NANOPARTICLES SUPPORTED ON CARBON NANOTUBES

4.1. INTRODUCTION

Increasing demand for clean energy technologies has attracted great interest in renewable energy conversion and storage systems.[1,2] Bifunctional oxygen electrocatalysts for both oxygen evolution reaction (OER) and oxygen reduction reaction (ORR) are ubiquitous and important in energy devices, such as unitized regenerative fuel cells and metal–air batteries.[3–12] The overall efficiency of these energy devices critically depends on the catalytic activities of bifunctional oxygen electrocatalysts. Due to involvement of the transfer of four electrons in both the OER and ORR, these reactions are energetically demanding and sluggish. As such, noble metal-based materials like IrO_2, RuO_2, and Pt with fast reaction kinetics have been used prevailently as bifunctional oxygen electrocatalysts; however, they are expensive and scarce.[13,14] In this context, cost-effective and earth-abundant transition metal oxides have emerged as a promising class of catalysts.[15–24] In particular, cobalt oxide-based bifunctional electrocatalysts have received attention as economically viable and efficient bifunctional oxygen electrocatalysts.[16–19,22–24]

Identification of the nature of the active species and reaction mechanism is critical for the design of advanced cobalt oxide-based electrocatalyst. Understanding the nanoscale particle size effects can provide important clues. The particle size effects in cobalt (oxide)-based catalysts have been established in some important reactions, including Fischer-Tropsch reaction and CO_2 hydrogenation.[25,26] However, such insights have not yet been gained for bifunctional oxygen electrocatalysis; only a few works on the size dependency for respective OER or ORR have been reported.[27,28] More importantly, an understanding of the size-dependent catalytic activity combined

with *in situ* spectroscopic characterization can further provide more compelling evidence for the relationships between structure (size, shape, and/or composition) and catalytic properties.[29]

In this work, the nanoscale size-dependent structure and catalytic activity of bifunctional electrocatalysts based on cobalt oxide nanoparticles (CoO_x NPs) for both OER and ORR is investigated. CoO_x NPs with four different particle sizes, controlled from 3 to 10 nm, were synthesized and loaded on acid-treated carbon nanotubes (CNTs), yieldng CoO_x/CNTs model catalysts to investigate bifunctional electrocatalysis in alkaline solutions. *In situ* X-ray absorption spectroscopy (XAS) analysis revealed that the phase composition of the size-controlled CoO_x NPs was invariably Co_3O_4 and CoOOH with small amount of $Co(OH)_2$ under electrochemical OER and ORR conditions. This result suggests that Co(III) species are the key elements for the OER, while they appear to be side products generated from the oxidation of Co(II) by peroxide intermediate during the ORR. The CoO_x/CNTs catalysts exhibited increasing OER activity with decreasing NP size, which could be attributed to abundant surface Co(III) species and the large surface area of small CoO_x NPs. In contrast, ORR activity was found not to rely on the size of the CoO_x NPs in the kinetic region; CoO_x NPs mainly played an auxiliary role, promoting the reduction or disproportionation of peroxide generated from the two-electron ORR.

4.2. EXPERIMENTAL METHODS

4.2.1. Synthesis of Size-Controlled CoO_x NPs

CoO_x NPs were synthesized as described in a previously report with some modifications.[26] Standard Schlenk techniques were used, and all manipulations with the cobalt carbonyl precursor were performed in a glove box. First, 73 μL of oleic acid (99%, Sigma-Aldrich) was added in a 100 mL round bottom flask, evacuated for 10 min, and saturated with Ar. Then, 7.5 mL of anhydrous *o*-dichlorobenzene (*o*-DCB, 99%, Sigma-Aldrich) were added. The flask was equipped with a Liebig condenser, volume spacer, and release line to accommodate the large volume of CO, which was produced upon decomposition of the carbonyl precursor. With vigorous stirring, the mixture was heated to a desired temperature (164, 168, 176, or 182 °C) from RT at a heating rate of 5 °C min^{-1} under an Ar atmosphere. After temperature stabilization, 1.5 mL of 0.5 M $Co_2(CO)_8$ (Sigma-Aldrich) dissolved in *o*-DCB were quickly injected into the hot solution. The transparent and brownish solution immediately turned black, indicating the formation of NPs. This colloidal suspension was aged for 20 min and then cooled in a flow of air. To separate the CoO_x NPs 5 mL of *o*-DCB and 25 mL of 2-propanol (99%, Sigma-Aldrich) were added to the suspension, followed by centrifugation at 8000 rpm for 15 min. The supernatant was decanted, and the precipitate was dispersed in chloroform (99.5%,

Samchun chemical).

4.2.2. Preparation of CoO$_x$/CNTs

Before the CoO$_x$ NPs were supported onto the CNTs, as-received CNTs were acid-treated to remove metallic impurities and to functionalize the CNT for better adhesion of the NPs. 2.5 g of the pristine multi-walled CNTs (MR 99, Carbon Nano-material Technology Co.) was mixed with 380 g of 6 M HCl (diluted from 35–37% HCl, Samchun chemical), and the mixture was stirred at 80 °C for 12 h. The suspension was filtered, washed with a large amount of DI water until the pH of the filtrate reached ~7, and dried at 60 °C. The HCl-treated CNTs were subsequently treated with 390 g of 6 M HNO$_3$ (diluted from 60% HNO$_3$, Samchun chemical) in the same manner. Then, the CoO$_x$ NPs were supported on CNTs as follows. First, 350 mg of the acid-treated CNTs were dispersed in 50 mL of chloroform in a 100 mL Erlenmeyer flask. After stirring for 15 min in the closed flask, 38.9 mg of the as-prepared CoO$_x$ NPs dispersed in chloroform (corresponding to the target loading of 10 wt% of CoO$_x$), was added dropwise to the solution. Subsequent sonication in ice-cold water for 3 h led to the homogeneous dispersion of CoO$_x$ NPs on CNTs. The product was separated by centrifugation and decantation, and dried at 60 °C. Finally, the surfactants (i.e., oleic acid) surrounding the NPs were removed following a previously reported method.[30] The dried CoO$_x$/CNTs was annealed at 185 °C for 5 h under air (temperature ramping rate: 1.4 °C min^{-1}). For fair comparison, the acid-treated CNTs without CoO$_x$ were also annealed and used for further characterizations.

4.2.3. Synthesis of Bulk-CoOOH

Bulk-CoOOH was synthesized for the use as a reference material for the XAS.[31] First, Co(OH)$_2$ powder (95%, Sigma-Aldrich) was added to 40 mL of DI water. 10 mL of 8 M NaOH (diluted from 98% NaOH, Samchun chemical) was added dropwise, and subsequently 4 mL of H$_2$O$_2$ (30%, Sigma-Aldrich) was added at once with vigorous stirring. This reaction explosively produces O$_2$ gas. The mixture was stirred at 45 °C for 28 h. The suspension was filtered, washed with DI water several times, and dried at 60 °C. The resulting CoOOH was found to be phase-pure with large crystallite size as revealed by XRD (**Figure 4.1**)
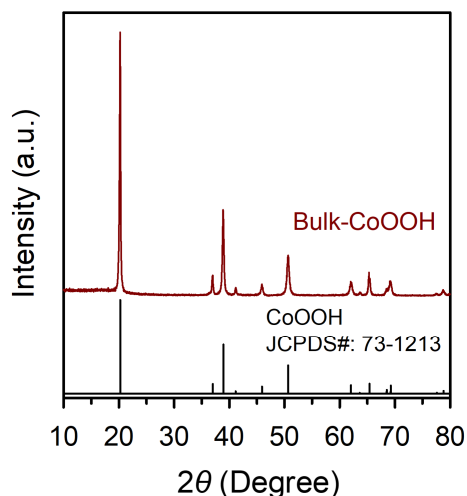
Figure 4.1. XRD pattern of the synthesized bulk-CoOOH and a standard CoOOH.

4.2.4. Characterization Methods

High-resolution transmission electron microscopy (HR-TEM) images were taken on a JEOL JEM-2100 electron microscope at an acceleration voltage of 200 kV. Atomic-resolution TEM (AR-TEM) images were taken with a low-voltage spherical aberration-corrected TEM (FEI Titan[3] G2 60-300 with an image Cs corrector) with an acceleration voltage of 80 kV. X-ray powder diffraction (XRD) patterns were obtained with a high-power X-ray diffractometer (D/MAX2500/PC, Rigaku) equipped with Cu Kα radiation, and operated at 40 kV and 200 mA. Wide-angle XRD patterns were measured in a 2θ range from 10° to 80° at a scan rate of 4° min^{-1}. The Co content in the catalysts was determined using an inductively coupled plasma optical emission spectrometry (ICP-OES) analyzer (700-ES, Varian). The ICP-OES analysis results are summarized in **Table 4.1**.

Table 4.1. Co contents in the CoO$_x$/CNTs analyzed by ICP-OES.

Sample	Co contents (%)
CoO$_x$(4.3)/CNTs	11.9
CoO$_x$(6.3)/CNTs	11.5
CoO$_x$(7.5)/CNTs	12.1
CoO$_x$(9.5)/CNTs	12.6

4.2.5. XAS Experiments

XAS experiments were conducted on the beamlines 6D and 10C of the Pohang Accelerator Laboratory (PAL) in South Korea with a beam energy and current of 3 GeV and 300 mA, respectively. X-ray photon energy was filtered with a Si(1 1 1) double-crystal monochromator, which was detuned by around 15% and 30% at the 6D and 10C beamlines, respectively, to remove high-order harmonics. *In situ* XAS spectra were obtained by using a home-made spectroelectrochemical cell in fluorescence mode (**Figure 4.2**). Catalyst ink (described in *Section 4.2.6*) was deposited and dried on a piece of carbon fiber paper. The catalyst film was attached on the window of the cell using a Kapton tape, while the catalyst layer was facing inward of the cell to be contacted with the electrolyte (0.1 M KOH). *In situ* XAS measurement was firstly conducted at the open circuit voltage (OCV), and the subsequent XAS scan was performed after applying ORR (0.6 V *vs* RHE, *iR*-corrected) or OER (1.8 V) potential for 1 h in order to give enough time for phase transformation. Background removal and normalization of the spectra were carried out by using IFEFFIT (Athena) software.[32]
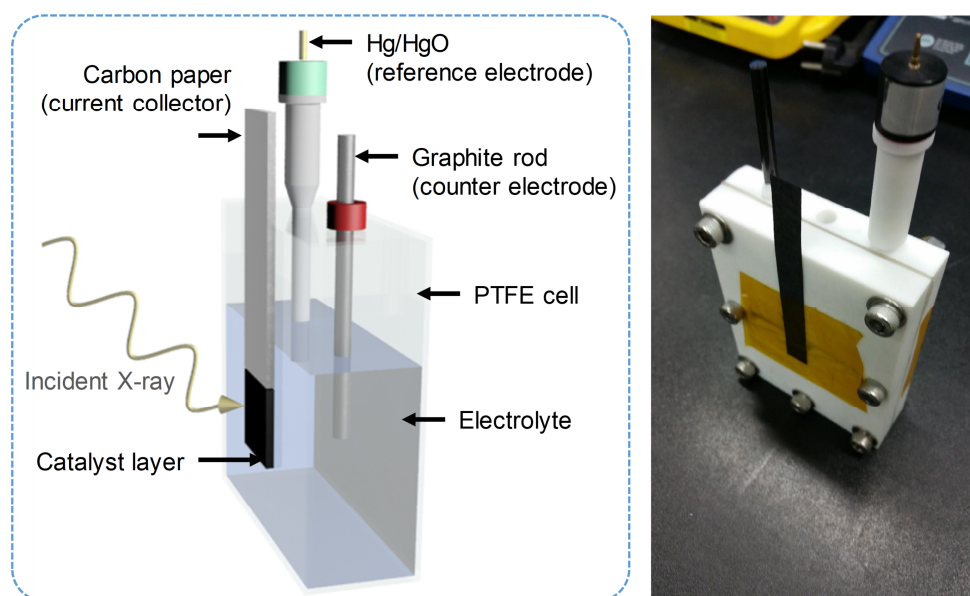
Figure 4.2. Schematic illustration and photograph of the home-made spectroelectrochemical cell and experimental setup.

4.2.6. Electrochemical Characterizations

Electrochemical characterizations of the catalysts were performed using an IviumStat electrochemical analyzer at RT and atmospheric pressure, using a three-electrode system. A graphite counter electrode and an Hg/HgO reference electrode (1 M KOH filling solution) were used. All potentials in this report were converted to the reversible hydrogen electrode (RHE) scale (experimental details in *Section 3.2.5*).

A rotating ring-disk electrode (RRDE, ALS) comprised of a glassy carbon (GC) disk (4 mm in diameter) and a Pt ring was used as a working electrode. The RRDE was polished with a 1.0 μm alumina suspension and then with a 0.3 μm suspension to generate a mirror finish before every use. The catalyst ink was prepared by mixing catalyst (7.5 mg), neutralized Nafion (0.2 mL), DI water (0.1 mL), and absolute ethanol (0.9 mL) and by sonicating for at least 1 h. Neutralized Nafion was prepared by mixing 0.1 M NaOH (diluted from 99.99% NaOH, Sigma-Aldrich) and Nafion (5 wt%, Sigma-Aldrich) in a ratio of 1:2 (v:v), considering the proton concentration of Nafion (~0.05 M), to minimize any transformation of the catalyst during the ink preparation.[33] Next, 3 μL of the catalyst ink were pipetted with a micro-syringe (Hamilton) and deposited onto the GC electrode and dried at 70 °C for 2 min. The catalyst loading was 0.15 mg cm^{-2}.

To investigate the redox properties of the samples, cyclic voltammetry (CV) from 0.05 to 1.50 V (*vs* RHE) was conducted in N$_2$-saturated 1 M KOH at a scan rate of 20 mV s^{-1}. Before the activity measurement, electrochemical impedance spectroscopy (EIS) was performed around at the OCV with a potential amplitude of 10 mV from 10000 to 1 Hz. Series resistance was determined at a high frequency intercept on the *x*-axis (real part of the impedance) of the EIS spectra, which was used to correct the *iR*-drop. The OER activity was obtained from 10 scans of CV in the range of 1.2 to 1.8 V (*vs* RHE) at a scan rate of 20 mV s^{-1} with an electrode rotation at 1,600 rpm to efficiently remove evolved O$_2$. The cathodic and anodic currents of the 10th CV were averaged. Linear sweep voltammetry (LSV) was performed to obtain the ORR polarization curves by sweeping the potential from 1.1 to 0.2 V (*vs* RHE) at a scan rate of 5 mV s^{-1} in O$_2$-saturated 0.1 M KOH with O$_2$ bubbling at a rotating speed of 1,600 rpm. The OER/ORR measurements were independently repeated three times, and the averaged and *iR*-compensated (100%) data are presented.

For the evaluation of the kinetics for the ORR, the kinetic current was extracted from the following equation

$$\frac{1}{j} = \frac{1}{j_k} + \frac{1}{j_d}$$

where j, j_k, and j_l represent the measured current density, the kinetic current density, and diffusion-limited current density, respectively (normalized by GC electrode area).

The logarithmic plot of the kinetic current density (the measured current density in the case of the OER) versus the overpotential gives a linear Tafel plot

$$\eta = -b\log j_k + b\log j_0$$

where η, b, and j_0 indicate the applied overpotential, the Tafel slope, and the exchange current density,

respectively.

Four-electron selectivity of the CoO$_x$/CNTs was analyzed by RRDE technique and calculated using a given equation

$$n = \frac{4}{1 + \dfrac{i_r}{N \times i_d}}$$

where n, N, i_r, and i_d stand for the electron transfer number (selectivity), the collection efficiency (0.40, provided by the manufacturer) indicate the applied overpotential, the Tafel slope, and the exchange current,

4.3. RESULTS AND DISCUSSION

4.3.1. Synthesis and Characterization of CoO$_x$/CNTs

The preparation of the CoO$_x$/CNTs model catalysts involved (i) the colloidal synthesis of CoO$_x$ NPs with tuned particle sizes,[26] (ii) the attachment of prepared NPs to acid-treated CNTs, and (iii) mild annealing to remove residual organic surfactants around the CoO$_x$ NPs. Monodisperse, size controlled CoO$_x$ NPs with average sizes of 3.0, 6.2, 7.4, and 9.1 nm were obtained at different synthesis temperatures (**Figures 4.3a–d,i**). HR-TEM images and the corresponding fast Fourier transform (FFT) patterns (**Figures 4.3e–h**) demonstrated that all the as-prepared NPs consisted of the crystalline CoO phase (cubic, a=4.22 Å).

CoO$_x$ NPs were then attached onto the acid-treated CNTs with ultra-sonication, followed by mild thermal annealing. We emphasize the use of undoped CNTs rather than N-doped CNTs as the support material and exclusion of N-containing chemicals during the preparation, because the presence of both CoO$_x$ and nitrogen synergistically enhances catalytic activity *via* the formation of Co–N bonding that can inhibit the extraction of catalytic activity from CoO$_x$ NPs.[16,34,35] The content of Co in the CoO$_x$/CNTs was around 12 wt%, as confirmed by ICP-OES analysis (**Table 4.1**). TEM images of the CoO$_x$/CNTs (**Figures 4.4a–d**) indicate that the CoO$_x$ NPs were successfully attached and uniformly distributed on the CNTs. The average particle sizes of the CoO$_x$ NPs in the CoO$_x$/CNTs were 4.3, 6.3, 7.5, and 9.5 nm (**Figure 4.4m**). The size of the smallest CoO$_x$ NPs increased from that of the as-prepared CoO$_x$ NPs (3.0 nm), due to progressive phase transformation from metallic Co to CoO/Co$_3$O$_4$ during the annealing step, and due to the smaller density of CoO/Co$_3$O$_4$ than that of Co phase. Hereafter, these CoO$_x$/CNTs are denoted as CoO$_x$(4.3)/CNTs, CoO$_x$(6.3)/CNTs, CoO$_x$(7.5)/CNTs, and CoO$_x$(9.5)/CNTs. The atomic-resolution TEM (AR-TEM) images and FFT

patterns (**Figures 4.4e–l**) show that the smallest NPs have crystalline spinel structures of Co_3O_4, indicating the phase change from CoO to Co_3O_4 after annealing, whereas the other NPs maintain the initial CoO crystal structure.
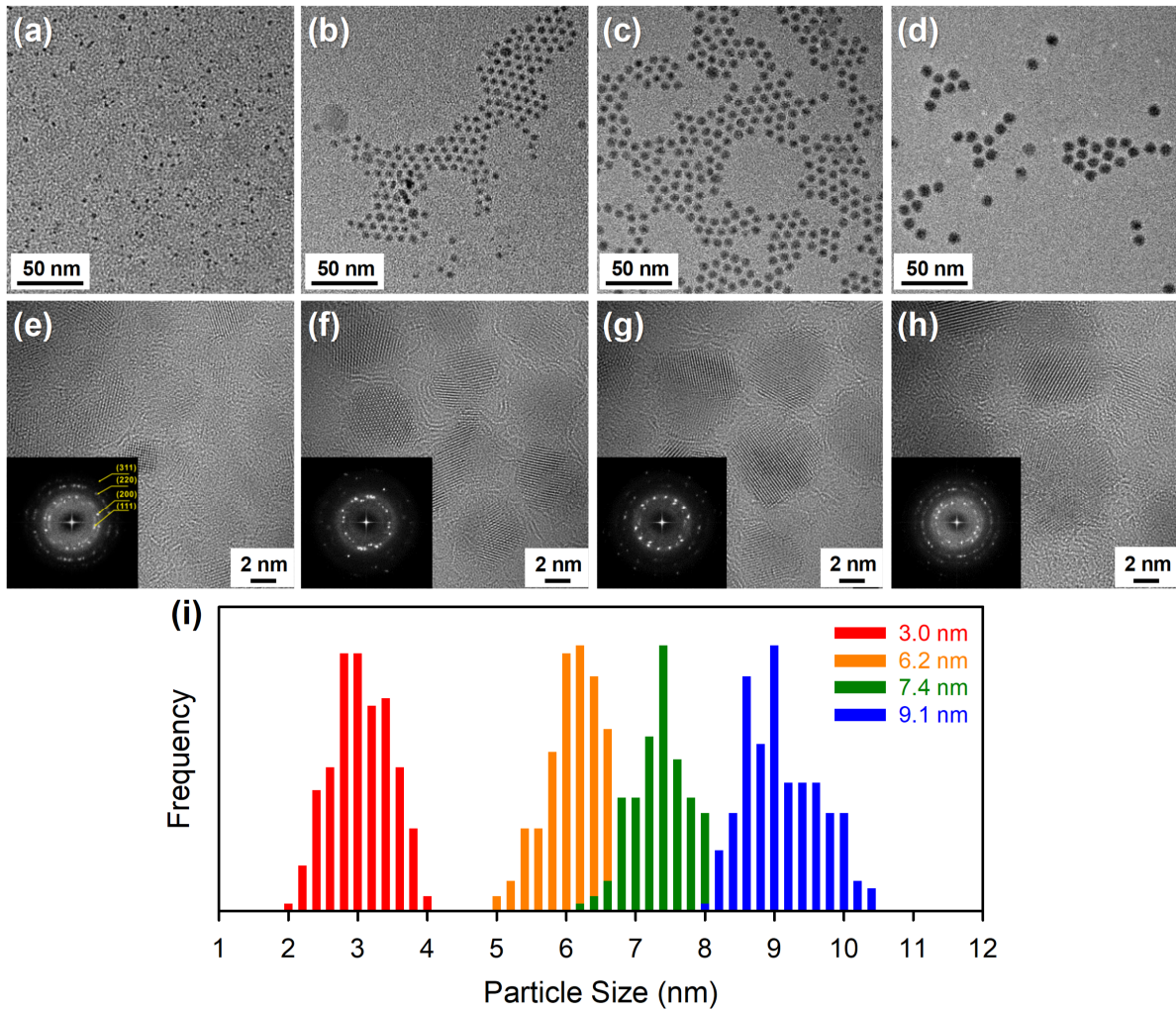
Figure 4.3. (a–d) TEM images of as-prepared (a) 3.0 nm CoO_x, (b) 6.2 nm CoO_x, (c) 7.4 nm CoO_x, and (d) 9.4 nm CoO_x NPs. (e–h) HR-TEM images and corresponding FFT patterns of as-prepared (a) 3.0 nm CoO_x, (b) 6.2 nm CoO_x, (c) 7.4 nm CoO_x, and (d) 9.4 nm CoO_x NPs. (i) Histograms of the particle size distribution of CoO_x NPs.
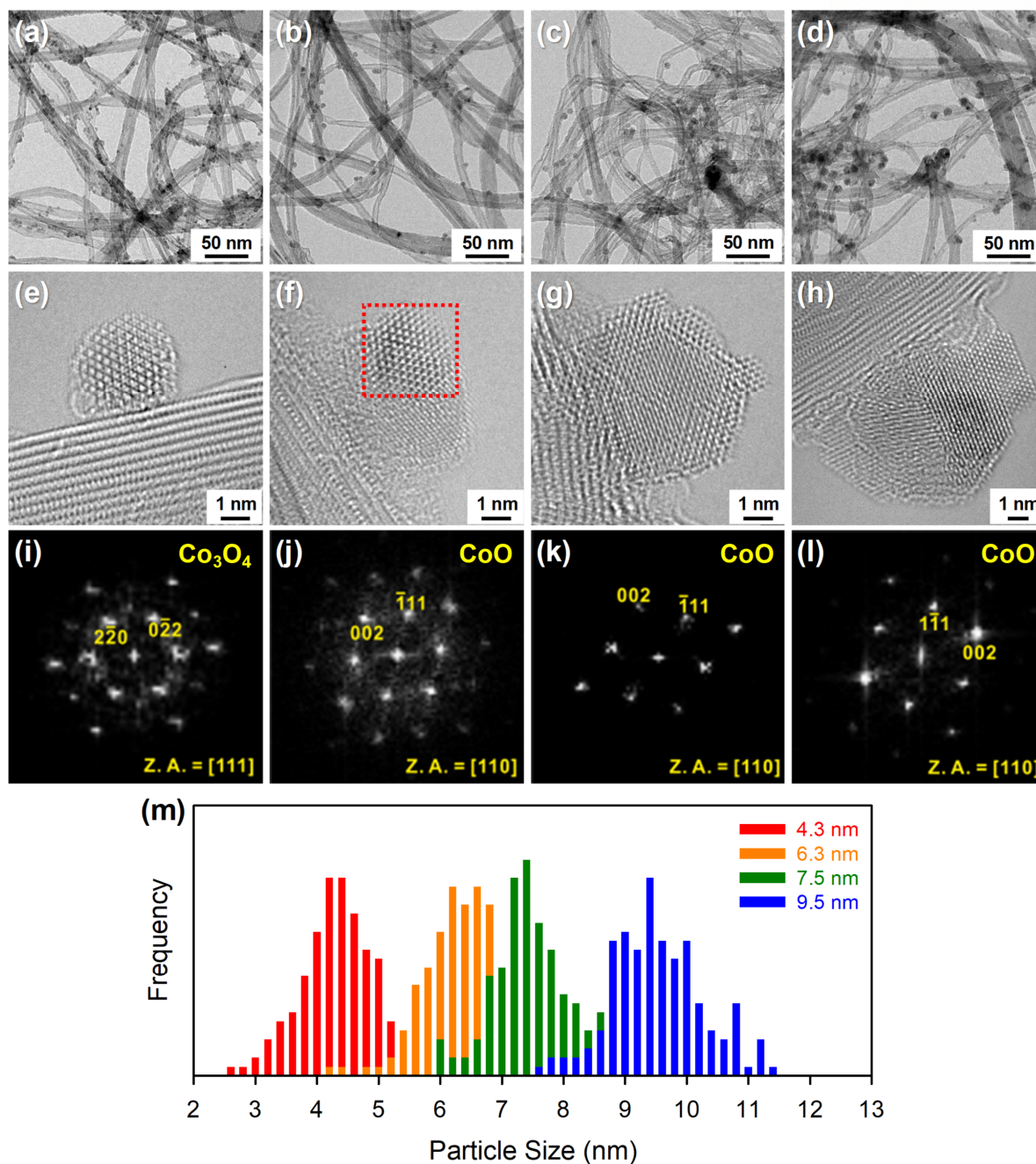
Figure 4.4. (a–d) TEM images of (a) CoO$_x$(4.3)/CNTs, (b) CoO$_x$(6.3)/CNTs, (c) CoO$_x$(7.5)/CNTs, and (d) CoO$_x$(9.5)/CNTs. (e–h) AR-TEM images and (i–l) corresponding FFT patterns of (e,i) CoO$_x$(4.3)/CNTs, (f,j) CoO$_x$(6.3)/CNTs, (g,k) CoO$_x$(7.5)/CNTs, and (h,l) CoO$_x$(9.5)/CNTs. The FFT pattern of the CoO$_x$(6.3)/CNTs was obtained in the selected area indicated by the dotted red box. (m) Histograms of the particle size distribution of CoO$_x$ NPs on the CoO$_x$/CNTs.

XRD patterns (**Figure 4.5a**) of all the samples show a common diffraction peak at $2\theta = 25.7°$ which appeared for the CNTs. The diffraction peaks at $2\theta = 36.5°$, $42.8°$, and $61.5°$ are commensurate with those of the CoO standard for CoO$_x$(6.3)/CNTs, CoO$_x$(7.5)/CNTs, and CoO$_x$(9.5)/CNTs. In the

case of the $CoO_x(4.3)$/CNTs, different diffraction peaks ($2\theta = 31.8°$, $36.8°$, $44.9°$, $59.4°$, and $65.2°$) are observed and well match those of spinel Co_3O_4 standard pattern. Radial distribution function (RDF) from Fourier transform of k^3-weighted extended X-ray absorption fine structure (EXAFS) spectrum (**Figure 4.5b**) of the $CoO_x(4.3)$/CNTs exhibits the major peaks at 1.54, 2.48, and 3.06 Å, corresponding to the Co–O, Co_{oct}–Co_{oct}, and Co_{tet}–Co_{tet}/Co_{tet}–Co_{oct} pairs in Co_3O_4, respectively.[22] The other three samples show the main RDF peaks at 1.75 and 2.67 Å, which originate from CoO crystal. As revealed by TEM, XRD, and EXAFS analyses, the $CoO_x(4.3)$/CNTs are mainly composed of Co_3O_4 nanocrystals, while the other three samples consisted of CoO nanocrystals.
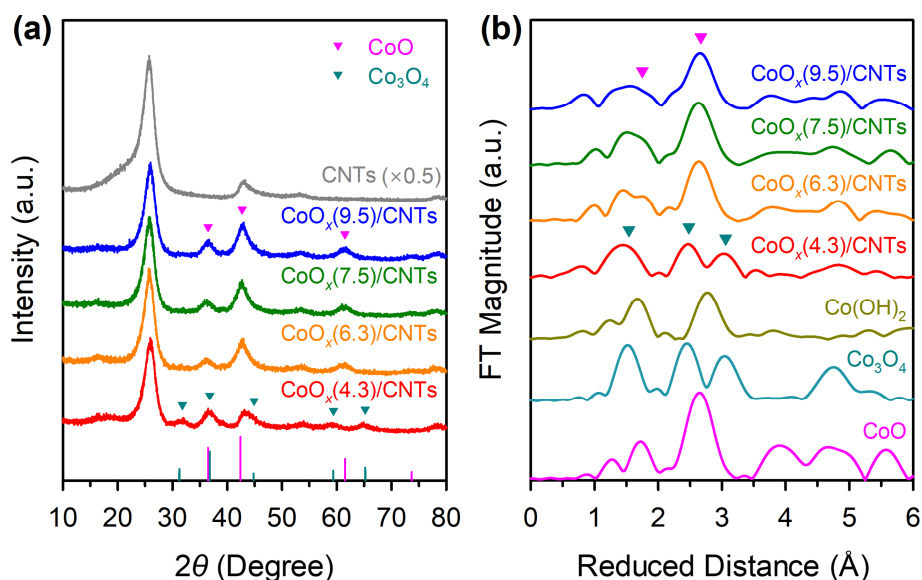
Figure 4.5. (a) XRD patterns of the CoO_x/CNTs and CNTs. Those of standard CoO (JCPDS#: 9-0402) and Co_3O_4 (JCPDS#: 9-0418) are shown in pink and cyan lines at the bottom. (b) RDFs of k^3-weighted Co K-edge *ex situ* EXAFS spectra of CoO_x/CNTs and bulk-CoO, Co_3O_4, and $Co(OH)_2$.

4.3.2. In Situ XAS Study

The structural change of the CoO_x NPs under the OER and ORR conditions was scrutinized using *in situ* electrochemical XAS with a home-made spectroelectrochemical cell (**Figure 4.2**). To understand the quantitative phase composition under different electrochemical conditions, we analyzed the *in situ* XANES spectra by linear combination fitting (LCF) (**Figure 4.6**).
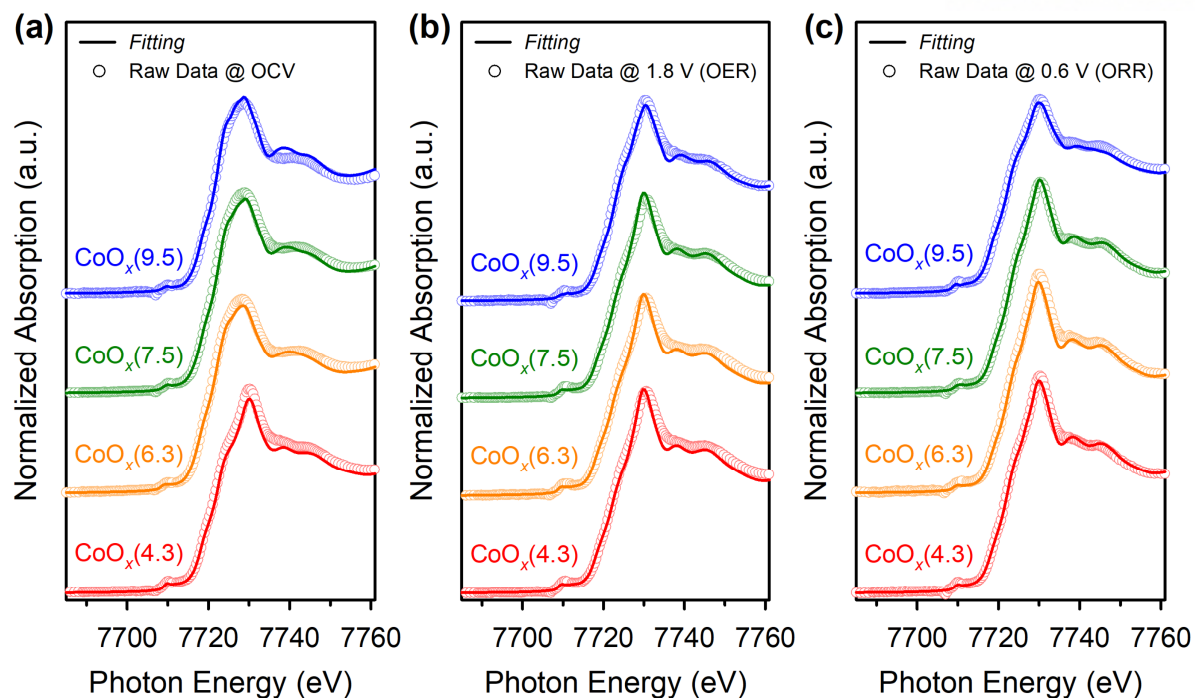
Figure 4.6. Raw *in situ* XANES spectra of the CoO$_x$/CNTs and the LCF spectra fitted using the XANES spectra of bulk-CoO, Co(OH)$_2$, Co$_3$O$_4$, and CoOOH obtained in 0.1 M KOH (a) without applied potential, (b) at 1.8 V (*vs* RHE), and (c) at 0.6 V.

Table 4.2. Phase composition and average Co valence of CoO$_x$/CNTs under applied potential or open circuit voltage (OCV) obtained by linear combination fitting analysis of XANES spectra.

Sample	Conditions	Co$_3$O$_4$	CoOOH	CoO	Co(OH)$_2$	Average Co Oxidation state
CoO$_x$(4.3)/CNTs	OCV	0.61	0.20	0.00	0.19	2.6
	1.8 V	0.55	0.42	0.01	0.02	2.8
	0.6 V	0.26	0.56	0.00	0.18	2.8
CoO$_x$(6.3)/CNTs	OCV	0.32	0.15	0.18	0.35	2.4
	1.8 V	0.54	0.41	0.03	0.02	2.8
	0.6 V	0.20	0.65	0.00	0.17	2.8
CoO$_x$(7.5)/CNTs	OCV	0.19	0.30	0.09	0.43	2.4
	1.8 V	0.44	0.50	0.00	0.06	2.8
	0.6 V	0.44	0.50	0.00	0.06	2.8
CoO$_x$(9.5)/CNTs	OCV	0.00	0.47	0.00	0.53	2.5
	1.8 V	0.29	0.49	0.00	0.22	2.7
	0.6 V	0.57	0.22	0.07	0.14	2.6

Figure 4.7a shows *in situ* Co K-edge X-ray absorption near edge spectroscopy (XANES) spectra of the CoO_x/CNTs, measured in 0.1 M KOH electrolyte. Under the OER potential (1.8 V *vs* RHE), all the samples exhibited similar XANES spectra resembling that of Co_3O_4 and CoOOH, regardless of the CoO_x NP size (dark-colored dotted lines). The detailed information about phase compositions and average Co oxidation states calculated by the relative amount of each phase is summarized in **Table 4.2** above. We found that when the OER potential was applied, the average oxidation state of Co increased for all the samples accompanied with the increased amount of CoOOH phase, which is believed as the active species for the OER. Under OER potential, the increment in the amount of Co_3O_4 in CoO_x(6.3)/CNTs, CoO_x(7.3)/CNTs, and CoO_x(9.5)/CNTs was also observed. For the CoO_x(4.3)/CNTs, large amount of Co_3O_4 was already present at OCV (61%) and a part of Co_3O_4 was transformed to CoOOH, leading to the rise in the Co oxidation state. The *in situ* XANES analysis indicates that the phase transformation occurred from Co_3O_4 and/or CoO to Co_3O_4/CoOOH mixed phase under the OER conditions. We observed the partial phase change from CoO to Co_3O_4 after the OER by an HR-TEM image of the CoO_x(9.5)/CNTs after the OER (**Figure 4.7c**).
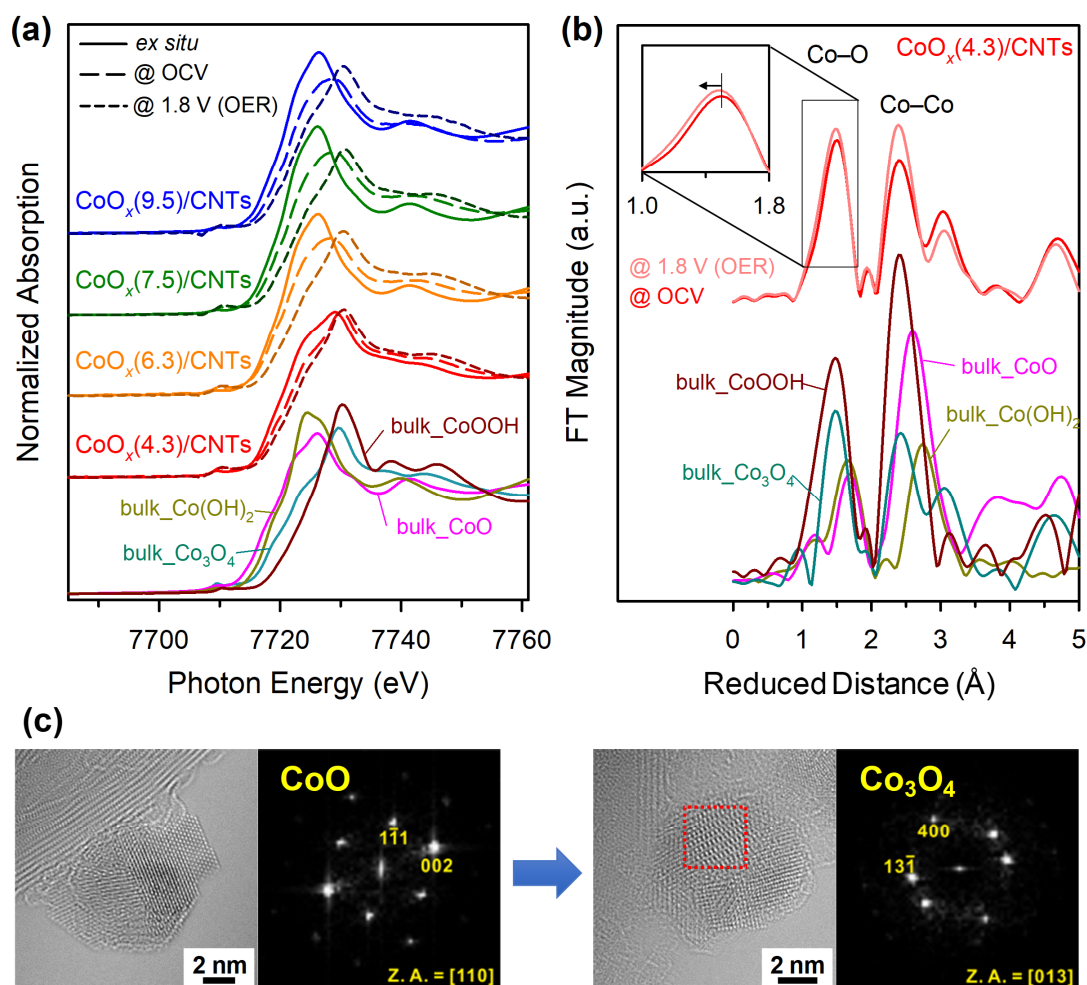
Figure 4.7. *In situ* XANES analyses under the OER conditions. (a) *Ex situ* and *in situ* XANES spectra of the CoO_x/CNTs obtained in 0.1 M KOH at OCV and 1.8 V (vs RHE). (b) Comparison of RDFs of

the *in situ* EXAFS spectra of the CoO_x(4.3)/CNTs at OCV and 1.8 V. Inset graph shows the enlarged RDFs. (c) AR-TEM images and the corresponding FFT patterns of CoO_x(9.5)/CNTs before and after the OER durability test, showing the phase transition from CoO to Co_3O_4.

Next, the change in the local environment was further observed by *in situ* EXAFS of the CoO_x(4.3)/CNTs (**Figure 4.7b**). The RDF under the OER potential compared to that under OCV shows three major changes. First, a slight shrinkage in the Co–O bond (~0.02 ± 0.01 Å decrease obtained by EXAFS first-shell fitting, the results not shown here) was observed under the OER potential for CoO_x(4.3)/CNTs when compared to that under OCV (inset of **Figure 4.7b**). This is an indication of increase in the oxidation state,[36] due to the transformation from Co_3O_4 to CoOOH in our case. Second, the RDF peak intensities for Co–O and Co–Co increased, which correspond to the increase in the amount of adjacent di-μ-oxo bridged CoO_6 octahedra (or edge-sharing octahedra). The edge-sharing octahedra is the structural feature of CoOOH,[37] which has been identified as active phase for OER.[38,39] Finally, under OER potential, the third major RDF peak intensity at 3.04 Å decreased and the fourth major peak at 4.69 Å was negatively shifted, which indicate the diminishment of Co_3O_4 phase as well as the evolution of CoOOH-like peaks at the OER potential. From these observations, we concluded that the phase of the CoO_x NPs changed into CoOOH under OER conditions. We note that CoOOH is a thermodynamically stable phase under oxidizing potentials.[40–42] It was found that the oxidation of the CoO_x NPs occurred even at the OCV, as revealed by significant changes from *ex situ* XANES spectra (solid curves in **Figure 4.7a**) to *in situ* XANES spectra at the OCV (long dashed curves in **Figure 4.7a**). We attributed it to the intermediate range of the OCV (0.9–1.1 V *vs* RHE), which is between the ORR and OER potentials. This phase transformation under non-electrocatalytic condition is beyond of the scope of this work and is subject to detailed investigation.

When the XANES spectra were measured under the ORR potential (0.6 V *vs* RHE), all the CoO_x/CNTs samples exhibited Co_3O_4/CoOOH-like XANES spectra, similar to the results of the XANES spectra taken under the OER potential, indicating the evolution of the Co(III) species during the ORR (**Figure 4.8a**). To access more detailed information, we scrutinized the XANES data with LCF analyses. The LCF analysis of the *in situ* XANES at 0.6 V revealed that the CoO_x NPs exist in Co_3O_4 and CoOOH phases with a small amount $Co(OH)_2$ in all samples (**Table 4.2**). The detailed numerical analysis reveals that with increased CoO_x size the portion of Co_3O_4 increases whereas that of CoOOH decreased. The comparison of average oxidation state indicated a slightly lower oxidation state of the CoO_x(9.5)/CNTs than that of the other CoO_x/CNTs samples, perhaps because of low surface fraction of the CoO_x NPs which can participate to phase transformation (**Table 4.2**).

The above XANES results under ORR potential could be further substantiated by *in situ*

EXAFS results, which also identified Co_3O_4 and CoOOH phases as major species (**Figure 4.8b**). In the RDFs of the *in situ* EXAFS spectra at 0.6 V, the first two peaks, corresponding to Co–O and Co–Co interatomic distances, appeared for all the CoO_x/CNTs. The other peaks at around 3.1 and 4.5 Å were also observed, which are known to originate from both Co_3O_4 and CoOOH phases (indicated by dashed lines in **Figure 4.8b**). The similar peak intensities between the samples except for the $CoO_x(9.5)$/CNTs indicate almost identical local structure at the ORR potential. The different structural properties of the $CoO_x(9.5)$/CNTs could be attributed to a lower portion of CoOOH and larger amount of Co_3O_4 comprising the $CoO_x(9.5)$/CNTs than the other samples, as evidenced by LCF analysis (**Table 4.2**).

Figure 4.8. *In situ* Co K-edge XANES analyses under the ORR conditions. (a) *Ex situ* and *in situ* XANES spectra of the CoO_x/CNTs obtained in 0.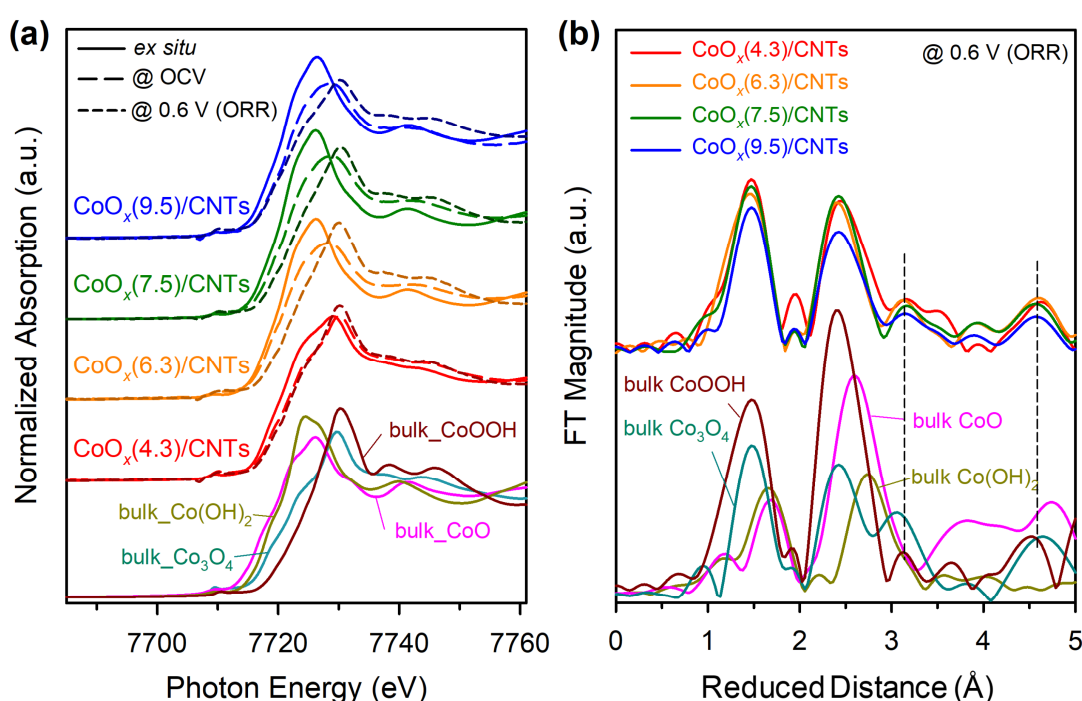1 M KOH at OCV and 0.6 V (vs RHE). (b) Comparison of RDFs of the *in situ* EXAFS spectra of the CoO_x/CNTs at OCV and 0.6 V.

When the applied potential was changed from OCV to the ORR potential (0.6 V), the average oxidation state increased from +2.5 to +2.8 (**Table 4.2**). The LCF analysis results indicate that Co(II) and Co(III) species were present in a ratio of around 1:1 at OCV, and Co(III) became the major species under the ORR conditions. Some previous works consistently suggested that Co(II) on CoO_x is relevant to catalytically active species for the ORR.[43–45] In another early work, theoretical calculations suggested that the ORR on CoOOH is initiated over Co(II) site followed by oxidation of the Co(II) to Co(III) species, which return to the Co(II) species for the next catalytic turnover.[46] However, our *in situ* XAS result could not confirmatively conclude that the Co(III) species evolved at

0.6 V represents the catalytic intermediate in the ORR. As discussed in the electrochemical analysis below, in the CoO_x/CNTs, O_2 is initially reduced to peroxide catalyzed predominantly by the CNTs, and subsequently the CoO_x NPs disproportionate the peroxide. The peroxide intermediate likely oxidizes the initial Co(II) species to Co(III) species concomitant to the peroxide disproportionation.

4.3.3. Electrochemical Redox Behavior by CV

Next, the redox behavior of the samples was assessed *via* CV in N_2-saturated 1 M KOH (**Figures 4.9** and **4.10**). The CV curves show the oxidation peaks **A**, **B**, and **C**, which could be attributed to the oxidation of Co(II) to Co(III), the phase transition from Co_3O_4 to CoOOH, and the oxidation of Co(III) to Co(IV), respectively.[41,45,47] During five CV scans of the CoO_x/CNTs, the gradual decrease of anodic peak **B** and nearly constant peak **C** was observed, indicating an irreversible transition of surface Co_3O_4 to CoOOH and the reversible transition of Co(III) to Co(IV), respectively. Frei and co-workers reported that Co(III) species act as an initiator for the OER process.[38] Stahl and co-workers suggested that the key process in the OER is related to the reversible interconversion between Co(III) and Co(IV).[48] The reversible redox transition between Co(III) and Co(IV) in the CoO_x/CNTs was also observed by the presence of anodic peak **C** in consecutive CV scans (**Figure 4.9**), which is consistent with these previous works.

Significantly, in the first CV curves, a negative shift of the oxidation peak **B** is observed with increased size of the CoO_x NPs (**Figure 4.10**). The result indicates that the smaller NPs contain larger amount of Co(III) species. As CoOOH is considered to be an important active initiator for the OER, a better OER activity of the smaller NPs is expected. However, the CV results are not well correlated to the *in situ* XAS results because the *in situ* XAS spectra were taken after applying potential for 1 h, which could provide sufficient time for complete phase transformation from Co_3O_4/CoO to CoOOH/Co_3O_4 in the CoO_x NPs. This pre-conditioning could lead to the results that the CoO_x NPs mainly consisted of Co_3O_4/CoOOH regardless of their particle sizes (**Table 4.2**). Hence, the experimental conditions for *in situ* XAS could not reflect the initial oxidation state of Co of the CoO_x/CNTs. In contrast, under the potentiodynamic condition of the CV scans, the step-by-step transitions of oxidation states in CoO_x NPs are detected.
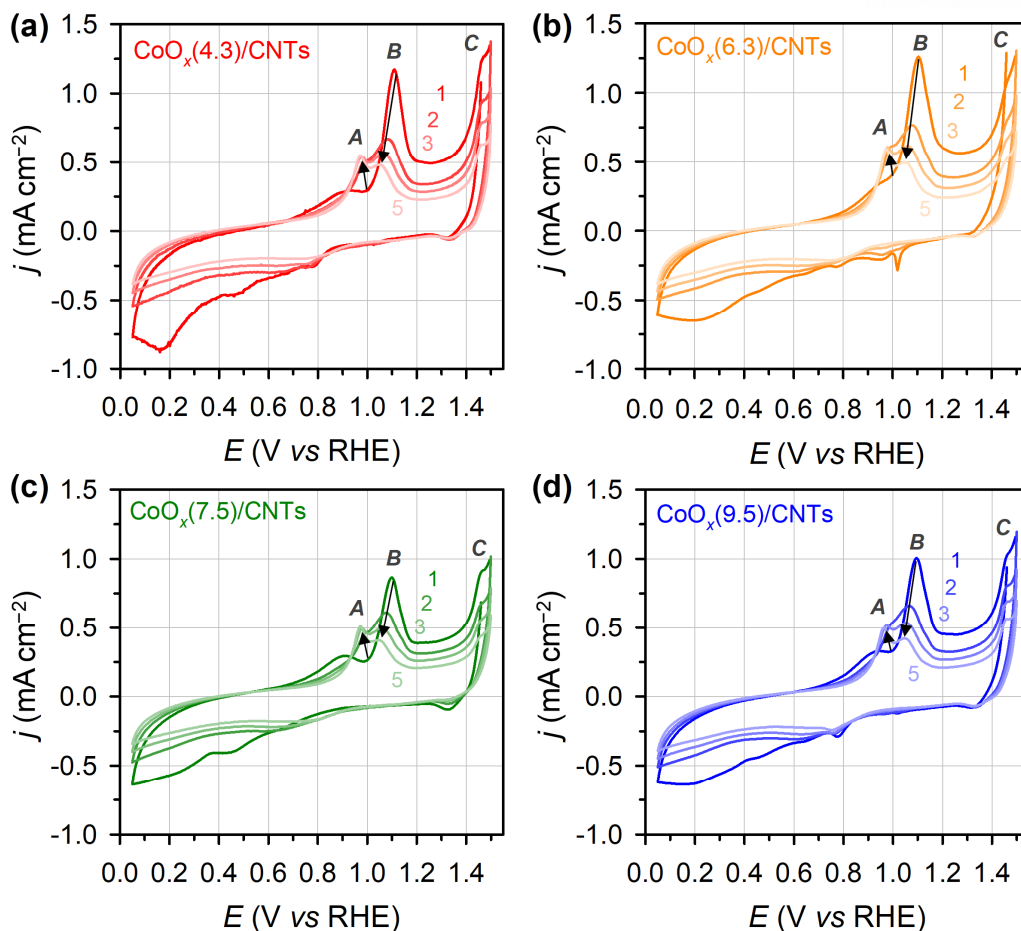
Figure 4.9. (a–d) Five CV scans for (a) $CoO_x(4.3)$/CNTs, (b) $CoO_x(6.3)$/CNTs, (c) $CoO_x(7.5)$/CNTs, and (d) $CoO_x(9.5)$/CNTs measured in N_2-saturated 1 M KOH at a scan rate of 20 mV s^{-1}.
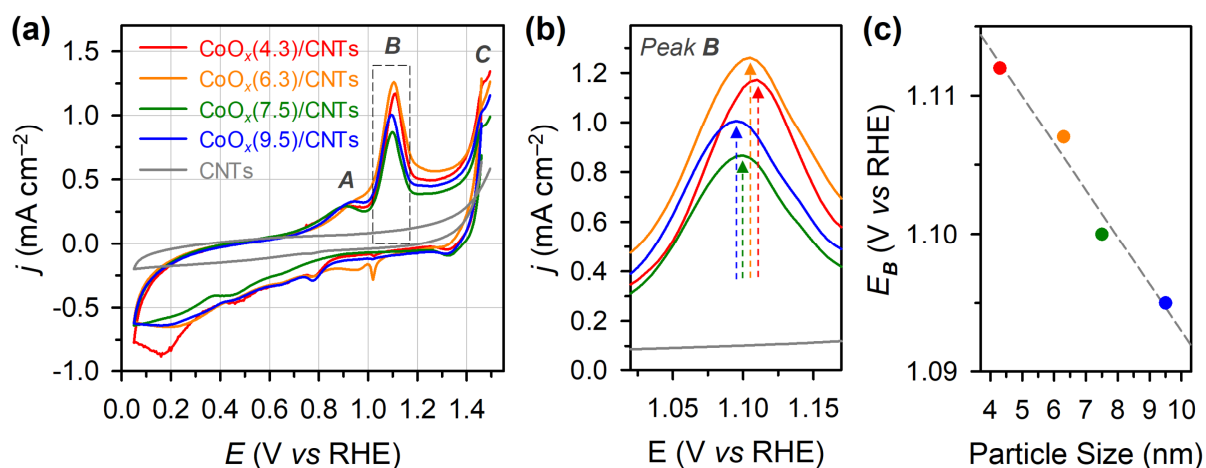
Figure 4.10. (a) The first scan of CV for the CoO_x/CNTs. (b) The enlarged CV around the oxidation peak **B**. (c) The potentials where the peak **B** appears plotted versus the particle sizes of CoO_x NPs.

4.3.4. Size-Dependent ORR and OER Activities

Electrocatalytic OER and ORR activities of the CoO_x/CNTs were measured using RRDE in 0.1 M KOH (**Figure 4.11**). The OER activities increased with decreasing NP size; the potentials required to deliver the current density of 10 mA cm^{-2} were 1.62, 1.64, 1.65, and 1.68 V (*vs* RHE) for the CoO_x(4.3)/CNTs, CoO_x(6.3)/CNTs, CoO_x(7.5)/CNTs, and CoO_x(9.5)/CNTs, respectively (**Figure 4.11a**). The greater OER activities in smaller CoO_x NPs were likely attributed to the large surface areas and the abundant Co(III) species as confirmed by the CV (**Figure 4.10**).[40,48] Tafel slopes were 69, 69, 73, and 80 mV dec^{-1} for the CoO_x(4.3)/CNTs, CoO_x(6.3)/CNTs, CoO_x(7.5)/CNTs, and CoO_x(9.5)/CNTs, respectively (**Figure 4.11b**). A smaller Tafel slope for the smaller CoO_x catalyst indicates more favorable reaction kinetics. In CoO_x-based OER catalysts, high oxidation state Co(IV) centers have been suggested to play a critical role in catalyzing the OER.[40,41,49,50] The Co(IV) species arise from the oxidation of Co(III) with increased potential, as evidenced by the anodic peak **C** in the CV (**Figure 4.9**).
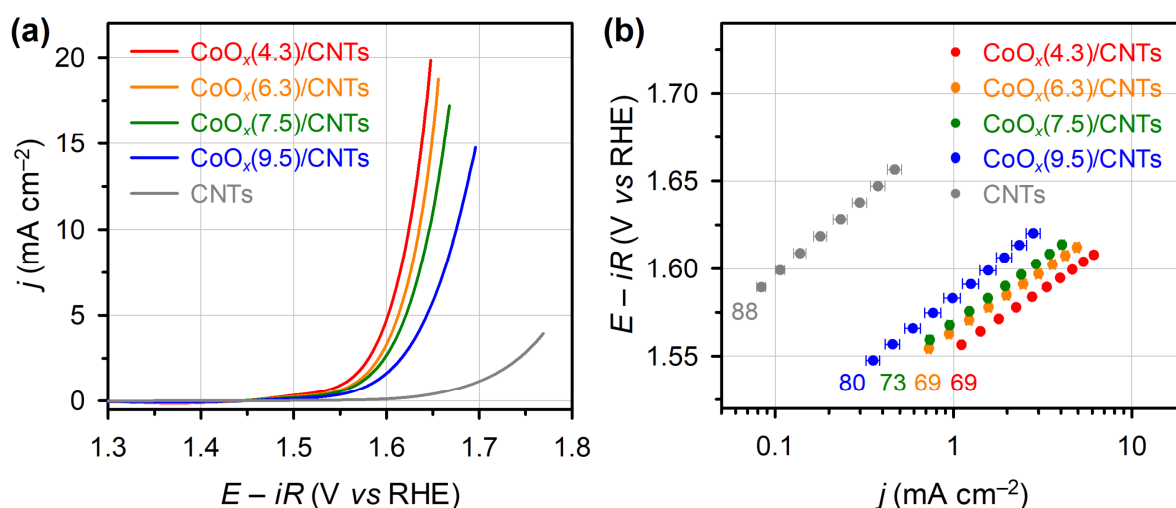
Figure 4.11. (a) OER polarization curves (10th CV scan, *iR*-corrected) of the CoO_x/CNTs and CNTs measured in 0.1 M KOH at a potential scan rate of 20 mV s^{-1} with an electrode rotation of 1,600 rpm. (b) The corresponding Tafel plots for the OER, where the number indicates the Tafel slope.

Unlike the case of the OER activities, the CoO_x/CNTs exhibited nearly identical activities for the ORR, independent of the CoO_x NP size (**Figure 4.12**). The onset potentials and diffusion-limited current densities of the CoO_x/CNTs are almost the same regardless of the NP sizes. Interestingly, the onset potential of the CoO_x/CNTs was the same as that of the CNTs, and the Tafel plots of the CoO_x/CNTs and CNTs almost overlapped (**Figure 4.12b**). This result suggested that the CoO_x NPs did not improve the intrinsic ORR activity; rather, CoO_x NPs appear to promote the reduction or disproportionation of peroxide species generated by the CNTs, as evidenced by the greater diffusion-

limited current density of the CoO$_x$/CNTs compared to that of the CNTs (−4 vs −3 mA cm^{-2}). In addition, the similar Tafel slopes may indicate that the reaction rates of the CoO$_x$/CNTs and CNTs are limited by the same step, which occurred on the CNTs.
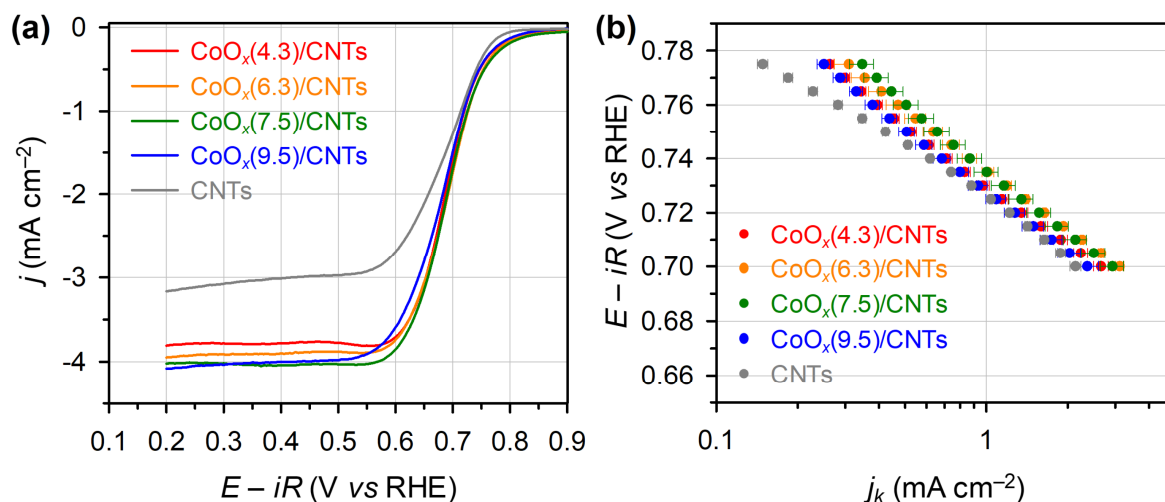
Figure 4.12. (a) ORR polarization curves (iR-corrected) of the CoO$_x$/CNTs and CNTs measured in O$_2$-saturated 0.1 M KOH at a potential scan rate of 5 mV s^{-1} with an electrode rotation of 1,600 rpm. (b) The corresponding Tafel plots for the ORR, where j_k indicates the kinetic current density.

Therefore, it can be deduced that the ORR was initiated by the CNTs via the two-electron transfer pathway and that the CoO$_x$ NPs mainly played an auxiliary role, promoting the reduction or disproportionation of the generated peroxide (**Figure 4.13**). The fast and repetitive disproportionation of peroxide by CoO$_x$ led to the quasi-four-electron pathway (2 + 1 + 0.5 + 0.25 + ... ≈ 4) for the ORR.[28,51,52] To confirm the catalytic role of the CoO$_x$ NPs, we prepared the CoO$_x$/CNTs with a higher CoO$_x$ loading (~35 wt%). The ORR activities of 32% CoO$_x$(4.3)/CNTs, 35% CoO$_x$(6.3)/CNTs, and 36% CoO$_x$(9.5)/CNTs are almost the same regardless of their particle sizes, as evidenced by their overlapping LSV curves (**Figure 4.14a**). Compared to CNTs, the CoO$_x$/CNTs show slightly higher diffusion-limited current densities and better 4-electron selectivity (**Figure 4.14b**). It should be also pointed out that that the high-loading 32% CoO$_x$(4.3)/CNTs showed only marginal improvement of the ORR activity in the kinetic region (i.e., 0.7–0.85 V) compared with the low-loading 9.4% CoO$_x$(4.3)/CNTs. We found that the previously reported, high-performance CoO$_x$/carbon hybrid catalysts usually contained nitrogen,[16,23,34] potentially creating Co–N moieties, which are known to be highly active species for the ORR. The rather low ORR performances of our CoO$_x$/CNTs are rationalized by the absence of nitrogen. We highlight the importance of preparing N-free metal oxides/carbon hybrid model catalysts to investigate the particle size-dependent ORR activity originating from metal oxides.
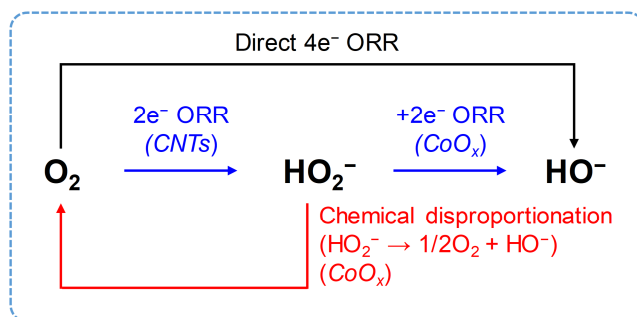
Figure 4.13. Schematic illustration of the ORR reaction pathways in alkaline electrolytes.
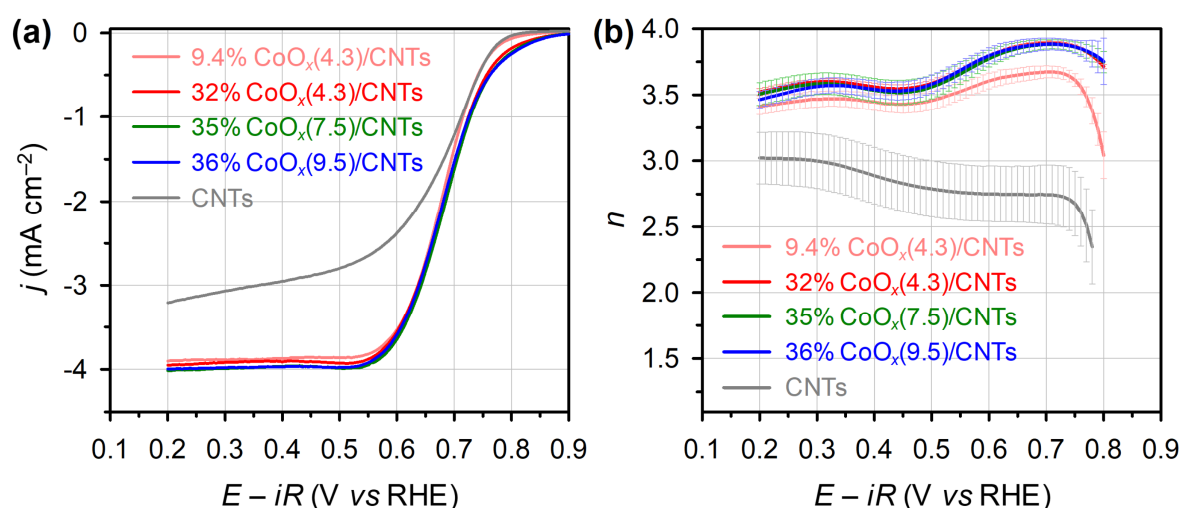
Figure 4.14. (a) ORR polarization curves of the CoO_x/CNTs with a higher loading of CoO_x NPs measured in O_2-saturated 0.1 M KOH at a potential scan rate of 5 mV s^{-1} with an electrode rotation of 1,600 rpm. (b) Electron transfer number (n) during the ORR obtained by RRDE measurements.

4.3.5. Stability Test and Post Mortem XPS Analysis

The long-term stability is a critical factor for practical applications. Chronopotentiometry (CP) was conducted at a current density of 5 mA cm^{-2} (**Figure 4.15a**). The CoO_x/CNTs catalysts exhibited excellent durability with a little decay in the OER activity and maintenance of their structures over 400 min of operation. TEM images after the CP measurements revealed that the phase of the CoO_x NPs was maintained as Co_3O_4 with retained particle sizes for the CoO_x(4.3)/CNTs (not shown here). However, long-term test under an applied OER potential resulted in the structural change from CoO to Co_3O_4 for the largest CoO_x NPs, as revealed by the FFT patterns in **Figure 4.7c**, which was consistent with the *in situ* XAS measurement results. In addition, we investigated the chemical states of Co before and after the OER measurements using X-ray photoelectron spectroscopy (XPS) (**Figure 4.15b**). For the CoO_x(4.3)/CNTs, the Co 2p XPS spectra before and after the OER almost overlapped.

For the CoO$_x$(9.5)/CNTs, the satellite peaks around 787 and 803 eV (indicated by dotted lines) disappeared after OER, indicating a decrease in the number of surface Co(II) species, concomitant of the oxidation of Co(II) species to Co(III). The results well support the conclusions drawn from the other characterizations, including TEM, XRD, *in situ* XAS, and CV curves.
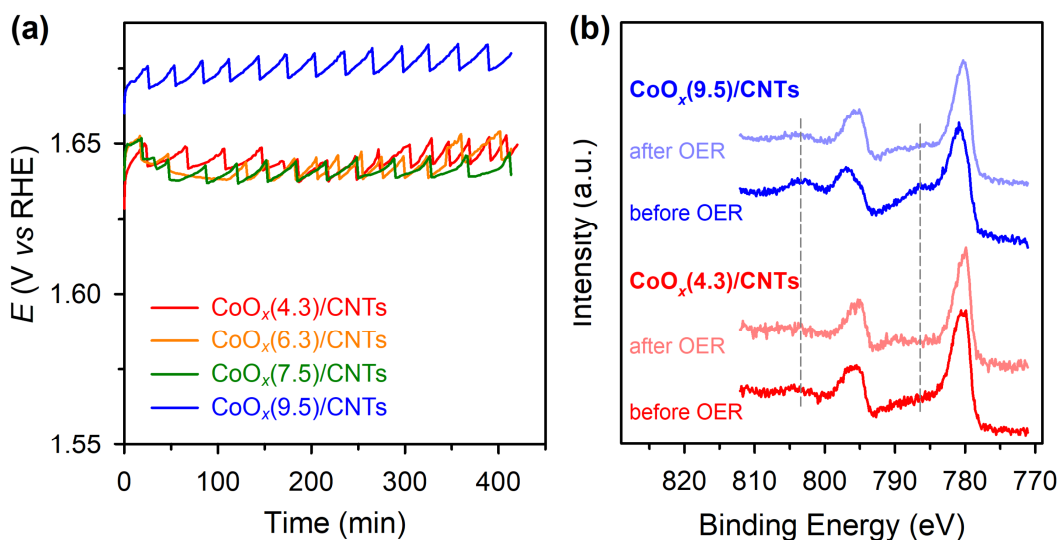
Figure 4.15. (a) CP responses for the CoO$_x$/CNTs at 5 mA cm^{-2} with an electrode rotation of 1,600 rpm. (b) Co 2p XPS spectra of the CoO$_x$(4.3)/CNTs and CoO$_x$(9.5)/CNTs before and after the CP test.

4.4. CONCLUSION

In summary, we have scrutinized the size-dependent structures and catalytic activities of CoO$_x$ NPs supported on CNTs for bifunctional oxygen electrocatalysis. *In situ* electrochemical XAS measurements revealed that Co$_3$O$_4$ and CoOOH are the major species regardless of the CoO$_x$ particle size under both OER and ORR conditions. The OER activities of the CoO$_x$/CNTs increased with decreasing particle size, which could be ascribed to the facile oxidation of the smaller NPs as the potential is applied. The ORR activity was independent of the CoO$_x$ NP size, revealing the auxiliary role of CoO$_x$ NPs for the reduction or disproportionation of peroxide rather than the reduction of oxygen. Combining *in situ* XAS with electrocatalytic activity trends, we suggested that the dominant Co(III) species are related to active intermediates for the OER, while they appear to be side products generated from the oxidation of Co(II) by peroxide intermediate during the ORR. This work can offer a platform to explore the structural changes and reaction pathways of CoO$_x$ for the rational design of advanced bifunctional oxygen electrocatalysts.

4.5. REFERENCES

(1) Cook, T. R.; Dogutan, D. K.; Reece, S. Y.; Surendranath, Y.; Teets, T. S.; Nocera, D. G. *Chem. Rev.* **2010**, *110*, 6474–6502.

(2) Chu, S.; Majumdar, A. *Nature* **2012**, *488*, 294–303.

(3) Park, S.; Shao, Y.; Liu, J.; Wang, Y. *Energy Environ. Sci.* **2012**, *5*, 9331–9334.

(4) Cao, R.; Lee, J.-S.; Liu, M.; Cho, J. *Adv. Energy Mater.* **2012**, *2*, 816–829.

(5) Katsounaros, I.; Cherevko, S.; Zeradjanin, A. R.; Mayrhofer, K. J. J. *Angew. Chem., Int. Ed.* **2014**, *53*, 102–121.

(6) Jiao, Y.; Zheng, Y.; Jaroniec, M.; Qiao, S. Z. *Chem. Soc. Rev.* **2015**, *44*, 2060–2086.

(7) Zhang, J.; Zhao, Z.; Xia, Z.; Dai, L. *Nat. Nanotechnol.* **2015**, *10*, 444–452.

(8) Duan, J.; Chen, S.; Jaroniec, M.; Qiao, S. Z. *ACS Catal.* **2015**, *5*, 5207–5234.

(9) Mitlitsky, F.; Myers, B.; Weisberg, A. H. *Energy Fuels* **1998**, *12*, 56–71.

(10) Ng, J. W. D.; Gorlin, Y.; Hatsukade, T.; Jaramillo, T. F. *Adv. Energy Mater.* **2013**, *3*, 1545–1550.

(11) Bruce, P. G.; Freunberger, S. A.; Hardwick, L. J.; Tarascon, J.-M. *Nat. Mater.* **2012**, *11*, 19–29.

(12) Cheng, F.; Chen, J. *Chem. Soc. Rev.* **2012**, *41*, 2172–2192.

(13) Ioroi, T.; Kitazawa, N.; Yasuda, K.; Yamamoto, Y.; Takenaka, H. *J. Electrochem. Soc.* **2000**, *147*, 2018–2022.

(14) Chen, G.; Bare, S. R.; Mallouk, T. E. *J. Electrochem. Soc.* **2002**, *149*, A1092–A1099.

(15) Gorlin, Y.; Jaramillo, T. F. *J. Am. Chem. Soc.* **2010**, *132*, 13612–13614.

(16) Liang, Y.; Li, Y.; Wang, H.; Zhou, J.; Wang, J.; Regier, T.; Dai, H. *Nat. Mater.* **2011**, *10*, 780–786.

(17) Cheng, F.; Shen, J.; Peng, B.; Pan, Y.; Tao, Z.; Chen, J. *Nat. Chem.* **2011**, *3*, 79–84.

(18) Maiyalagan, T.; Jarvis, K. A.; Therese, S.; Ferreira, P. J.; Manthiram, A. *Nat. Commun.* **2014**, *5*, 3949.

(19) Indra, A.; Menezes, P. W.; Sahraie, N. R.; Bergmann, A.; Das, C.; Tallarida, M.; Schmeiβer, D.; Strasser, P.; Driess, M. *J. Am. Chem. Soc.* **2014**, *136*, 17530–17536.

(20) Jung, J.-I.; Jeong, H. Y.; Lee, J.-S.; Kim, M. G.; Cho, J. *Angew. Chem., Int. Ed.* **2014**, *53*, 4582–4586.

(21) Chen, S.; Duan, J.; Bian, P.; Tang, Y.; Zheng, R.; Qiao, S.-Z. *Adv. Energy Mater.* **2015**, *5*, 1500936.

(22) Sa, Y. J.; Kwon, K.; Cheon, J. Y.; Kleitz, F.; Joo, S. H. *J. Mater. Chem. A* **2013**, *1*, 9992–10001.

(23) Masa, J.; Xia, W.; Sinev, I.; Zhao, A.; Sun, Z.; Grützke, S.; Weide, P.; Muhler, M.; Schuhmann, W. *Angew. Chem., Int. Ed.* **2014**, *53*, 8508–8512.

(24) Ma, T. Y.; Dai, S.; Jaroniec, M.; Qiao, S. Z. *J. Am. Chem. Soc.* **2014**, *136*, 13925–13931.

(25) den Breejen, J. P.; Radstake, P. B.; Bezemer, G. L.; Bitter, J. H.; Frøseth, V.; Holmen, A.; de Jong, K. P. *J. Am. Chem. Soc.* **2009**, *131*, 7197–7203.

(26) Iablokov, V.; Beaumont, S. K.; Alayoglu, S.; Pushkarev, V. V.; Specht, C.; Gao, J.; Alivisatos, A. P.; Kruse, N.; Somorjai, G. A. *Nano Lett.* **2012**, *12*, 3091–3096.

(27) Esswein, A. J.; McMurdo, M. J.; Ross, P. N.; Bell, A. T.; Tilley, T. D. *J. Phys. Chem. C* **2009**, *113*, 15068–15072.

(28) Liu, J.; Jiang, L.; Zhang, B.; Jin, J.; Su, D. S.; Wang, S.; Sun, G. *ACS Catal.* **2014**, *4*, 2998–3001.

(29) Rosen, J.; Hutchings, G. S.; Lu, Q.; Forest, R. V.; Moore, A.; Jiao, F. *ACS Catal.* **2015**, *5*, 4586–4591.

(30) Li, D.; Wang, C.; Tripkovic, D.; Sun, S.; Markovic, N. M.; Stamenkovic, V. R. *ACS Catal.* **2012**, *2*, 1358–1362.

(31) Yang, J.; Liu, H.; Martens, W. N.; Frost, R. L. *J. Phys. Chem. C* **2010**, *114*, 111–119.

(32) Ravel, B.; Newville, M. *J. Synchrotron Radiat.* **2005**, *12*, 537–541.

(33) Suntivich, J.; Gasteiger, H. A.; Yabuuchi, N.; Shao-Horn, Y. *J. Electrochem. Soc.* **2010**, *157*, B1263–B1268.

(34) Olson, T. S.; Pylypenko, S.; Atanassov, P.; Asazawa, K.; Yamada, K.; Tanaka, H. *J. Phys. Chem. C* **2010**, *114*, 5049–5059.

(35) Jin, H.; Wang, J.; Su, D.; Wei, Z.; Pang, Z.; Wang, Y. *J. Am. Chem. Soc.* **2015**, *137*, 2688–2694.

(36) Friebel, D.; Louie, M. W.; Bajdich, M.; Sanwald, K. E.; Cai, Y.; Wise, A. M.; Cheng, M.-J.; Sokaras, D.; Weng, T.-C. Alonso-Mori, R.; Davis, R. C.; Bargar, J. R.; Nørskov, J. K.; Nilsson, A.; Bell, A. T. *J. Am. Chem. Soc.* **2015**, *137*, 1305–1313.

(37) Risch, M.; Zaharieva, K. I.; Gerencser, L.; Chernev, P.; Dau, H. *J. Am. Chem. Soc.* **2009**, *131*, 6936–6937.

(38) Zhang, M.; de Respinis, M.; Frei, H. *Nat. Chem.* **2014**, *6*, 362–367.

(39) Plaisance, C. P.; van Santen, R. A. *J. Am. Chem. Soc.* **2015**, *137*, 14660–14672.

(40) Liu, Y.-C.; Koza, J. A.; Switzer, J. A. *Electrochim. Acta* **2014**, *140*, 359–365.

(41) Yeo, B. S.; Bell, A. T. *J. Am. Chem. Soc.* **2011**, *133*, 5587–5593.

(42) Subbaraman, R.; Tripkovic, D.; Chang, K.-C.; Strmcnik, D.; Paulikas, A. P.; Hirunsit, P.; Chan, M.; Greeley, J.; Stamenkovic, V.; Markovic, N. M. *Nat. Mater.* **2012**, *11*, 550–557.

(43) Xiao, J.; Kuang, Q.; Yang, S.; Xiao, F.; Wang, S.; Guo, L. *Sci. Rep.* **2013**, *3*, 2300.

(44) Menezes, P. W.; Indra, A.; González-Flores, D.; Sahraie, N. R.; Zaharieva, I.; Schwarze, M.; Strasser, P.; Dau, H.; Driess, M. *ACS Catal.* **2015**, *5*, 2017–2027.

(45) Liang, Y.; Wang, H.; Diao, P.; Chang, W.; Hong, G.; Li, Y.; Gong, M.; Xie, L.; Zhou, J.; Wang, J.; Regier, T. Z.; Wei, F.; Dai, H. *J. Am. Chem. Soc.* **2012**, *134*, 15849–15857.

(46) Wass, J. R. T. J.; Panas, I.; Ásbjörnsson, J.; Ahlberg, E. *J. Electroanal. Chem.* **2007**, *599*, 295–312.

(47) Wu, L.; Li, Q.; Wu, C. H. Zhu, H.; Mendoza-Garcia, A.; Shen, B.; Guo, J.; Sun, S. *J. Am. Chem.*

Soc. **2015**, *137*, 7071–7074.

(48)   Gerken, J. B.; McAlpin, J. G.; Chen, J. Y. C.; Rigsby, M. L.; Casey, W. H.; Britt, R. D.; Stahl, S. S. *J. Am. Chem. Soc.* **2011**, *133*, 14431–14442.

(49)   McAlpin, J. G.; Surendranath, Y.; Dincă, M.; Stich, T. A.; Stoian, S. A.; Casey, W. H.; Nocera, D. G.; Britt, R. D. *J. Am. Chem. Soc.* **2010**, *132*, 6882–6883.

(50)   Song, F.; Hu, X. *J. Am. Chem. Soc.* **2014**, *136*, 16481–16484.

(51)   Liu, J.; Jiang, L.; Tang, Q.; Zhang, B.; Su, D. S.; Wang, S.; Sun, G. *ChemSusChem* **2012**, *5*, 2315–2318.

(52)   Gorlin, Y.; Chung, C.-J.; Nordlund, D.; Clemens, B. M.; Jaramillo, T. F. *ACS Catal.* **2012**, *2*, 2687–2694.

5

STRUCTURE–ACTIVITY CORRELATION AND KINETIC INSIGHTS FOR HYDROGEN EVOLUTION REACTION BY CO–N/C ELECTROCATALYSTS

5.1. INTRODUCTION

Clean and sustainable hydrogen production is a key ingredient for realizing hydrogen-based energy infrastructure.[1] Electrolysis of water in conjunction with renewable energy sources such as solar and wind power represents the most promising way for pollution-free and sustainable H_2 production.[2,3] Efficient electrochemical production of H_2 is dependent critically on the high-performance electrode catalysts, and hence requires the use of precious metal catalysts such as Pt for the hydrogen evolution reaction (HER) at the cathode of the electrolyzer.[4,5] However, the scarcity and high price of Pt has hampered the widespread deployment of this technology. This situation has prompted the development of non-precious metal based HER catalysts, including transition metal dichalcogenides,[6–12] nitrides,[13,14] carbides,[15–17] and phosphides.[18–21]

As a class of non-precious HER catalysts, molecular catalysts mimicking naturally-occurring enzymes are highly intriguing, since they hold great potential for activity improvement approaching to Nature's enzyme and the ability of full utilization of the active sites. Cobalt-based complexes incorporating Co–N coordination bonds (Co–N_x), such as cobalt porphyrin,[22,23] cobalt glyoxime,[24–26] and diamine-dioxime cobalt,[27,28] have demonstrated promise as electrocatalysts for the HER. Importantly, these inorganic molecular catalysts could serve as model catalysts for studying the impacts of coordination and electronic structures on the reactivity for the HER, as well as for investigating HER reaction kinetics. However, only few complexes have been proven to perform properly in aqueous electrolytes, wherein current electrolyzers operate.[23] In addition, they still require high overpotentials to deliver the current and suffer from instability during prolonged operation. In this context, the heterogenized version of molecular catalysts have attracted significant interest from catalysis community, as they can bridge the homogeneous and heterogeneous catalysis, and take advantages of both class of catalysts.

In the design of cobalt-based heterogenized molecular catalysts, the Co–N_x molecular active

sites are usually incorporated into the carbons which are conductive and porous support materials (Co–N/C catalysts). Doping and complexation of Co and N atoms onto the carbons require high-temperature pyrolysis of a mixture containing Co, N, and C sources or Co macrocycles.[29] The high-temperature treatment step can play multiple roles that critically affect the structure of the resulting Co–N/C catalysts. First, it improves the electrical conductivity of the carbon. Second, atomically dispersed Co–N_x sites can be generated. However, such harsh synthetic conditions undesirably result in the aggregation of Co atoms to form metallic Co nanoparticles (NPs). Co NPs then catalyze Fischer-Tropsch reaction *in situ*, resulting in the encapsulation of the Co NPs with graphitic carbon shells (Co@C species). The co-existence of Co–N_x and Co@C sites in Co–N/C catalysts hinders the identification of the active sites for the HER. Indeed, Müllen and Tour groups suggested that Co–N_x sites are responsible for high HER activity,[30,31] whereas many other groups proposed that Co@C, though Co is not exposed on the surface, can indirectly participate in the HER *via* tuning electronic structure of the outermost carbon shells.[32–36] Furthermore, detailed kinetics information over Co–N/C catalysts for the HER are still largely unexplored.

The present work was undertaken to reconcile the on-going controversy over HER sites in the Co–N/C catalysts and to uncover their kinetics for the electrocatalytic HER. For this purpose, we prepared a series of Co–N/C catalysts with controlled ratios of Co–N_x to Co@C sites to identify the active species for the HER. The Co–N/C catalysts were prepared by mixing cobalt(II) phthalocyanine (Co^{II}Pc) and carbon nanotube (CNT), the adsorption of Co^{II}Pc at intermediate temperature, the silica coating, and the high-temperature pyrolysis, yielding Co-phthalocyanic carbon on CNT (CNT/Co-PcC) catalysts. We found the silica coating prior to the pyrolysis is critical to produce CNT/Co-PcC catalyst predominantly comprised of Co–N_x sites without Co@C sites. The control of the site density of Co–N_x and Co@C was achieved by changing the experimental parameters. Structural characterization and electrocatalytic activity evaluation could establish a structure–activity correlation that Co–N_x sites mainly contribute the HER activity both in acidic and alkaline electrolytes. The reaction kinetics of the CNT/Co-PcC catalyst with ~100% Co–N_x sites was investigated by pH-dependent HER activity measurements. The kinetics study suggested the possible rate determining step (RDE) on Co–N_x sites as hydrogen adsorption (Volmer reaction). Furthermore, temperature-dependent HER activity trends revealed that the activation energy of CNT/Co-PcC is comparable to Pt catalyst at high pH. Finally, the long-term operation test over 30 h revealed the excellent stability of our catalyst retaining ~90% of initial activity in alkaline electrolyte.

5.2. EXPERIMENTAL METHODS

5.2.1. Synthesis of CNT/Co-PcC Catalysts

Prior to the synthesis of CNT/Co-PcC, CNT was treated with acids (AT-CNT) to remove metallic impurities. 10.0 g of multiwalled CNTs (MR 99, Carbon Nano-material Technology Co.) were mixed with 715 g of 6 M HNO_3 (diluted from 60 wt% HNO_3, Samchun chemical), and the mixture was stirred at 80 °C for 12 h. The suspension was filtered, washed with copious amounts of DI water until the pH of the filtrate reached 7, and dried at 60 °C. The HNO_3-treated CNTs were subsequently treated with 700 g of 6 M HCl (diluted from 36 wt% HCl, Samchun chemical) as described above.

0.60 g of AT-CNT and 0.60 g of $Co^{II}Pc$ were ground in an agate mortar until the color and the texture did not change (for ~20 min). The mixture was heated at 500 °C under 1 L min^{-1} N_2 flow (99.9999%, KOSEM, Korea) for 3 h (ramping rate: ~2.1 °C min^{-1}). A part of heat-treated powder was mixed with TEOS (0.5 mL per 0.10 g of AT-CNT used) using mortar and pestle. The same volume of formic acid was added to the paste-like mixture to initiate the polymerization of TEOS. The mixture was dried at RT, ground to fine powder, and pyrolyzed at 850 °C under 1 L min^{-1} N_2 flow for 3 h (ramping rate: ~2.1 °C min^{-1}). To dissolve the silica and any acid-soluble Co-species, the pyrolyzed powders were added to an acid solution containing 4 M HF and 2 M HCl (diluted from 50 wt% HF from JT Baker and 36 wt% HCl) with a similar volume of ethanol (94.5%), and stirred at RT for 30 min. The mixture was filtered and washed with ethanol. Stirring in the acid solution and filtering were repeated once more in the same manner. The product was dried at 60 °C and collected. Co-free CNT/PcC catalyst was synthesized *via* the same procedure, except the use of 0.40 g of AT-CNT and 0.36 g of phthalocyanine (equimolar to 0.40 g of $Co^{II}Pc$) were used. The preparation for the other series of CNT/Co-PcC catalysts is carried out with different synthetic parameters (**Table 5.1**).

Table 5.1. Summary of the synthetic conditions for a series of CNT/Co-PcC catalysts.

Sample	$Co^{II}Pc$/CNT (w/w)	Silica Coating	Pyrolysis Time
CNT/Co-PcC-1	1	O	3 h
CNT/Co-PcC-1_w/o SiO_2	1	X	3 h
CNT/Co-PcC-1_w/o SiO_2_24h	1	X	24 h
CNT/Co-PcC-3	3	O	3 h
CNT/Co-PcC-3_w/o SiO_2	3	X	3 h
CNT/Co-PcC-3_w/o SiO_2_24h	3	X	24 h

5.2.2. Characterization Methods

Transmission electron microscopy (TEM) images were taken on a JEOL JEM-2100 electron microscope at an acceleration voltage of 200 kV. X-ray powder diffraction (XRD) patterns of the catalysts were obtained with a high-power X-ray diffractometer (D/MAX2500V/PC, Rigaku) equipped with Cu Kα radiation, and operating at 40 kV and 200 mA. The XRD patterns were measured in a 2θ range from 10° to 80° at a scan rate of 2° min^{-1}. X-ray photoelectron spectroscopy (XPS) measurements were performed with a K-alpha instrument (ThermoFisher Scientific), equipped with a monochromatic Al Kα X-ray source (1486.6 eV). Co 2p and N 1s XPS spectra were deconvoluted using the XPSPeak41 software with the mixed (Gaussian 70, Lorentzian 30)-function after a linear (Shirley)-type background correction. The Co content in the catalysts was analyzed using an inductively coupled plasma optical emission spectrometry (ICP-OES) analyzer (700-ES, Varian).

5.2.3. XAS Experiments

X-ray absorption spectroscopy (XAS) was performed at beamline 6C of Pohang Accelerator Laboratory. Storage ring was operated at an energy of 3 GeV and a beam current of 360 mA. The incident beam was filtered by Si (1 1 1) double crystal monochromator, and detuned by 30% to remove high-order harmonics. The incident photon energy was then calibrated using a standard Co foil where the maximum of the first derivative of absorption of the Co foil to be located at 7709 eV. The powder sample was pressed using a hand-pelletizer to a desired thickness that X-ray beam could pass through enough number of Co atoms, resulting in the absorption edge step ranging from 0.3 to 1.1. Background removal and normalization of the Co K-edge XAS spectra were conducted using the Athena software.[37] Fourier transform of k^3-weighted extended X-ray absorption fine structure (EXAFS) spectra was carried out using the Artemis software to obtain coordination numbers and interatomic distances. The fitting was conducted in k range of 2.5–10.5 Å^{-1} and under simultaneous k^1, k^2, and k^3 weighing.[38] Throughout the fitting analysis, the amplitude reduction factor (S_0^2) was fixed at 0.75, which was obtained by the fitting of the EXAFS spectrum of the Co foil.

5.2.4. Electrochemical Characterizations

Electrochemical measurements were performed on an electrochemical workstation (CHI760E, CH Instruments) at atmospheric pressure. Three-electrode system was built with a rotating ring disk electrode (RRDE, AFE7R9GCPT, Pine Research Instrumentation), a graphite counter electrode and a reference electrode. Hg/HgO (CHI152, CH Instruments, filled with 1 M KOH) and saturated calomel

electrode (RE-2B, ALS, filled with saturated KCl) were used as the reference electrodes for the measurement in alkaline and acidic electrolytes, respectively. The electrolytes were prepared from the dilution of 99.999% H_2SO_4 (Sigma-Aldrich) and 99.99% KOH (Sigma-Aldrich) in 18.2 MΩ cm Millipore water.

Before every measurement, the RRDE was polished on a micro-cloth with an aqueous suspension of 1.0 μm alumina and then 0.3 μm alumina to generate a mirror finish. The catalyst ink was prepared by mixing 30 mg of catalyst, 100 μL of DI water (0.1 mL), 75 μL of Nafion (D521, DuPont), and 1.0 mL of absolute ethanol and homogenizing in an ultrasonic bath (Branson) for at least 40 min. 8 μL of the catalyst ink were deposited onto glassy carbon (GC) disk (5.61 mm in diameter) using a micropipette and dried at RT. The resulting catalyst loading was 0.8 mg cm^{-2}.

The catalyst film deposited on the RRDE was immersed into the electrolyte. First, cyclic voltammetry (CV) was performed to clean and to make the catalyst fully wet at a scan rate of 100 mV s^{-1} for 20 cycles between 0.30 to −0.10 V (*vs* RHE) in N_2-saturated electrolyte. Then, electrochemical impedance spectroscopy (EIS) was conducted at a fixed potential of −0.10 V from 100,000 to 1 Hz with a potential amplitude of 10 mV and an electrode rotation speed of 1,600 rpm. Series resistance was estimated to be the real impedance at the lowest imaginary impedance in the high-frequency region. EIS measurement was repeated until the same series resistance value was consistently obtained. HER activity was measured by linear sweep voltammetry (LSV) experiment from 0.05 to −0.30 ~ −0.60 V (depending on the catalysts) at a scan rate of 2 mV s^{-1} with an electrode rotation speed of 1,600 rpm.

For pH-dependent experiment for CNT/Co-PcC-1 catalyst, the concentration of H_2SO_4 was controlled from 0.5 M (pH 0.20) to 0.045 M (pH 1.65) while Na_2SO_4 (>99%, Sigma-Aldrich) was added to the solution to adjust the total electrolyte concentration of 0.5 M. Likewise, that of KOH was varied from 1.0 M (pH 13.80) to 0.56 M (pH 12.85) while the total concentration was balanced with K_2HPO_4 (>98%, Sigma-Aldrich) to 1.0 M. The pH of every electrolyte was measured using a digital pH meter (Orion), which was calibrated using standard solutions with pH 4.01, 7.00, and 10.01 before the measurement.

To measure the activation energy for the HER, the HER activity of the CNT/Co-PcC-1 catalyst was tested in temperature-controlled electrolytes (25, 35, 45, and 55 °C). The experiment was performed in a water bath and the temperature inside the cell was monitored using a mercury thermometer. Before every experiment, the temperature of the electrochemical cell was immersed in the water bath for at least 15 min to reach a temperature equilibration. During the experiment, the evaporation of water in the bath was negligible due to short measurement time (<60 min for each measurement), and only marginal temperature fluctuation was observed (< ±1 °C). Logarithmic plot

of the current with respect to the potential gave Tafel plot. The linear region of the Tafel plot was extrapolated to the point of zero overpotential to obtain exchange current, according to the following Tafel equation

$$\eta = -b \log i + b \log i_0$$

where η, b, i, and i_0 represent the overpotential, the Tafel slope, the measured current, and the exchange current, respectively.

Except for the temperature-control experiment, the above-stated measurements were all conducted at 25 ± 1 °C. The catalyst film was replaced as a fresh one after every measurement, and independently repeated at least three times for each catalyst/test, and the averaged and post-*iR*-corrected data are shown.

5.3. RESULTS AND DISCUSSION

5.3.1. Synthesis and Characterization of CNT/Co-PcC Catalysts

Co–N/C catalysts primarily composed of atomically dispersed Co–N$_x$ sites were prepared by the "silica-protective-layer-assisted" method as reported by our group.[39] AT-CNT was mixed with cobalt(II) phthalocyanine (Co^{II}Pc) and annealed at 500 °C to adsorb the Co^{II}Pc molecules on the CNT. Silica layers were then overcoated on the CNT adsorbed with Co^{II}Pc-based layer, and the ternary composite was pyrolyzed at 850 °C. Subsequent removal of silica and Co-related species by acid treatment (HF–HCl solution) yielded CNT/Co-PcC-1 catalyst. To verify the role of the silica, another catalyst pyrolyzed without the silica coating was also prepared (CNT/Co-PcC-1_w/o SiO$_2$, 1_w/o SiO$_2$ for short).

XRD pattern of CNT/Co-PcC-1 shows only peaks from the CNT appearing at around 26 and 43°, indicating the absence of large and crystalline Co-based species (**Figure 5.1a**). In contrast, the catalyst prepared without the silica protective layer (1_w/o SiO$_2$) exhibits the XRD peaks at 44.4 and 51.5° corresponding to (111) and (101) lattice planes of face-centered cubic Co phase. XPS was conducted to investigate the chemical structure of Co and N on the catalyst surfaces. In Co 2p XPS spectra, both catalysts commonly show two main peaks at 780.0 and 795.4 eV with corresponding satellite peaks at 784.0 and ~802 eV, respectively (**Figure 5.1b**), which are characteristic features of Co^{2+} state.[40] For 1_w/o SiO$_2$ sample, XPS signal for the metallic Co species is not observed, implying that the metallic Co species are encapsulated in the carbon shell generated *in situ* during the pyrolysis. N 1s XPS spectra were deconvoluted into five peaks (**Figure 5.1c**). Both samples showed similar N 1s scan that is indicative of almost identical surface N chemical state. TEM image of the CNT/Co-

PcC-1 catalyst shows a hybrid structure of CNT and carbon particles intimately contacting each other, where the latter is considered to be carbonized $Co^{II}Pc$ (**Figure 5.2a**). Importantly, no particulate species were observed for CNT/Co-PcC-1 catalyst, suggesting that Co-based species are predominantly present as the molecularly dispersed state. However, silica-uncoated 1_w/o SiO_2 showed a significant quantity of NPs with the size of a few tens of nanometers (**Figure 5.2b**). A closer look (inset of **Figure 5.2b**) revealed that the NPs were covered by graphitic carbon layers, which are consistent with XRD and XPS analyses.
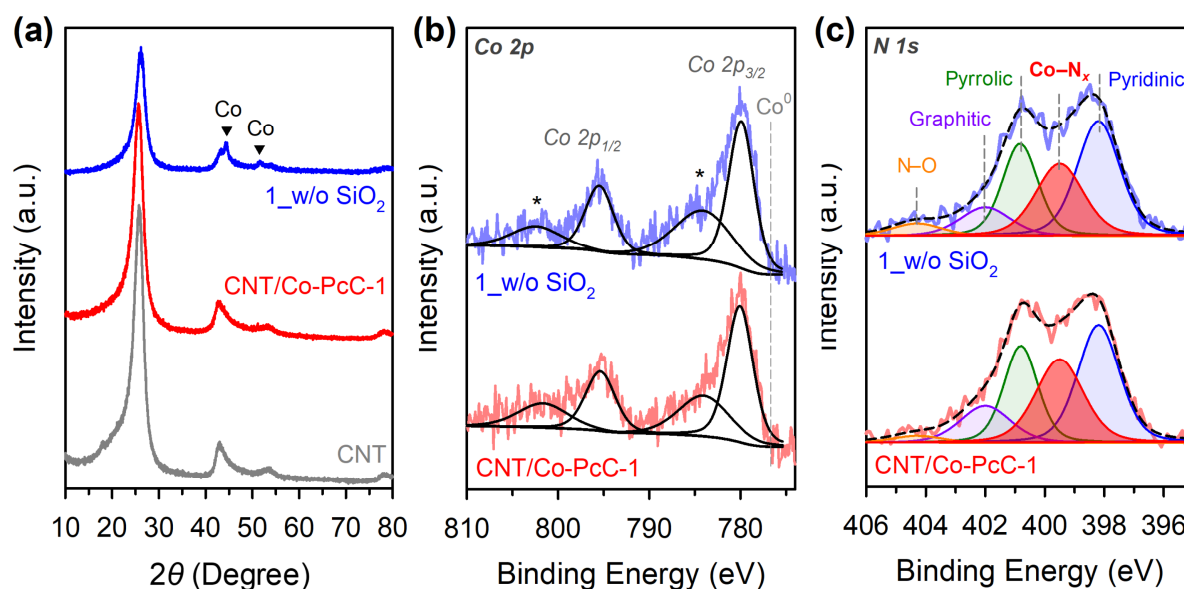
Figure 5.1. (a) XRD pattern of CNT/Co-PcC-1, 1_w/o SiO_2 catalysts, and CNT. (b) XPS Co 2p and (c) N 1s spectra and deconvoluted peaks for CNT/Co-PcC-1 and 1_w/o SiO_2.
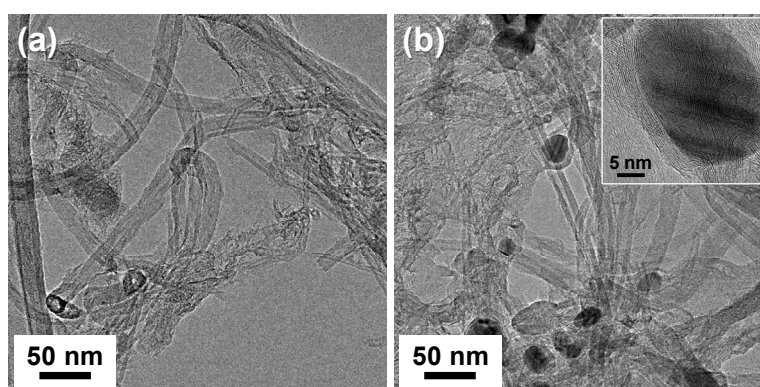
Figure 5.2. TEM images of (a) CNT/Co-PcC-1 and (b) 1_w/o SiO_2.

The local structures around Co in the catalysts were analyzed by using Co K-edge XAS (**Figure 5.3**). X-ray absorption near edge structure (XANES) spectra of $Co^{II}Pc$ shows a sharp pre-edge peak at

7716 eV (peak C) originating from the square planar symmetry (D_{4h}) of Co–N_4 structure in the $Co^{II}Pc$ molecule (**Figure 5.3a**). This pre-edge peak is not clearly observed for the pyrolyzed catalysts, indicating the symmetry change after the heat-treatment. For CNT/Co-PcC-1 catalyst, a new pre-edge peak A appears at 7710 eV. The peak A can be assigned as penta-coordinated or distorted local structure of atomically dispersed Co–N_x sites originating from the transformation of the initial square planar Co–N_4 sites.[41,42] The XANES spectrum of 1_w/o SiO_2 catalyst looks similar to that of CNT/Co-PcC-1, but also shows remarkable spectral features of the Co foil (peaks B and D). This suggests that 1_w/o SiO_2 has a significant amount of metallic Co phase, which is in line with the XRD and TEM analyses. The short range atomic order was investigated by extended X-ray absorption fine structure (EXAFS) analysis. Radial distribution function (RDF) obtained from Fourier transform (FT) of k^3-weighted EXAFS spectra for CNT/Co-PcC-1 catalyst shows the main RDF peak at 1.4 Å corresponding to Co–N and Co–O bonds (hardly distinguishable by distance in EXAFS). The small peak at 2.4 Å is assignable to Co–C interatomic distance where the C atom is the most adjacent to the N atom bonding to the Co atom, suggesting the Co–N–C local structure is present in the catalyst. The EXAFS analysis confirms that CNT/Co-PcC-1 catalyst consists predominantly of Co–N_x sites. In contrast, 1_w/o SiO_2 catalyst shows additional RDF peaks at 2.1, 3.8, and 4.5 Å, which are attributed to metallic Co phase (**Figure 5.3b**). Therefore, we verified that the silica coating was effective to prepare Co–N/C catalysts exclusively comprised of Co–N_x sites, otherwise significant amounts of Co@C species were formed.
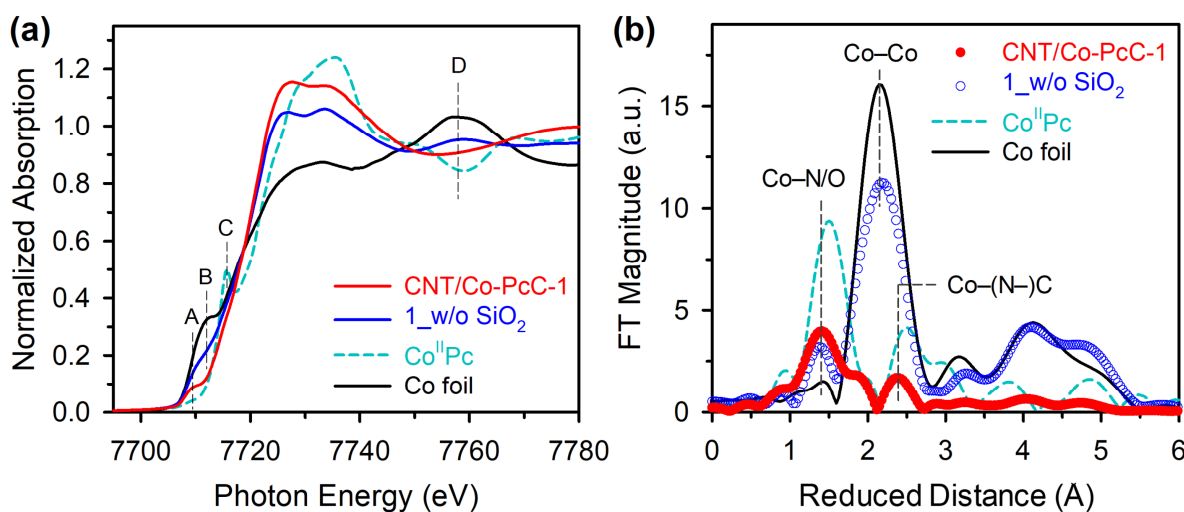
Figure 5.3. (a) Co K-edge XANES spectra and (b) RDFs of k^3-weighted EXAFS spectra of CNT/Co-PcC-1, CNT/Co-PcC-1_w/o SiO_2, $Co^{II}Pc$, and Co foil.

5.3.2. HER Activity of CNT/Co-PcC Catalysts

The electrocatalytic HER activities of CNT/Co-PcC-1 and 1_w/o SiO₂ were compared in both acidic (0.5 M H₂SO₄) and alkaline (1 M KOH) solutions (**Figure 5.4**). In the acidic electrolyte, it was found that the silica coated catalyst (CNT/Co-PcC-1) exhibited higher HER activity than 1_w/o SiO₂, evidenced with a positive shift of overpotential by 15 mV at −10 mA cm⁻² (**Figure 5.4a**). In 1 M KOH, the apparent HER activity only slightly differs between the two catalysts (**Figure 5.4b**). However, considering the Co contents in the two catalysts (1.4 and 3 wt% for CNT/Co-PcC-1 and 1_w/o SiO₂, respectively, analyzed by ICP-OES), CNT/Co-PcC-1 shows 3 and 2.4 times higher mass activity (normalized by the Co contents) than 1_w/o SiO₂ catalyst in 0.5 M H₂SO₄ and 1 M KOH, respectively (**Figures 5.4c,d**). CNT/Co-PcC-1 catalyst is mainly composed of Co–N$_x$ sites, while the 1_w/o SiO₂ catalyst contains significant amounts of Co@C species. Therefore, Co–N$_x$ sites contribute to the high HER activity while the presence of the Co@C species is responsible for the lower mass activity.
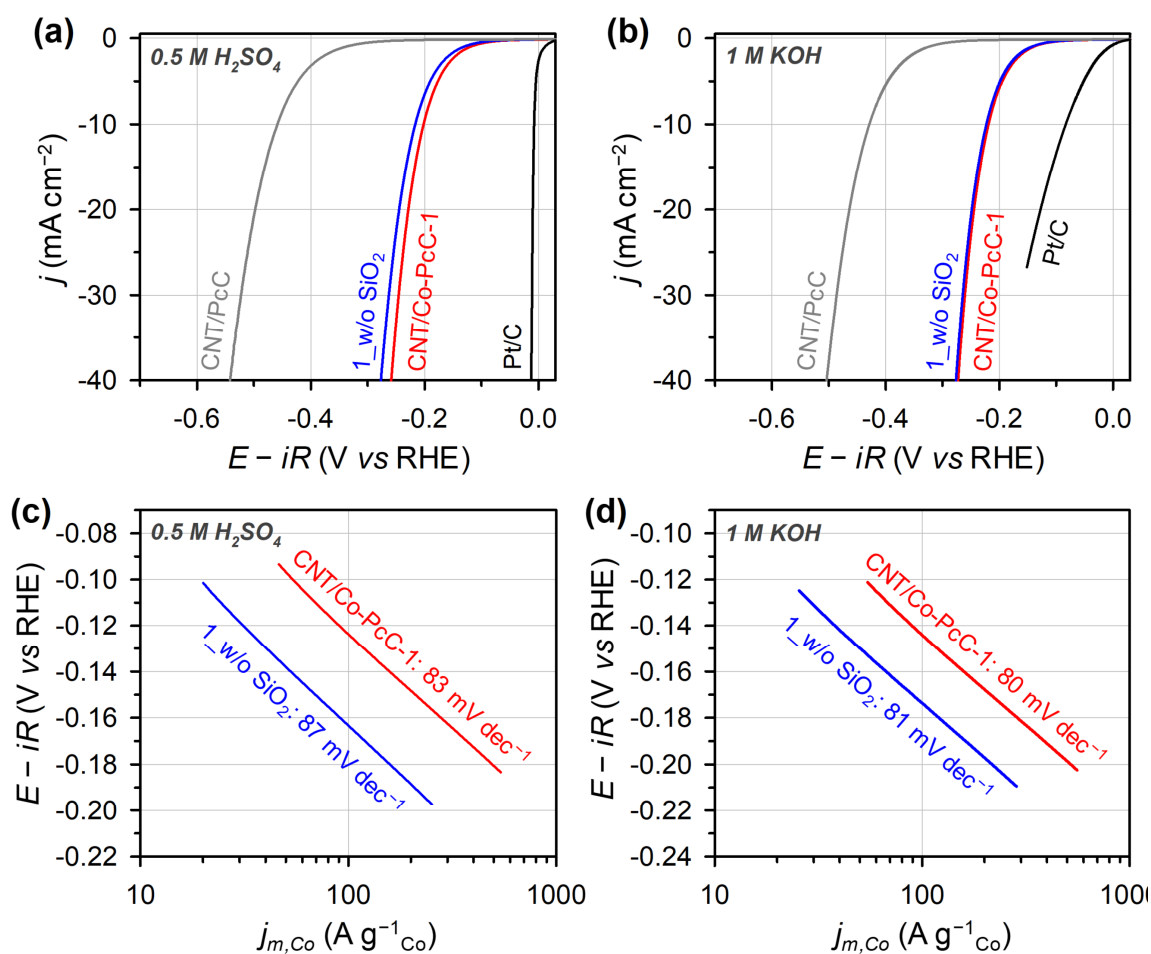
Figure 5.4. (a,b) HER polarization curves and (c,d) corresponding Tafel plots of CNT/Co-PcC-1, 1_w/o SiO₂, CNT/PcC, and Pt/C catalysts measured in (a,c) 0.5 M H₂SO₄ and (b,d) 1 M KOH.

Besides Co–N_x and Co@C sites, CNT/Co-PcC-1 and 1_w/o SiO$_2$ also contain N-doped carbon species (C–N). To investigate the catalytic activity of C–N species, Co-free N-doped carbon catalyst (CNT/PcC) was also prepared in the same manner as CNT/Co-PcC except the use of metal-free phthalocyanine precursor. The CNT/PcC catalyst exhibits much inferior HER activity to CNT/Co-PcC (**Figures 5.4a,b**). The overpotential required to drive −10 mA cm^{-2} is −202 ± 2 and −459 ± 4 mV in 0.5 M H$_2$SO$_4$ and −219 ± 2 and −429 ± 3 mV in 1 M KOH for CNT/Co-PcC-1 and CNT/PcC, respectively. The huge activity difference suggests the importance of Co–N_x sites in the HER, while C–N sites have only a marginal catalytic capability.

Improving the HER activity in alkaline solutions is important because even the best Pt-based catalysts suffer from sluggish HER kinetics at high pH. The HER rate on Pt is around ~200 times slower in alkaline electrolytes than in acidic electrolytes.[43] This slow alkaline HER activity of Pt catalysts has been explained by the sluggish supply of H from the dissociation of H$_2$O,[44] or unfavorable H-binding energy in alkaline electrolytes.[45] Comparing CNT/Co-PcC-1 with Pt/C, it is noteworthy that the HER activity of CNT/Co-PcC-1 is comparable to a commercial Pt/C catalyst in 1 M KOH (**Figure 5.4b**). If the costs of Pt (30 $ g_{Pt}^{-1}) and Co (0.067 $ g_{Co}^{-1}) are considered,[46,47] our CNT/Co-PcC-1 catalysts is 40 times more cost-efficient than Pt/C (**Figure 5.5**). More significantly, the efficiency difference would be larger at a higher current density, relevant to practical operation conditions. In this regard, we suggest that CNT/Co-PcC catalyst is promising as the replacement of Pt/C in alkaline water electrolyzer.
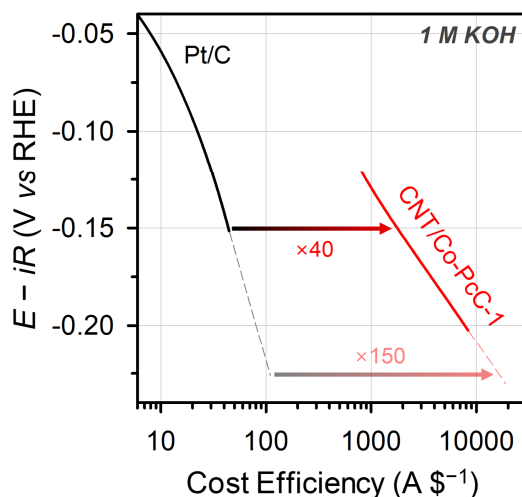
Figure 5.5. Cost efficiency of CNT/Co-PcC-1 and Pt/C for the HER. The value was obtained by normalization of the HER mass activity (**Figure 5.4d**) by the price of Co and Pt metals.[46,47]

To further investigate the role of Co in the Co–N_x sites, we prepared other metal-based CNT/M-PcC catalysts from different metal phthalocyanine precursors (M = Mn, Fe, Ni, and Cu). It was found that the HER activities of other CNT/M-PcC were much lower HER activity than that of CNT/Co-PcC (**Figure 5.6**), which is consistent to previous results that investigated the metal effect of M–N/C catalysts on the HER activity.[48,49] Since any metallic phase was not detected by XRD for our CNT/M-PcC catalysts, the CNT/M-PcC catalysts were regarded to mainly contain M–N_x sites. Therefore, we can conclude that Co–N_x sites are the most active among other M–N_x species. This result also indirectly proves that the molecular Co–N_x sites are involved in the HER electrocatalysis.
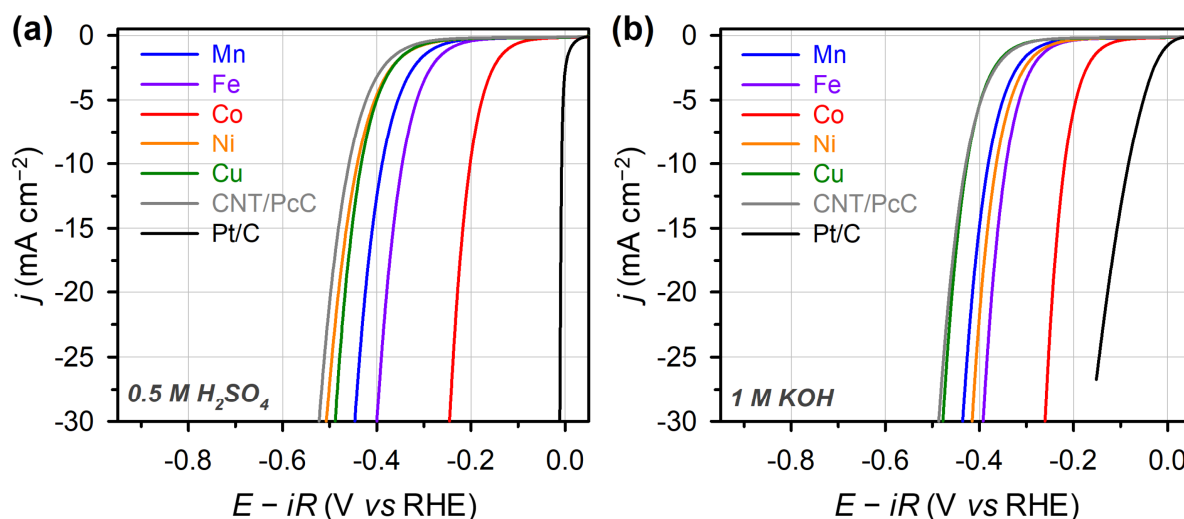
Figure 5.6. HER polarization curves of CNT/M-PcC, CNT/PcC, and Pt/C catalysts measured in (a) 0.5 M H_2SO_4 and (b) 1 M KOH.

5.3.3. Control of Active Site Density

To prepare CNT/Co-PcC catalysts with controlled ratios of Co–N_x and Co@C sites, we synthesized a series of samples by controlling synthetic parameters such as the amount of $Co^{II}Pc$ precursor and high-temperature pyrolysis time (detailed information in section *5.2.1.* and **Table 5.1**). The prepared four samples were also extensively characterized using XRD, XPS, ICP-OES, and XAS (**Figures 5.7** and **5.8**, and **Tables 5.2** and **5.3**). First, we increased a mass ratio of CNT to $Co^{II}Pc$ in the precursor mixture to 3.0 to yield CNT/Co-PcC-3 catalyst. Despite three-fold increase in the amount of $Co^{II}Pc$ precursor in CNT/Co-PcC-3 compared to that in CNT/Co-PcC-1, only a small amount of Co NPs (**Figure 5.7a**) was generated, confirming the role of silica layer that suppresses the formation of aggregated Co NPs. However, when the silica coating was not applied, sharp and highly intense peaks corresponding to metallic Co were detected by XRD (3_w/o SiO_2, **Figure 5.7a**). In addition, we prepared another set of catalysts by extending the pyrolysis time from 3 h to 24 h for silica-uncoated samples to induce more severe destruction of $Co^{II}Pc$ precursors and aggregation of Co atoms under

the high-temperature treatments (denoted as 1_w/o SiO$_2$_24h and 3_w/o SiO$_2$_24h). The increased pyrolysis time led to the decrease in the amount of Co NPs, indicating the Co NPs formed during the pyrolysis were removed by the acid-washing step (**Figure 5.7a**). Regardless of the synthetic conditions, the surface Co species in all the samples were found to exist in oxidized states (Co^{2+}) without exposed metallic Co (**Figure 5.7b**), implying the Co NPs detected by the XRD are encapsulated in carbon shells. N 1s XPS spectra could be deconvoluted into five peaks as described above (**Figure 5.7c**).
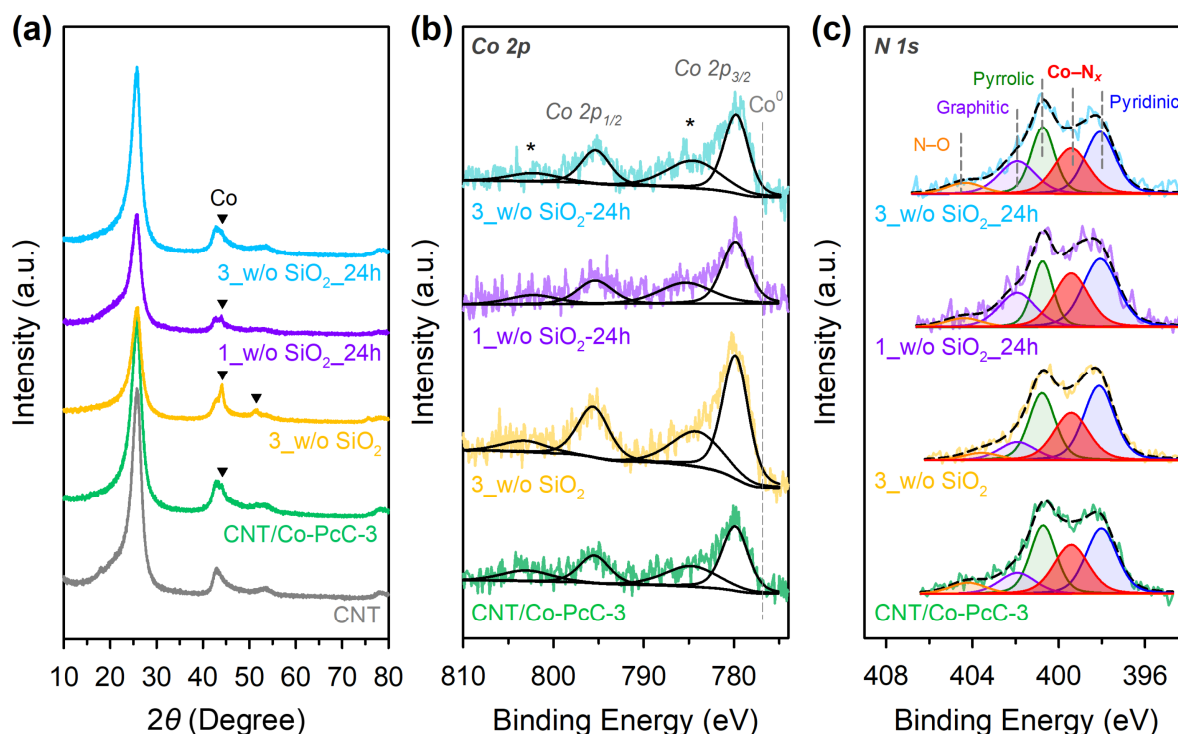
Figure 5.7. (a) XRD pattern, (b) XPS Co 2p, and (c) N 1s spectra and deconvoluted peaks of other series of CNT/Co-PcC catalysts.

Table 5.2. Co contents of a series of CNT/Co-PcC catalysts analyzed by ICP-OES.

Sample	Co Content (wt%)
CNT/Co-PcC-1	1.39
1_w/o SiO$_2$	2.99
1_w/o SiO$_2$_24h	1.76
CNT/Co-PcC-3	1.45
3_w/o SiO$_2$	3.79
3_w/o SiO$_2$_24h	1.41

5.3.4. Structure–Activity Correlation

To gain structural insights into the Co-based sites in a series of CNT/Co-PcC catalysts, we conducted EXAFS fitting analyses (**Figure 5.8**). The coordination number and bond distances obtained from the EXAFS fittings are summarized in **Table 5.3**. CNT/Co-PcC-1 (red-colored data set) catalyst was found to contain only Co–N/O interactions, as the addition of another shell to fit the shoulder peak at 1.9 Å resulted in very poor fitting results, indicating this peak is adventitious. The coordination number and the bond distance for Co–N/O shell are 5.0 ± 1.0 and 1.93 ± 0.02 Å, respectively. The coordination number of 5.0 may indicate the formation of the additional bonds to Co–N_4 sites in Co^{II}Pc during the catalyst synthesis. This is consistent with the appearance of the pre-edge peak A in the XANES spectrum of CNT/Co-PcC-1 (**Figure 5.3a**).
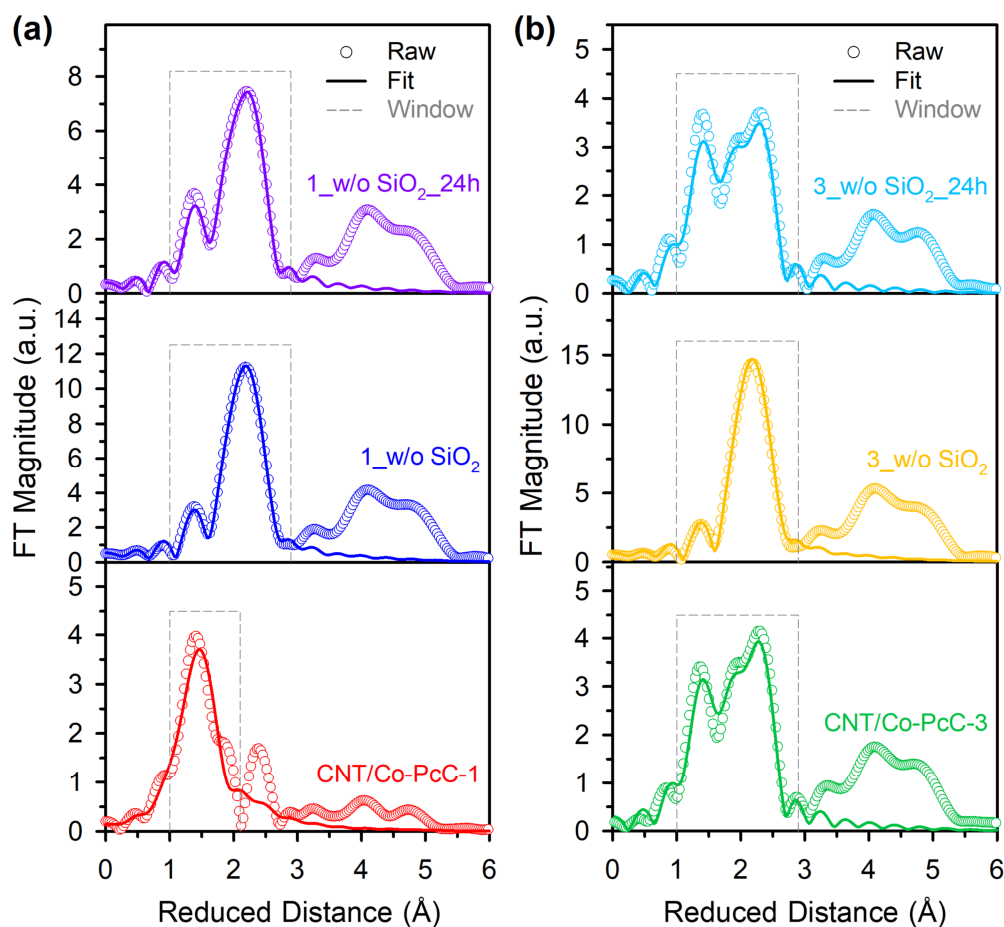
Figure 5.8. RDFs of k^3-weighted EXAFS spectra and EXAFS fit of (a) CNT/Co-PcC-1 series and (b) CNT/Co-PcC-3 series.

The interatomic distance for Co–N/O of the other samples is commonly within 1.93 ± 0.02 Å. However, the relative peak intensity for Co–N/O is smaller due to presence of the additional RDF peaks corresponding to Co–Co from metallic Co. It is worthwhile to note that XAS is bulk-averaging technique, and thus the decrease in the Co–N/O coordination number ($CN_{Co–N/O}$) for the other samples compared with CNT/Co-PcC-1 can be ascribed to the presence of Co@C species because Co metal does not show Co–N/O scattering signal. On the basis of this rationale, we could estimate the ratio of Co–N$_x$ using the coordination number ratio.

$$\frac{CN_{Co-N/O}}{CN_{Co-N/O} + CN_{Co-Co}}$$

Table 5.3. Summary of EXAFS fitting parameters of CNT/Co-PcC catalysts.

Sample	Shell	CN [a]	ΔE_0 (eV)	R (Å)	σ^2 ($\times 10^{-3}$ Å^{-2}) [b]
CNT/Co-PcC-1	Co–N/O	5.0 ± 1.0	8 ± 2	1.93 ± 0.02	15.3 ± 4.5
1_w/o SiO$_2$	Co–N/O	2.6 ± 0.2	7 ± 2	1.93 ± 0.03	15.3 [c]
	Co–Co	4.0 ± 0.1	6.9 [d]	2.49 ± 0.00	5 [e]
1_w/o SiO$_2$_24h	Co–N/O	3.3 ± 0.3	7 ± 2	1.92 ± 0.02	15.3 [c]
	Co–Co	2.7 ± 0.1	6.9 [d]	2.49 ± 0.00	5 [e]
CNT/Co-PcC-3	Co–N/O	4.0 ± 0.3	8 ± 2	1.94 ± 0.02	15.3 [c]
	Co–Co	1.5 ± 0.1	6.9 [d]	2.49 ± 0.01	5 [e]
3_w/o SiO$_2$	Co–N/O	1.9 ± 0.4	6 ± 4	1.92 ± 0.05	15.3 [c]
	Co–Co	5.2 ± 0.2	6.9 [d]	2.49 ± 0.00	5 [e]
3_w/o SiO$_2$_24h	Co–N/O	3.8 ± 0.3	8 ± 2	1.94 ± 0.02	15.3 [c]
	Co–Co	1.3 ± 0.1	6.9 [d]	2.50 ± 0.01	5 [e]

[a] Coordination number
[b] Debye-Waller factor
[c] This value was fixed according to the EXAFS fitting result of CNT/Co-PcC-1
[d] This value was fixed according to the EXAFS fitting result of Co foil
[e] This value was fixed according to the EXAFS fitting result of Co foil

The coordination number ratio, $CN_{Co–N/O}/(CN_{Co–N/O} + CN_{Co-Co})$, of the catalysts and their HER mass activity at −0.2 V (*vs* RHE) measured in both alkaline and acidic solutions are correlated (**Table 5.4**). Interestingly, we could obtain a nearly linear relation between the $CN_{Co–N/O}$ proportion and the HER mass activity (**Figure 5.9**). Higher $CN_{Co–N/O}/(CN_{Co–N/O} + CN_{Co-Co})$ value means that there are relatively larger quantities of Co–N$_x$ sites than Co@C species in the catalyst. Therefore, the linear

correlation suggests that the Co–N_x sites are the main active species for the HER both in alkaline and acidic electrolytes.
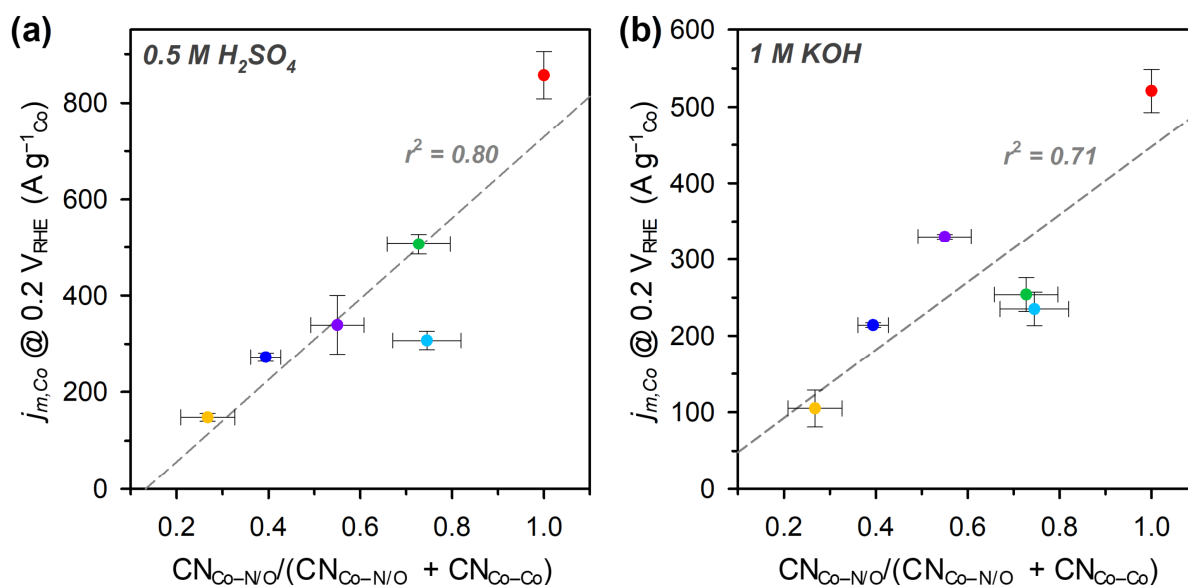
Figure 5.9. Correlation between the HER mass activity and the fraction of the coordination number for Co–N/O ($CN_{Co–N/O}$) in (a) 0.5 M H_2SO_4 and (b) 1 M KOH.

Table 5.4. Summary of the fraction of $CN_{Co–N/O}$ analyzed by the EXAFS fitting and the HER mass activity in 0.5 M H_2SO_4 and 1 M KOH of the series CNT/Co-PcC catalysts.

Sample	$CN_{Co–N/O}$ /$(CN_{Co–N/O} + CN_{Co–Co})$	$j_{m,Co}$ @ 0.2 V_{RHE} (A g^{-1}), 0.5 M H_2SO_4	$j_{m,Co}$ @ 0.2 V_{RHE} (A g^{-1}), 1 M KOH
CNT/Co-PcC-1	1.0	857 ± 48	521 ± 28
1_w/o SiO$_2$	0.39 ± 0.03	272 ± 9	214 ± 3
1_w/o SiO$_2$_24h	0.55 ± 0.06	339 ± 61	330 ± 3
CNT/Co-PcC-3	0.73 ± 0.07	507 ± 21	254 ± 22
3_w/o SiO$_2$	0.27 ± 0.06	148 ± 8	105 ± 24
3_w/o SiO$_2$_24h	0.75 ± 0.07	307 ± 19	235 ± 22

Turnover frequency (TOF), representing the reaction rate per a single active site, of CNT/Co-PcC-1 was calculated to be 0.26 H_2 s^{-1} per a Co–N_x site at −0.2 V (vs RHE), assuming all the sites are equally active. This value is rather lower than recently reported Co–N/C catalysts by Müllen et al. and Tour et al., which exhibited TOFs of 6.5 and 1.2 H_2 s^{-1} site^{-1},[30,31] respectively. We note, however, that during the preparation of their catalysts, second heat-treatment step or NH$_3$-activation process was included. Such a synthetic step has been known to further activate the M–N/C catalysts, thereby

increasing the surface area of catalysts and exposing more active sites.

It is noteworthy that in other previous works suggesting Co@C species as the HER active site, the catalysts were prepared by the pyrolysis of a precursor mixture comprising Co, N, and C.[32–36] This is the same synthetic approach to make Co–N/C catalysts primarily composed of Co–N_x sites except some additional modifications such as second heat-treatments and acid-treatments. We therefore assume that previously reported Co@C catalysts are not completely free of Co–N_x sites, which might participate in the HER. A simple calculation under the given assumption of TOF: 0.5 H_2 s^{-1} $site^{-1}$, Co content: 0.5 wt%, and the catalyst loading: 0.5 mg cm^{-2} results in the expected current density of 4.3 mA cm^{-2}. Only 0.5 wt% Co–N_x sites can deliver a considerable HER activity, while 0.5 wt% out of few wt% is anticipated to be hardly distinguished by means of spectroscopies. In addition, Co–N_x sites only could be detected atomic-resolution TEM method, and thus the presence of the atomically dispersed Co–N_x active sites is prone to be excluded.

5.3.5. Reaction Kinetics Study

HER proceeds through three well-known elementary steps: Volmer, Tafel, and Heyrovsky reactions. First, Volmer step (1) is proton discharge reaction leading to hydrogen adsorption onto the active site; we obtain Tafel slope of (~118 mV dec^{-1}) if Volmer step is the RDS. The combination of two adsorbed hydrogen (H_{ads}) producing hydrogen gas (Tafel step) yields Tafel slope of ~30 mV (2). Tafel slope of ~39 mV results from Heyrovsky step (3) describing electrochemical desorption of the adsorbed hydrogen. In alkaline solutions, the hydrogen atoms are supplied from H_2O molecules (4,5).[50]

$$
\begin{aligned}
\textit{Volmer (acid):} \quad & H^+ + e^- + S \rightarrow S\text{–}H_{ads} & (1) \\
\textit{Tafel:} \quad & S\text{–}H_{ads} + S\text{–}H_{ads} \rightarrow H_2 & (2) \\
\textit{Heyrovsky (acid):} \quad & S\text{–}H_{ads} + H^+ + e^- \rightarrow H_2 & (3) \\
\textit{Volmer (alkali):} \quad & H_2O + e^- \rightarrow S\text{–}H_{ads} + OH^- & (4) \\
\textit{Heyrovsky (alkali):} \quad & S\text{–}H_{ads} + H_2O + e^- \rightarrow H_2 + OH^- & (5)
\end{aligned}
$$
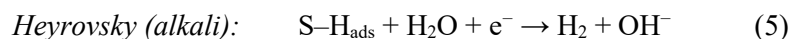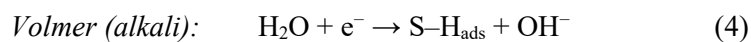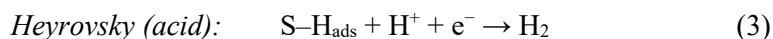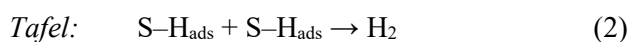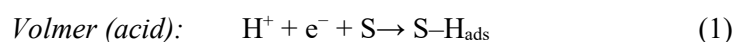
Here, S stands for the active site. HER catalysts follow either Volmer–Tafel or Volmer–Heyrovsky reaction pathway. However, we note that the involvement of Tafel reaction is unlikely on the Co–N/C catalysts as the atomically dispersed Co–N_x sites are isolated,[51] and the Volmer–Heyrovsky is plausible. The Tafel slope of around 80 mV dec^{-1} for the CNT/Co-PcC-1 catalyst (**Figures 5.4c,d**) is not well explained by the known models. It is attributed that the typical Tafel slope values of 30, 39, 118 mV dec^{-1} explaining the HER kinetics were obtained using very simplified kinetics model and

extreme assumptions.[50] Tilak et al. suggested a more realistic, generalized expression of Tafel slope for the HER under the assumption of steady-state and Temkin isotherm of adsorbed hydrogen intermediate.[52] They explained that the Tafel slope of ~90 mV dec^{-1} (at 298 K) can be obtained when slow-Volmer and subsequent fast-Heyrovsky steps are involved under the conditions where the coverage is very small and the rate constant for Heyrovsky step is few tens times higher than that of Volmer step.[52]
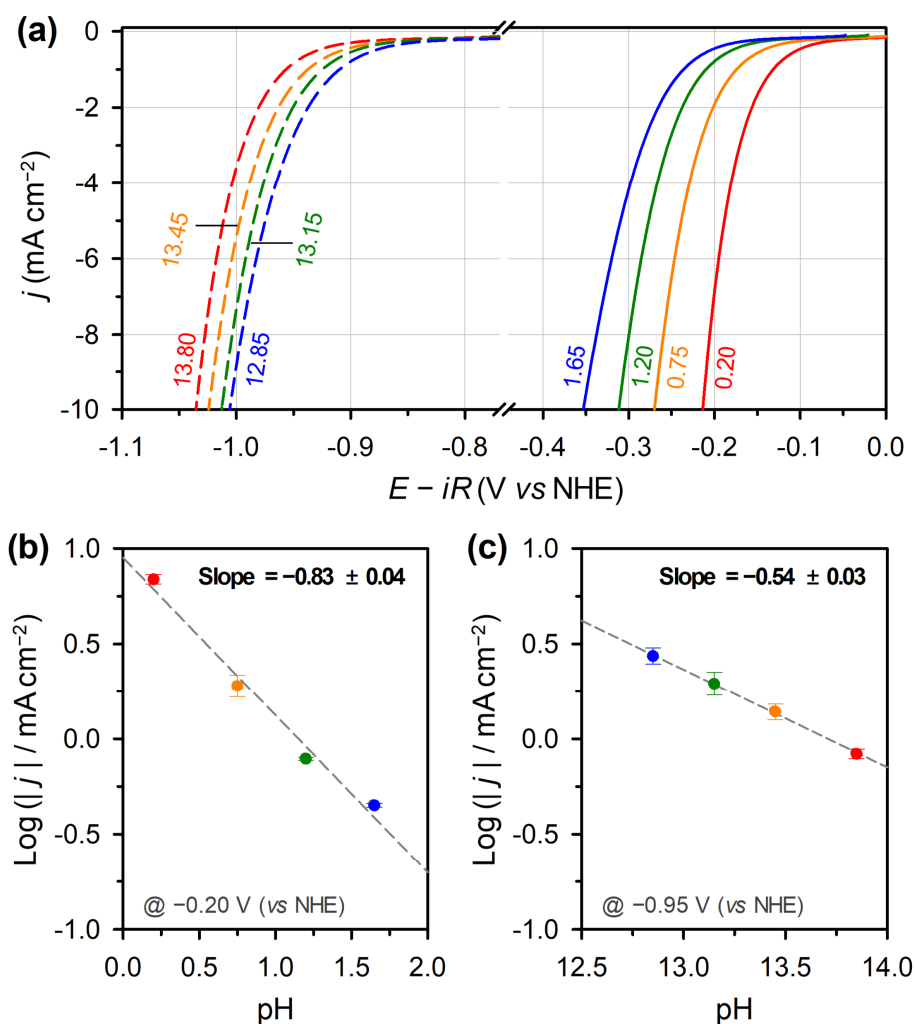
Figure 5.10. (a) HER polarization curves of the CNT/Co-PcC-1 catalyst measured at various pH. (b,c) Logarithmic current density plotted versus pH (b) at low pH region (0.20–1.65) and (c) at high pH region (12.85–13.80).

The pH-dependence of the reaction rate provides complementary kinetic information to Tafel slope and therefore allows us to better understand the HER kinetics of Co–N$_x$ sites. We performed the HER measurements with the CNT/Co-PcC-1 catalyst with ~100% Co–N$_x$ sites in acidic and alkaline electrolytes with various pH. The pH of the acidic and alkaline solutions was adjusted by changing the ratio of H$_2$SO$_4$: Na$_2$SO$_4$ and KOH : K$_2$HPO$_4$, respectively (to a final molarity of 0.5 and 1 M,

respectively). The pH-dependent HER activity of the CNT/Co-PcC catalyst is shown in **Figure 5.10a**. The HER polarization curves shift consistently to the negative potential as pH increases. However, the shift with respect to the pH appears larger at low pH (0.20–1.65) than high pH (12.85–13.80). Linear fitting of the log j plot versus pH gives us a slope, $(\partial \log j/\partial \text{pH})_E$, directly relating to the reaction order (**Figures 5.10b,c**).

At the low pH (0.20–1.65), a slope of -0.83 ± 0.04 is obtained. The reaction order in the acidic electrolyte is therefore (**Figure 5.10b**)

$$(\partial \log j/\partial a_{H^+})_E = -(\partial \log j/\partial \text{pH})_E = 0.83 \pm 0.04$$

where a_{H^+} indicates the proton activity. The value approximates to ~1, indicating that the reaction rate on the CNT/Co-PcC-1 catalyst follows near first-order kinetics with respect to the proton activity. In the Tilak's work,[52] the reaction order under Temkin adsorption mode, can be expressed as

$$\text{Reaction order} = 2 - \theta \times (1 + k_H/k_V)$$

where θ, k_H, and k_V stand for the coverage, the forward rate constant for Heyrovsky and Volmer steps, respectively. If Heyrovsky step is the RDS, k_H/k_V is close to 0. In this case, unity reaction order is obtained at a high coverage (i.e., $\theta \to 1$), which however results in Tafel slope of ~118 mV dec^{-1} (at 298 K) being not consistent with our results.[52] Tafel slope and reaction order possibly suggest that Volmer step is the RDS for CNT/Co-PcC-1 catalyst.

In the alkaline solution (pH 12.85–13.80), the reaction order with respect to the activity of OH$^-$ (a_{OH^-}) is measured as (**Figure 5.10c**)

$$(\partial \log j/\partial a_{OH^-})_E = -(\partial \log j/\partial \text{pOH})_E = (\partial \log j/\partial \text{pH})_E = -0.54 \pm 0.03$$

This fractional reaction order of ca. -0.5 is not well explained using the traditional Volmer and Heyrovsky steps for the alkaline HER (eqs. 2, 4, 5). Trasatti et al. observed -0.5 reaction order with respect to OH$^-$ activity for the alkaline HER on Co$_3$O$_4$ surface.[53] The fractional reaction order in Trasatti's work was ascribed to the reaction rate limited by Volmer step in the presence of the interfacial potential built by OH$^-$ activity-dependent surface charged species.

$$\text{S–OH} + \text{OH}^- \rightleftharpoons \text{S–O}^- + \text{H}_2\text{O}$$
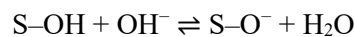
In addition, the existence of [Co$^\text{II}$–OH] state at high pH and low potential (where the HER occurs) was suggested by a Pourbaix diagram for a Co-pyridyl complex.[54] Similar to those cases, Co–N$_x$ sites in CNT/Co-PcC may be present in OH-adsorbed resting state in alkaline conditions, which is

equilibrated with the charged oxo species. Therefore, pH-dependence experiments combined with the Tafel slope analyses suggest that the RDS for the HER on our CNT/Co-PcC catalyst is the first hydrogen adsorption (Volmer step).

We next explored temperature-dependent HER activity to access the activation energy of CNT/Co-PcC-1 catalyst. To this end, we measured the HER activity of the CNT/Co-PcC-1 catalyst at varied temperatures from 25 to 55 °C in both 0.5 M H_2SO_4 and 1 M KOH (**Figure 5.11**).
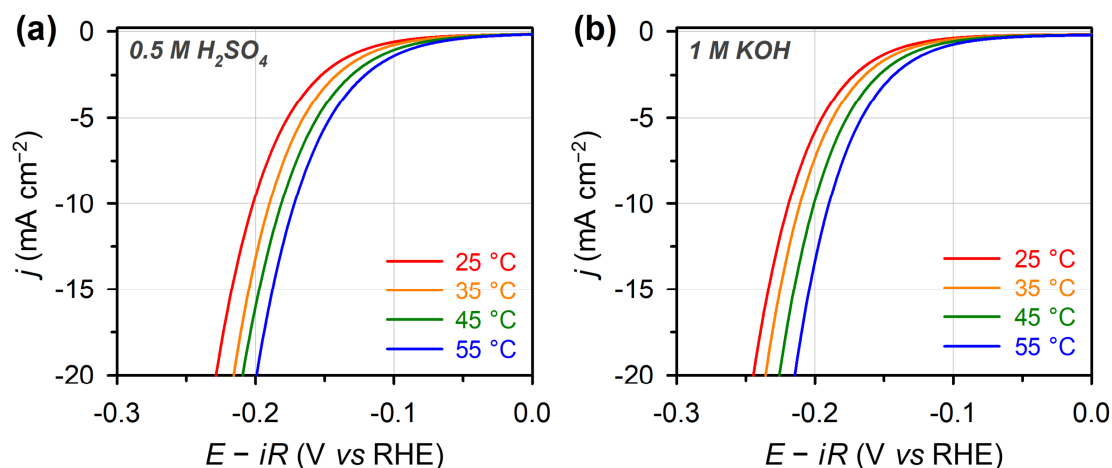
Figure 5.11. HER polarization curves of the CNT/Co-PcC-1 catalyst at various reaction temperatures measured in (a) 0.5 M H_2SO_4 and (b) 1 M KOH.

The variation of the HER exchange currents extracted from Tafel equation can be depicted by the temperature change according to the Arrhenius equation[55]

$$\left(\frac{\partial \log i_0}{\partial(1/T)}\right) = -\frac{E_a}{\ln(10) \times R}$$

where i_0, T, E_a, and R represent the exchange current, the temperature, the apparent activation energy, and the universal gas constant (8.314 J K^{-1} mol^{-1}), respectively.

Figure 5.12 shows the Arrhenius plots for the CNT/Co-PcC-1 catalyst. The data were well fitted to a line resulting in a slope from which the E_a values of 28 ± 2 and 25 ± 2 kJ mol^{-1} were obtained in 0.5 M H_2SO_4 and 1 M KOH, respectively. We note that the activation energy of Co–N/C-type catalyst is determined for the first time in this work. The activation energies of CNT/Co-PcC-1 were compared with those of representative catalysts (**Table 5.5**). Pt(110) single crystal, which has been shown to exhibit the highest activity for the HER, had the E_a value of 9.5 and 23 kJ mol^{-1} in acidic and alkaline solutions, respectively.[55,56] Pt/C, commonly used for practical application, was found to possess the activation barrier of ~16 and 29 kJ mol^{-1} at low and high pH, respectively.[45,57,58]

Reported Pt catalysts that we surveyed have shown the activation energy of on average 14 and 32 kJ mol^{-1}.[55–58] Notably, when the E_a values of CNT/Co-PcC-1 are compared with those of Pt catalysts, the CNT/Co-PcC-1 catalyst possessed similar higher activation barrier to Pt at high pH. In addition, the CNT/Co-PcC-1 catalyst showed the lower activation barrier than non-precious Ni and Co metals.[59,60] Therefore, Co–N/C shows a better promise as a replacement of Pt in alkaline water electrolysis by further optimization of active site structure and increased active site density.
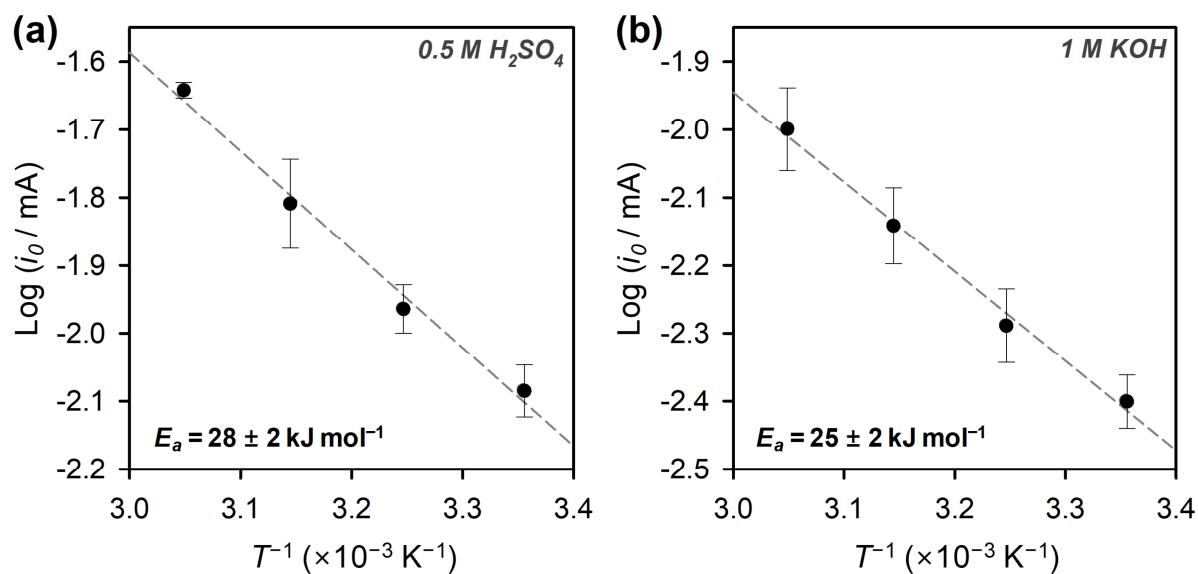
Figure 5.12. Arrhenius plots for the CNT/Co-PcC-1 measured in (a) 0.5 M H$_2$SO$_4$ and (b) 1 M KOH.

Table 5.5. Summary of the activation energies of the CNT/Co-PcC-1 and some reported catalysts.

Catalyst	Electrolyte	E_a (kJ mol^{-1})	Reference
CNT/Co-PcC	0.5 M H$_2$SO$_4$	28 ± 2	This work
	1 M KOH	25 ± 2	
Pt(111)	0.05 M H$_2$SO$_4$	18	
Pt(110)	0.05 M H$_2$SO$_4$	9.5	55
Pt(100)	0.05 M H$_2$SO$_4$	12	
Pt(111)	0.1 M KOH	46	56
Pt(110)	0.1 M KOH	23	
Pt/C	0.1 M KOH	28.9 ± 4.3	57
Pt/C	PEM (pH ~ 0)	16 ± 2	58
Pt/C	0.1 M KOH	29.6 ± 0.4	45
Ni	30 wt% KOH	38.1	59

| Co | | 60.4 | |
| Co | 30 wt% KOH | 84 | 60 |

5.3.6. Durability and Stability Tests

The long-term durability/stability of electrocatalysts is highly important for practical application. Durability and stability stand for the catalyst's capability to retain the initial activity during the potential cycling and under constant current/potential conditions, respectively. We assessed the durability and stability of CNT/Co-PcC-1 catalyst by the potential cycling tests for 5,000 times and chronoamperometry (CA). For the measurements, the catalyst was deposited onto a piece of carbon paper for efficient removal of produced H_2 gas on the electrode surface. **Figures 5.13a** and **5.13b** shows the HER polarization curves before (solid curves) and after (dashed curves) 5,000 cyclic voltammetry tests between 0.1 and −0.4 V (*vs* RHE, without *iR*-correction) at a scan rate of 100 mV s^{-1} in 0.5 M H_2SO_4 and 1 M KOH, respectively. A slight decline of the HER activity was observed in the acidic electrolyte, evidenced by 27 mV negative shift of the potential at −10 mA cm^{-2}. In contrast, no deactivation was observed in 1 M KOH, indicating our CNT/Co-PcC-1 catalyst is more durable for the potential cycling in alkaline solutions. Next, the stability of CNT/Co-PcC-1 and Pt/C catalysts was examined at a constant applied potential (**Figures 5.13c,d**). In acidic solution, the CNT/Co-PcC-1 catalyst could stably deliver the current, and 69% and 62% of the current were retained from the initial current density of −10 and −20 mA cm^{-2} after 15 and 30 h operation, respectively (**Figure 5.13c**). Whereas, Pt/C catalyst suffered a severe deactivation to less than 20%. Importantly, CNT/Co-PcC-1 maintained its initial activity almost without a decline in the current during 20–30 h of stability test in 1 M KOH (**Figure 5.13d**). In contrast, the HER activity Pt/C catalyst rapidly declined to less than 24–27% of the initial current density just within 5 h. Therefore, the durability/stability tests in combination with the activation energy measurement suggest that CNT/Co-PcC-1 catalyst would be more suitable than Pt-based catalysts for the water electrolysis in alkaline conditions.

To investigate the change in the chemical states of surface species, we carried out XPS measurements of the catalyst films after the stability (CA) tests. We noted that Co 2p XPS spectra were too noisy due to low concentration of Co. Instead, the changes in the N 1s XPS spectra were analyzed as shown in **Figure 5.14**. For comparison, the catalyst film immersed in 0.5 M H_2SO_4 and 1 M KOH at open circuit voltage (OCV, no current flow conditions) for around 20 h was also prepared. In 0.5 M H_2SO_4, major changes in the N 1s spectra after the CA test are the decreased areas for pyridinic and pyrrolic peaks and an increased peak area at 402 eV corresponding to quaternary N (**Figure 5.14a**). These alterations can be explained by protonation of pyridinic and pyrrolic N atoms, where the signals for those species appear at around 402 eV, overlapping with the peak for the

quaternary N.[61–63] In 1 M KOH, a diminished peak area for pyridinic N is remarkable after the CA test (**Figure 5.14b**). This is possibly attributed to the formation of pyridone N species.[64,65] However, in the both electrolytes, the spectral modifications were also observed after the catalysts were just immersed in the electrolytes without current flow. These results suggest that the transformation of the doped N species is not related to the HER electrocatalysis.
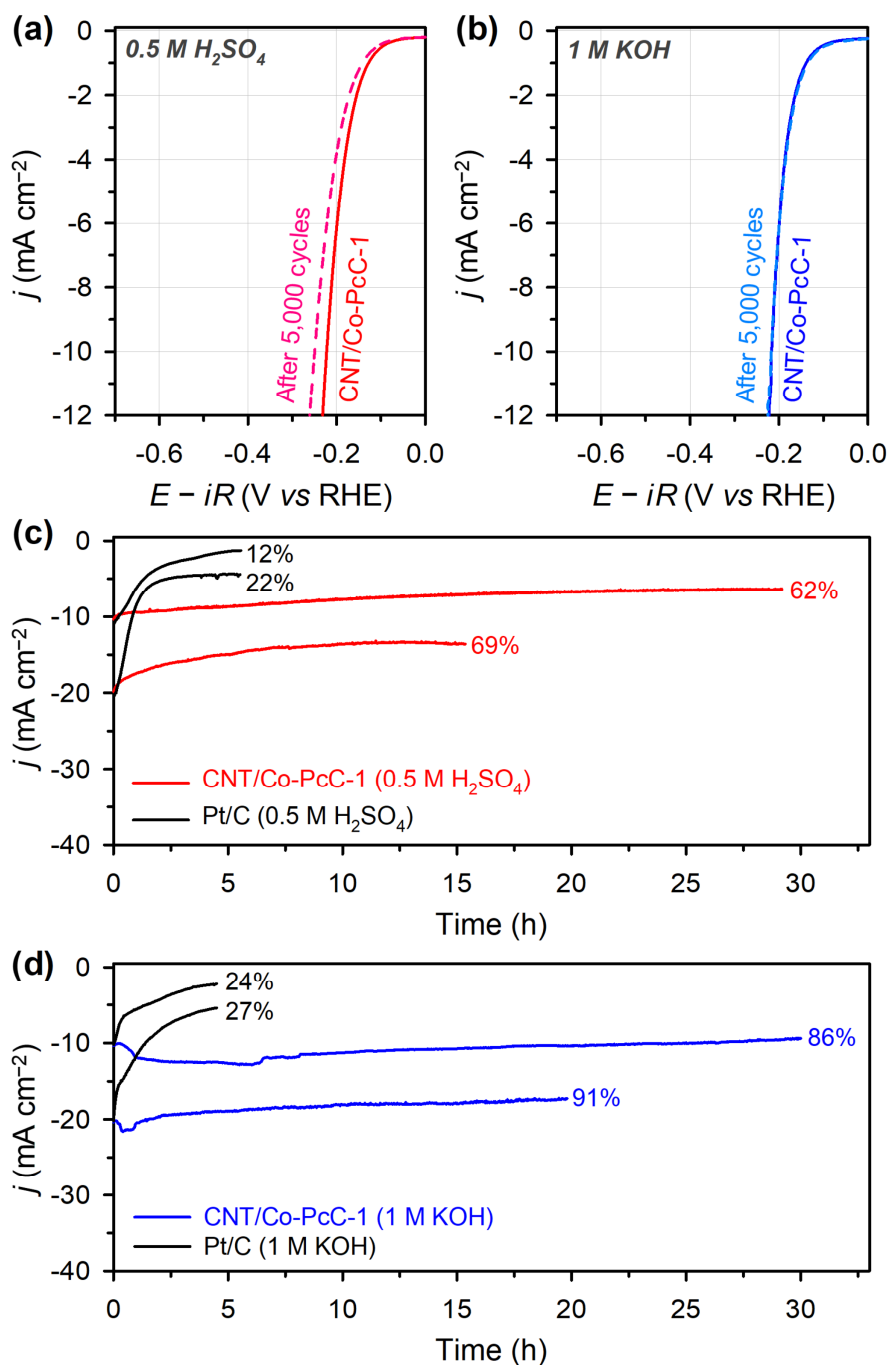
Figure 5.13. (a,b) HER polarization curves of CNT/Co-PcC-1 before and after 5,000 potential cycling tests measured in (a) 0.5 M H_2SO_4 and (b) 1 M KOH. (c,d) Chronoamperometry responses for the CNT/Co-PcC-1 and Pt/C catalysts at the potentials to drive initial current densities of −10 and −20 mA cm^{-2} measured in (c) 0.5 M H_2SO_4 and (d) 1 M KOH.
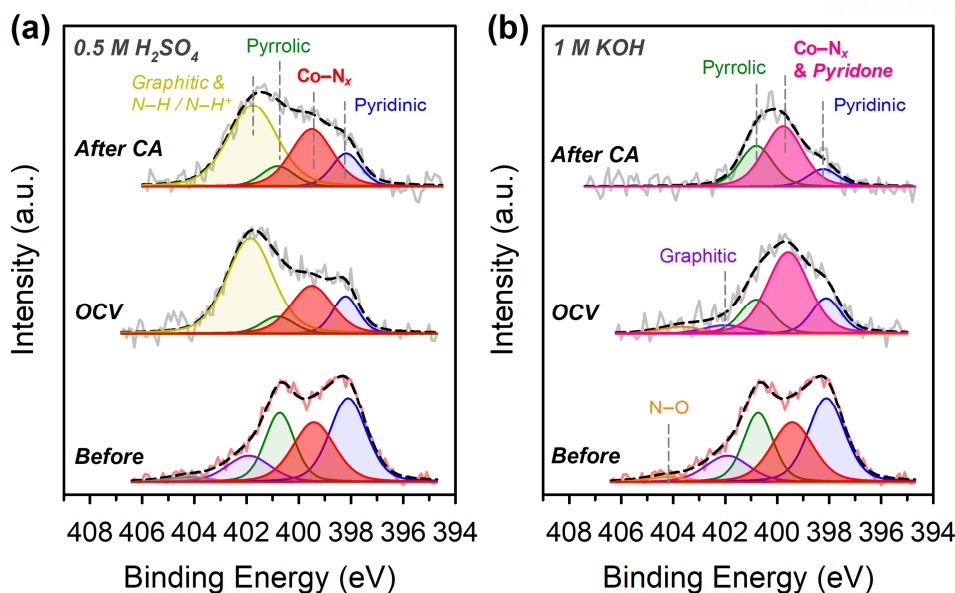
Figure 5.14. N 1s XPS spectra and deconvoluted peaks for the CNT/Co-PcC-1 catalyst before and after the CA tests in (a) 0.5 M H_2SO_4 and (b) 1 M KOH. For comparison, the catalyst film was soaked in each electrolyte at OCV (no current flow) for 20 h.

5.4. CONCLUSION

A series of Co–N/C catalysts with different ratios of Co–N_x and Co@C sites were synthesized to systematically investigate the genuine active site for the HER and detailed kinetic insights. Pyrolysis of $Co^{II}Pc$ and CNT mixture under the protection of the silica layer yielded CNT/Co-PcC catalyst with exclusive presence of Co–N_x sites. In contrast, heat-treatment of $Co^{II}Pc$-rich mixture produced large amounts of Co@C sites. On the basis of HER activity measurements and EXAFS analyses, active site structure–HER activity correlation could be established, which suggests that Co–N_x sites play a predominant role for the HER both in acidic and alkaline media, while Co@C has only marginal catalytic effect. The correlation provided an important synthetic guideline for the development of novel Co–N/C catalysts: the formation of Co@C sites is disadvantageous for the HER in terms of the loss of the active sites and the blocking the active sites. Kinetics studies *via* the pH-and temperature-dependence enabled better understanding about the RDS and the activation energy of the Co–N_x active sites for the HER. Finally, CNT/Co-PcC catalyst exhibited superior durability and stability to Pt/C catalyst. The durability and stability of CNT/Co-PcC catalyst much better than Pt/C combined with the activation energy of CNT/Co-PcC comparable to Pt catalyst in alkaline solutions proposed the potential applicability of Co–N/C catalysts in alkaline water electrolysis.

5.5. REFERENCES

(1)   Turner, J. A. *Science* **2004**, *305*, 972–974.

(2)   Lewis, N. S.; Nocera, D. G. *Proc. Natl. Acad. Sci. USA* **2006**, *103*, 15729–15735.

(3)   Walter, M. G.; Warren, E. L.; McKone, J. R.; Boettcher, S. W.; Mi, Q.; Santori, E. A.; Lewis, N. S. *Chem. Rev.* **2010**, *110*, 6446–6473.

(4)   Nørskov, J. K.; Bligaard, T.; Logadottir, A.; Kitchin, J. R.; Chen, J. G.; Pandelov, S.; Stimming, U. *J. Electrochem. Soc.* **2005**, *152*, J23–J26.

(5)   Greeley, J.; Jaramillo, T. F.; Bonde, J.; Chorkendorff, I.; Nørskov, J. K. *Nat. Mater.* **2006**, *5*, 909–913.

(6)   Jaramillo, T. F.; Jørgensen, K. P.; Bonde, J.; Nielsen, J. H.; Horch, S.; Chorkendorff, I. *Science* **2007**, *317*, 100–102.

(7)   Li, Y.; Wang, H.; Xie, L.; Liang, Y.; Hong, G.; Dai, H. *J. Am. Chem. Soc.* **2011**, *133*, 7296–7299.

(8)   Lukowski, M. A.; Daniel, A. S.; Meng, F.; Forticaux, A.; Li, L.; Jin, S. *J. Am. Chem. Soc.* **2013**, *135*, 10274–10277.

(9)   Seo, B.; Jung, G. Y.; Sa, Y. J.; Jeong, H. Y.; Cheon, J. Y.; Lee, J. H.; Kim, H. Y.; Kim, J. C.; Shin, H. S.; Kwak, S. K.; Joo, S. H. *ACS Nano* **2015**, *9*, 3728–3739.

(10)   Voiry, D.; Yamaguchi, H.; Li, J.; Silva, R.; Alves, D. C. B.; Fujita, T.; Chen, M.; Asefa, T.; Shenoy, V. B.; Eda, G.; Chhowalla, M. *Nat. Mater.* **2013**, *12*, 850–855.

(11)   Kong, D.; Wang, H.; Lu, Z.; Cui, Y. *J. Am. Chem. Soc.* **2014**, *136*, 4897–4900.

(12)   Kornienko, N.; Resasco, J.; Becknell, N.; Jiang, C.-M.; Liu, Y.-S.; Nie, K.; Sun, X.; Guo, J.; Leone, S. R.; Yang, P. *J. Am. Chem. Soc.* **2015**, *137*, 7448–7455.

(13)   Chen, W.-F.; Sasaki, K.; Ma, C.; Frenkel, A. I.; Marinkovic, N.; Muckerman, J. T.; Zhu, Y.; Adzic, R. R. *Angew. Chem., Int. Ed.* **2012**, *51*, 6131–6135.

(14)   Cao, B.; Veith, G. M.; Neuefeind, J. C.; Adzic, R. R.; Khalifah, P. G. *J. Am. Chem. Soc.* **2013**, *135*, 19186–19192.

(15)   Vrubel, H.; Hu, X. *Angew. Chem., Int. Ed.* **2012**, *51*, 12703–12706.

(16)   Wan, C.; Regmi, Y. N.; Leonard, B. M. *Angew. Chem., Int. Ed.* **2014**, *53*, 6407–6410.

(17)   Gong, Q.; Wang, Y.; Hu, Q.; Zhou, J.; Feng, R.; Duchesne, P. N.; Zhang, P.; Chen, F.; Han, N.; Li, Y.; Jin, C.; Li, Y.; Lee, S.-T. *Nat. Commun.* **2016**, *7*, 13216.

(18)   Popczun, E. J.; McKone, J. R.; Read, C. G.; Biacchi, A. J.; Wiltrout, A. M.; Lewis, N. S.; Schaak, R. E. *J. Am. Chem. Soc.* **2013**, *135*, 9267–9270.

(19)   Popczun, E. J.; Read, C. G.; Roske, C. W.; Lewis, N. S.; Schaak, R. E. *Angew. Chem., Int. Ed.* **2014**, *53*, 5427–5430.

(20)   Jiang, P.; Liu, Q.; Liang, Y.; Tian, J.; Asiri, A. M.; Sun, X. *Angew. Chem., Int. Ed.* **2014**, *53*, 12855–12859.

(21)   Shi, Y.; Zhang, B. *Chem. Soc. Rev.* **2016**, *45*, 1529–1541.

(22)   Roubelakis, M. M.; Bediako, K.; Dogutan, D. K.; Nocera, D. G. *Energy Environ. Sci.* **2012**, *5*, 7737–7740.

(23)   Beyene, B. B.; Mane, S. B.; Hung, C.-H. *Chem. Commun.* **2015**, *51*, 15067–15070.

(24)   Connolly, P.; Espenson, J. H. *Inorg. Chem.* **1986**, *25*, 2684–2688.

(25)   Hu, X.; Brunschwig, B. S.; Peters, J. C. *J. Am. Chem. Soc.* **2007**, *129*, 8988–8998.

(26)   Solis, B. H.; Hammes-Schiffer, S. *J. Am. Chem. Soc.* **2011**, *133*, 19036–19039.

(27)   Jacques, P.-A.; Artero, V.; Pécaut, J.; Fontecave, M. *Proc. Natl. Acad. Sci. USA* **2009**, *106*, 20627–20632.

(28)   Kaeffer, N.; Chavarot-Kerlidou, M.; Artero, V. *Acc. Chem. Res.* **2015**, *48*, 1286–1295.

(29)   Gupta, S.; Tryk, D.; Bae, I.; Yeager, A. E. *J. Appl. Electrochem.* **1989**, *19*, 19–27.

(30)   Liang, H.-W.; Brüller, S.; Dong, R.; Zhang, J.; Feng, X.; Müllen, K. *Nat. Commun.* **2015**, *6*, 7992.

(31)   Fei, H.; Dong, J.; Arellano-Jiménez, M. J.; Ye, G.; Kim, N. D.; Samuel, E. L. G.; Peng, Z.; Zhu, Z.; Qin, F.; Bao, J.; Yacaman, M. J.; Ajayan, P. M.; Chen, D.; Tour, J. M. *Nat. Commun.* **2015**, *6*, 8668.

(32)   Zou, X.; Huang, X.; Goswami, A.; Silva, R.; Sathe, B. R.; Mikmeková, E.; Asefa, T. *Angew. Chem., Int. Ed.* **2014**, *53*, 4372–4376.

(33)   Deng, J.; Ren, P.; Deng, D.; Yu, L.; Yang, F.; Bao, X. *Energy Environ. Sci.* **2014**, *7*, 1919–1923.

(34)   Xing, Z.; Liu, Q.; Xing, W.; Asiri, A. M.; Sun, X. *ChemSusChem* **2015**, *8*, 1850–1855.

(35)   Zhou, W.; Zhou, J.; Zhou, Y.; Lu, J.; Zhou, K.; Yang, L.; Tang, Z.; Li, L.; Chen, S. *Chem. Mater.* **2015**, *27*, 2026–2032.

(36)   Zhang, H.; Ma, Z.; Duan, J.; Liu, H.; Liu, G.; Wang, T.; Chang, K.; Li, M.; Shi, L.; Meng, X.; Wu, K.; Ye, J. *ACS Nano* **2016**, *10*, 684–694.

(37)   Ravel, B.; Newville, M. *J. Synchrotron Radiat.* **2005**, *12*, 537–541.

(38)   Jia, Q.; Ramaswamy, N.; Hafiz, H.; Tylus, U.; Strickland, K.; Wu, G.; Barbiellini, B.; Bansil, A.; Holby, E. F.; Zelenay, P.; Mukerjee, S. *ACS Nano* **2015**, *9*, 12496–12505.

(39)   Sa, Y. J.; Seo, D.-J.; Woo, J.; Lim, J. T.; Cheon, J. Y.; Yang, S. Y.; Lee, J. M.; Kang, D.; Shin, T. J.; Shin, H. S.; Jeong, H. Y.; Kim, C. S.; Kim, M. G.; Kim, T.-Y.; Joo, S. H. *J. Am. Chem. Soc.* **2016**, *138*, 15046–15056.

(40)   van Elp, J.; Wieland, J. L.; Eskes, H.; Kuiper, P.; Sawatzky, G. A.; de Groot, F. M. F.; Turner, T. S. *Phys. Rev. B* **1991**, *44*, 6090–6103.

(41)   Ziegelbauer, J. M.; Olson, T. S.; Pylypenko, S.; Alamgir, F.; Jaye, C.; Atanassov, P.; Mukerjee, S. *J. Phys. Chem. C* **2008**, *112*, 8839–8849.

(42)   Li, N.; Lu, W.; Pei, K.; Chen, W. *RCS Adv.* **2015**, *5*, 9374–9380.

(43)   Durst, J.; Siebel, A.; Simon, C.; Hasché, F.; Herranz, J.; Gasteiger, H. A. *Energy Environ. Sci.* **2014**, *7*, 2255–2260.

(44) Subbaraman, R.; Tripkovic, D.; Strmcnik, D.; Chang, K.-C.; Uchimura, M.; Paulikas, A. P.; Stamenkovic, V.; Markovic, N. M. *Science* **2011**, *334*, 1256–1260.

(45) Zheng, J.; Sheng, W.; Zhuang, Z.; Xu, B.; Yan, Y. *Sci. Adv.* **2016**, *2*, e1501602.

(46) Platinum prices and platinum price charts. http://www.infomine.com/investment/metal-prices/platinum (accessed Dec 6, 2017).

(47) Cobalt prices and cobalt price charts. http://www.infomine.com/investment/metal-prices/cobalt (accessed Dec 6, 2017).

(48) Morozan, A.; Goellner, V.; Nedellec, Y.; Hannauer, J.; Jaouen, F. *J. Electrochem. Soc.* **2015**, *162*, H719–H726.

(49) Shahraei, A.; Moradabadi, A.; Martinaiou, I.; Lauterbach, S.; Klemenz, S.; Dolique, S.; Kleebe, H.-J.; Kaghazchi, P.; Kramm, U. I. *ACS Appl. Mater. Interfaces* **2017**, *9*, 25184–25193.

(50) Bockris, J. O'M.: Nagy, Z. *J. Chem. Educ.* **1973**, *50*, 839–843.

(51) Bagger, A.; Ju, W.; Varela, A. S.; Strasser, P.; Rossmeisl, J. *Catal. Today* **2017**, *288*, 74–78.

(52) Tilak, B. V.; Chen, C.-P. *J. Appl. Electrochem.* **1993**, *23*, 631–640.

(53) Krstajic, N.; Trasatti, S. *J. Appl. Electrochem.* **1998**, *28*, 1291–1297.

(54) Wasylenko, D. J.; Ganesamoorthy, C.; Borau-Garcia, J.; Berlinguette, C. P. *Chem. Commun.* **2011**, *47*, 4249–4251.

(55) Marković, N. M.; Grgur, B. N.; Ross, P. N. *J. Phys. Chem. B* **1997**, *101*, 5405–5413.

(56) Schmidt, T. J.; Ross, P. N.; Markovic, N. M. *J. Electroanal. Chem.* **2002**, *524–525*, 252–260.

(57) Sheng, W.; Gasteiger, H. A.; Shao-Horn, Y. *J. Electrochem. Soc.* **2010**, *157*, B1529–B1536.

(58) Durst, J.; Simon, C.; Hasché, F.; Gasteiger, H. A. *J. Electrochem. Soc.* **2015**, *162*, F190–F193.

(59) Fan, C. L.; Piron, D. L.; Miao, H. J.; Rojas, M. *J. Appl. Electrochem.* **1993**, *23*, 985–990.

(60) González-Buch, C.; Herraiz-Cardona, I.; Ortega, E.; García-Antón, J.; Pérez-Herranz, V. *Int. J. Hydrogen Energy* **2013**, *38*, 10157–10169.

(61) Liu, G.; Li, X.; Lee, J.-W.; Popov, B. N. *Catal. Sci. Technol.* **2011**, *1*, 207–217.

(62) Eskelsen, J. R.; Qi, Y.; Schneider-Pollack, S.; Schmitt, S.; Hipps, K. W.; Mazur, U. *Nanoscale* **2014**, *6*, 316–327.

(63) Chebil, S.; Monod, M. O.; Fisicaro, P. *Electrochim. Acta* **2014**, *123*, 527–534.

(64) Pels, J. R.; Kapteijn, F.; Moulijn, J. A.; Zhu, Q.; Thomas, K. M. *Carbon* **1995**, *33*, 1641–1653.

(65) Xing, T.; Zheng, Y.; Li, L. H.; Cowie, B. C. C.; Gunzelmann, D.; Qiao, S. Z.; Huang, S.; Chen, Y. *ACS Nano* **2014**, *8*, 6856–6862.

6

SUMMARY AND SUGGESTIONS FOR FUTURE WORKS

6.1. SUMMARY

This dissertation presents the development of non-precious metal catalysts (NPMC) based on CNTs for efficient electrocatalysis towards ORR, OER, and HER, which are essential component in future hydrogen-driven energy distribution system.

First, a novel synthetic method for nanostructured carbon catalysts was developed comprising core CNTs coated by active carbon layers, which provide electric conductivity and the active sites exposed on the catalyst surface, respectively. It was demonstrated that the various types of active layers can be generated from different sources of coating materials: the heteroatom-doped carbon coated on CNT (CNT/HDC) from metal-free ionic liquid, and the porphyrinic carbon wrapped on CNT (CNT/PC) from Fe porphyrin. The synthesis involves solution-free mixing of precursors, silica coating, heat-treatment, and silica etching, and thus is very facile and scalable.

CNT/HDC, as a metal-free heteroatom-doped carbon catalyst, showed high ORR activity close to a commercial Pt/C catalyst, and better durability as well as better poison tolerance than Pt/C in alkaline media. The high ORR activity of the CNT/HDC catalyst was translated to anion exchange membrane fuel cell (AEMFC). Meanwhile, CNT/PC, an iron- and nitrogen-codoped carbon (Fe–N/C) catalyst that is one of the most promising ORR catalysts, exhibited excellent ORR activity and kinetics which rivaled the Pt/C catalyst, and much more stable than the Pt/C over 10,000 potential cycles in alkaline electrolytes. The CNT/PC showed very high fuel cell performance in both an alkaline AEMFC and an acidic proton exchange membrane fuel cell (PEMFC). The AEMFC with a CNT/PC cathode exhibited record high current and power densities among reported NPMC-based AEMFC. Therefore, we successfully demonstrated the practical applicability of developed CNT/HDC and CNT/PC catalysts in single-cell operation.

Besides realizing high catalytic activity, the preparation chemistry to reveal the role of the silica coating for the CNT/PC catalysts was investigated. The intermediate silica coating step during synthesis was found to be critical for the preferential formation of catalytically active Fe–N$_x$ coordination sites, while preventing the aggregation of Fe atoms from the Fe porphyrin precursor to

generate less-active large Fe-based particles. Temperature-dependent *in situ* X-ray absorption spectroscopy (XAS) provided evidences for the stabilizing role of the silica layer of Fe–N_x sites at high temperatures as well as the formation of more active distorted Fe–N_x sites.

Next, using the size-controlled CoO_x nanoparticles (NPs) anchored on the CNTs, we could gain the relationship between the catalyst structures and catalytic activities for bifunctional oxygen electrocatalysis (ORR & OER). *In situ* electrochemical XAS measurements revealed that Co_3O_4 and CoOOH were the major species regardless of the CoO_x particle size under both OER and ORR conditions. Size-dependent activity trends revealed the catalytic role of CoO_x NPs; OER activity increased as the size increased, and ORR activity was independent on the size. *In situ* XAS and electrochemical characterizations indicated that the abundant Co(III) species is important for the OER. In contrast, the Co(III) species observed under the ORR conditions appeared to be side product from the reaction of Co(II) with peroxide intermediate during the ORR, not to be reaction intermediate product from the direct O_2 reduction of CoO_x NPs.

In addition, the structure–activity correlation in Co–N/C catalysts was established for the HER using a suite of active-site-controllable synthesis of the hybrid between Co phthalocyanic carbon and CNT (CNT/Co-PcC). The correlation identified the active sites of Co–N/C catalyst for the HER as Co–N_x coordination site in both acidic and alkaline electrolytes. It also showed that Co@C is a possible side product from the pyrolysis step, decreasing the utilization of the active Co–N_x sites by blocking them. Kinetic insights into the active Co–N_x sites from pH-dependence showed the possible rate determining step as the hydrogen adsorption step (Volmer step). In addition, the temperature-dependence measurement revealed that the activation energy of the CNT/Co-PcC catalyst was comparable to Pt/C catalyst in 1 M KOH. This result combined with the stable long-term HER operation of the CNT/Co-PcC for 30 hours in alkaline solutions shows that Co–N/C catalysts are promising alternatives for Pt-based catalysts.

Overall, our works demonstrated i) the synthesis of novel CNT-based electrocatalysts towards ORR, OER, and HER, ii) the achievement of high activity in half-cell configurations and high performance in practical PEMFC and AEMFC, iii) the investigation of the preparation chemistry for the rational design of active electrocatalysts, and iv) the exploration for the active sites of the catalysts. The CNT-based synthetic strategy introduced in this dissertation can be further extended to a wide range of other core carbon materials (graphene, carbon nanofiber, carbon blacks) with variety types of active materials that enable application-oriented design of novel carbon nanohybrids for electrochemical energy conversion and storage devices. We particularly highlight that the "silica-protective-layer" was revealed to play a critical role on enhancing the performance of the active layers. Furthermore, the structure–activity correlations could identify the active sites. These unprecedented insights into the active sites and into the chemistry to control the properties of the active layers can

provide a general platform enabling judicious preparation of high performance electrode materials.

6.2. SUGGESTIONS FOR FUTURE WORKS

We suggest some future works to understand the chemistry underpinning the "silica-protective-layer-assisted" preparation of M–N/C catalysts and active site structures. We also point out a couple of the current issues in the oxygen and hydrogen electrocatalysis and propose future research direction.

The promotional role of the silica should be understood in the molecular level. Although we have demonstrated a spectroscopic evidence of the formation of the axial bonding of the silica to Fe–N_4 site in Fe porphyrin (**Chapter 3**), detailed molecular structure after the silica coating is still unknown, which can provide important insight into the role of the silica. The chemical environment change of Si atoms can be traced by ^{29}Si nuclear magnetic resonance (NMR) study along the preparation steps. The electronic structure modification by the silica coating can be investigated by ^{57}Fe Mössbauer spectroscopy. We hypothesize that the silica coating strongly affects the thermal decomposition behavior of the Fe porphyrin precursor during the pyrolysis. The decomposed gaseous intermediate product can be analyzed using thermogravimetric analysis/mass spectrometry (TGA/MS) to verify the silica effect.

We will extend our "silica-coating" strategy to various types of precursors containing other metals and ligands. The prepared new M–N/C catalysts will be applied for other electrocatalytic reactions such as carbon dioxide (CO_2) reduction to valuable chemical products (CO, hydrocarbons) and nitrogen (N_2) reduction to ammonia, and some important catalytic conversion of organic molecules such as selective methane activation and hydrogenation reactions.[1–4]

The active site investigation using *in situ* analysis needs further advancement in terms of acquisition time for a single spectrum. Current *in situ* experiments during the electrocatalysis are typically performed at a constant potential in a steady-state environment. It is not suitable for observing the active site transition over the potential change. *In situ* quick-XAS technique can be used to observe the time-resolved structure change that cannot only provide information about the instant appearance of the reaction intermediate but also kinetic insights into the intermediate species, enabling deeper understanding into the reaction mechanism.[5]

From the perspective of the practical application in fuel cell, Fe–N/C catalysts are the most promising candidates as the replacements of Pt/C. The high ORR activity of Fe–N/C comparable to Pt/C has been primarily demonstrated in lab-scale half-cell measurement. However, the single-cell performance of Fe–N/C is still far inferior to that of Pt/C. This can be attributed to the fact that the single-cell measurement requires much more elaborate optimization of experimental parameters, and

the effect of each parameter is still mostly unknown. We will explore the improvement principles for a better single-cell performance. Another issue in the single-cell operation with the Fe–N/C catalysts is its instability during the operation. The fast deactivation of the Fe–N/C-based single-cell has been known as the membrane (Nafion) deterioration by hydro(pero)xyl free radical species.[6] The radicals are formed by Fenton reaction of peroxide intermediates, which are formed by the less-efficient 2-electron ORR, with Fe^{2+} and Fe^{3+}.

$$Fe^{2+} + H_2O_2 \rightarrow Fe^{3+} + HO\bullet + OH^-$$

$$Fe^{3+} + H_2O_2 \rightarrow Fe^{2+} + HOO\bullet + H^+$$

To solve the long-term stability issue in single-cell, a design strategy for novel Fe–N/C catalysts with near 4-electron selective $Fe–N_x$ active sites will be proposed to minimally produce the peroxide species. As an alternative, the Fe sites could be substituted by other active $Co–N_x$ sites.

6.3. REFERENCES

(1)   Lin, S.; Diercks, C. S.; Zhang, Y.-B.; Kornienko, N.; Nichols, E. V.; Zhao, Y.; Paris, A. R.; Kim, D.; Yang, P.; Yaghi, O. M.; Chang, C. J. *Science* **2015**, *349*, 1208–1213.

(2)   Tanaka, H.; Nishibayashi, Y.; Yoshizawa, K. *Acc. Chem. Res.* **2016**, *49*, 987–995.

(3)   Shan, J.; Li, M.; Allard, L. F.; Lee, S.; Flytzani-Stephanopoulos, M. *Nature* **2017**, *551*, 605–608.

(4)   Liu, W.; Zhang, L.; Yan, W.; Liu, X.; Yang, X.; Miao, S.; Wang, W.; Wang, A.; Zhang, T. *Chem. Sci.* **2016**, *7*, 5758–5764.

(5)   Milne, C. J.; Penfold, T. J.; Chergui, M. *Coord. Chem. Rev.* **2014**, *277–278*, 44–68.

(6)   Goellner, V.; Armel, V.; Zitolo, A.; Fonda, E.; Jaouen, F. *J. Electrochem. Soc.* **2015**, *162*, H403–H414.

Young Jin Sa
CURRICULUM VITAE

EDUCATION

2013–2017	M.S.-Ph.D. Program in Chemistry, Ulsan National Institute of Science and Technology (UNIST) (Advisor: Prof. Sang Hoon Joo)
2009–2012	B.S. Degree in Chemical Engineering, UNIST, *Summa Cum Laude*, February 2013.

AWARDS & HONORS

2018	**Best Graduate Student Award**, Korean Institute of Chemical Engineers
2017	**Excellent Poster Award**, Korean Chemical Society
2017	**Korea Dow Chemical Excellent Paper Award**, Korean Chemical Society
2013–2017	**Global Ph.D. Fellowship**, National Research Foundation (NRF) of Korea
2014	**Best Poster Award**, 2014 KCS Yeongnam Regional Meeting, Korean Chemical Society

RESEARCH INTERESTS

– Development of novel catalysts for oxygen and hydrogen electrocatalysis (ORR, OER, HER, and HOR) and application to practical single cell in PEMFC, AEMFC, and PEM electrolyzer
– Design of new electrode materials for electrocatalytic CO_2 reduction
– *In situ* analysis and identification of active sites in electrocatalysts

INTERNATIONAL PUBLICATION

[30] **Young Jin Sa**, Jinwoo Woo, and Sang Hoon Joo*
"Strategies for Enhancing the Electrocatalytic Activity of M−N/C Catalysts for the Oxygen Reduction Reaction"
Topic. Catal. Accepted for Publication (2017).

[29] **Young Jin Sa**, Jae Hyung Kim, and Sang Hoon Joo*
"Recent Progress in the Identification of Active Sites in Pyrolyzed Fe−N/C Catalysts and Insights into Their Roles in Oxygen Reduction Reaction"
J. Electrochem. Sci. Technol. *8*, 169–182 (2017).

[28] Saerom Ohn, Seung Yeon Kim, Seon Kyu Mun, Junghoon Oh, **Young Jin Sa**, Sunghee Park, Sang Hoon Joo, Seong Jung Kwon*, and Sungjin Park*
"Molecularly Dispersed Nickel-Containing Species on C_3N_4 Network as Electrocatalysts for Oxygen Evolution Reaction"
Carbon *124*, 180–187 (2017).

[27] Yeonjun Shim, **Young Jin Sa**, Yunseok Shin, Junghoon Oh, Hyunchul Ju, Sang Hoon Joo, and Sungjin Park*
"Electrocatalysts Composed of Co(acetylacetonate)$_2$ Molecule and Refluxed Graphene Oxide for

Oxygen Reduction Reaction"
New J. Chem. *41*, 6203−6209 (2017).

[26] Jongsik Park[†], **Young Jin Sa**[†], Hionsuck Baik, Taehyun Kwon, Sang Hoon Joo*, and Kwangyeol Lee* ([†]equal contribution)
"Iridium-Based Multimetallic Nanoframe@Nanoframe Structure: An Efficient and Robust Electrocatalyst toward Oxygen Evolution Reaction"
ACS Nano 11, 5500−5509 (2017).

[25] Nitin Kaduba Chaudhari, Aram Oh, **Young Jin Sa**, Haneul Jin, Hionsuck Baik, Sang Gu Kim, Suk Joong Lee, Sang Hoon Joo, and Kwangyeol Lee*
"Morphology Controlled Synthesis of 2-D Ni–Ni_3S_2 and Ni_3S_2 Nanostructures on Ni Foam towards Oxygen Evolution Reaction"
Nano Convergence 4, 7 (2017).

[24] Jae Hyung Kim, **Young Jin Sa**, Hu Young Jeong, and Sang Hoon Joo*
"Roles of Fe−N_x and Fe−Fe_3C@C Species in Fe−N/C Electrocatalysts for Oxygen Reduction Reaction"
ACS Appl. Mater. Interfaces 9, 9567−9575 (2017).

[23] Taehyun Kwon[†], Hyeyoun Hwang[†], **Young Jin Sa**[†], Jongsik Park, Hionsuck Baik, Sang Hoon Joo*, and Kwangyeol Lee* ([†]equal contribution)
"Cobalt Assisted Synthesis of IrCu Hollow Octahedral Nanocages as Highly Active Electrocatalysts toward Oxygen Evolution Reaction"
Adv. Funct. Mater. 27, 1604688 (2016).

[22] **Young Jin Sa**, Dong-Jun Seo, Jinwoo Woo, Jung Tae Lim, Jae Yeong Cheon, Seung Yong Yang, Jae Myeong Lee, Dongwoo Kang, Tae Joo Shin, Hyeon Suk Shin, Hu Young Jeong, Chul Sung Kim*, Min Gyu Kim*, Tae-Young Kim*, and Sang Hoon Joo*
"A General Approach to Preferential Formation of Active Fe−N_x Sites in Fe−N/C Electrocatalysts for Efficient Oxygen Reduction Reaction"
J. Am. Chem. Soc. 138, 15046−15056 (2016).

[21] Ho Young Kim[†], Seonghun Cho[†], **Young Jin Sa**, Sun-Mi Hwang, Gu-Gon Park, Tae Joo Shin, Hu Young Jeong, Sung-Dae Yim*, and Sang Hoon Joo* ([†]equal contribution)
"Self-Supported Mesostructured Pt-Based Bimetallic Nanospheres Containing an Intermetallic Phase as Ultrastable Oxygen Reduction Electrocatalysts"
Small 12, 5347−5353 (2016).

[20] Yeonjun Shim, Jongwoo Han, **Young Jin Sa**, Seungjun Lee, Kwangrok Choi, Junghoon Oh, Sujin Kim, Sang Hoon Joo, and Sungjin Park*
"Electrocatalytic Performances of Heteroatom-Containing Functionalities in N-Doped Reduced Graphene Oxides"
J. Ind. Eng. Chem. 42, 149−156 (2016).

[19] Aram Oh[†], **Young Jin Sa**[†], Hyeyoun Hwang[†], Hionsuck Baik, Jun Kim, Byeongyoon Kim, Sang Hoon Joo*, and Kwangyeol Lee*

"Rational Design of Pt-Ni-Co Ternary Alloy Nanoframe Crystals as Highly Efficient Catalysts toward Alkaline Hydrogen Evolution Reaction"
Nanoscale 8, 16379−16386 (2016).

[18]   Bora Seo [†], Dusan Baek[†], **Young Jin Sa**, Sang Hoon Joo* ([†]equal contribution)
"Shape Effects of Nickel Phosphide Nanocrystals on the Hydrogen Evolution Reaction"
CrystEngComm 18, 6083−6089 (2016).

[17]   Bora Seo [†], **Young Jin Sa**[†], Jinwoo Woo, Kyungjung Kwon, Jongnam Park, Tae Joo Shin, Hu Young Jeong*, Sang Hoon Joo* ([†]equal contribution)
"Size-Dependent Activity Trends Combined with *in situ* X-Ray Absorption Spectroscopy Reveal Insights into Cobalt Oxide/Carbon Nanotube-Catalyzed Bifunctional Oxygen Electrocatalysis"
ACS Catal. 6, 4347−4355 (2016).

[16]   Jisun Yoon[†], Jongsik Park[†], **Young Jin Sa**[†], Yoojin Yang, Hionsuck Baik, Sang Hoon Joo*, and Kwangyeol Lee* ([†]equal contribution)
"Synthesis of Bare Pt_3Ni Nanorod from PtNi@Ni Core-Shell Nanorod by Acid Etching: One Step Surfactant Removal and Phase Conversion for Optimal Electrochemical Performance toward Oxygen Reduction Reaction"
CrystEngComm 18, 6002−6007 (2016).

[15]   Nam-In Kim[†], **Young Jin Sa**[†], Sung-Hwa Cho, Insub So, Kyungjung Kwon, Sang Hoon Joo*, and Jun-Young Park* ([†]equal contribution)
"Enhancing Activity and Stability of Cobalt Oxide Electrocatalysts for the Oxygen Evolution Reaction *via* Transition Metal Doping"
J. Electrochem. Soc. 163, F3020−F3028 (2016).

[14]   Seongwan Jang[†], **Young Jin Sa**[†], Sang Hoon Joo*, and Kang Hyun Park* ([†]equal contribution)
"Ordered Mesoporous Copper Oxide Nanostructures as Highly Active and Stable Catalysts for Aqueous Click Reactions"
Catal. Commun. 81, 24−28 (2016).

[13]   Jae Yeong Cheon, Kyoungho Kim, **Young Jin Sa**, Sun Hye Sahgong, Yugyeong Hong, Jinwoo Woo, Sung-Dae Yim, Hu Young Jeong, Youngsik Kim*, and Sang Hoon Joo*
"Graphitic Nanoshell/Mesoporous Carbon Nanohybrids as Highly Efficient and Stable Bifunctional Oxygen Electrocatalysts for Rechargeable Aqueous Na-Air Batteries"
Adv. Energy Mater. 6, 1501794 (2016).

[12]   Jongwoo Han, **Young Jin Sa**, Yeonjun Shim, Min Choi, Noejung Park, Sang Hoon Joo*, and Sungjin Park*
"Coordination Chemistry of [Co(acac)₂] with N-Doped Graphene: Implications for Oxygen Reduction Reaction Reactivity of Organometallic $Co-O_4-N$ Species"
Angew. Chem. Int. Ed. 54, 12622−12626 (2015).

[11]   Bora Seo, Gwan Yeong Jung, **Young Jin Sa**, Hu Young Jeong, Jae Yeong Cheon, Jeong Hyeon Lee, Ho Young Kim, Jin Chul Kim, Hyeon Suk Shin, Sang Kyu Kwak*, and Sang Hoon Joo*
"Monolayer-Precision Synthesis of Molybdenum Sulfide Nanoparticles and Their Nanoscale Size

Effects in the Hydrogen Evolution Reaction"
ACS Nano 9, 3728−3739 (2015).

[10]   Kyungjoo Lee, **Young Jin Sa**, Hu Young Jeong, Christopher W. Bielawski, Sang Hoon Joo, and Hoi Ri Moon*
"Simple Coordination Complex–Derived Three-Dimensional Mesoporous Graphene as an Efficient Bifunctional Oxygen Electrocatalyst"
Chem. Commun. 51, 6773−6776 (2015).

[9]   Young-Eun Shin, **Young Jin Sa**, Seungyoung Park, Jiwon Lee, Kyung-Hee Shin, Sang Hoon Joo*, and Hyunhyun Ko*
"Ice-Templated, pH-Tunable Self-Assembly Route to Hierarchically Porous Graphene Nanoscroll Networks"
Nanoscale 6, 9734−9741 (2014).

[8]   Jae Hwa Lee[†], **Young Jin Sa**[†], Tae Kyung Kim, Hoi Ri Moon*, and Sang Hoon Joo* ([†]equal contribution)
"A Transformative Route to Nanoporous Manganese Oxides of Controlled Oxidation States with Identical Textural Properties"
J. Mater. Chem. A 2, 10435−10443 (2014).

[7]   **Young Jin Sa**[†], Chiyoung Park[†], Hu Young Jeong, Seok-Hee Park, Zonghoon Lee, Kyuoung Taek Kim, Gu-Gon Park, and Sang Hoon Joo* ([†]equal contribution)
"Carbon Nanotubes/Heteroatom-Doped Carbon Core-Sheath Nanostructures as Highly Active, Metal-Free Oxygen Reduction Electrocatalysts for Alkaline Fuel Cells"
Angew. Chem. Int. Ed. 53, 4102−4106 (2014).

[6]   Boram Jun, Kwang-Eun Jeong, Sang Hoon Joo, **Young Jin Sa**, Sung Hoon Park, Jong-Ki Jeon, and Young-Kwon Park*
"Catalytic Conversion of *Undaria Pinnatifida* over Nanoporous Materials Using Py-GC/MS"
J. Nanosci. Nanotech. 13, 7794−7800 (2013).

[5]   Jae Yeong Cheon, Taeyoung Kim, YongMan Choi, Hu Young Jeong, Min Gyu Kim, **Young Jin Sa**, Jaesik Kim, Zonghoon Lee, Tae-Hyun Yang, Kyungjung Kwon, Osamu Terasaki, Gu-Gon Park*, Radoslav R. Adzic*, and Sang Hoon Joo*
"Ordered Mesoporous Porphyrinic Carbons with Very High Electrocatalytic Activity for the Oxygen Reduction Reaction"
Scientific Reports 3, 2715 (2013).

[4]   **Young Jin Sa**[†], Kyungjung Kwon[†], Jae Yeong Cheon, Freddy Kleitz, and Sang Hoon Joo* ([†]equal contribution)
"Ordered Mesoporous Co_3O_4 Spinels as Stable, Bifunctional, Noble Metal-Free Oxygen Electrocatalysts"
J. Mater. Chem. A 1, 9992−10001 (2013).

[3]   Mi-Jin Jeon, Jong-Ki Jeon, Dong Jin Suh, Sung Hoon Park, **Young Jin Sa**, Sang Hoon Joo, and Young-Kwon Park*

"Catalytic Pyrolysis of Biomass Component over Mesoporous Catalysts Using Py-GC/MS"
Catal. Today 204, 170−178 (2013).

[2]   Ju-Hwan Oh, **Young Jin Sa**, Sang Hoon Joo*, and Jae-Seung Lee*
"Assembling Gold Nanocubes Into a Nanoporous Gold Material"
Bull. Kor. Chem. Soc. 33, 1777−1780 (2012).

[1]   Kyungjung Kwon, **Young Jin Sa**, Jae Yeong Cheon, and Sang Hoon Joo*
"Ordered Mesoporous Carbon Nitrides with Graphitic Frameworks as Metal-Free, Highly Durable, Methanol-Tolerant Oxygen Reduction Catalysts in an Acidic Medium"
Langmuir 28, 991−996 (2012).

DOMESTIC PUBLICATION

[3]   **Young Jin Sa**, Jinwoo Woo, Jae Hyung Kim, and Sang Hoon Joo*
"전이금속−질소/탄소 기반 산소환원반응 촉매의 최신 연구 동향"
Catalysis 33, 34 (2017).

[2]   **Young Jin Sa**, and Sang Hoon Joo*
"Recent Advances in M–N/C Electrocatalysts for Polymer Electrolyte Membrane Fuel Cells"
NICE (News and Information for Chemical Engineers) 35, 264 (2017).

[1]   **Young Jin Sa**, and Sang Hoon Joo*
"Recent Trends and Perspectives in Non-Platinum Oxygen Reduction Reaction Catalysts"
E. Chem Magazine 5, 28−39 (2014).

PATENTS

[2]   Sang Hoon Joo, Jinwoo Woo, and **Young Jin Sa**
"M-N-C계 전극촉매 및 그 제조방법과 Fe-N-C계 전극촉매를 포함하는 연료전지"
"M-N-C Electrocatalyst, Method of Manufacturing the Same and Fuel Cell Comprising Fe-N-C Electrocatalyst"
Korea Patent Appl. 10-2017-0123479 (Sep. 25, 2017).

[1]   Sang Hoon Joo, **Young Jin Sa**, and Tae Young Kim
"Fe-N-C계 전극촉매 및 그 제조방법과 Fe-N-C계 전극 촉매를 포함하는 연료전지"
"Fe-N-C Electrocatalyst, Method of Manufacturing the Same and Fuel Cell Comprising Fe-N-C Electrocatalyst"
Korea Patent Appl. 10-2016-0097317 (Jul. 29, 2016).